Computational Design of Structures for Enhanced Failure Resistance

Jonathan Brent Russ

Submitted in partial fulfillment of the
requirements for the degree of
Doctor of Philosophy
under the Executive Committee
of the Graduate School of Arts and Sciences

COLUMBIA UNIVERSITY

2021

ABSTRACT

Computational Design of Structures for Enhanced Failure Resistance

Jonathan Brent Russ

The field of structural design optimization is one with great breadth and depth in many engineering applications. From the perspective of a designer, three distinct numerical methodologies may be employed. These include size, shape, and topology optimization, in which the ordering typically (but not always) corresponds to the order of increasing complexity and computational expense. This, of course, depends on the particular problem of interest and the selected numerical methods. The primary focus of this research employs density-based topology optimization with the goal of improving structural resistance to failure.

Beginning with brittle fracture, two topology optimization based formulations are proposed in which low weight designs are achieved with substantially increased fracture resistance. In contrast to the majority of the current relevant literature which favors stress constraints with linear elastic physics, we explicitly simulate brittle fracture using the phase field method during the topology optimization procedure. In the second formulation, a direct comparison is made against results obtained using conventional stress-constrained topology optimization and the improved performance is numerically demonstrated. Multiple enhancements are proposed including a numerical efficiency gain based on the Schur-complement during the analytical sensitivity analysis and a new function which provides additional path information to the optimizer, making the gradient-based optimization problem more tractable in the presence of brittle fracture physics.

Subsequently, design for ductile failure and buckling resistance is addressed and a numerically efficient topology optimization formulation is proposed which may provide significant design improvements when ductile materials are used and extreme loading situations are anticipated. The proposed scheme is examined regarding its impact on both the peak load carrying capacity of the structure and the amount of external work required to achieve this peak load, past which the structure may no longer be able to support any increase in the external force. The optimized structures are

also subjected to a post-optimization verification step in which a large deformation phase field fracture model is used to numerically compare the performance of each design. Significant gains in structural strength and toughness are demonstrated using the proposed framework.

Additionally, the failure behavior of 3D-printed polymer composites is investigated, both numerically and experimentally. A large deformation phase field fracture model is derived under the assumption of plane-stress for numerical efficiency. Experimental results are compared to numerical simulations for a composite system consisting of three stiff circular inclusions embedded into a soft matrix. In particular, we examine how geometric parameters, such as the distances between inclusions and the length of initial notches affect the failure pattern in the soft composites. It is shown that the mechanical performance of the system (e.g. strength and toughness) can be tuned through selection of the inclusion positions which offers useful insight for material design.

Finally, a size optimization technique for a cardiovascular stent is proposed with application to a balloon expandable prosthetic heart valve intended for the pediatric population born with Congenital Heart Disease (CHD). Multiple open heart surgical procedures are typically required in order to replace the original diseased valve and subsequent prosthetic valves with those of larger diameter as the patient grows. Most expandable prosthetic heart valves currently in development to resolve this issue do not incorporate a corresponding expandable conduit that is typically required in a neonate without a sufficiently long Right Ventricular Outflow Tract (RVOT). Within the context of a particular design, a numerical methodology is proposed for designing a metallic stent incorporated into the conduit between layers of polymeric glue. A multiobjective optimization problem is solved, not only to resist the retractive forces of the glue layers, but also to ensure the durability of the stent both during expansion and while subject to the anticipated high cycle fatigue loading. It is demonstrated that the surrogate-based optimization strategy is effective for understanding the trade-offs between each performance metric and ultimately efficiently arriving at a single optimized design candidate. Finally, it is shown that the desired expandability of the device from 12mm to 16mm inner diameter is achievable, effectively eliminating at least one open heart surgical procedure for certain children born with CHD.

Table of Contents

List of Tables

List of Figures

Acknowledgements

As 17th century English poet John Donne once wrote, "no man is an island, entire of itself", and I am certainly no exception. There are seemingly countless people with whom I have interacted over the past few years, and benefited greatly from, both intellectually and professionally. Although it is not possible to adequately convey my gratitude to everyone, I feel the need to personally thank a number of people for their time and effort during my doctoral studies.

First, my sincerest thanks go to my advisor, Professor Haim Waisman, for countless hours spent providing suggestions and guidance along the way. I will always be grateful for the help he has given me and am especially grateful for the consistent encouragement throughout my time at Columbia.

I would also like to thank the other members of my dissertation committee including Professor Jacob Fish, Professor WaiChing Sun, Professor Jeffrey Kysar, and Dr. Miguel Aguilo of Sandia National Laboratories. Their time and effort is very sincerely appreciated.

For the many intellectually fruitful discussions, I would like to thank my student colleagues. In particular I would like to personally thank Lampros Svolos, Rilin Shen, Eric Bryant, and Timothy Artz for the innumerable hours spent discussing research and life in general. To my officemate, Eric Bryant, I am also grateful for the seemingly random cacophony of laughter that made the longest days seem a little bit shorter.

This dissertation would not have been possible without the funding received from the Presidential Fellowship at Columbia University and the Guggenheim Fellowship granted to me by the Department of Civil Engineering and Engineering Mechanics.

Finally, I am forever indebted to my friends and family who have stayed by my side throughout my life, including through the tumultuous emotional roller coaster of a doctoral program.

"Who is wise? One who learns from every man.

Who is strong? One who overpowers his evil inclinations.

Who is rich? One who is satisfied with his lot.

Who is honorable? One who honors his fellows."

- Simeon ben Zoma

Chapter 1

Introduction

1.1 Background and motivation

1.1.1 Topology optimization for brittle fracture resistance

The field of optimal structural design is fascinating one with a great deal of breadth. Within this context, topology optimization has enjoyed a large amount of success since its introduction in the work of Bendsøe and Kikuchi [1]. In particular, with recent advancements in additive manufacturing techniques, many of the resulting designs can be physically realized [2]. This method has been applied to a wide variety of interesting engineering problems and has had a large impact across many fields. Deaton and Grandhi [3] provide an excellent survey of the field, including multiphysics applications and other recent advancements. Brittle fracture is one such type of failure physics which, in general, a designer might wish to avoid.

Failure prevention has historically been included in topology optimization formulations via stress-constraints in which the material is not allowed to exceed some percentage of the yield stress. This has been explored in many works ([4, 5, 6, 7, 8] to only name a few). In recent years, the use of topology optimization incorporating material damage in the formulation has received increasingly more attention. Originally explored by Bendsøe and Diaz [9], the effect of material degradation has been included in topology optimization procedures in a number of works. Jansen et al. [10] model damage as a loss of stiffness in regions with a fixed shape in order to increase structural redundancy. Amir and Sigmund [11] maximize the stiffness of a reinforced concrete structure through optimal layout of steel reinforcing bars in concrete, which explicitly included nonlocal damage. Amir [12] extended this idea to simultaneously optimize the steel reinforcement bars and concrete, again

including nonlocal damage, in order to produce minimum weight designs. James and Waisman [13] also explicitly model the evolution of brittle damage and directly constrain the local damage intensity. Multiple load cases were considered and a damage superposition approach was explored in James and Waisman [14]. The extension to ductile materials will be discussed in the subsequent section.

Similar to brittle damage, albeit less frequently, brittle fracture resistance has also been explored previously. Challis et al. [15] used a level-set approach and obtained brittle fracture resistance via minimization of an aggregate objective including the elastic energy released by virtual crack extension. Kang et al. [16] employed the J-integral at predefined locations in the design domain in order to predict crack propagation. In both of these works, fracture propagation was not explicitly modeled. Subsequently, Xia et al. [17] and Da et al. [18] used the phase field fracture method in order to increase the fracture resistance of a two phase composite structure. The topology of an inclusion phase was optimized to increase the resistance to brittle fracture via work maximization. This followed the work of San and Waisman [19] in which the arrangement of inclusions in a polymer composite microstructure was optimized for rupture resistance, also explicitly simulating fracture via the phase field method.

The phase field approach to fracture modeling, based on the work of Francfort and Marigo [20], Bourdin et al. [21], Miehe et al. [22, 23, 24] and others, has many important benefits over other approaches. The method has been widely adopted due to its ease in handling complex crack topologies through an additional scalar field equation. This additional field equation governs the evolution of the crack topology and, therefore, removes the complexities associated with explicitly tracking the fracture surface. In the context of density-based topology optimization the use of a fixed design mesh is very convenient (as also mentioned in Da et al. [18]).

Here it should be noted that there are now several different topology optimization approaches, including the traditional density-based method [1], a level-set method [25], a phase field method [26, 27], and others (see [28, 3]). In this thesis the density-based design parameterization is employed rather than the phase field method for topology optimization, which is distinct from the phase field

method for fracture modeling. All subsequent references to the phase field method refer to phase field fracture.

While great progress has been made in the field of topology optimization for brittle failure resistance, much of the work avoids the explicit modeling of brittle fracture during the optimization procedure, assumes cracks form at locations known a-priori, or is only intended for changing the topology of an inclusion phase in a composite structure. In this context, we wish to extend the current state-of-the-art further into the realm of homogeneous material brittle fracture and determine whether explicitly modeling the fracture physics during the optimization procedure introduces some advantages or disadvantages over current techniques.

1.1.2 Topology optimization for ductile failure and buckling resistance

While design for resistance to brittle failure is quite important in many fields, design for ductile failure and buckling resistance poses multiple additional layers of complexity in many engineering specialties. In the context of extreme contingency load cases when the primary structural components are comprised of a ductile material, failure is typically associated with a complete loss of the structure's integrity and load carrying capacity. Exceeding a structure's peak load carrying capacity may result in ductile fracture or buckling of structural components and, therefore, should be carefully considered during the design process.

Elastoplastic continuum topology optimization has been studied quite extensively since the work of Swan and Kosaka [29] and Maute et al. [30]. In [30] the importance of considering both elastoplastic and buckling responses is mentioned explicitly in the introduction, although the paper deals only with the material nonlinearity. Since these works, there have been significant additional strides taken along similar lines with a few particular ones we wish to note, including [31, 32, 33, 34, 35]. Amir [36] used elastoplasticity as a means to enforce stress constraints. Inertial effects have been included in some rate-independent [37] and rate-dependent [38, 39] plasticity works. Additionally, finite strain kinematics have been considered in [40, 38, 39] for example. These works are particularly impressive due to the difficulties associated with element inversion in low

density regions. Alberdi and Khandelwal [39] have partially remedied this problem via bi-material optimization in which voids are no longer present. Notable related work in the context of multiscale topology optimization with elastoplastic material effects includes [41, 42] for instance. Finally, and more recently, Fin et al. [43] proposed a limit analysis technique to increase a structures peak load. However, this seems to rely on a perfect elastic-plastic material model which is limited to certain classes of materials. A material which exhibits a significant amount of strain hardening would not be accounted for.

While structural failure in topology optimization has traditionally focused on brittle failure as mentioned in the previous subsection, ductile failure has also been handled in a number of interesting ways. These include directly constraining local failure/damage indicators [44, 45, 46] that are uncoupled from (i.e. do not affect) the forward analyses. However, these works typically employ p-norm aggregation functions to enforce the local constraints. These uncoupled damage indicators are typically preferred for reasons of computational efficiency and robustness, as is mentioned explicitly in [45]. This strategy is in contrast to the explicit simulation of damage during the optimization procedure as was done in Li et al. [47] with a local damage model and, subsequently, in Li et al. [48] which included the use of a nonlocal damage model, which helped alleviate mesh dependency in the forward analyses.

In the context of the density-based topology optimization formulation, the sensitivity analysis of the functions involved in the mathematical optimization statement is of the utmost importance due primarily to the large number of design variables defined in a typical topology optimization problem. To this end we use the adjoint framework set forth by Michaleris et al. [49] and subsequently expanded upon by Alberdi et al. [50]. While Fin et al. [43] remark on the cost of the sensitivity analysis of the incremental formulation, if many increments are required for a particular problem, perhaps techniques such as those noted in Wang et al. [51] could be used in order to significantly reduce this expense, or check-pointing techniques could be employed such as those in [52].

Finally, to the best of our knowledge, none of the aforementioned works have included the effects of structural buckling in their optimization formulations, which may be the *actual* failure

mode of a structure in many situations. Design for buckling using continuum topology optimization formulations appears to have begun with the efforts of Neves at al. [53] in which the critical buckling load factor was maximized. Since then a number of papers have emerged including those accounting for geometric nonlinearity [54, 55, 56, 57, 58] for which the nonlinear buckling sensitivity analysis was first presented in Reitinger and Ramm [59]. In the more specific context of buckling of microstructures, the works [60, 61] are also noteworthy. Among the many issues encountered in continuum topology optimization in the context of buckling, the appearance of pseudo buckling modes in regions of low density has received significant attention [62, 63, 64]. More recently, Ferrari and Sigmund [65] have "revisited" the use of small deformation, linear elastic buckling analysis, and provided a set of useful studies which included comparisons with aggregation functions such as the one used in Chin and Kennedy [66]. Subsequently, Ferrari and Sigmund [67] proposed a method for large scale topology optimization including buckling constraints using a multi-level solution strategy.

None of the aforementioned continuum buckling works have included the effects of elastoplastic material response. This may be due to a number of factors, the most important of which being the very large computational burden associated with not only a nonlinear forward analysis in which large deformation kinematics may be used and arc-length methods may be required, but also the sensitivity analysis associated with buckling load factors. The buckling load factors themselves also may no longer be physically meaningful due to the assumption of linearity, particularly with regards to the stress response, when the eigenproblem is solved. Nonetheless, notable literature include the work of Kaliszky and Logo [68] in which elastoplastic material response of truss structures is considered along with compressive stress constraints for buckling resistance, and Schwarz and Ramm [69] which demonstrate the direct (rather than adjoint) sensitivity analysis for use in shape optimization of structures including elastoplasticity, large deformations, and buckling.

Since both ductile failure and buckling of a structure under a particular load are possible, it is clear that a designer should consider these failure modes in the design process if large contingency loads are expected. However, due to the inherent computational expense of simulating the large

deformation ductile failure and/or buckling of a structure this concept has not yet been achieved in the topology optimization literature. Therefore, we wish to provide a computationally efficient framework for practicing designers that provides both resistance to ductile failure and buckling of structural members.

1.1.3 Failure behavior of hyperelastic composites

While design for brittle and ductile failure resistance is clearly of great importance in engineering applications, ultimately the computational methods used during the design phase are only useful if they are sufficiently accurate. Since fracture of many engineering materials is still quite difficult to predict with high accuracy, validation exercises are extraordinarily important. One very interesting, intellectually rich area of potential research is in the field of soft composite failure modeling. Polymeric composites are versatile high performance materials that are widely used in a variety of engineering applications. These composites, typically consisting of a polymer matrix reinforced by hard-inclusions, offer significant advantages over pure polymers. For example, well-designed combinations of these components may lead to superior mechanical and thermal properties that are infeasible using a single material [70]. In particular, since the strength and stiffness of the inclusion phase is typically much higher than those of the matrix material, the stiffness of the composite is typically improved in addition to the material toughness due to the treacherous path cracks must traverse through the matrix in order for the structure to fail catastrophically.

The use of 3D-printing for rapid manufacturing of polymer composites has gained significant attention in the last two decades [71]. This additive manufacturing technique can produce polymer composites with complex geometries and precise inclusion positions/shapes specified using computer aided design software. However, while the addition of inclusions in a polymer matrix may enhance its strength, it may also decrease its toughness [72]. In particular, a different arrangement of inclusions may entirely alter the failure pattern of the polymer composite, thereby affecting its macroscopic properties.

Theoretical and numerical predictions together with the observed performance of natural

and biological materials indicate that microstructural design holds significant potential for the development of superior materials. The physical realization of these ideas relies on advances in material fabrication techniques and the ability to produce microstructures at various length scales. Thus, for example, Slesarenko et al. [73, 74] experimentally realized the underlining failure mechanisms in nacre-like 3D-printed composite structures. In particular, they observed distinct single-step and two-step failure modes in the soft interfaces depending on the loading direction relative to microstructures. Buehler and co-authors [75, 76] employed 3D-printing to illustrate the improved toughness performance of the numerically predicted bio-inspired composites based on mineralized natural materials with soft interfaces. Ryvkin et al. [77] realized fault-tolerant lattice structures through pre-designed failure in weak links, thus, preventing damage propagation, and promoting even damage distribution. Alternative strategies such as crack tip blunting [75], microstructure-guided crack deflection [78], and shielding [79] have been successfully demonstrated for 3D-printed composites. Liu and Li [80] reported increased fracture toughness in 3D-printed composites due to weak wavy interfaces. We note, however, that the fracture behavior of the soft materials is rate-sensitive [81], and this aspect can play an important role in the failure mechanisms of dynamically loaded composites [82].

Computational modeling of polymer composite failure at large deformation remains a significant challenge. Beyond the hyperelastic material modeling and complex geometries, numerical methods that attempt to model fracture must be able to capture crack nucleation at multiple arbitrary spatial locations and crack propagation along complex trajectories while accounting for crack coalescence and branching. Furthermore, these methods should also be numerically robust (e.g. capable of handling large element distortions), insensitive to the choice of mesh discretization, and well-posed (e.g. convergent under mesh refinement).

The phase field method is one such promising method that has emerged in the past two decades [20, 21, 22, 23, 24], and has already been explored in a variety of areas including quasi-brittle fracture [83, 84, 85, 86], ductile fracture [87, 88, 89, 90], fracture of geological materials including hydraulic fracture [91, 92, 93, 94], interphasial fracture [95, 86, 96], anisotropic fracture [97], bone

fracture [98], and fracture of viscoelastic materials [98]. In the phase field method, the discrete crack surface is approximated by a diffusive crack representation via an auxiliary scalar field. The evolution of the fracture surface is captured by an additional PDE, which can be derived variationally [21] or using thermodynamic principles [87]. The majority of phase field methods published in the literature require only a few parameters, including one controlling the width of the diffusive fracture surface l_0, and either the critical energy release rate, G_c, or the critical tensile energy density Ψ_c, which may be viewed as material parameters (although the more recent cohesive phase field methods treat the length scale simply as a numerical regularization parameter).

In the context of large strain fracture of hyperelastic materials, several notable phase field fracture methods have been published. Miehe et al. [99] was the first to propose large deformation brittle fracture formulation for rubbery polymers. Wu et al. [100] proposed a stochastic fracture analysis of rubber reinforced with carbon black inclusions, which provided insight for better design of these materials. Subsequent work by San and Waisman proposed optimization of the particle locations in a soft polymer matrix to achieve more failure resistant designs [101].

Raina and Miehe [102] and Gultekin et al. [103] studied the fracture of soft biological tissues accounting for anisotropic hyperelasticity with different fiber orientations. Talamini et al. [104] proposed a new energy split in the phase field formulation to account for chain bond deformation, which resulted in a modified phase field driving force. This formulation was later extended by Mao and Anand [105] to model fracture of polymeric gel. Bilgen and Weinberg [106] also developed new ad-hoc driving forces, which were motivated by general fracture mechanics considerations. Kumar et al. [107] derived toughness functions to model the fracture and healing of elastomers undergoing large deformations. Yin et al. [108] studied fracture of exotic natural structures (Bouligand structures), and compared their numerical results with 3D-printed samples. Additionally, rate dependent rubber fracture has been studied by Loew et al. [109] and Yin and Kaliske [110].

It should be noted that, as with most numerical methods, there are also drawbacks of the phase field method when compared with other techniques. A few important cons, such as the computational cost, are discussed in the work of Wu et al. [111]. Advancements in mesh adaptivity

seek to alleviate some of the computational burden (see [112] for example). Additionally, in classical phase field models the strength of the material is tied to the length scale (see Borden et al. [83] for 1D analysis).

Finally, it is important to mention other interesting failure models for soft materials that have been proposed. In particular, the work of Volokh on hyperelasticity with softening, based on the idea of energy limiters, and more recently the material sink formulation [113, 114, 115] also seems to be promising.

While all of the aforementioned work significantly contributes to either our physical understanding of soft composites or our ability to numerically predict their failure behavior, very few works combine the two in order to enhance our collective knowledge. In this context, we wish to provide not just a simple validation exercise for one particular version of phase field fracture, but also use it in conjunction with experimental data in an effort to better understand the failure behavior of soft composite materials with hard inclusions.

1.1.4 Cardiovascular stent design for an expandable valved conduit

Congenital heart disease (CHD) affects an estimated 40,000 children per year in the United States alone [116, 117, 118], within which an estimated 20% of cases involve abnormalities in the right ventricular outflow tract (RVOT) [116, 119] and may require pulmonary valve replacement. This typically involves multiple invasive surgeries to replace the diseased original valve and subsequent prosthetic replacement valves with those of increasingly larger diameter as the patient grows into adulthood [120, 121]. Multiple experimental and numerical studies in the existing literature have contributed to eventually resolving this important issue [122, 123, 124, 125, 126, 127, 128]. While strides have been made in recent years towards the development of an expandable prosthetic valve replacement [129, 130, 131], none of the current designs yet incorporate an integrated and expandable conduit for concomitant repair of the RVOT [132]. Therefore, the design need for a corresponding expandable replacement conduit clearly exists.

One particularly attractive option for achieving this incorporates a metallic stent (which may

be optimized) in the valved region. A number of relevant works exist in the literature regarding the computational design of cardiovascular stents, however the vast majority are designed for coronary arteries. The review articles of Bressloff et al. [133] and Karanasiou et al. [134] provide comprehensive summaries of the current state of the art, including stent materials, geometric parameterizations, and quantitative performance metrics. Numerical stent optimization and parameter studies have been performed for stents constructed of various materials including nitinol [135, 136], 316L stainless steel [137, 138, 139, 140, 141, 142, 143, 136], cobalt chromium [144], and various polymers [145, 146, 147].

Size optimization techniques may be employed, examining the impact of geometric parameters such as the width and thickness of the stent struts. While most works utilize low-dimensional geometric parameterizations or compare the performance of existing stent geometries, others increase the design freedom using techniques in shape optimization with mesh-morphing [148, 149] or a design parameterization based on nonuniform rational B-splines (NURBS) [150].

Desired mechanical properties vary across the literature but generally include measures of fatigue resistance, peak stress or strain, radial recoil, foreshortening, flexibility, and expansion uniformity (i.e. whether the dog-boning phenomena occurs [140, 151, 152]). Within the specific context considered in this dissertation, we are interested in achieving uniform permanent expansion of the entire device using a non-compliant balloon, in addition to optimizing performance metrics related to stent durability and expandability.

Typical stent expansion finite element simulations involve large deformations, contact, and material nonlinearity (e.g. hyperelasticity, elastoplasticity) all of which greatly increase the computational expense. In order to alleviate some of the numerical burden, the majority of existing works employ surrogate-based optimization techniques using relatively few detailed computational analyses. To this end, Kriging-based surrogate models have dominated much of the literature [135, 153, 152, 151, 145, 154, 155, 156, 157], although others have used polynomial based response surfaces [146], or provide a comparison of multiple approaches [156].

It should also be noted that most of the aforementioned works typically only employ structural

finite element analyses due primarily to the generally larger numerical expense of computational fluid dynamics (CFD) simulations. However a few works have also investigated stent design for hemodynamic performance [154, 158, 159]. In the current context, the stent is not directly in the flow path, therefore mitigating the need for CFD simulations at this particular stage of the design process.

1.2 Dissertation outline

In Chapters 2 and 3, we propose two topology optimization based formulations for computationally achieving low weight structural designs with enhanced resistance to brittle fracture. The failure physics are explicitly simulated during the optimization process utilizing the phase field method for brittle fracture. A density-based topology optimization formulation is used and the analytical sensitivities of the relevant functions used in each mathematical optimization problem statement are derived. Additionally, a numerical efficiency gain based on the Schur-complement is presented for use during the analytical sensitivity computation. In the first formulation, the phase field approximation of the fracture surface energy is directly constrained in order to provide the desired resistance to brittle failure. In the second, a new objective function is proposed which provides additional path information to the optimizer. Increased local control of the topology is introduced via a smoothed threshold function in the phase field fracture formulation and a constraint relaxation continuation scheme is proposed to alleviate some numerical difficulty during the initial optimization iterations.

Subsequently, a new formulation is proposed in Chapter 4 for incorporating local ductile failure constraints and buckling resistance into elastoplastic structural design. While a lot of recent progress has been made within the context of continuum topology optimization with elastoplasticity and buckling separately, these phenomena are typically not considered together. The proposed formulation is computationally efficient and robust, partly due to its reliance on small strain kinematics and a separation of the elastoplastic response from the buckling load factors computed during the optimization procedure. An aggregate objective function is constructed in which the total

work in an elastoplastic analysis is maximized and an aggregation function of the load factors from a separate linear elastic buckling analysis is included. Additionally, local ductile failure constraints are handled via a framework without aggregation functions and a new pseudo buckling mode filter is proposed. Each of the resulting designs are then subject to a verification step in which a large strain ductile failure model is used in order to compare the performance of the optimized designs obtained for three numerical examples. The results demonstrate that structural responses such as peak load carrying capacity and total external work required to reach the peak load may be significantly improved using the suggested framework.

In Chapter 5, we investigate the failure behavior of 3D-printed polymer composites undergoing large deformation. Experimental results are compared to numerical simulations using the phase field fracture method with an energetic threshold and a numerically efficient plane-stress implementation. The developed numerical/experimental strategy is applied to a composite system consisting of three stiff circular inclusions embedded into a soft matrix. In particular, we examine how geometric parameters, such as the distances between inclusions and the length of initial notches, affect the failure pattern in the soft composites. We observe complex failure sequences including crack arrest and secondary crack initiation in the bulk material. It is demonstrated that our numerical simulations capture these essential features of the composite failure behavior and the numerical results are in good agreement with the experiments. We find that the mechanical performance of the composites (i.e. strength and toughness) can be tuned through selection of the inclusion positions. These findings offer useful insight for the design of soft composite materials with improved failure resistance.

In Chapter 6 we investigate the design of a cardiovascular stent for potential use in a balloon expandable valved conduit. More specifically, we consider a polymeric replacement conduit within which a prosthetic valve resides. The valve itself is assumed to be constructed using a polymeric material (similar to that of the conduit) and is adhered to the conduit via an intermediate polymeric glue layer. After an initial device implantation, valve expansion can occur through transcatheter balloon dilation of the entire device, which would permanently deform to a larger desired diameter.

However, the region in which the polymeric glue resides would likely undergo smaller permanent dilation than the rest of the device due to differences in the mechanical properties of the conduit material and the polymeric glue. In order to counteract the anticipated retractive behavior in the valved region, a stent can be inserted between the inner valve structure and the outer conduit. A numerical strategy for the design of an appropriate stent in this specific context is proposed to achieve this goal. Additionally, metrics associated with both resistance to ductile fracture and high cycle fatigue are concurrently optimized. Due to the large computational expense of each high-fidelity finite element expansion simulation, a surrogate-based optimization technique is employed. The defined multiobjective optimization problem is then solved using the surrogate functions and a highly effective algorithm for obtaining a set of Pareto-optimal designs. The associated trade-offs between various performance metrics are then graphically illustrated. Subsequently, a normalized aggregate objective function with unit weighting is also employed within a single objective optimization problem in order to identify one optimized design candidate with high performance.

Finally, concluding remarks are provided in Chapter 7, along with a summary of the main contributions of this thesis and plans for future work and improvement.

Chapter 2

A topology optimization formulation for brittle fracture resistance

This chapter is published as a journal article in: J. B. Russ and H. Waisman, "Topology optimization for brittle fracture resistance", Computer Methods in Applied Mechanics and Engineering, vol. 347, pp. 238–263, Apr. 2019, doi: 10.1016/j.cma.2018.12.031.

2.1 Introduction

In this chapter we explore the use of topology optimization for obtaining minimum weight designs with higher brittle fracture resistance by directly constraining the phase field approximation of the fracture surface energy. A single material phase is considered and the total weight is minimized. Additionally, we investigate the use of the two most common energy splits and degradation functions in the phase field formulation. As previously discussed in Da et al. [18], the phase field approximation for fracture has many benefits in topology optimization including the use of a fixed design mesh in which crack nucleation is handled naturally. We derive the path-dependent sensitivities for the relevant functions via a computationally-efficient adjoint formulation and illustrate a Schur-complement type approach at the element level during the sensitivity analysis.

The remainder of the chapter is organized as follows: In Section 2.2 we review the governing equations for quasi-static brittle fracture via the standard phase field formulation and provide the details of the finite element discretization. We then review the density-based design parameterization, define the optimization problem, and derive the analytical sensitivities in Section 2.3. The effect of the energy split, degradation function, and length scale parameter in the phase field fracture formulation is investigated briefly in Section 2.4, along with two numerical examples that demonstrate the effectiveness of this approach.

2.2 Standard phase field fracture formulation

In this section we briefly summarize the phase field description of quasistatic, brittle fracture adopted herein. Following the work of Francfort and Marigo [20], Bourdin et al. [21] and Miehe et al. [22, 23], we provide a short derivation of the two-field coupled problem for brittle crack evolution. Subsequently, the details of the finite element discretization are provided.

2.2.1 Phase field formulation for brittle fracture

In [20], the variational approach to brittle fracture is introduced as an energy minimization problem for a continuum body, Ω. In the absence of body forces and point loads, the total potential energy of a solid is defined as

$$\Pi(\boldsymbol{u}, \Gamma) = \int_{\Omega \setminus \Gamma} \psi_e(\nabla \boldsymbol{u}) dV + \int_{\Gamma} G_c dS - \int_{\partial \Omega^t} \boldsymbol{t} \cdot \boldsymbol{u} dS \tag{2.2.1}$$

in which $\boldsymbol{u}$ is the displacement field, Γ represents the crack surface, G_c is the Griffith-type critical energy release rate, and $\boldsymbol{t}$ represents any external tractions applied to the body's surface. The stored elastic energy density, ψ_e, is a function of the displacement gradient, $\nabla \boldsymbol{u}$. The first term in the expression represents the amount of elastic energy stored in the material, while the second term is the crack surface energy or the energy dissipated due to crack formation. The final term represents the work due to the external forces.

Fracture surface energy approximation

In the phase field approach, Equation (2.2.1) is approximated with a spatially-regularized functional in which the fracture surface energy is replaced by an elliptic functional of a scalar field, $d \in [0, 1]$, and its gradient [21].

$$\psi_f(\Gamma) = \int_{\Gamma} G_c dS \;\approx\; \hat{\psi}_f(d) = G_c \int_{\Omega} \left(\frac{1}{4 l_0} d^2 + l_0 \nabla d \cdot \nabla d \right) dV \tag{2.2.2}$$

In this way, a sharp crack discontinuity is approximated by a diffuse crack topology with a small width, l_0, spatially-regularizing the original problem. The minimization of this functional yields the diffuse crack topology [21, 22], which is illustrated in Figure 2.1.

$$d(\boldsymbol{x}) = \text{Arg}\left\{\inf_{d\in\mathcal{S}_\Gamma} \hat{\psi}_f(d)\right\} \tag{2.2.3}$$

$$\mathcal{S}_\Gamma = \{d \mid d \in H^1,\ d(\boldsymbol{x}) = 1 \text{ when } \boldsymbol{x} \in \Gamma\} \tag{2.2.4}$$

Note that d is the phase field parameter, $\mathcal{S}_\Gamma$ is the set of admissible fields satisfying the Dirchlet-type conditions on the crack surface, H^1 is the Sobolev function space defined below, and $\boldsymbol{x}$ signifies the spatial location in the domain.

$$H^1 = \left\{v \;\middle|\; \int_\Omega v^2 d\boldsymbol{x} < +\infty, \text{ and } \int_\Omega |\nabla v|^2 d\boldsymbol{x} < +\infty\right\} \tag{2.2.5}$$

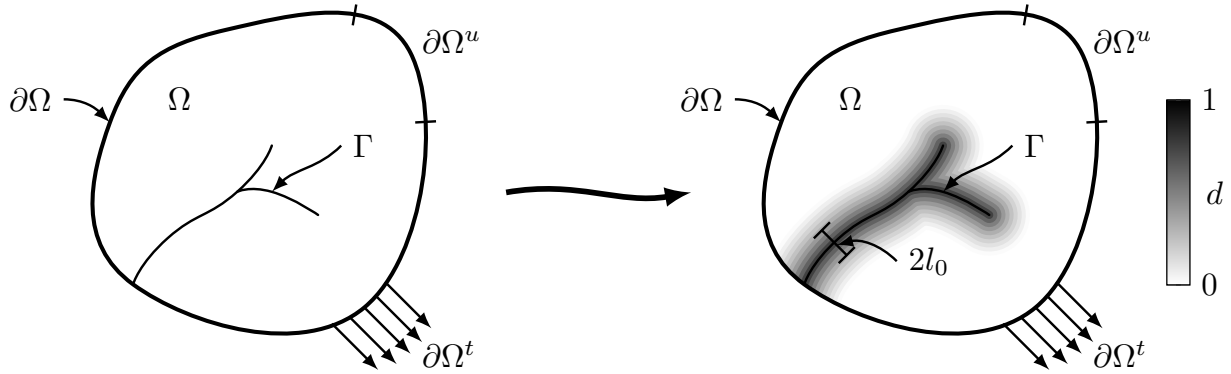

Figure 2.1: Phase field approximation of a sharp crack discontinuity

Stored elastic energy approximation

The stored elastic energy is additively decomposed into contributions from tensile and compressive energy, such that

$$\psi_e(\boldsymbol{\varepsilon}, d) = \psi_e^-(\boldsymbol{\varepsilon}) + (g(d) + k)\psi_e^+(\boldsymbol{\varepsilon}) \tag{2.2.6}$$

The elastic free energy is assumed to be a function of the phase field, d, and the small strain tensor, $\boldsymbol{\varepsilon}$, which is defined as the symmetric gradient of the displacement field.

$$\boldsymbol{\varepsilon}(\boldsymbol{u}) = \frac{1}{2}\left(\nabla \boldsymbol{u} + \nabla \boldsymbol{u}^T\right) \tag{2.2.7}$$

The tensile component of the energy is degraded by the action of a so-called degradation function, $g(d)$, which must satisfy certain requirements [22]. Additionally, k is a small parameter representing the artificial residual strength of the material [22], however, Borden et al. [83] remark that its inclusion appears to be unnecessary. In all subsequent examples in this chapter k is set to 10^{-8}.

Note that the stress may be obtained directly from the elastic potential through standard arguments in thermodynamics. That is,

$$\boldsymbol{\sigma} = \underbrace{\frac{\partial \psi_e^-}{\partial \boldsymbol{\varepsilon}}}_{\boldsymbol{\sigma}^-} + (g(d) + k) \underbrace{\frac{\partial \psi_e^+}{\partial \boldsymbol{\varepsilon}}}_{\boldsymbol{\sigma}^+} \tag{2.2.8}$$

where $\boldsymbol{\sigma}$ is the damaged stress tensor and $\boldsymbol{\sigma}^-/\boldsymbol{\sigma}^+$ are the undamaged, compressive and tensile stress tensors, respectively.

The degradation function, $g(d)$, can drastically affect the amount of elastic energy degradation caused by nonzero values of the phase field. Here we use the parameterized cubic function given in Equation (2.2.9), proposed in Borden [160]. The parameter, s, controls the initial slope, and, consequently, the amount of elastic energy degradation that results from moderate values of the phase field. Increasingly brittle behavior can be obtained by decreasing this parameter. Setting $s = 2$, the quadratic degradation function is recovered.

$$g(d) = (s-2)(1-d)^3 + (3-s)(1-d)^2 \tag{2.2.9}$$

Here we provide the anisotropic degradation of the elastic energy based on two energy splits.

The first is the volumetric-deviatoric split proposed in Amor et al. [161],

$$\psi_e^-(\boldsymbol{\varepsilon}) = \frac{\kappa}{2}\langle \mathrm{tr}[\boldsymbol{\varepsilon}]\rangle_-^2 \tag{2.2.10}$$

$$\psi_e^+(\boldsymbol{\varepsilon}) = \frac{\kappa}{2}\langle \mathrm{tr}[\boldsymbol{\varepsilon}]\rangle_+^2 + \mu\boldsymbol{\varepsilon}^{dev} : \boldsymbol{\varepsilon}^{dev} \tag{2.2.11}$$

where κ is the undegraded material bulk modulus, μ is the undegraded material shear modulus, $\mathrm{tr}[\cdot]$ is the trace operator, and $\boldsymbol{\varepsilon}^{dev} : \boldsymbol{\varepsilon}^{dev} = \sum_{i,j} \varepsilon_{ij}^{dev}\varepsilon_{ij}^{dev}$. Note that for an isotropic, linear elastic material $\kappa = E/(3(1-2\nu))$ and $\mu = E/(2(1+\nu))$, where E and ν are the elastic modulus and Poisson's ratio, respectively. The deviatoric strain tensor, $\boldsymbol{\varepsilon^{dev}}$, represents the deviatoric projection of the strain tensor. It is given by

$$\boldsymbol{\varepsilon}^{dev} = \mathbb{P}^{dev} : \boldsymbol{\varepsilon} = \left(\mathbb{I} - \mathbb{P}^{vol}\right) : \boldsymbol{\varepsilon} = \boldsymbol{\varepsilon} - \frac{\mathrm{tr}[\boldsymbol{\varepsilon}]}{3}\mathbf{1} \tag{2.2.12}$$

where $\mathbb{I}$ is the fourth order identity tensor, $\mathbf{1}$ is the second order identity tensor, and $\mathbb{P}^{vol}$/$\mathbb{P}^{dev}$ are the fourth order volumetric/deviatoric projection tensors, respectively. Note that $\mathbb{P}^{vol} = \frac{1}{3}(\mathbf{1}\otimes\mathbf{1})$. The second and fourth order identity tensors are defined as $\mathbf{1} = \delta_{ij}\boldsymbol{e}_i\otimes\boldsymbol{e}_j$ and $\mathbb{I} = \delta_{ik}\delta_{jl}\boldsymbol{e}_i\otimes\boldsymbol{e}_j\otimes\boldsymbol{e}_k\otimes\boldsymbol{e}_l$, where δ_{ij} is the Kronecker delta and $\{\boldsymbol{e}_i\}$ represents the basis vectors. Finally, the Macaulay brackets, $\langle\cdot\rangle_\pm$, are defined such that $\langle\cdot\rangle_+ = \max(\cdot, 0)$ and $\langle\cdot\rangle_- = \min(\cdot, 0)$. This energy split results in the constitutive relationship,

$$\boldsymbol{\sigma} = (g(d)+k)\left(\kappa\langle \mathrm{tr}[\boldsymbol{\varepsilon}]\rangle_+ \mathbf{1} + 2\mu\boldsymbol{\varepsilon}^{dev}\right) + \kappa\langle \mathrm{tr}[\boldsymbol{\varepsilon}]\rangle_- \mathbf{1} \tag{2.2.13}$$

An alternative energy split based on a principal/spectral decomposition of the strain tensor, as

presented by Miehe et al. [22], takes the following form

$$\boldsymbol{\varepsilon} = \sum_{a=1}^{3} \varepsilon_a \boldsymbol{n}_a \otimes \boldsymbol{n}_a \tag{2.2.14}$$

$$\psi_e^-(\boldsymbol{\varepsilon}) = \frac{\lambda}{2} \langle \varepsilon_1 + \varepsilon_2 + \varepsilon_3 \rangle_-^2 + \mu \left(\langle \varepsilon_1 \rangle_-^2 + \langle \varepsilon_2 \rangle_-^2 + \langle \varepsilon_3 \rangle_-^2 \right) \tag{2.2.15}$$

$$\psi_e^+(\boldsymbol{\varepsilon}) = \frac{\lambda}{2} \langle \varepsilon_1 + \varepsilon_2 + \varepsilon_3 \rangle_+^2 + \mu \left(\langle \varepsilon_1 \rangle_+^2 + \langle \varepsilon_2 \rangle_+^2 + \langle \varepsilon_3 \rangle_+^2 \right) \tag{2.2.16}$$

in which $\{(\varepsilon_a, \boldsymbol{n}_a), a = 1, 2, 3\}$ are the eigenpairs or principal strains and principal directions of the strain tensor and (λ, μ) are the standard lame parameters of the undamaged material. Note that $\lambda = E\nu/((1+\nu)(1-2\nu))$. The resulting constitutive law takes the following form,

$$\boldsymbol{\sigma} = (g(d) + k) \left(\lambda \langle \mathrm{tr}[\boldsymbol{\varepsilon}] \rangle_+ \mathbf{1} + 2\mu\boldsymbol{\varepsilon}^+ \right) + \lambda \langle \mathrm{tr}[\boldsymbol{\varepsilon}] \rangle_- \mathbf{1} + 2\mu\boldsymbol{\varepsilon}^- \tag{2.2.17}$$

where

$$\boldsymbol{\varepsilon}^+ = \sum_{a=1}^{3} \langle \varepsilon_a \rangle_+ \boldsymbol{n}_a \otimes \boldsymbol{n}_a \tag{2.2.18}$$

$$\boldsymbol{\varepsilon}^- = \sum_{a=1}^{3} \langle \varepsilon_a \rangle_- \boldsymbol{n}_a \otimes \boldsymbol{n}_a \tag{2.2.19}$$

The effect of the energy split on the optimization results will be briefly explored in Section 2.4.

Regularized total potential energy

With the above approximations at hand, the total potential energy in Equation (2.2.1) may be written in regularized form.

$$\begin{aligned} \tilde{\Pi}(\boldsymbol{u}, d) = &\int_\Omega \left(\psi_e^-(\boldsymbol{\varepsilon}(\boldsymbol{u})) + (g(d) + k)\psi_e^+(\boldsymbol{\varepsilon}(\boldsymbol{u})) \right) dV \\ &+ G_c \int_\Omega \left(\frac{1}{4l_0} d^2 + l_0 \nabla d \cdot \nabla d \right) dV - \int_{\partial\Omega^t} \boldsymbol{t} \cdot \boldsymbol{u} dS \end{aligned} \tag{2.2.20}$$

At a minimum, the first variation of the total potential with respect to the displacement and

phase field must vanish, $\delta\tilde{\Pi} = 0$. Application of this principle and the divergence theorem yields the following result

$$\begin{aligned}\delta\tilde{\Pi}(\boldsymbol{u}, d) = &- \int_{\Omega} (\nabla \cdot \boldsymbol{\sigma}) \cdot \delta\boldsymbol{u} dV + \int_{\partial\Omega} (\boldsymbol{n} \cdot \boldsymbol{\sigma} - \boldsymbol{t}) \cdot \delta\boldsymbol{u} dS \\ &+ \int_{\Omega} \left(\frac{\partial g}{\partial d}\psi_e^+ + \frac{G_c}{2l_0} d - 2G_c l_0 \nabla \cdot \nabla d \right) \delta d \; dV \\ &+ 2G_c l_0 \int_{\partial\Omega} (\boldsymbol{n} \cdot \nabla d) \;\; \delta d \; dS = 0\end{aligned} \tag{2.2.21}$$

Since this must hold for all admissible variations in the displacement and phase field we arrive at the strong form of the governing equations

$$\nabla \cdot \boldsymbol{\sigma} = \boldsymbol{0} \qquad \text{in } \Omega \tag{2.2.22}$$

$$\frac{G_c}{2l_0} d - 2G_c l_0 \nabla \cdot \nabla d = -\frac{\partial g}{\partial d}\psi_e^+ \qquad \text{in } \Omega \tag{2.2.23}$$

$$\boldsymbol{n} \cdot \boldsymbol{\sigma} = \boldsymbol{t} \qquad \text{on } \partial\Omega^t \tag{2.2.24}$$

$$\boldsymbol{u} = \hat{\boldsymbol{u}} \qquad \text{on } \partial\Omega^u \tag{2.2.25}$$

$$\boldsymbol{n} \cdot \nabla d = 0 \qquad \text{on } \partial\Omega \tag{2.2.26}$$

where the additional Dirichlet boundary condition has been added (Equation (2.2.25)) and $\partial\Omega^t \cap \partial\Omega^u = \emptyset$. Equation (2.2.22) is the usual linear momentum equation for static equilibrium in the absence of body forces, Equation (2.2.23) governs the evolution of the phase field, and Equation (2.2.26) enforces the no flux requirement of the phase field through the body's surface.

Finally, in order to enforce irreversibility of crack growth, the local history field proposed in Miehe et al. [23] is used in place of ψ_e^+ on the right hand side of Equation (2.2.23). Note that in the equation below, t, is not an actual time variable but a pseudo-time variable representing the load increments.

$$\mathcal{H}(\boldsymbol{x}, t) = \max_{\tau \in [0,t]} \psi_e^+(\boldsymbol{x}, \tau) \tag{2.2.27}$$

2.2.2 Finite element discretization

The weak form of the governing equations is obtained in the usual manner by multiplication of the strong form equations with admissible test functions, integration over the domain, and application of the divergence theorem. The test functions are denoted $\boldsymbol{w}^u$ and w^d for the linear momentum and phase field equations, respectively. The residual form of the equations for the displacement field, R_u, and phase field, R_d, can then be written as follows

$$R_u = \int_\Omega \boldsymbol{\sigma} : \nabla \boldsymbol{w}^u dV - \int_{\partial\Omega^t} \boldsymbol{t} \cdot \boldsymbol{w}^u dS = 0 \tag{2.2.28}$$

$$R_d = \int_\Omega \left(\frac{G_c}{2l_0} d \; w^d + 2G_c l_0 \nabla d \cdot \nabla w^d + \frac{\partial g}{\partial d} w^d \; \mathcal{H} \right) dV = 0 \tag{2.2.29}$$

We search for $u_i \in \mathcal{S}^{u_i}$ and $d \in \mathcal{S}^d$ such that Equations (2.2.28) and (2.2.29) are satisfied $\forall w_i^u \in \mathcal{V}^{w_i^u}$ and $\forall w^d \in \mathcal{V}^{w^d}$ where these function spaces are defined below. Note that H^1 corresponds to the previous definition in Equation (2.2.5).

$$\mathcal{S}^{u_i} = \{ u_i \mid u_i \in H^1, \; \& \; u_i = \hat{u}_i \text{ on } \partial\Omega^u \} \tag{2.2.30}$$

$$\mathcal{S}^d = \{ d \mid d \in H^1 \} \tag{2.2.31}$$

$$\mathcal{V}^{w_i^u} = \{ w_i^u \mid w_i^u \in H^1, \; \& \; w_i^u = 0 \text{ on } \partial\Omega^u \} \tag{2.2.32}$$

$$\mathcal{V}^{w^d} = \{ w^d \mid w^d \in H^1 \} \tag{2.2.33}$$

The above equations are then discretized and solved incrementally using the finite element method. The 2D domain is partitioned using 4-node quadrilateral elements and the approximate displacement field and phase field are both interpolated with bilinear shape functions such that

$$\boldsymbol{u}(\boldsymbol{x}) \approx \boldsymbol{N}_{\boldsymbol{u}}(\boldsymbol{x}) \bar{\boldsymbol{u}}, \quad d(\boldsymbol{x}) \approx \boldsymbol{N}_d(\boldsymbol{x}) \bar{\boldsymbol{d}} \tag{2.2.34}$$

$$\varepsilon(\boldsymbol{u}(\boldsymbol{x})) \approx \boldsymbol{B}_{\boldsymbol{u}}(\boldsymbol{x}) \bar{\boldsymbol{u}}, \quad \nabla d(\boldsymbol{x}) \approx \boldsymbol{B}_d(\boldsymbol{x}) \bar{\boldsymbol{d}} \tag{2.2.35}$$

The interpolation matrices for the displacement and phase field are represented by $\boldsymbol{N_u}$ and $\boldsymbol{N}_d$, respectively, while the vectors of the nodal degrees of freedom are denoted by $\bar{\boldsymbol{u}}$ and $\bar{\boldsymbol{d}}$. Similarly, the matrices $\boldsymbol{B_u}$ and $\boldsymbol{B}_d$ contain the derivatives of the relevant shape functions. The discretized residual equations then become

$$\boldsymbol{R}_{\bar{\boldsymbol{u}}} = \int_{\hat{\Omega}} \boldsymbol{B}_{\boldsymbol{u}}^T \hat{\boldsymbol{\sigma}} \, dV - \int_{\partial \hat{\Omega}^t} \boldsymbol{N}_{\boldsymbol{u}}^T \boldsymbol{t} \, dS = \boldsymbol{0} \tag{2.2.36}$$

$$\boldsymbol{R}_{\bar{\boldsymbol{d}}} = \int_{\hat{\Omega}} \left(\frac{G_c}{2l_0} \boldsymbol{N}_{\boldsymbol{d}}^T \boldsymbol{N_d} + 2G_c l_0 \boldsymbol{B}_{\boldsymbol{d}}^T \boldsymbol{B_d} \right) \bar{\boldsymbol{d}} \, dV + \int_{\hat{\Omega}} \frac{\partial g(\boldsymbol{N_d} \bar{\boldsymbol{d}})}{\partial d} \boldsymbol{N}_{\boldsymbol{d}}^T \mathcal{H} \, dV = \boldsymbol{0} \tag{2.2.37}$$

where, $\hat{\boldsymbol{\sigma}}$ is the stress tensor in Voigt notation and $\hat{\Omega}$ represents the discretized domain.

For each increment in load, marked by an increase in the pseudo-time variable t, the nodal solution is updated monolithically via a Newton-Raphson type iterative scheme, as follows

$$\begin{pmatrix} \bar{\boldsymbol{u}} \\ \bar{\boldsymbol{d}} \end{pmatrix}_{(k+1)} = \begin{pmatrix} \bar{\boldsymbol{u}} \\ \bar{\boldsymbol{d}} \end{pmatrix}_{(k)} - \begin{bmatrix} \boldsymbol{J}_{\bar{\boldsymbol{u}}\bar{\boldsymbol{u}}} & \boldsymbol{J}_{\bar{\boldsymbol{u}}\bar{\boldsymbol{d}}} \\ \boldsymbol{J}_{\bar{\boldsymbol{d}}\bar{\boldsymbol{u}}} & \boldsymbol{J}_{\bar{\boldsymbol{d}}\bar{\boldsymbol{d}}} \end{bmatrix}_{(k)}^{-1} \begin{pmatrix} \boldsymbol{R}_{\bar{\boldsymbol{u}}} \\ \boldsymbol{R}_{\bar{\boldsymbol{d}}} \end{pmatrix}_{(k)} \tag{2.2.38}$$

where k signifies the iteration number for a fixed pseudo-time increment. Each term in the monolithic jacobian is computed as defined below

$$\boldsymbol{J}_{\bar{\boldsymbol{u}}\bar{\boldsymbol{u}}} = \frac{\partial \boldsymbol{R}_{\bar{\boldsymbol{u}}}}{\partial \bar{\boldsymbol{u}}} = \int_{\hat{\Omega}} \boldsymbol{B}_{\boldsymbol{u}}^T \boldsymbol{D} \boldsymbol{B_u} \, dV \tag{2.2.39}$$

$$\boldsymbol{J}_{\bar{\boldsymbol{u}}\bar{\boldsymbol{d}}} = \frac{\partial \boldsymbol{R}_{\bar{\boldsymbol{u}}}}{\partial \bar{\boldsymbol{d}}} = \int_{\hat{\Omega}} \frac{\partial g(\boldsymbol{N_d} \bar{\boldsymbol{d}})}{\partial d} \boldsymbol{B}_{\boldsymbol{u}}^T \hat{\boldsymbol{\sigma}}^+ \boldsymbol{N_d} \, dV \tag{2.2.40}$$

$$\boldsymbol{J}_{\bar{\boldsymbol{d}}\bar{\boldsymbol{u}}} = \frac{\partial \boldsymbol{R}_{\bar{\boldsymbol{d}}}}{\partial \bar{\boldsymbol{u}}} = \int_{\hat{\Omega}} \frac{\partial g(\boldsymbol{N_d} \bar{\boldsymbol{d}})}{\partial d} \boldsymbol{N}_{\boldsymbol{d}}^T \frac{\partial \mathcal{H}(\boldsymbol{\varepsilon}(\boldsymbol{B_u} \bar{\boldsymbol{u}}))}{\partial \bar{\boldsymbol{u}}} \, dV \tag{2.2.41}$$

$$\boldsymbol{J}_{\bar{\boldsymbol{d}}\bar{\boldsymbol{d}}} = \frac{\partial \boldsymbol{R}_{\bar{\boldsymbol{d}}}}{\partial \bar{\boldsymbol{d}}} = \int_{\hat{\Omega}} \left(\left(\frac{G_c}{2l_0} + \frac{\partial^2 g(\boldsymbol{N_d} \bar{\boldsymbol{d}})}{\partial d^2} \mathcal{H} \right) \boldsymbol{N}_{\boldsymbol{d}}^T \boldsymbol{N_d} + 2G_c l_0 \boldsymbol{B}_{\boldsymbol{d}}^T \boldsymbol{B_d} \right) \, dV \tag{2.2.42}$$

The constitutive matrix, $\boldsymbol{D}$, used in Equation (2.2.39), is related to the tensor form of the stress-strain constitutive law. Generally, the linearization of the constitutive law may be expressed with a fourth-order tensor, $\mathbb{C} = \frac{\partial \boldsymbol{\sigma}}{\partial \boldsymbol{\varepsilon}}$. The fourth-order constitutive tensor for the volumetric deviatoric split

of the elastic energy may be expressed as follows,

$$\mathbb{C} = \frac{\partial \boldsymbol{\sigma}}{\partial \boldsymbol{\varepsilon}} = \begin{cases} (g(d) + k) \left(\kappa \mathbb{P}^{vol} + 2\mu \mathbb{P}^{dev} \right), & \text{if } \mathrm{tr}[\boldsymbol{\varepsilon}] > 0 \\ \kappa \mathbb{P}^{vol} + (g(d) + k) \left(2\mu \mathbb{P}^{dev} \right), & \text{otherwise} \end{cases} \tag{2.2.43}$$

A more complex representation of this fourth order tensor is required in the case of the spectral split of the elastic energy. This is provided in A.1. The jacobian and residual equations are integrated using a standard second-order gauss quadrature rule and the irreversibility requirement is enforced via a history variable stored at each quadrature point.

2.2.3 Alternative formulation of the discrete equations

Due to the nature of the irreversibility constraint, the value of an objective or constraint function may become dependent on the incremental solution path. When computing the path dependent sensitivities of these functions it is convenient to replace the history function, $\mathcal{H}$ (defined in Equation (2.2.27)), with an additional degree of freedom in the monolithic system.

These additional equations take the form

$$H^{n+1}(\boldsymbol{\xi}_i) = 0 = \begin{cases} h^{n+1}(\boldsymbol{\xi}_i) - h^n(\boldsymbol{\xi}_i), & \text{if } \psi_e^+(\boldsymbol{\xi}_i) < h^n(\boldsymbol{\xi}_i) \\ h^{n+1}(\boldsymbol{\xi}_i) - \psi_e^+(\boldsymbol{\xi}_i), & \text{otherwise} \end{cases} \tag{2.2.44}$$

where $\boldsymbol{\xi}_i$ corresponds to the i^{th} quadrature point in the *global* finite element mesh, $\psi_e^+(\boldsymbol{\xi}_i) = \psi_e^+(\boldsymbol{\varepsilon}(\boldsymbol{B_u}(\boldsymbol{\xi}_i)\bar{\boldsymbol{u}}^{n+1}))$, and where the superscript $(\cdot)^n$ implies the quantity corresponds to pseudo-time, t_n. Note that this additional equation at each quadrature point replaces the history function, $\mathcal{H}$, with the new independent variable, h.

Augmenting the previous monolithic residual vector with the additional gauss point equations, $\boldsymbol{H_h} = \left[H^{n+1}(\boldsymbol{\xi}_1), \ldots, H^{n+1}(\boldsymbol{\xi}_{N_{gp}}) \right]$ (where N_{gp} is the total number of quadrature points in the finite

element model) we have

$$\boldsymbol{R}^n = \begin{pmatrix} \boldsymbol{R}_{\bar{\boldsymbol{u}}} \\ \boldsymbol{R}_{\bar{\boldsymbol{d}}} \\ \boldsymbol{H}_{\boldsymbol{h}} \end{pmatrix}^n \tag{2.2.45}$$

where the history function, $\mathcal{H}$, in $\boldsymbol{R}_{\bar{\boldsymbol{d}}}$ (Equation (2.2.37)) is replaced with the independent variable, $h(\boldsymbol{\xi}_i)$, when the integrand is evaluated at the corresponding quadrature point. The new jacobian of this augmented system then takes on the following block structure

$$\frac{\partial \boldsymbol{R}}{\partial \boldsymbol{z}} = \begin{bmatrix} \frac{\partial \boldsymbol{R}_{\bar{\boldsymbol{u}}}}{\partial \bar{\boldsymbol{u}}} & \frac{\partial \boldsymbol{R}_{\bar{\boldsymbol{u}}}}{\partial \bar{\boldsymbol{d}}} & \boldsymbol{0} \\ \boldsymbol{0} & \frac{\partial \boldsymbol{R}_{\bar{\boldsymbol{d}}}}{\partial \bar{\boldsymbol{d}}} & \frac{\partial \boldsymbol{R}_{\bar{\boldsymbol{d}}}}{\partial \boldsymbol{h}} \\ \frac{\partial \boldsymbol{H}_{\boldsymbol{h}}}{\partial \bar{\boldsymbol{u}}} & \boldsymbol{0} & \frac{\partial \boldsymbol{H}_{\boldsymbol{h}}}{\partial \boldsymbol{h}} \end{bmatrix} \tag{2.2.46}$$

where $\boldsymbol{z}$ is the augmented solution vector,

$$\boldsymbol{z} = \begin{pmatrix} \bar{\boldsymbol{u}} \\ \bar{\boldsymbol{d}} \\ \boldsymbol{h} \end{pmatrix} \tag{2.2.47}$$

2.3 Topology optimization formulation

As discussed in the introduction, we are interested in obtaining minimum weight designs with an increased strength prior to fracture. In this section, the density-based design parameterization is first presented. Subsequently, the optimization problem is clearly defined and the filtering and projection schemes used in this chapter are then provided. Finally, in the last subsection, the analytical, path-dependent sensitivities are derived.

2.3.1 Design parameterization

Consistent with the well-known SIMP formulation (Solid Isotropic Material with Penalization [162, 163]), each finite element within the discretized domain is parameterized with a pseudo-density, ρ_e, which is allowed to vary continuously in the range $(0, 1]$. A pseudo-density of 1 corresponds to an element completely filled with material, while a value of ≈ 0 approximates a void in the domain. The pseudo-density for an element enters the constitutive relation through the computation of an effective elastic modulus,

$$E = \rho_e^p \; E_0 \tag{2.3.1}$$

where E_0 is the elastic modulus corresponding to the solid material and p is the SIMP penalization parameter. Values of p greater than one make elements with intermediate densities less efficient and, consequently, the optimizer will drive the solution closer to a desired "black and white" (or 0-1) design.

In order to effectively address the subsequently mentioned difficulties in Section 2.3.3 and 2.3.4, the design variables, $\boldsymbol{\theta}$, are filtered and projected. Therefore the element pseudo-density, ρ_e, that enters into Equation (2.3.1), is actually a composite function

$$\rho_e = \rho_e \left(\hat{\rho}_e \left(\boldsymbol{\theta} \right) \right) \tag{2.3.2}$$

where $\boldsymbol{\theta}$ is controlled by the optimizer, $\{\hat{\rho}_e\}$ are the filtered design variables, and $\{\rho_e\}$ are the projection of the filtered design variables.

2.3.2 Optimization problem statement

In order to achieve minimum weight designs with more resistance to fracture, we minimize the total volume fraction subject to a lower bound constraint on the compliance, C_{min}, and an upper bound constraint on the phase field approximation of the fracture surface energy, $\hat{\psi}_f^{max}$. Minimizing

the volume fraction is equivalent to minimizing the weight since we use only a single material with uniform density in the analyses. A lower bound is placed on the compliance since an enforced displacement loading is utilized for stability of the optimization procedure (due to the effect of strain softening). Since there is a nonzero displacement assigned to some degrees of freedom, this constraint has the effect of placing a lower bound on the reaction force at those degrees of freedom at the final time step. The upper bound on the fracture energy functional effectively constrains the level of accumulated phase field, which indirectly increases the fracture resistance of the design.

The mathematical optimization problem statement is defined to be

$$
\begin{aligned}
\underset{\boldsymbol{\theta}}{\text{minimize}} \quad & \frac{1}{V_{total}} \sum_{e=1}^{N_{elem}} \rho_e(\boldsymbol{\theta}) V_e \\
\text{subject to} \quad & \theta_{min} \leq \theta_e \leq 1, \ e = 1, \ldots, N_{elem} \\
& C_{min} \leq \boldsymbol{f}^T \boldsymbol{u} \\
& \hat{\psi}_f \leq \hat{\psi}_f^{max} \\
& \boldsymbol{R}^i = \boldsymbol{0}, \ i = 1, \ldots, N_{steps}
\end{aligned}
$$

in which V_e is the volume of element, Ω_e, V_{total} is the total design domain volume, $\boldsymbol{f}$ is the external force vector, $\hat{\psi}_f$ is the fracture energy functional from Equation (2.2.2), and the final constraint equation requires equilibrium and history variable consistency at each load step of the forward analyses. A flowchart of the optimization procedure is provided in Figure 2.2.

The displacement loads applied in the examples provided in Section 2.4 typically do not induce fracture of the topologies. Consequently, the approximation of the fracture surface energy does not have the typical physical meaning, but rather simply represents the energy dissipated from the accumulation of phase field. However, we note here that the fracture energy functional provides a natural aggregation function for the phase field. Alternative aggregation functions might also be used such as the p-norm type function used in [6, 13] for example.

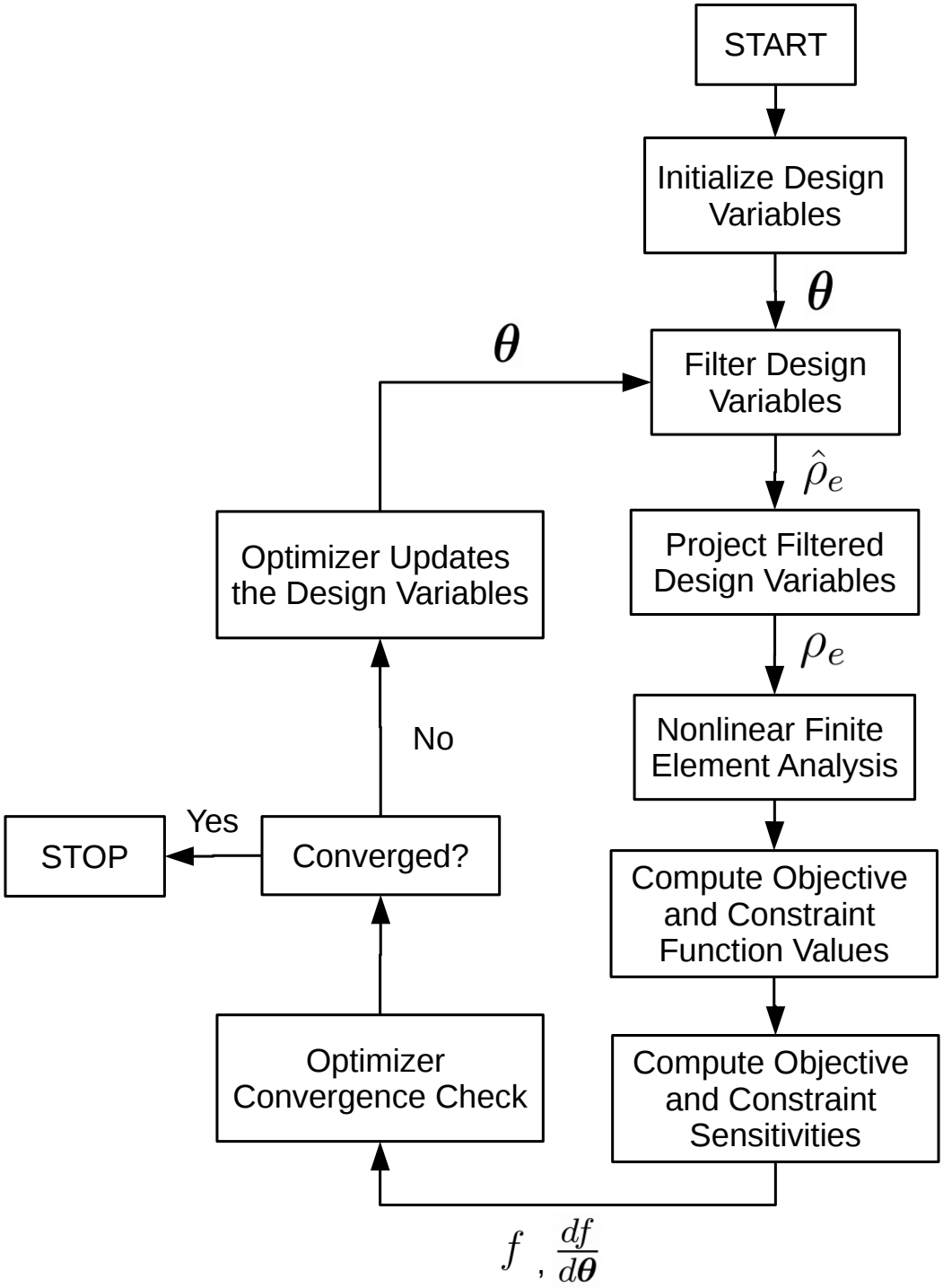

Figure 2.2: Flow chart illustrating the optimization procedure

2.3.3 Density filter

As is now common in density-based topology optimization, a density filter may be applied in order to remove instabilities such as checkerboard patterns and to provide mesh independence as is discussed in Sigmund and Petersson [164]. The gaussian weighting function proposed in Bruns and Tortorelli [165] is applied to the densities within a specified radius, introducing a design length scale which regularizes the problem. The design variables may be filtered utilizing a filter matrix of weighting coefficients, W_{ej},

$$\hat{\rho}_e = \sum_{j=1}^{N_{elem}} W_{ej}\theta_j \tag{2.3.3}$$

in which the components of the matrix are

$$W_{ej} = \frac{w_{ej}}{\sum_{i=1}^{N_{elem}} w_{ei}} \tag{2.3.4}$$

$$w_{ej} = \begin{cases} \exp\left(-\frac{r_{ej}^2}{r_{min}^2}\right), & \text{if } r_{ej} \leq r_{min} \\ 0, & \text{otherwise} \end{cases} \tag{2.3.5}$$

where $r_{ej} = ||\boldsymbol{X}_e - \boldsymbol{X}_j||_2$ is the distance between the centroids of elements Ω_e and Ω_j. The parameter r_{min} controls the length scale of features in the final topology.

2.3.4 Density projection

The filtered densities are then projected in order to help eliminate much of the transition region (with densities between 0 and 1) that is created by the filtering scheme. We employ a projection that is consistent with previous work by Guest et al. [166] and Wang et al. [167] that assists in obtaining black and white designs.

$$\rho_e = \frac{\tanh(\beta\eta) + \tanh(\beta(\hat{\rho}_e - \eta))}{\tanh(\beta\eta) + \tanh(\beta(1 - \eta))} \tag{2.3.6}$$

Note here that η governs the density threshold at which the projection takes place and β governs the strength of the projection operation. These effects are illustrated in Figure 2.3.

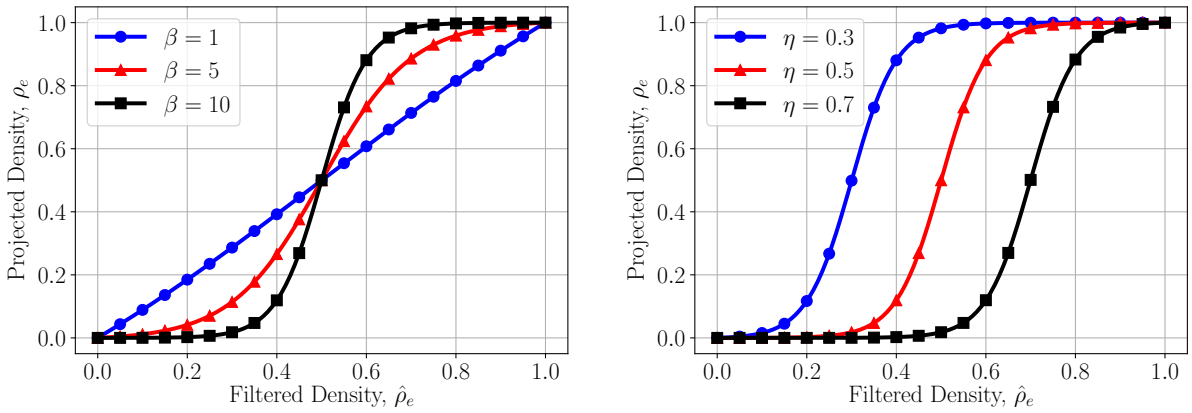

(a) Effect of β for $\eta = 0.5$

(b) Effect of η for $\beta = 10$

Figure 2.3: Plots of the projection function in Equation (2.3.6)

In all subsequent analyses η is fixed at 0.5 and β is increased slowly from an initial value of 1 up to a maximum value of 10 during the optimization procedure.

2.3.5 Derivation of analytical sensitivities

The dimension of the design space is exceptionally large in most topology optimization formulations. Therefore, optimizers which utilize the gradients of the objective and constraint functions are typically used. Consequently, it is highly desirable to be able to compute analytical derivatives of these functions with respect to the design variables efficiently.

As is now standard in density-based topology optimization, we use a computationally efficient, path-dependent adjoint method which is based on the previous work of Micheleris [49]. The path-dependence arises due to the irreversibility condition for the evolution of the phase field (i.e. enforced via Equation (2.2.27)). Due to the alternate formulation of the governing equations provided in Section 2.2.3, the augmented residual equation (Equation (2.2.45)) at pseudo-time t_n, becomes a function of only the pseudo-densities and the augmented solution vector at the current

and previous time step.

$$\boldsymbol{R}^n = \boldsymbol{R}^n\left(\boldsymbol{\rho}, \boldsymbol{z}^n, \boldsymbol{z}^{n-1}\right), \text{ where } n = 1, \ldots, N_{steps} \tag{2.3.7}$$

The objective and constraint functions given in Section 2.3.2 may all be represented as a general function of the design variables and the solution vector at the final time increment, $f(\boldsymbol{\rho}, \boldsymbol{z}^N)$, where we have used the short-hand notation, $N = N_{steps}$. Augmenting this function with the sum of the inner product of the residual at each time increment (Equation (2.3.7)) and an unknown vector, $\boldsymbol{\psi}^n$ (referred to as an adjoint vector hereafter), we have

$$\hat{f}(\boldsymbol{\rho}, \boldsymbol{z}^N, \ldots, \boldsymbol{z}^0) = f(\boldsymbol{\rho}, \boldsymbol{z}^N) + \sum_{n=1}^{N} \boldsymbol{\psi}^{n^T} \boldsymbol{R}^n\left(\boldsymbol{\rho}, \boldsymbol{z}^n, \boldsymbol{z}^{n-1}\right) \tag{2.3.8}$$

where the value of the function and its derivative remain unchanged since the residual must always vanish due to equilibrium requirements. Here, we assume the structure is initially unloaded and undamaged so that $\boldsymbol{z}^0 = \boldsymbol{0}$. Taking the derivative of this augmented function with respect to a single element density, ρ_e, results in the following expression

$$\begin{aligned}\frac{d\hat{f}}{d\rho_e} =& \frac{\partial f}{\partial \rho_e} + \frac{\partial f}{\partial \boldsymbol{z}^N}\frac{d\boldsymbol{z}^N}{d\rho_e} + \\ & \sum_{n=1}^{N} \boldsymbol{\psi}^{n^T}\left(\frac{\partial \boldsymbol{R}^n}{\partial \rho_e} + \frac{\partial \boldsymbol{R}^n}{\partial \boldsymbol{z}^n}\frac{d\boldsymbol{z}^n}{d\rho_e} + \frac{\partial \boldsymbol{R}^n}{\partial \boldsymbol{z}^{n-1}}\frac{d\boldsymbol{z}^{n-1}}{d\rho_e}\right)\end{aligned} \tag{2.3.9}$$

where, upon grouping terms, we obtain

$$\begin{aligned}\frac{d\hat{f}}{d\rho_e} =& \frac{\partial f}{\partial \rho_e} + \sum_{n=1}^{N} \boldsymbol{\psi}^{n^T}\frac{\partial \boldsymbol{R}^n}{\partial \rho_e} + \left(\frac{\partial f}{\partial \boldsymbol{z}^N} + \boldsymbol{\psi}^{N^T}\frac{\partial \boldsymbol{R}^N}{\partial \boldsymbol{z}^N}\right)\frac{d\boldsymbol{z}^N}{d\rho_e} + \\ & \sum_{n=1}^{N-1}\left(\boldsymbol{\psi}^{(n+1)^T}\frac{\partial \boldsymbol{R}^{n+1}}{\partial \boldsymbol{z}^n} + \boldsymbol{\psi}^{n^T}\frac{\partial \boldsymbol{R}^n}{\partial \boldsymbol{z}^n}\right)\frac{d\boldsymbol{z}^n}{d\rho_e}\end{aligned} \tag{2.3.10}$$

Choosing the adjoint vectors $\boldsymbol{\psi}^n,\ n = 1, \ldots, N$, such that the terms in parentheses disappear, we avoid the costly derivatives of the finite element fields with respect to the design variables.

The adjoint vectors are then obtained beginning with $\boldsymbol{\psi}^N$ and cycling backwards through the load increments via the solutions of the linear systems below.

$$\left[\frac{\partial \boldsymbol{R}^N}{\partial \boldsymbol{z}^N}\right]^T \boldsymbol{\psi}^N = -\frac{\partial f}{\partial \boldsymbol{z}^N} \tag{2.3.11}$$

$$\left[\frac{\partial \boldsymbol{R}^n}{\partial \boldsymbol{z}^n}\right]^T \boldsymbol{\psi}^n = -\left[\frac{\partial \boldsymbol{R}^{n+1}}{\partial \boldsymbol{z}^n}\right]^T \boldsymbol{\psi}^{n+1},\ n = N-1, \ldots, 1 \tag{2.3.12}$$

Once the adjoint vectors are obtained, the derivative in Equation (2.3.10) simplifies to

$$\frac{d\hat{f}}{d\rho_e} = \frac{\partial f}{\partial \rho_e} + \sum_{n=1}^{N} \boldsymbol{\psi}^{n^T} \frac{\partial \boldsymbol{R}^n}{\partial \rho_e} \tag{2.3.13}$$

where $\frac{\partial \boldsymbol{R}^n}{\partial \rho_e}$ is a simple computation, performed at the element level. The required explicit derivatives for the compliance and fracture energy functional constraints used in this chapter are provided in Section 2.3.6.

Note that the necessary derivatives are with respect to the design variables, $\boldsymbol{\theta}$. Hence the chain rule is required due to Equation (2.3.2),

$$\frac{d\hat{f}}{d\theta_j} = \sum_{i=1}^{N_{elem}} \frac{d\hat{f}}{d\rho_i} \frac{d\rho_i}{d\hat{\rho}_i} \frac{d\hat{\rho}_i}{d\theta_j} \tag{2.3.14}$$

$$= \sum_{i=1}^{N_{elem}} \frac{d\hat{f}}{d\rho_i} \frac{d\rho_i}{d\hat{\rho}_i} W_{ij} \tag{2.3.15}$$

where W_{ij} is the previously presented filter matrix which may be constructed once and reused throughout the optimization procedure.

Adjoint vector solution technique

The solution of the aforementioned linear systems demands much more effort than the linear solves required in the forward analyses due to the additional equation at every quadrature point. Defining N_{gp}^e as the number of quadrature points in a typical finite element, Ω_e, the dimension of the resulting linear system increases by the factor $N_{gp}^e \times N_{elem}$, which can be very large with respect

to the total number of nodal degrees of freedom. Consequently, it is beneficial to avoid the naive solution of this larger system.

In this particular problem, the quadrature point degrees of freedom are independent of each other so we employ a special solution technique via a Schur-complement type approach at the element level, rather than the global level. This concept will be illustrated for functions like the compliance and fracture energy functional which are not an explicit function of the quadrature point variables. In an effort to make the derivation in this section clearer, we group the nodal degrees of freedom into a vector, $\bar{\boldsymbol{y}} = [\ \bar{\boldsymbol{u}};\ \bar{\boldsymbol{d}}\ ]$, which yields the following system at the global level corresponding to Equation (2.3.11).

$$\begin{bmatrix} \frac{\partial \boldsymbol{R}_{\bar{\boldsymbol{y}}}}{\partial \bar{\boldsymbol{y}}} & \frac{\partial \boldsymbol{R}_{\bar{\boldsymbol{y}}}}{\partial \boldsymbol{h}} \\ \frac{\partial \boldsymbol{R}_{\boldsymbol{h}}}{\partial \bar{\boldsymbol{y}}} & \frac{\partial \boldsymbol{R}_{\boldsymbol{h}}}{\partial \boldsymbol{h}} \end{bmatrix}^T \begin{pmatrix} \boldsymbol{\psi}_{\bar{\boldsymbol{y}}} \\ \boldsymbol{\psi}_{\boldsymbol{h}} \end{pmatrix} = \begin{pmatrix} -\frac{\partial f}{\partial \bar{\boldsymbol{y}}} \\ \boldsymbol{0} \end{pmatrix} \tag{2.3.16}$$

Rearranging this system of equations via the Schur-complement and noting that $\frac{\partial \boldsymbol{R}_{\boldsymbol{h}}}{\partial \boldsymbol{h}} = \boldsymbol{I}$ we obtain

$$\left(\left[\frac{\partial \boldsymbol{R}_{\bar{\boldsymbol{y}}}}{\partial \bar{\boldsymbol{y}}} \right] - \left[\frac{\partial \boldsymbol{R}_{\bar{\boldsymbol{y}}}}{\partial \boldsymbol{h}} \right] \left[\frac{\partial \boldsymbol{R}_{\boldsymbol{h}}}{\partial \bar{\boldsymbol{y}}} \right] \right)^T \boldsymbol{\psi}_{\bar{\boldsymbol{y}}} = -\frac{\partial f}{\partial \bar{\boldsymbol{y}}} \tag{2.3.17}$$

$$\boldsymbol{\psi}_{\boldsymbol{h}} = -\left[\frac{\partial \boldsymbol{R}_{\bar{\boldsymbol{y}}}}{\partial \boldsymbol{h}} \right]^T \boldsymbol{\psi}_{\bar{\boldsymbol{y}}} \tag{2.3.18}$$

which must first be solved at the global level for $\boldsymbol{\psi}_{\bar{\boldsymbol{y}}}$ and, subsequently, at the element level for each component of $\boldsymbol{\psi}_{\boldsymbol{h}}$. Conveniently, the global linear operator on the left hand side of Equation (2.3.17) is simply the transpose of the jacobian used in the forward analyses.

Subsequent adjoint vectors may be obtained in a manner consistent with Equation (2.3.12). In order to illustrate this, we first provide the detailed form of the linear operator on the right hand side

of the same equation.

$$\left[\frac{\partial \boldsymbol{R}^{n+1}}{\partial \boldsymbol{z}^{n}}\right] = \begin{bmatrix} \mathbf{0} & \mathbf{0} \\ \mathbf{0} & \frac{\partial \boldsymbol{H}^{n+1}}{\partial \boldsymbol{h}^{n}} \end{bmatrix} \tag{2.3.19}$$

$$\frac{\partial H_i^{n+1}}{\partial h_j^n} = \begin{cases} -1 & \text{, if } i = j \text{ and } \psi_e^{+^{n+1}}(\boldsymbol{\xi}_i) < h^n(\boldsymbol{\xi}_i) \\ 0 & \text{, otherwise} \end{cases} \tag{2.3.20}$$

With this diagonal matrix structure at hand, Equation (2.3.12) takes the form

$$\begin{bmatrix} \frac{\partial \boldsymbol{R}_{\bar{\boldsymbol{y}}}^n}{\partial \bar{\boldsymbol{y}}^n} & \frac{\partial \boldsymbol{R}_{\bar{\boldsymbol{y}}}^n}{\partial \boldsymbol{h}^n} \\ \frac{\partial \boldsymbol{R}_{\boldsymbol{h}}^n}{\partial \bar{\boldsymbol{y}}^n} & \boldsymbol{I} \end{bmatrix}^T \begin{pmatrix} \boldsymbol{\psi}_{\bar{\boldsymbol{y}}}^n \\ \boldsymbol{\psi}_{\boldsymbol{h}}^n \end{pmatrix} = - \begin{bmatrix} \mathbf{0} & \mathbf{0} \\ \mathbf{0} & \frac{\partial \boldsymbol{H}^{n+1}}{\partial \boldsymbol{h}^n} \end{bmatrix} \begin{pmatrix} \boldsymbol{\psi}_{\bar{\boldsymbol{y}}}^{n+1} \\ \boldsymbol{\psi}_{\boldsymbol{h}}^{n+1} \end{pmatrix} = \begin{pmatrix} \mathbf{0} \\ \hat{\boldsymbol{\psi}}_{\boldsymbol{h}}^{n+1} \end{pmatrix} \tag{2.3.21}$$

where

$$\hat{\boldsymbol{\psi}}_{\boldsymbol{h}}^{n+1} \equiv -\frac{\partial \boldsymbol{H}^{n+1}}{\partial \boldsymbol{h}^n} \boldsymbol{\psi}_{\boldsymbol{h}}^{n+1} \tag{2.3.22}$$

Performing the Schur-complement of this global system we have

$$\left(\left[\frac{\partial \boldsymbol{R}_{\bar{\boldsymbol{y}}}^n}{\partial \bar{\boldsymbol{y}}}\right] - \left[\frac{\partial \boldsymbol{R}_{\bar{\boldsymbol{y}}}^n}{\partial \boldsymbol{h}}\right] \left[\frac{\partial \boldsymbol{R}_{\boldsymbol{h}}^n}{\partial \bar{\boldsymbol{y}}}\right] \right)^T \boldsymbol{\psi}_{\bar{\boldsymbol{y}}}^n = - \left[\frac{\partial \boldsymbol{R}_{\boldsymbol{h}}^n}{\partial \bar{\boldsymbol{y}}}\right]^T \hat{\boldsymbol{\psi}}_{\boldsymbol{h}}^{n+1} \tag{2.3.23}$$

$$\boldsymbol{\psi}_{\boldsymbol{h}}^n = \hat{\boldsymbol{\psi}}_{\boldsymbol{h}}^{n+1} - \left[\frac{\partial \boldsymbol{R}_{\bar{\boldsymbol{y}}}^n}{\partial \boldsymbol{h}}\right]^T \boldsymbol{\psi}_{\bar{\boldsymbol{y}}}^n \tag{2.3.24}$$

which has two nice properties. The first is the global linear operator on the left hand side of Equation (2.3.23) is simply the transpose of the jacobian used in the forward analyses at the n^{th} step just as before. Secondly, the global right hand side of Equation (2.3.23) and (2.3.24) may be assembled at the element level, so the global linear operators on the right hand side of each equation need not be formed explicitly.

This approach significantly reduces the computational effort required to obtain the path-

dependent sensitivities, especially in the case of many load increments. The much larger matrix in Equation (2.2.46) is never formed explicitly and only the much smaller matrices used in the forward analyses are factored. To the author's best knowledge, this approach is unique in that the solution is obtained without explicitly performing a global Schur-complement solution of the linear system during the sensitivity analysis.

2.3.6 Required derivatives for analytical sensitivities

The analytical sensitivity derivation previously provided in Section 2.3.5 was completed for a general function of the design variables and the solution vector at the final time increment, $f(\boldsymbol{\rho}, \boldsymbol{z}^N)$. In order to complete this derivation for a *specific* function of this form, we must provide the expressions for the partial derivatives, $\frac{\partial f}{\partial \boldsymbol{z}^N}$ and $\frac{\partial f}{\partial \rho_e}$. In this section, these will be explicitly given for the compliance and fracture energy functional used as constraint functions in this chapter.

Compliance derivatives

The compliance function used herein is the inner product of the external force vector, $\boldsymbol{f}$, and the vector of nodal displacements, $\boldsymbol{u}$. In order to make this derivation clearer, we partition these vectors into components corresponding to the Dirichlet-type boundary condition on the displacement field, $(\cdot)_D$, and components which are free, $(\cdot)_F$. With this notation at hand, the compliance function may be written as

$$C(\boldsymbol{\rho}, \boldsymbol{z}^N) = \begin{pmatrix} \boldsymbol{f}_D \\ \boldsymbol{f}_F \end{pmatrix}^T \begin{pmatrix} \boldsymbol{u}_D \\ \boldsymbol{u}_F \end{pmatrix} \tag{2.3.25}$$

Note that, due to equilibrium requirements and the use of displacement control, the components of the external force vector, $\boldsymbol{f}_F$, are zero. Therefore this expression simplifies to $C(\boldsymbol{\rho}, \boldsymbol{z}^N) = \boldsymbol{f}_D^T \, \boldsymbol{u}_D$.

Taking the partial derivative of this expression with respect to ρ_e gives the following result

$$\frac{\partial C}{\partial \rho_e} = \frac{\partial \boldsymbol{f}_D}{\partial \rho_e}^T \boldsymbol{u}_D + \boldsymbol{f}_D^T \cancelto{\mathbf{0}}{\frac{\partial \boldsymbol{u}_D}{\partial \rho_e}} \tag{2.3.26}$$

Since $\boldsymbol{u}_D$ is known, we only need to compute $\frac{\partial \boldsymbol{f}_D}{\partial \rho_e}$. Note that, since this formulation is quasi-static, the internal force must equal the external force in order to satisfy equilibrium. Identifying the internal force vector, $\boldsymbol{f}_{int}$, from the residual in Equation (2.2.36), we see that $\frac{\partial \boldsymbol{f}_D}{\partial \rho_e}$ may be computed via the expression

$$\frac{\partial \boldsymbol{f}_{int}}{\partial \rho_e} = \int_{\hat{\Omega}} \boldsymbol{B}_{\boldsymbol{u}}^T \frac{\partial \hat{\boldsymbol{\sigma}}}{\partial \rho_e} \, dV \tag{2.3.27}$$

at the corresponding Dirichlet degrees of freedom. Recall that ρ_e enters the expression for the stress tensor through the effective elastic modulus, E (Equation (2.3.1)). Since the stress is linear in E, we simply replace E with the partial derivative, $\frac{\partial E}{\partial \rho_e} = p \, \rho_e^{p-1} E_0$, in the stress computation in order to obtain the necessary derivative, $\frac{\partial \hat{\boldsymbol{\sigma}}}{\partial \rho_e}$, above.

Subsequently, we provide the partial derivative of the compliance function with respect to the solution vector at the final time increment, $\boldsymbol{z}^N$. Noting again that the Dirichlet degrees of freedom are known and constant we obtain the following expression,

$$\frac{\partial C}{\partial \boldsymbol{z}^N} = \left[\frac{\partial \boldsymbol{f}_D}{\partial \boldsymbol{z}^N} \right]^T \boldsymbol{u}_D \tag{2.3.28}$$

This may be computed via a summation of the rows of the monolithic jacobian matrix at the final time increment corresponding to the Dirichlet displacement degrees of freedom, multiplied by the corresponding prescribed displacement.

Fracture energy functional derivatives

The required derivatives of the fracture energy functional ($\hat{\psi}_f$ in Equation (2.2.2)) are simple to compute. Since there is no explicit dependence on the pseudo-densities, we see that $\frac{\partial \hat{\psi}_f}{\partial \rho_e} = 0$. Next

we compute the partial derivative with respect to the solution vector at the final time increment, $\frac{\partial \hat{\psi}_f}{\partial \boldsymbol{z}^N}$. First, we substitute the phase field finite element approximations (i.e. Equations (2.2.34) and (2.2.35)) into the expression for the fracture energy functional,

$$\hat{\psi}_f(\boldsymbol{N}_d \bar{\boldsymbol{d}}) = G_c \int_{\hat{\Omega}} \left(\frac{1}{4l_0} \left(\boldsymbol{N}_d \bar{\boldsymbol{d}} \right)^2 + l_0 \left(\boldsymbol{B}_d \bar{\boldsymbol{d}} \right) \cdot \left(\boldsymbol{B}_d \bar{\boldsymbol{d}} \right) \right) dV \tag{2.3.29}$$

where we see that $\frac{\partial \hat{\psi}_f}{\partial \bar{\boldsymbol{u}}^N} = \boldsymbol{0}$ and $\frac{\partial \hat{\psi}_f}{\partial \boldsymbol{h}^N} = \boldsymbol{0}$. The only nonzero part of the required derivative is with respect to the phase field and may be expressed as follows

$$\frac{\partial \hat{\psi}_f}{\partial \bar{\boldsymbol{d}}} = G_c \int_{\hat{\Omega}} \left(\frac{1}{2l_0} \boldsymbol{N}_d^T \boldsymbol{N}_d \bar{\boldsymbol{d}} + 2l_0 \boldsymbol{B}_d^T \boldsymbol{B}_d \bar{\boldsymbol{d}} \right) dV \tag{2.3.30}$$

completing the expression, $\frac{\partial \hat{\psi}_f}{\partial \boldsymbol{z}^N}$.

Sensitivity verification

The Schur-complement procedure to compute the path-dependent sensitivities is verified for the following example problem by computing the approximate sensitivities numerically with simple finite differences for each element in the domain. The geometry, mesh, and boundary conditions are shown in Figure 2.4a and the phase field is shown on the deformed shape at the peak load in Figure 2.4b. A prescribed downward displacement is linearly increased to a value of 0.1mm and then linearly decreased to a value of 0.05mm in order to trigger the path-dependence due to irreversibility. Relevant material properties used in this example are provided in Table 2.1, corresponding to a mild steel. In this example, the length scale parameter, l_0, is set to $0.5mm$ and the pseudo-densities are initialized to 0.9.

Table 2.1: Material properties for mild steel [168]

E_0 [GPa]	ν	G_c $[kJ/m^2]$
200	0.29	12

The finite element mesh consists of 812 4-node quadrilateral elements. A simple forward

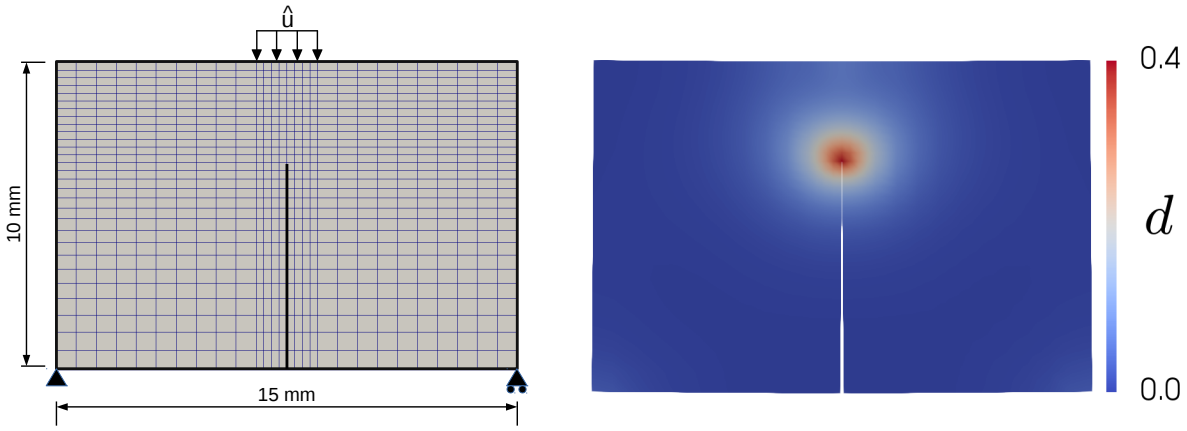

(a) Geometry and mesh

(b) Phase field at peak load

Figure 2.4: Verification problem for analytical sensitivity computation

difference approximation of the sensitivities is used such that for a function, $f(\boldsymbol{\rho})$, the sensitivity is approximated by

$$\frac{df}{d\rho_e} \approx \frac{f(\rho_1, \ldots, \rho_e + \Delta\rho_e, \ldots, \rho_{N_{elem}}) - f(\rho_1, \ldots, \rho_e, \ldots, \rho_{N_{elem}})}{\Delta\rho_e} \tag{2.3.31}$$

where a full, nonlinear finite element analysis is required for each element density perturbation. In this procedure the density perturbation and density exponent were set to $\Delta\rho_e = 10^{-5}$ and $p = 3$, respectively.

Both, the compliance and fracture energy functional sensitivities are verified and the results are illustrated in Figure 2.5. Note that the sensitivities have been sorted consistently from smallest to largest value for clarity. It can be seen that numerical differentiation and the analytical calculation based on the Schur-complement give nearly identical results.

2.4 Numerical examples

In this section we present two examples demonstrating the effectiveness of this approach. In the first example (the portal frame structure) an investigation into the effect of the energy split (volumetric-deviatoric/principal) from Section 2.2.1 is also explored. Additionally, we investigate

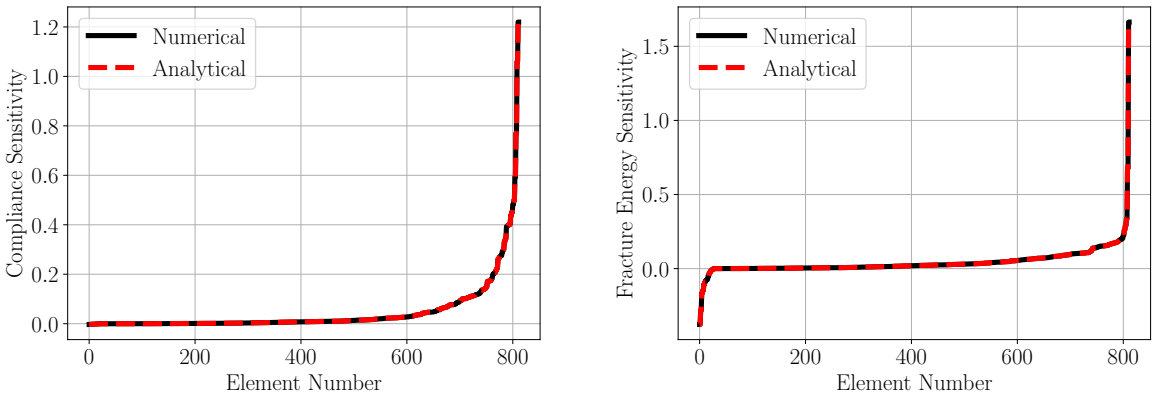

(a) Compliance sensitivity

(b) Fracture energy sensitivity

Figure 2.5: Numerical verification of the analytical sensitivities

the effect of the degradation function (cubic/quadratic) on the final topology and also explore the change in the fracture energy functional sensitivities with respect to changes in the length scale parameter, l_0, and the degradation function, $g(d)$.

The solution of the forward problem is implemented in the finite element program, FEAP [169], which leverages the PETSc library for parallel, sparse linear algebra [170]. Additionally, the open source interior point optimizer, IPOPT [171], is used in which the analytical gradients of the objective and constraint functions are utilized. This optimizer provides a nice C++/Fortran interface through which it is convenient to couple a finite element solver. An L-BFGS style update of the hessian of the Lagrangian is used by the optimizer with the maximum number of associated history vectors set to 30. Additionally, the solver convergence tolerance was set to 10^{-5} as is discussed in Lambe et al. [172]. Mesh generation was performed using CUBIT [173] and post-processing was completed using Paraview [174] and Matplotlib [175]. Finally, note that the lower bound on the pseudo-densities, ρ_{min}, is set to 0.001 in all subsequent analyses. The corresponding lower bound on the design variables is obtained by substituting ρ_{min} for ρ_e and θ_{min} for $\hat{\rho}_e$ into Equation (2.3.6) and solving for θ_{min} given a specified value of β.

2.4.1 Portal frame

In the following example, the portal frame structure shown in Figure 2.6 is subjected to a prescribed downward displacement distributed over a narrow area at the top of the frame. The geometry is discretized with 7,636 quadrilateral elements and the relevant material and numerical parameters are provided in Table 2.1 and 2.2, respectively.

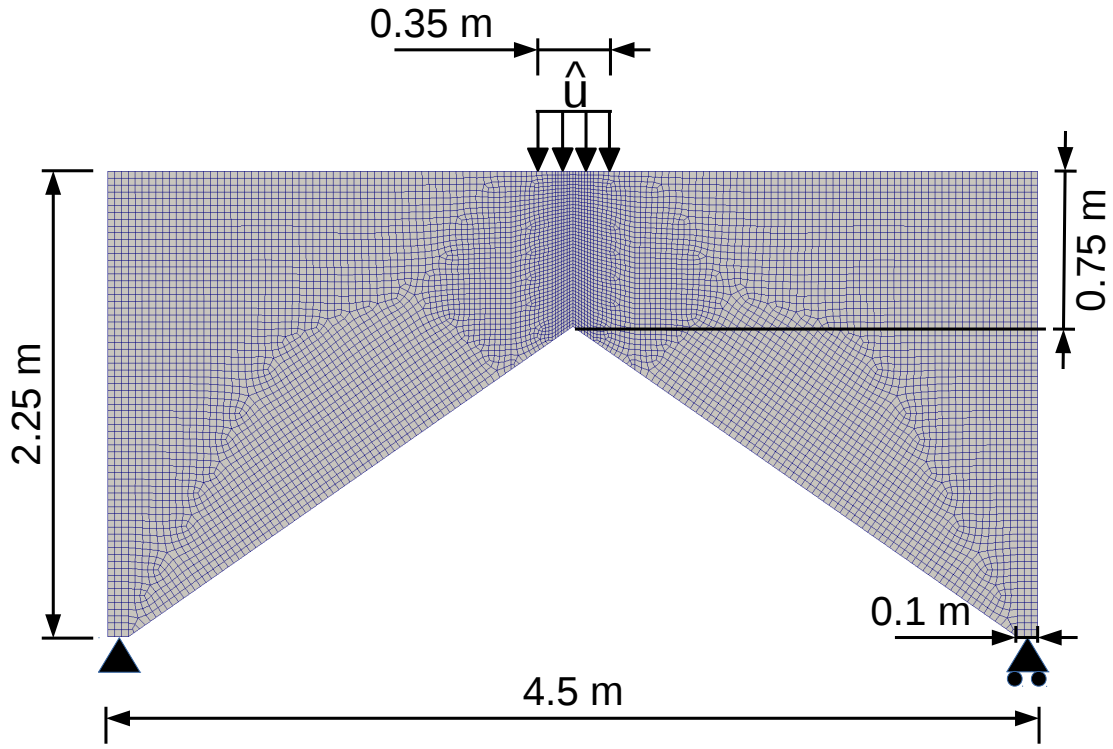

Figure 2.6: Portal frame geometry and finite element mesh

Table 2.2: Portal frame numerical parameters

r_{min} $[m]$	p	C_{min} $[kJ]$
0.1	3	14

In this example we first compare the effect of the energy split, which determines the evolution of the phase field parameter, on the final topology of the structure. In order to draw a comparison between the two, we take the following approach. Consistent with previous work [176, 83], we

view the length scale parameter as a material parameter and calibrate the model response using the two energy splits to yield similar force-displacement curves. First, we set the length scale using the principal split to $l_0 = 0.1m$. All of the element pseudo-densities are set to 1 and the frame is loaded until fracture. Subsequently the volumetric-deviatoric energy split is used and the force-displacement curve is approximately calibrated to that of the principal split using the length scale parameter. Since more of the stored elastic energy is typically degraded when using the volumetric-deviatoric split, the value of l_0 is decreased to $0.045m$ during calibration. The resulting force-displacement curves are provided in Figure 2.7 and the crack topologies are given in Figure 2.8. In this study we use the quadratic degradation function, presented in Equation (2.2.9), by setting the parameter $s = 2$. It is clearly seen that both approaches give a similar response of the original non-optimized structure, which serves as the basis for the following comparison.

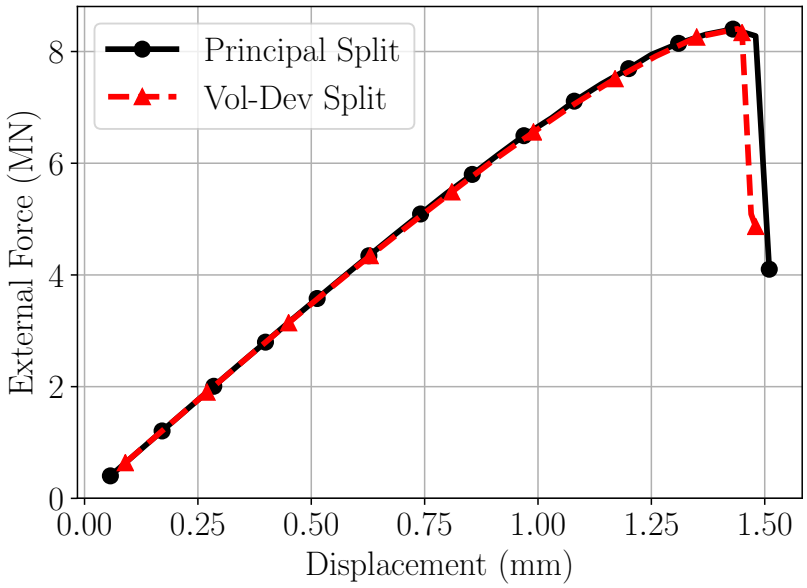

Figure 2.7: Result of force-displacement curve calibration

After calibration, each model (with the respective length scale parameter) is optimized first without the fracture energy functional constraint and subsequently with it. A peak downward prescribed displacement of $1.9mm$ is applied. This corresponds to a value which nearly induces fracture at the re-entrant corner when the optimal topology using only linear elastic physics (shown

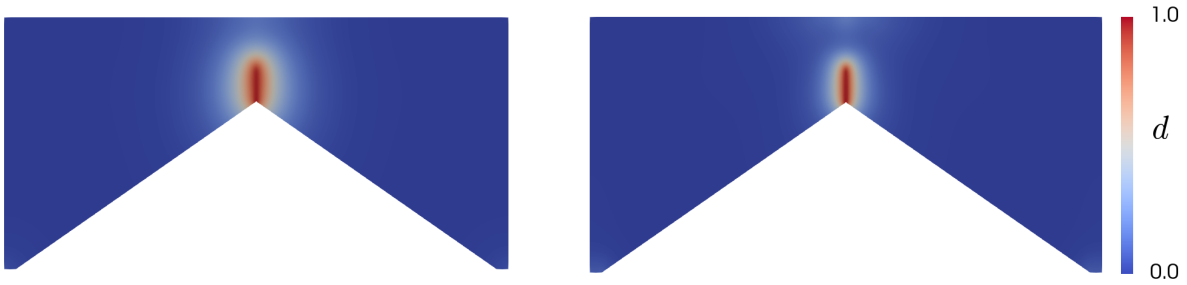

(a) Principal split (b) Volumetric-deviatoric split

Figure 2.8: Phase field crack topologies with different elastic energy splits

in Figure 2.9a) is selected. Note that this load does not induce fracture in any of the subsequent locally optimal designs. The load should be chosen large enough to induce non-negligible values of phase field. This simply avoids the potential numerical difficulties associated with computing the value of the fracture energy functional and its sensitivity with values near machine precision. The authors have obtained nearly identical results for this example using half of the specified applied displacement. The resulting topologies without the fracture energy functional constraint are provided in Figure 2.9 along with the topology resulting from simple linear elastic physics. Here we see that the designs obtained without the additional constraint are all quite similar.

(a) Linear elastic (b) Principal split (c) Vol-dev split

Figure 2.9: Topologies obtained without a fracture energy functional constraint

In order to draw a qualitative comparison of the resulting constrained topologies, the upper bound on the fracture energy functional, $\hat{\psi}_f^{max}$, is slowly decreased (in each case to a different value) until the optimization problem becomes infeasible. Infeasibility is marked by the inability of the optimizer to satisfy the constraints within 500 iterations.

As shown in Figure 2.10, the fracture energy functional constraint produces very different topologies with the different energy splits in this example. When using the volumetric-deviatoric

split, the center region of the frame is filled in with full density due to the introduction of phase field throughout this region. In contrast, the principal split results in very little phase field creation at the top of the frame which is primarily in compression (see Figure 2.11). Consequently, a much larger hole is placed in this region.

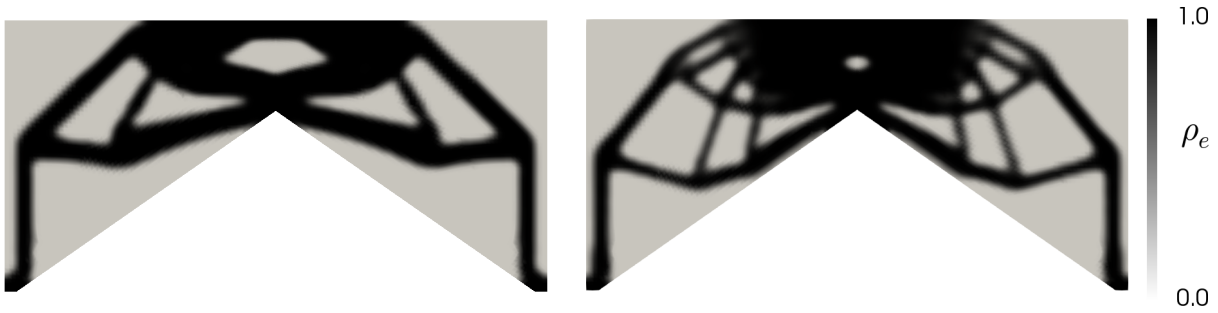

(a) Principal split (b) Volumetric-deviatoric split

Figure 2.10: Topologies obtained with a fracture energy functional constraint

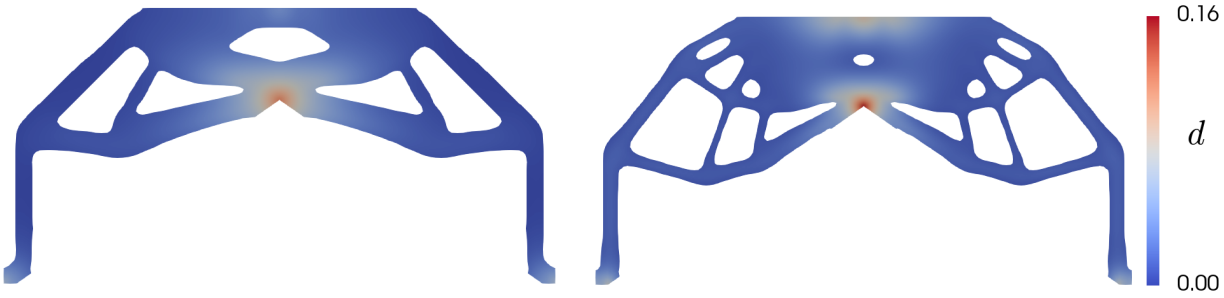

(a) Principal split (b) Volumetric-deviatoric split

Figure 2.11: Phase field comparison at final load step

Subsequently each of the resulting designs with and without the fracture energy functional constraint are loaded until fracture. The resulting force-displacement and fracture energy functional curves are provided in Figure 2.12. The optimized result using the principal split results in a 19.85% increase in the peak load prior to fracture, compared with a 15.79% increase using the volumetric-deviatoric split. The numerical results are tabulated in Table 2.3. Note that the optimized structure using the principal split of the elastic energy results in a lower volume fraction and a more

fracture-resistant design. Again we note that the lower volume fraction implies a lower weight structure since we use a single material with uniform density.

Consequently, in the subsequent examples, only results obtained using the principal energy split are presented. Figure 2.13 illustrates the optimizer convergence histories for both energy splits, demonstrating that the fracture energy functional constraint is active in each final design.

Table 2.3: Portal frame results (FEC = Fracture Energy Constraint)

Energy Split	FEC	Volume Fraction	Peak Load $[MN]$	$\hat{\psi}_f^{max}$ $[J]$
Principal	No	0.382	8.06	172
Principal	Yes	0.435	9.66	86
Vol-Dev	No	0.389	7.98	255
Vol-Dev	Yes	0.443	9.24	178

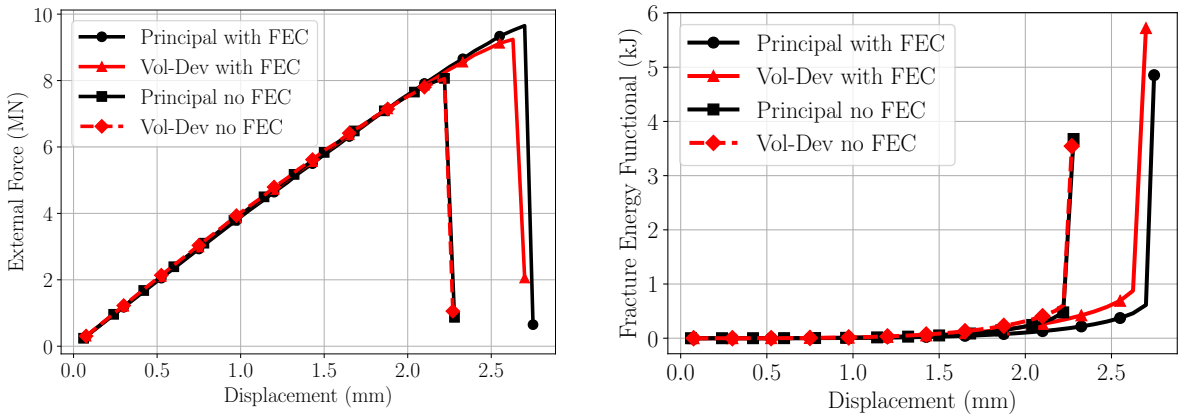

(a) (b)

Figure 2.12: Force-displacement (a) and fracture energy functional (b) curves. Note that FEC = Fracture Energy Constraint

Finally, since we select the principal split of the elastic energy for the aforementioned reasons, we provide exclusively the results using the principal split versus the linear elastic results in Figure 2.14 for clarity.

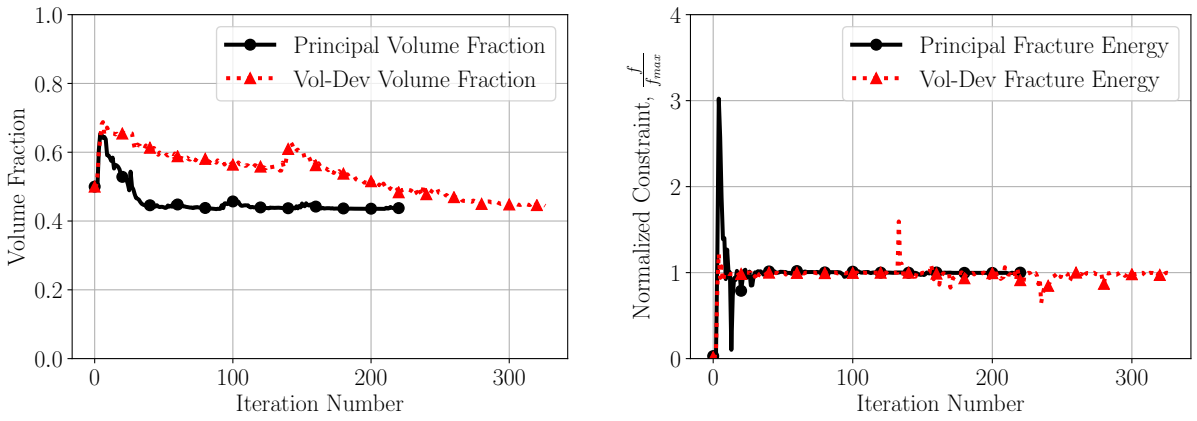

(a) (b)

Figure 2.13: Convergence history for each energy split demonstrating that the fracture energy functional constraint is active. The pseudo-densities are uniformly initialized to 0.5 and the final converged designs correspond to Figure 2.10.

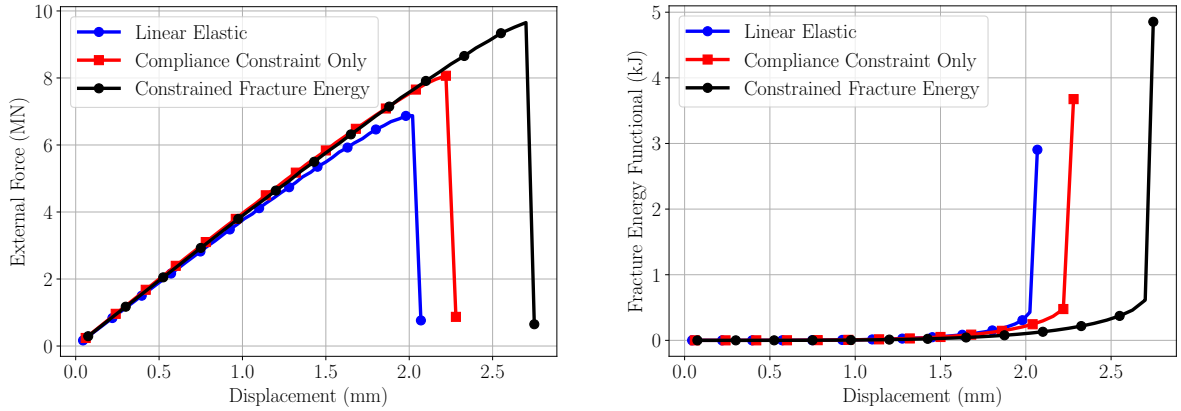

(a) (b)

Figure 2.14: Force-displacement (a) and fracture energy functional (b) curves using the principal split of the elastic energy and the quadratic degradation function for the three topologies given in Figures 2.9a, 2.9b, and 2.10a Note that the linear elastic curves correspond to the forward problem, employing the phase field method for fracture using the optimal topology obtained without the phase field method (illustrated in Figure 2.9a)

Portal frame results using cubic degradation function

Next, we briefly investigate the effect of the parameterized cubic degradation function (provided in Equation (2.2.9)), which was originally proposed by Borden [160]. To this end, we set $s = 0.5$ and repeat the portal frame optimization procedure using the principal split of the elastic energy.

Both quadratic/cubic degradation functions are illustrated in Figure 2.15. Since increasingly brittle behavior is obtained with the cubic function, a larger displacement must be applied in order to achieve a non-negligible level of phase field. Hence, a downward displacement of $2.65mm$ is applied and the corresponding minimum compliance, C_{min}, is set to $28kN$ (versus the $1.9mm$ and $14kN$ using the quadratic degradation function). These values were selected using the cubic degradation function and topology from Figure 2.9a. The applied displacement was increased until the value of the fracture energy functional matched the value using the quadratic degradation function, the same topology, and the previously applied displacement of $1.9mm$. At this new load level, the corresponding compliance ($28kN$) was set as the new lower bound. This procedure serves as the basis for our comparison. The upper bound on the fracture energy functional is slowly decreased, again, until the problem becomes infeasible, consistent with the previously presented methodology.

The resulting topology is provided in Figure 2.16 and the associated force-displacement curves are given in Figure 2.17a. Although one may not compare the resulting topologies directly since the physics and constraint bounds are different, we note that the resulting topologies have almost indistinguishable general features. Therefore, in this example, the designs do not appear to be sensitive to the degradation function selected.

As shown in Figure 2.17a, the cubic degradation function results in the expected increasingly brittle behavior with less softening prior to fracture. The design obtained using the quadratic degradation function results in a 38.4% increase in the peak load with respect to the linear elastic design (i.e. the topology given in Figure 2.9a), while the design obtained using the cubic degradation function results in a 42.8% increase.

Finally, note that it is merely a coincidence that the resulting force-displacement curves are similar for the linear elastic design using the cubic degradation function and for the topology obtained by constraining the fracture energy functional with a quadratic degradation function. In the former case, the cubic degradation function effectively gives the material response increased strength, while in the latter the strength is gained by changing the topology of the structure.

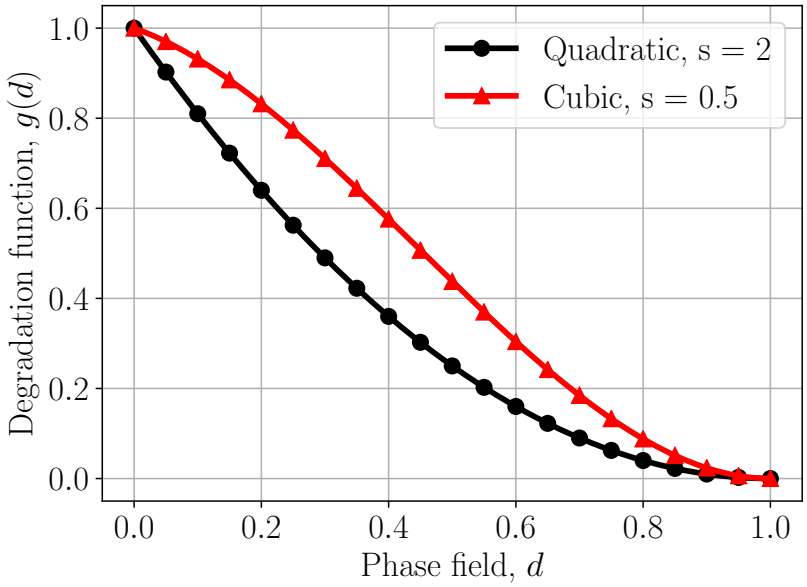

Figure 2.15: Degradation function in Equation (2.2.9)

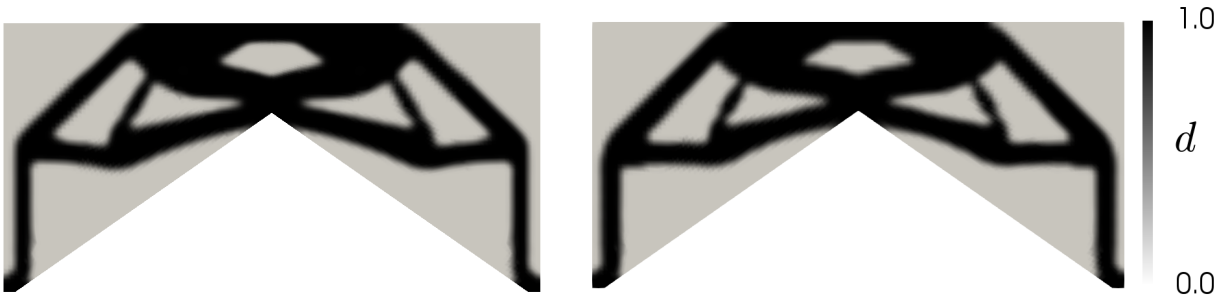

(a) Quadratic (s = 2)

(b) Cubic (s = 0.5)

Figure 2.16: Topology obtained using a cubic degradation function, compared with the quadratic degradation function result from Figure 2.10 (both results were obtained by constraining the fracture energy functional)

Effect of l_0 and $g(d)$ on the fracture energy functional sensitivities

Finally we investigate the sensitivity of the optimization procedure with respect to the length scale parameter, l_0, and the degradation function, $g(d)$. By changing the material behavior, one may drastically change the constraint functions themselves. In general, it is difficult to compare results or number of optimization iterations directly since topology optimization problems are usually non-convex. In order to provide some potentially useful insight in an optimizer-independent

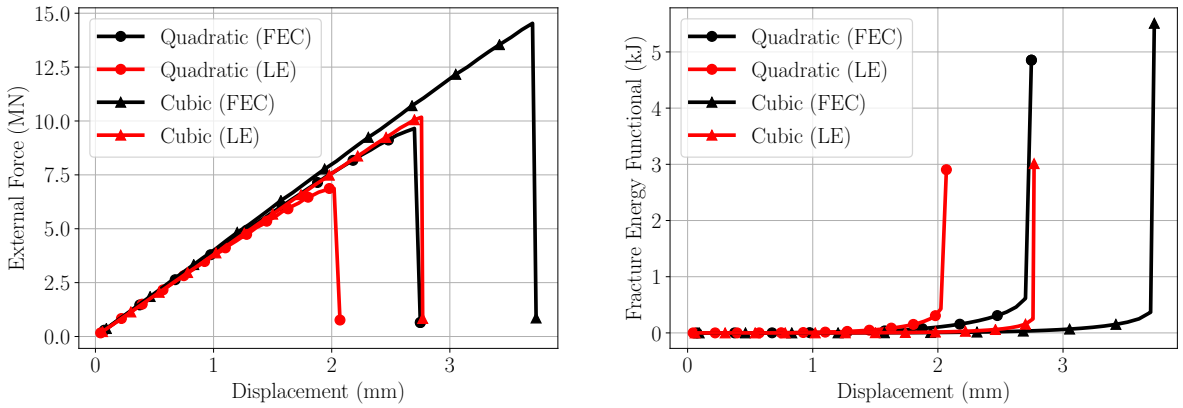

(a) (b)

Figure 2.17: Force-displacement (a) and fracture energy functional (b) curves for two different degradation functions (FEC = Fracture Energy Constraint, LE = Linear Elastic Design). Note that the linear elastic design refers to the optimal topology obtained without the phase field method (illustrated in Figure 2.9a), however the curves shown correspond to the forward problem, employing the phase field method for fracture.

manner, we present the sensitivity contours of the fracture energy functional, $\hat{\psi}_f$ (Equation (2.2.2)), corresponding to three different values of this constraint function, each differing by an order of magnitude. It is very difficult to say anything about the nonlinearity of this function in the design space since the dimension of the design space is so large, however, we believe this simple strategy for a fixed design provides some insight.

The portal frame example is used, along with the principal split of the elastic energy. The projection parameter, β, from Equation (2.3.6) is set to 1 in order to have negligible effect on the resulting sensitivities. Baseline contours using identical parameters from Section 2.4.1 are first presented. Since changing l_0 or the degradation function results in different values of $\hat{\psi}_f$ before fracture, a different prescribed displacement load is applied in each case in order to achieve the same value of $\hat{\psi}_f$. The parameters used for this comparison are given in Table 2.4 and the three different values of $\hat{\psi}_f$ are given in Table 2.5. The largest of the three values corresponds to a state of the system that is closest to fracture.

The resulting $\hat{\psi}_f$ sensitivity contours for each case are provided in Figure 2.18 and the peak sensitivity magnitudes are given in Table 2.6. For each corresponding value of $\hat{\psi}_f$, the change in

Table 2.4: Parameters used for $\hat{\psi}_f$ sensitivity comparison

	l_0 [mm]	s from Equation (2.2.9)
Baseline parameters	0.1	2 (quadratic)
Effect of l_0	0.2	2 (quadratic)
Effect of $g(d)$	0.1	0.5 (cubic)

Table 2.5: Investigated values of the fracture energy functional, $\hat{\psi}_f$

$\hat{\psi}_f$ $[J]$	3.45	34.5	345

magnitude of the peak sensitivity varying either l_0 or $g(d)$ is of interest.

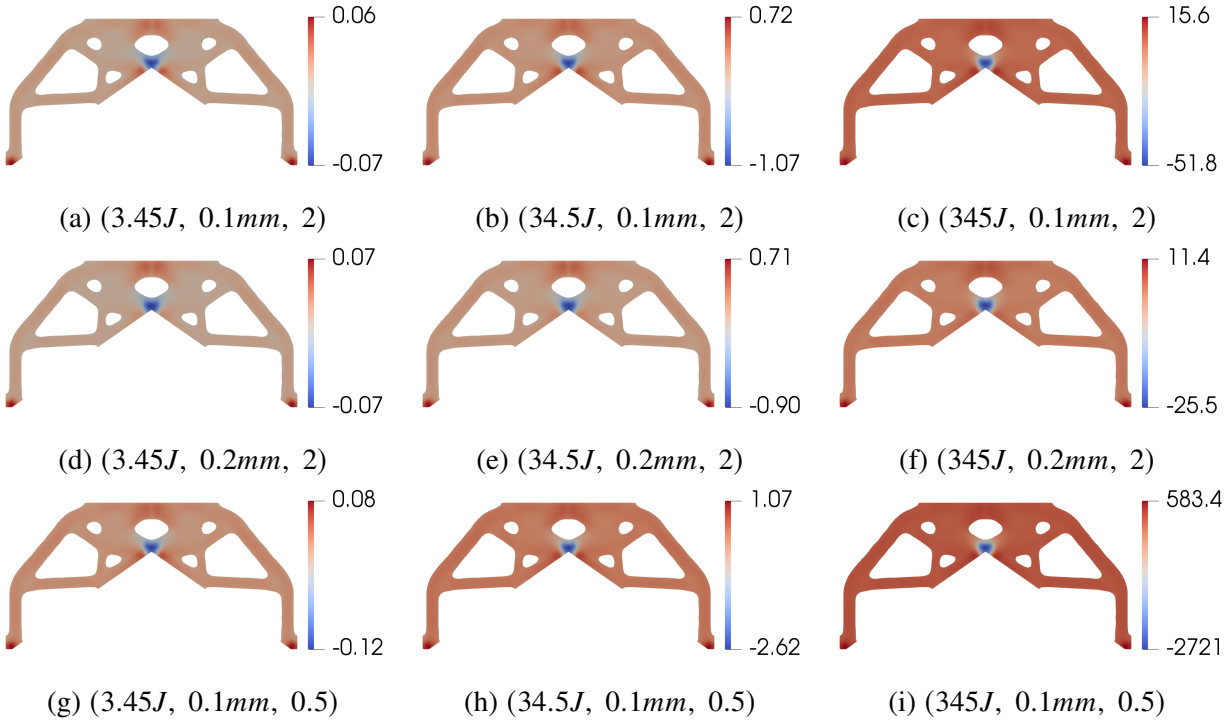

(a) $(3.45J,\ 0.1mm,\ 2)$ (b) $(34.5J,\ 0.1mm,\ 2)$ (c) $(345J,\ 0.1mm,\ 2)$

(d) $(3.45J,\ 0.2mm,\ 2)$ (e) $(34.5J,\ 0.2mm,\ 2)$ (f) $(345J,\ 0.2mm,\ 2)$

(g) $(3.45J,\ 0.1mm,\ 0.5)$ (h) $(34.5J,\ 0.1mm,\ 0.5)$ (i) $(345J,\ 0.1mm,\ 0.5)$

Figure 2.18: Fracture energy functional, $\hat{\psi}_f$, sensitivity contours. Subcaptions contain the tuple ($\hat{\psi}_f$, l_0, s) from Table 2.4 and 2.5.

Based on the data provided in Table 2.6, the effect of increasing the length scale parameter, l_0, is a relatively modest decrease in the peak sensitivity magnitude for each value of the fracture energy functional. Since the peak sensitivity does not change drastically from a change in l_0, it seems that there is little numerical benefit (from an optimizer perspective) to choosing a different value. Consequently, the authors believe l_0 should be selected in the usual manner (i.e. such that the

Table 2.6: Peak $\hat{\psi}_f$ sensitivity magnitudes (percent difference with respect to the peak sensitivity magnitude using the baseline parameters from Table 2.4 are provided in parentheses)

	$\hat{\psi}_f = 3.45J$	$\hat{\psi}_f = 34.5J$	$\hat{\psi}_f = 345J$
Baseline param.	$7.3e$-2 (-)	$1.1e0$ (-)	$5.1e1$ (-)
Effect of l_0	$7.0e$-2 (-4.1%)	$9.0e$-1 (-15.9%)	$2.5e1$ (-50.6%)
Effect of $g(d)$	$1.1e$-1 (59.4%)	$2.6e0$ (144.3%)	$2.7e3$ (5159.5%)

material response is more accurate).

However, changing the degradation function has a much larger impact on the peak sensitivity. In the case corresponding to the largest value of the fracture energy functional, the peak sensitivity increases by two orders of magnitude! Therefore, it is possible that if, during the optimization procedure, the applied load results in a system state that is very close to the softening point for the trial topology (corresponding to a larger value of the fracture energy functional), use of the cubic degradation function may result in a large change in the constraint sensitivities. Consequently, in this case, optimizer convergence *may* be impacted. Assuming the material response can be adequately captured using the quadratic degradation function, it is likely beneficial from a numerical perspective to avoid the use of the cubic degradation function. This is especially true in this case since the resulting topologies do not appear to be substantially different.

2.4.2 Cantilever Beam

In this example, a simple cantilever beam problem is investigated. The geometry, mesh, and boundary conditions are illustrated in Figure 2.19. The mesh consists of approximately 10,000 quadrilateral elements and the same material parameters from the previous example (shown in Table 2.1) are used with the exception of l_0 which is set to $2mm$. Additionally, the quadratic degradation function, presented in Equation (2.2.9), is employed in this example by setting the parameter $s = 2$.

The right edge of the beam is subjected to a prescribed downward displacement of $0.45mm$. This value is selected using the optimal topology from a linear elastic problem subject to the same compliance constraint (Figure 2.20a). When this topology is loaded, a prescribed displacement

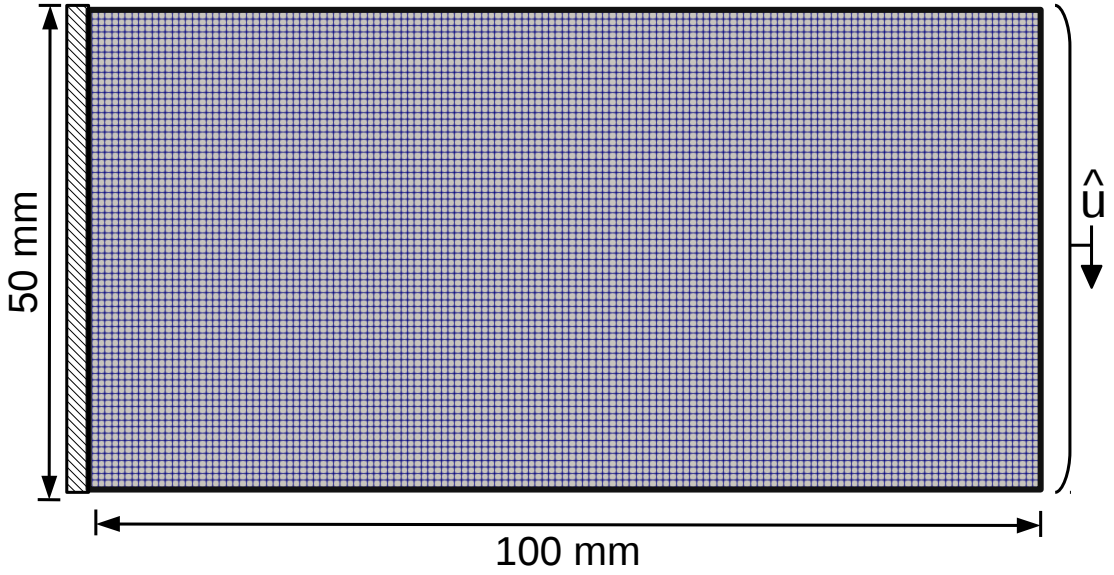

Figure 2.19: Cantilever beam geometry, mesh, and boundary conditions

of $0.45mm$ is slightly larger than the fracture inducing displacement. The relevant numerical optimization parameters for this problem are provided in Table 2.7 and three optimized topologies are presented in Figure 2.20.

Table 2.7: Cantilever beam numerical parameters

$r_{min}\ [mm]$	p	$C_{min}\ [J]$	$\hat{\psi}_f^{max}\ [J]$
2.0	3	480	1.5

Figure 2.20a corresponds to the optimal result for a linear elastic material model with only the compliance constraint. Figure 2.20b illustrates the topology using the coupled linear elastic with phase field material model also without a constraint on the fracture energy functional. Note that in this case the thickness of the members must be increased in order to satisfy the compliance requirement since some of the elastic energy is degraded by the presence of nonzero phase field values. Nevertheless, the general topology is close to the linear elastic design.

Finally, Figure 2.20c shows the optimal topology obtained when placing the fracture energy functional constraint on the design. It is clear that this topology is significantly different from the other two, which were obtained without this additional constraint. The design is no longer

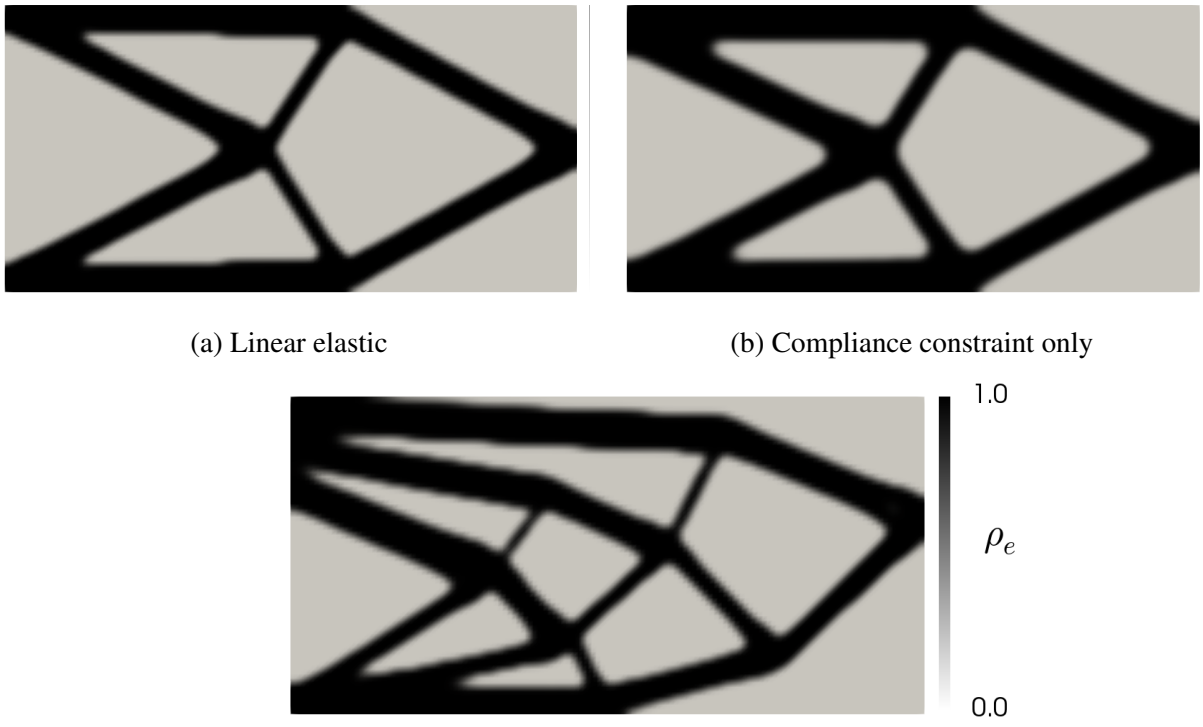

(a) Linear elastic

(b) Compliance constraint only

(c) Constrained fracture energy functional

Figure 2.20: Cantliever beam optimized topologies

symmetric due to the constraint reinforcing regions with high tensile energy. This is similar to the effect noted in Duysinx [177] where different stress limits are imposed in tension and compression. Additionally, this asymmetry is also noted in Liu et al. [178] in which a multi-material structure is studied with material interfaces primarily undergoing compression in the optimized designs.

The resulting values of the relevant functions are provided in Table 2.8. We note that for a 26.5% increase in the volume fraction with respect to the linear elastic design (8.7% additional volume fraction), the design resulting from the fracture energy functional constraint results in a 121.1% increase in the peak load prior to fracture. The corresponding load displacement and fracture energy functional curves for each design are provided in Figure 2.21 and the fractured states are illustrated in Figure 2.22. It can be seen that this approach results in a design with significantly increased strength when compared with the design obtained using only linear elastic physics.

Table 2.8: Cantilever beam results

	Volume Fraction	Peak Load $[MN]$	$\hat{\psi}_f^{max}$ $[J]$
Linear Elastic	0.328	0.862	–
Compliance Constraint Only	0.363	1.165	5.8
Constrained Fracture Energy	0.415	1.906	1.5

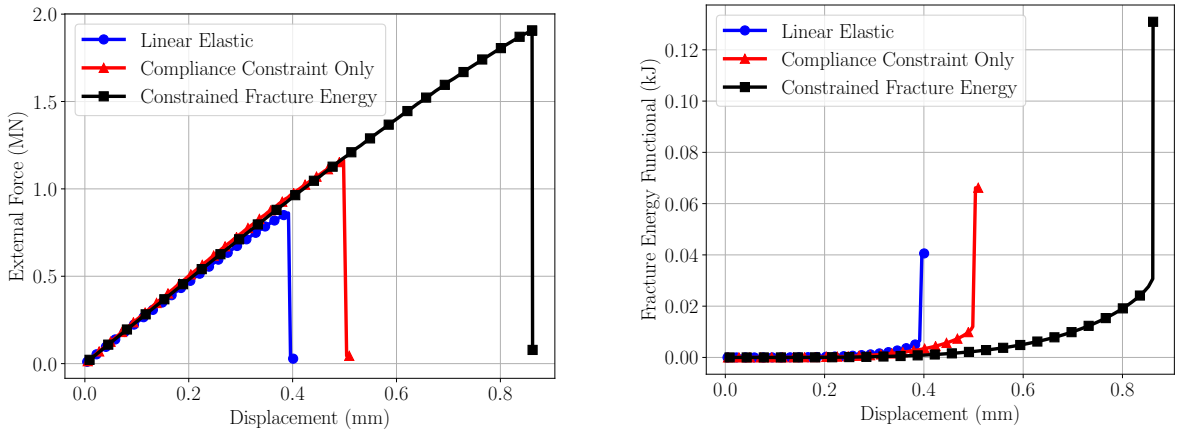

(a) (b)

Figure 2.21: Cantilever beam force-displacement (a) and fracture energy functional (b) curves. Note that the linear elastic curves correspond to the forward problem, employing the phase field method for fracture using the optimal topology obtained without the phase field method (illustrated in Figure 2.22a)

2.5 Conclusion

A framework utilizing density-based topology optimization for producing structures that are more resistant to brittle fracture is proposed which employs the phase field formulation for brittle fracture prediction. It is shown that constraining the phase field approximation of the fracture energy before fracture may induce large topological changes that result in a higher load carrying capacity prior to fracture. Two examples are provided which demonstrate the effectiveness of this approach. Additionally, we briefly explore the use of the two most common stored elastic energy splits and degradation functions in the literature, concluding that the use of the spectral energy split along with the typical quadratic degradation function may be preferred.

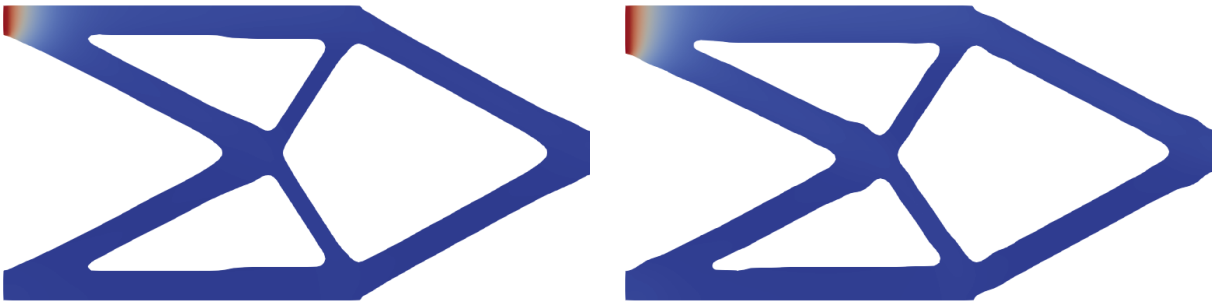

(a) Linear elastic

(b) Compliance constraint only

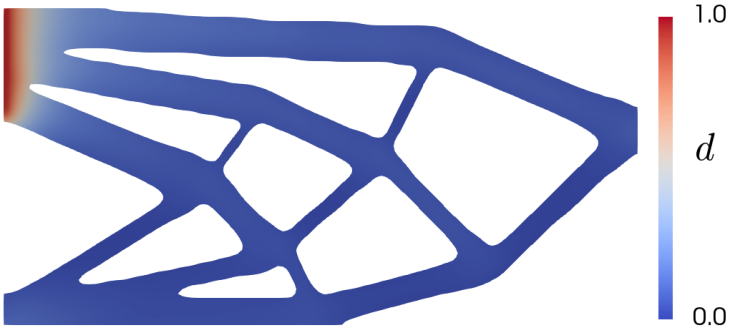

(c) Constrained fracture energy functional

Figure 2.22: Final phase field fracture contours corresponding to Figure 2.21

Chapter 3

An improved optimization formulation for brittle fracture resistance

This chapter is published as a journal article in: J. B. Russ and H. Waisman, "A novel topology optimization formulation for enhancing fracture resistance with a single quasi-brittle material", International Journal for Numerical Methods in Engineering, vol. 121, no. 13, pp. 2827–2856, 2020, doi: 10.1002/nme.6334.

3.1 Introduction

With respect to the previous chapter, here we propose several significant enhancements for obtaining fracture resistance of structures comprised of a single quasi-brittle material. A new function, which we refer to as the integrated fracture energy, is introduced into an aggregate objective that provides additional path information to the optimizer. This aggregate objective function, comprised of the volume fraction and the integrated fracture energy, is minimized, providing low-weight structures with significantly increased strength prior to fracture. As mentioned in the previous chapter, no fracture took place during the optimization iterations. Fracture is avoided due to the sudden change in system state before and after crack propagation significantly impacting optimizer convergence as a result of large discontinuities in the constraint functions chosen (e.g. the compliance and fracture energy). However, the functions proposed in this chapter provide the optimizer with additional information through the function sensitivities that allows fracture to take place during the initial design iterations with significantly less impact on optimizer convergence. Additionally, due to the significant nonlinearity associated with brittle fracture, we propose a constraint relaxation continuation scheme which assists the optimizer in finding an unfractured topology during these initial iterations.

Additionally, a phase field fracture formulation with an energetic threshold presented in Miehe et al. [24] is employed in order to avoid damage accumulation at low stress levels (here we note an energetic threshold had previously been proposed by Pham et al. [179] among others). This also greatly enhances the local control of the topology during the optimization process since phase field only accumulates in regions in which the energetic threshold has been exceeded as opposed to everywhere with nonzero tensile energy. Although this method has been used before in similar works [18, 17], here it takes on additional importance. Namely, since the optimizer eventually arrives at a set of designs that do not fracture under the prescribed load, this local accumulation of phase field acts as a fracture indicator in regions where cracks may nucleate. Since the magnitude of the phase field in these regions is typically much less than 1 in later iterations, it is important for the phase field to only accumulate locally in regions in which cracks may nucleate so that the sensitivities drive relevant local topological changes. Without the energetic threshold, structural members that are in tension are artificially strengthened due to the unnecessary energy degradation caused by the accumulation of nonzero phase field values (this phenomenon was also noted in the previous chapter for the cantilever beam example). In the current chapter, this energetic crack driving force is also smoothed in an effort to improve the convergence characteristics of the optimization process. This allows nonzero function sensitivities to be computed even in regions in which the tensile energy density does not exceed the critical value, avoiding the discontinuity in the derivative when the tensile energy density is close to the threshold but has not yet exceeded it.

The remainder of the chapter is organized as follows: In Section 3.2 we review the governing equations for quasi-static brittle fracture via the phase field formulation and introduce our smooth version of the energetic threshold proposed in Miehe et al. [24]. We then provide the details of the density-based design parameterization, define the optimization problem, and derive the analytical sensitivities in Section 3.3. Additionally, we compare the analytical sensitivities of the chosen objective and constraint functions against those in the previous chapter in an effort to justify our selection. Finally, the results from two benchmark numerical examples are presented in Section 3.4.

3.2 Phase field fracture model with energetic threshold

In this section we outline a phase field fracture formulation with energetic threshold based on the work of Miehe et al. [24], along with the details of the finite element discretization and numerical solution method.

3.2.1 Phase field fracture formulation

In a manner similar to the standard phase field fracture formulation outlined in Section 2.2, the total potential energy of a continuum body, Ω, may be expressed as

$$\Pi(\boldsymbol{u}, \Gamma) = W_{elas}(\nabla \boldsymbol{u}) + W_{frac}(\Gamma) - W_{ext}(\boldsymbol{u}) \tag{3.2.1}$$

in which the stored elastic energy, W_{elas}, is a function of the displacement gradient ($\nabla \boldsymbol{u}$), the fracture surface energy, W_{frac}, depends on the crack surface, and we assume the external work, W_{ext}, is only a function of the displacement field. Here we let $\boldsymbol{u}$ represent the displacement field and Γ represent the crack surface. Similar approximations of these quantities are used in which the key difference rests in the phase field approximation of the fracture surface energy. As presented in Miehe et al. [24], a strain criterion with an energetic threshold may be introduced in order to prevent degradation of the elastic energy at low stress levels. This updated model is used in this chapter where the fracture surface energy approximation may be expressed as

$$\hat{W}_{frac}(d) = \int_{\Omega} 2\psi_c \left(d + 2l_0^2 \nabla d \cdot \nabla d \right) dV \tag{3.2.2}$$

in which ψ_c represents a critical fracture energy per unit volume and the length scale, l_0, controls the width of the regularized fracture surface. A comparison of a Mode-I fracture using the phase field model with and without the energy threshold is provided in Figure 3.1 (both of these methods are detailed in Miehe et al. [24]). It is clear that use of the energetic threshold prevents much of the accumulation of phase field away from the fracture surface, thereby avoiding unnecessary elastic

energy degradation. The absolute difference between the phase field in Figures 3.1a and 3.1b is provided in Figure 3.2a for convenience. Additionally we provide a force-displacement curve in Figure 3.2b which is intended to illustrate the significant deviation from linear elastic behavior without the energetic threshold.

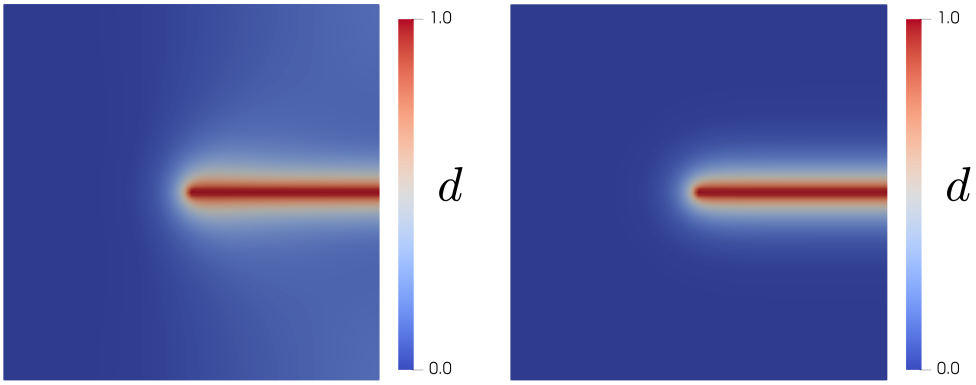

(a) Without energy threshold (b) With energy threshold

Figure 3.1: Mode-I fracture modeled with and without the energy threshold

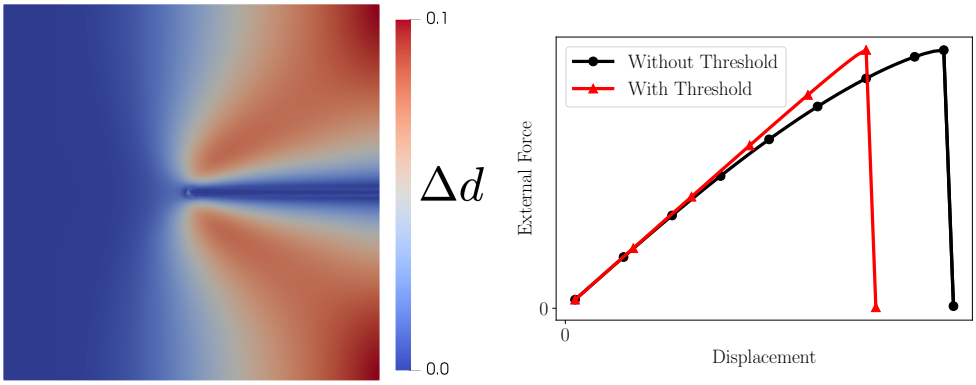

(a) Absolute difference (b) Force-displacement behavior

Figure 3.2: (a) Absolute difference between the phase field in Figure 3.1a and 3.1b. (b) Force-displacement comparison with responses calibrated to the same the peak load

The stored isotropic elastic energy density is additively decomposed into tensile and compressive components according to [23],

$$\psi_e(\varepsilon, d) = \psi_e^-(\varepsilon) + (g(d) + k)\psi_e^+(\varepsilon) \tag{3.2.3}$$

where the energy split based on a spectral decomposition of the strain tensor is used [22] (expressed as $\boldsymbol{\varepsilon} = \sum_{a=1}^{3} \varepsilon_a \boldsymbol{n}_a \otimes \boldsymbol{n}_a$ where $\{(\varepsilon_a, \boldsymbol{n}_a), a = 1, 2, 3\}$ represent the principal strains and associated directions). The compressive and tensile elastic energy densities may be defined as

$$\psi_e^-(\boldsymbol{\varepsilon}) = \frac{\lambda}{2} \langle \varepsilon_1 + \varepsilon_2 + \varepsilon_3 \rangle_-^2 + \mu \left(\langle \varepsilon_1 \rangle_-^2 + \langle \varepsilon_2 \rangle_-^2 + \langle \varepsilon_3 \rangle_-^2 \right) \tag{3.2.4}$$

$$\psi_e^+(\boldsymbol{\varepsilon}) = \frac{\lambda}{2} \langle \varepsilon_1 + \varepsilon_2 + \varepsilon_3 \rangle_+^2 + \mu \left(\langle \varepsilon_1 \rangle_+^2 + \langle \varepsilon_2 \rangle_+^2 + \langle \varepsilon_3 \rangle_+^2 \right) \tag{3.2.5}$$

in which (λ, μ) are the standard lame parameters of the undamaged material. Note that $\lambda = E\nu/((1+\nu)(1-2\nu))$ and $\mu = E/(2(1+\nu))$, where E and ν are the elastic modulus and Poisson's ratio, respectively. The Macaulay brackets are defined such that $\langle \cdot \rangle_+ = \max(\cdot, 0)$ and $\langle \cdot \rangle_- = \min(\cdot, 0)$. The total stored elastic energy is then obtained via integration over the volume.

$$\hat{W}_{elas}(\boldsymbol{\varepsilon}, d) = \int_\Omega \psi_e(\boldsymbol{\varepsilon}, d) dV \tag{3.2.6}$$

The phase field parameter, d, affects the stored elastic energy via the action of the so-called degradation function, $g(d) = (1 - d)^2$. In addition to the phase field parameter, the stored elastic energy is postulated to be a function of the small strain tensor, $\boldsymbol{\varepsilon}$, defined as the symmetric gradient of the displacement field, $\boldsymbol{\varepsilon}(\boldsymbol{u}) = \frac{1}{2} \left(\nabla \boldsymbol{u} + \nabla \boldsymbol{u}^T \right)$. Finally, we include a small constant parameter, k, in order to ensure the problem remains well-posed [22]. In all subsequent examples in this chapter k is set to 10^{-8}.

Note that the stress may be obtained directly from the elastic potential through standard arguments in thermodynamics. That is,

$$\boldsymbol{\sigma} = \underbrace{\frac{\partial \psi_e^-}{\partial \boldsymbol{\varepsilon}}}_{\boldsymbol{\sigma}^-} + (g(d) + k) \underbrace{\frac{\partial \psi_e^+}{\partial \boldsymbol{\varepsilon}}}_{\boldsymbol{\sigma}^+} \tag{3.2.7}$$

where $\boldsymbol{\sigma}$ is the damaged stress tensor and $\boldsymbol{\sigma}^-/\boldsymbol{\sigma}^+$ are the undamaged, compressive and tensile stress

tensors, respectively. The constitutive law then takes the following form,

$$\boldsymbol{\sigma} = (g(d) + k)\left(\lambda \langle \mathrm{tr}[\boldsymbol{\varepsilon}] \rangle_+ \mathbf{1} + 2\mu\boldsymbol{\varepsilon}^+\right) + \lambda \langle \mathrm{tr}[\boldsymbol{\varepsilon}] \rangle_- \mathbf{1} + 2\mu\boldsymbol{\varepsilon}^- \tag{3.2.8}$$

where $\boldsymbol{\varepsilon}^+$ and $\boldsymbol{\varepsilon}^+$ may be expressed via $\boldsymbol{\varepsilon}^\pm = \sum_{a=1}^{3} \langle \varepsilon_a \rangle_\pm \boldsymbol{n}_a \otimes \boldsymbol{n}_a$. Note that $\mathbf{1}$ is the second order identity tensor defined as $\mathbf{1} = \delta_{ij}\boldsymbol{e}_i \otimes \boldsymbol{e}_j$, in which δ_{ij} is the Kronecker delta and $\{\boldsymbol{e}_i\}$ represents an orthonormal basis.

Inserting the energy approximations in Equations (3.2.2) and (3.2.6) into the total potential energy in Equation (3.2.1), performing some algebra, and applying standard variational arguments yields the strong form of the governing equations.

$$\nabla \cdot \boldsymbol{\sigma} = \mathbf{0} \quad \text{in } \Omega \tag{3.2.9}$$

$$2\psi_c d - 8l_0^2\psi_c \nabla \cdot \nabla d - 2(1-d)(\psi_e^+ - \psi_c) = 0 \quad \text{in } \Omega \tag{3.2.10}$$

$$\boldsymbol{n} \cdot \boldsymbol{\sigma} = \boldsymbol{t} \quad \text{on } \partial\Omega^t \tag{3.2.11}$$

$$\boldsymbol{u} = \hat{\boldsymbol{u}} \quad \text{on } \partial\Omega^u \tag{3.2.12}$$

$$\boldsymbol{n} \cdot \nabla d = 0 \quad \text{on } \partial\Omega \tag{3.2.13}$$

Equation (3.2.9) represents quasi-static equilibrium in the absence of body forces while Equation (3.2.10) governs the evolution of the phase field. Finally, Equation (3.2.10) is modified in order to enforce irreversibility of crack growth. The local history field, $\mathcal{H}$, proposed in Miehe et al. [23], is used in order to ensure the local crack driving force is nondecreasing. Note that in the equation below, t, is a pseudo-time variable related to the incremental external loading.

$$\mathcal{H}(\boldsymbol{x}, t) = \max_{\tau \in [0,t]} \left\langle \psi_e^+(\boldsymbol{x}, \tau) - \psi_c \right\rangle_+ \tag{3.2.14}$$

In an effort to improve the convergence characteristics of the optimization procedure introduced later, the argument of the max operator is smoothed via a Kreisselmeier-Steinhauser-type function

controlled by the smoothing parameter, η_{ks}. This is similar to the smoothed damage evolution law described in James and Waisman [13]. The smooth approximation, $\mathcal{H}_s$, where $\mathcal{H}_s \approx \mathcal{H}$, may be expressed as

$$\mathcal{H}_s(\boldsymbol{x}, t) = \max_{\tau \in [0,t]} \frac{\psi_e^+(\boldsymbol{x}, \tau)}{\eta_{ks}} \ln \left[1 + \exp \left(\eta_{ks} \left(1 - \frac{\psi_c}{\psi_e^+(\boldsymbol{x}, \tau)} \right) \right) \right] \tag{3.2.15}$$

We propose this form in order to delay a potential numerical overflow of the exponential function and maintain the accuracy of the approximation (i.e. we avoid having large numbers within the exponential function which are typical of a tensile energy density, $\psi_e^+(\boldsymbol{x}, \tau)$ for certain engineering problems). The argument is set to 0 whenever ψ_e^+ is 0 in order to avoid the singularity and the effect of η_{ks} is illustrated in Figure 3.3. Note that the smooth threshold has very little effect on the physics, as is demonstrated in A.2. The final phase field equation is provided below.

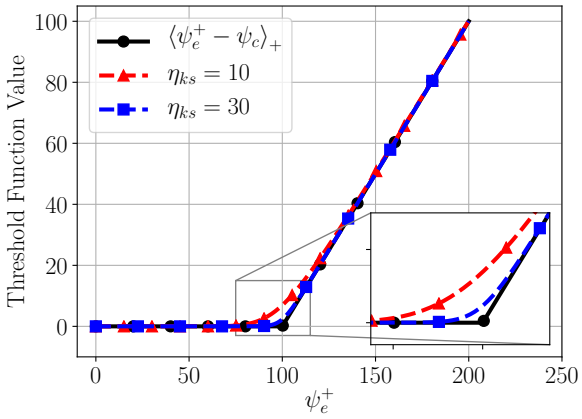

Figure 3.3: Threshold function versus smooth replacement for $\psi_c = 100$

$$2\psi_c d - 8l_0^2 \psi_c \nabla \cdot \nabla d - 2(1-d)\mathcal{H}_s = 0 \quad \text{in } \Omega \tag{3.2.16}$$

3.2.2 Finite element discretization

The weak form of the governing equations is obtained in the usual manner by multiplication of the strong form equations with admissible test functions, integration over the domain, and

application of the divergence theorem. The test functions are denoted $\boldsymbol{w}^u$ and w^d for the linear momentum and phase field equations, respectively. The residual form of the equations for the displacement field, R_u, and phase field, R_d, can then be written as follows

$$R_u = \int_\Omega \boldsymbol{\sigma} : \nabla \boldsymbol{w}^u dV - \int_{\partial\Omega^t} \boldsymbol{t} \cdot \boldsymbol{w}^u dS = 0 \tag{3.2.17}$$

$$R_d = \int_\Omega \left(2\psi_c d\ w^d + 8l_0^2 \psi_c \nabla d \cdot \nabla w^d - 2(1-d)\mathcal{H}_s\ w^d \right) dV = 0 \tag{3.2.18}$$

The above equations are then discretized and solved incrementally using the finite element method with appropriately chosen finite dimensional subspaces. The 2D domain is partitioned using 4-node quadrilateral elements and the same Lagrange basis functions are used for the test and trial spaces, consistent with the Galerkin formulation. Within an element, the approximate displacement field and phase field are both interpolated with bilinear shape functions such that

$$\boldsymbol{u}(\boldsymbol{x}) \approx \boldsymbol{N_u}(\boldsymbol{x})\bar{\boldsymbol{u}}, \quad d(\boldsymbol{x}) \approx \boldsymbol{N}_d(\boldsymbol{x})\bar{\boldsymbol{d}} \tag{3.2.19}$$

$$\varepsilon(\boldsymbol{u}(\boldsymbol{x})) \approx \boldsymbol{B_u}(\boldsymbol{x})\bar{\boldsymbol{u}}, \quad \nabla d(\boldsymbol{x}) \approx \boldsymbol{B}_d(\boldsymbol{x})\bar{\boldsymbol{d}} \tag{3.2.20}$$

The symbolic representation of the global interpolation matrices for the displacement and phase field are denoted by $\boldsymbol{N_u}$ and $\boldsymbol{N}_d$, respectively, while the vectors of the nodal degrees of freedom are represented with $\bar{\boldsymbol{u}}$ and $\bar{\boldsymbol{d}}$. Similarly, the matrices $\boldsymbol{B_u}$ and $\boldsymbol{B}_d$ contain the derivatives of the relevant shape functions. The global discretized residual equations may then be expressed as

$$\boldsymbol{R}_{\bar{\boldsymbol{u}}} = \int_{\hat{\Omega}} \boldsymbol{B}_{\boldsymbol{u}}^T \hat{\boldsymbol{\sigma}}\ dV - \int_{\partial\hat{\Omega}^t} \boldsymbol{N}_{\boldsymbol{u}}^T \boldsymbol{t}\ dS = \boldsymbol{0} \tag{3.2.21}$$

$$\begin{aligned} \boldsymbol{R}_{\bar{\boldsymbol{d}}} = &\int_{\hat{\Omega}} \left(2\psi_c \boldsymbol{N}_{\boldsymbol{d}}^T \boldsymbol{N_d} + 8l_0^2 \psi_c \boldsymbol{B}_{\boldsymbol{d}}^T \boldsymbol{B_d} \right) \bar{\boldsymbol{d}}\ dV - \\ &\int_{\hat{\Omega}} 2(1 - \boldsymbol{N_d}\bar{\boldsymbol{d}}) \boldsymbol{N}_{\boldsymbol{d}}^T\ \mathcal{H}_s\ dV = \boldsymbol{0} \end{aligned} \tag{3.2.22}$$

where, $\hat{\boldsymbol{\sigma}}$ is the stress tensor in Voigt notation and $\hat{\Omega}$ represents the discretized domain. Note that although we express the global residual form for convenience, in practice the contributions are

computed element-wise and assembled into the global system.

For each increment in load, the nodal solution may be obtained by an iterative Newton method, in which the solution is updated via the linearized nodal residual equations until a tolerance on the relative l_2-norm of the residual is obtained. Grouping these equations, $\boldsymbol{R_y} = [\boldsymbol{R_{\bar{u}}}\,;\boldsymbol{R_{\bar{d}}}]$, and the degrees of freedom, $\boldsymbol{y} = [\bar{\boldsymbol{u}}\,;\bar{\boldsymbol{d}}]$, we have

$$\boldsymbol{y}^{(k+1)} = \boldsymbol{y}^{(k)} - \left[\frac{\partial \boldsymbol{R}_{\boldsymbol{y}}^{(k)}}{\partial \boldsymbol{y}}\right]^{-1} \boldsymbol{R}_{\boldsymbol{y}}^{(k)} \tag{3.2.23}$$

where the superscript k implies the quantity corresponds to iteration k and the Jacobian matrix may be expressed as

$$\boldsymbol{J} = \left[\frac{\partial \boldsymbol{R}_{\boldsymbol{y}}}{\partial \boldsymbol{y}}\right] = \begin{bmatrix} \boldsymbol{J}_{\bar{\boldsymbol{u}}\bar{\boldsymbol{u}}} & \boldsymbol{J}_{\bar{\boldsymbol{u}}\bar{\boldsymbol{d}}} \\ \boldsymbol{J}_{\bar{\boldsymbol{d}}\bar{\boldsymbol{u}}} & \boldsymbol{J}_{\bar{\boldsymbol{d}}\bar{\boldsymbol{d}}} \end{bmatrix} \tag{3.2.24}$$

In contrast to the previous chapter in which the nodal solution was updated monolithically, Equation (3.2.23) is replaced with a staggered update of each nodal variable via the following equations,

$$\bar{\boldsymbol{u}}^{(k+1)} = \bar{\boldsymbol{u}}^{(k)} - \left[\boldsymbol{J}_{\bar{\boldsymbol{u}}\bar{\boldsymbol{u}}}^{(k)}\left(\bar{\boldsymbol{u}}^{(k)}, \bar{\boldsymbol{d}}^{(k)}\right)\right]^{-1} \boldsymbol{R}_{\bar{\boldsymbol{u}}}^{(k)}\left(\bar{\boldsymbol{u}}^{(k)}, \bar{\boldsymbol{d}}^{(k)}\right) \tag{3.2.25}$$

$$\bar{\boldsymbol{d}}^{(k+1)} = \bar{\boldsymbol{d}}^{(k)} - \left[\boldsymbol{J}_{\bar{\boldsymbol{d}}\bar{\boldsymbol{d}}}^{(k)}\left(\bar{\boldsymbol{u}}^{(k+1)}, \bar{\boldsymbol{d}}^{(k)}\right)\right]^{-1} \boldsymbol{R}_{\bar{\boldsymbol{d}}}^{(k)}\left(\bar{\boldsymbol{u}}^{(k+1)}, \bar{\boldsymbol{d}}^{(k)}\right) \tag{3.2.26}$$

Each of the relevant terms in the jacobian matrix may be computed as defined below.

$$\boldsymbol{J}_{\bar{\boldsymbol{u}}\bar{\boldsymbol{u}}} = \frac{\partial \boldsymbol{R}_{\bar{\boldsymbol{u}}}}{\partial \bar{\boldsymbol{u}}} = \int_{\hat{\Omega}} \boldsymbol{B}_{\boldsymbol{u}}^T \boldsymbol{D} \boldsymbol{B}_{\boldsymbol{u}}\, dV \tag{3.2.27}$$

$$\boldsymbol{J}_{\bar{\boldsymbol{d}}\bar{\boldsymbol{d}}} = \frac{\partial \boldsymbol{R}_{\bar{\boldsymbol{d}}}}{\partial \bar{\boldsymbol{d}}} = \int_{\hat{\Omega}} \left((2\psi_c + 2\mathcal{H}_s)\, \boldsymbol{N}_{\boldsymbol{d}}^T \boldsymbol{N}_{\boldsymbol{d}} + 8 l_0^2 \psi_c \boldsymbol{B}_{\boldsymbol{d}}^T \boldsymbol{B}_{\boldsymbol{d}}\right)\, dV \tag{3.2.28}$$

$$\boldsymbol{J}_{\bar{\boldsymbol{u}}\bar{\boldsymbol{d}}} = \frac{\partial \boldsymbol{R}_{\bar{\boldsymbol{u}}}}{\partial \bar{\boldsymbol{d}}} = \int_{\hat{\Omega}} -2(1 - \boldsymbol{N}_{\boldsymbol{d}}\bar{\boldsymbol{d}}) \boldsymbol{B}_{\boldsymbol{u}}^T \hat{\boldsymbol{\sigma}}^+ \boldsymbol{N}_{\boldsymbol{d}}\, dV \tag{3.2.29}$$

$$\boldsymbol{J}_{\bar{\boldsymbol{d}}\bar{\boldsymbol{u}}} = \frac{\partial \boldsymbol{R}_{\bar{\boldsymbol{d}}}}{\partial \bar{\boldsymbol{u}}} = \int_{\hat{\Omega}} 2(1 - \boldsymbol{N}_{\boldsymbol{d}}\bar{\boldsymbol{d}}) \boldsymbol{N}_{\boldsymbol{d}}^T \frac{\partial \mathcal{H}_s}{\partial \bar{\boldsymbol{u}}}\, dV \tag{3.2.30}$$

The constitutive matrix, $\boldsymbol{D}$, used in Equation (3.2.27), is related to the tensor form of the stress-strain

constitutive law which we have explicitly provided in A.1. The jacobian and residual equations are integrated using a standard 4-point Gauss quadrature rule for a quadrilateral element and the irreversibility requirement is enforced via a history variable stored at each quadrature point. Additionally, the staggered solution algorithm is outlined below. Note that this procedure is largely identical to that of Miehe et al. [23] except that we employ the residual convergent variant of the original algorithm, in a manner similar to [180].

Algorithm 1 Iterative staggered update of nodal degrees of freedom, $(\bar{\boldsymbol{u}}, \bar{\boldsymbol{d}})$

$t \leftarrow 0$
$\bar{\boldsymbol{u}}, \bar{\boldsymbol{d}} \leftarrow \boldsymbol{0}$
while $t < t_{final}$ **do**
  $t \leftarrow t + \Delta t$
  $\hat{\boldsymbol{u}} \leftarrow \min(t, 1.0) \cdot \hat{\boldsymbol{u}}_{final}$ {Update prescribed displacements}
  $k \leftarrow 0$
  while $||\boldsymbol{R}^{(k)}_{\bar{\boldsymbol{u}}}||_2 \,/\, ||\boldsymbol{R}^{(0)}_{\bar{\boldsymbol{u}}}||_2 > 10^{-8}$ **or** $||\boldsymbol{R}^{(k)}_{\bar{\boldsymbol{d}}}||_2 \,/\, ||\boldsymbol{R}^{(0)}_{\bar{\boldsymbol{d}}}||_2 > 10^{-8}$ **do**
    $k \leftarrow k + 1$
    Compute $\boldsymbol{J}^{(k)}_{\bar{\boldsymbol{u}}\bar{\boldsymbol{u}}}$ and $\boldsymbol{R}^{(k)}_{\bar{\boldsymbol{u}}}$
      Update $\bar{\boldsymbol{u}}$ via Equation (3.2.25)
    Update $\mathcal{H}_s$ using updated $\bar{\boldsymbol{u}}$
    Compute $\boldsymbol{J}^{(k)}_{\bar{\boldsymbol{d}}\bar{\boldsymbol{d}}}$ and $\boldsymbol{R}^{(k)}_{\bar{\boldsymbol{d}}}$
      Update $\bar{\boldsymbol{d}}$ via Equation (3.2.26)
  end while
end while

3.2.3 Expanded form of the discretized equations

Path-dependence is introduced into the governing equations via the history variable in Equation (3.2.15) in order to satisfy irreversibility requirements for the evolution of the phase field. Consequently, functions used in the optimization problem definition which have a dependence on the field quantities $(\boldsymbol{u}, d)$ will also be dependent on the solution path. Computation of the function sensitivities in this case may be simplified by introducing another independent variable, h, at every quadrature point in the domain which replaces the history function, $\mathcal{H}_s$. This is similar to the procedure outlined in Alberdi et al. [50] for the local variables of a plasticity model which evolve in time according

to their own rules. Additionally, introducing this new independent variable during the sensitivity analysis allows the residual equations to be written such that they depend only on the solution at the current and previous time steps, rather than the entire time history preceding the current time (since the history function is a maximum over all previous time increments).

The evolution of this new quantity is controlled by a corresponding additional equation which is added to the monolithic system. Note that the number of additional equations is also equal to the number of quadrature points in the finite element mesh. These equations take the following form

$$H^{n+1}(\boldsymbol{\xi}_i) = 0 = \begin{cases} h^{n+1}(\boldsymbol{\xi}_i) - h^n(\boldsymbol{\xi}_i), & \text{if } \alpha(\boldsymbol{\xi}_i) < h^n(\boldsymbol{\xi}_i) \\ h^{n+1}(\boldsymbol{\xi}_i) - \alpha(\boldsymbol{\xi}_i), & \text{otherwise} \end{cases} \tag{3.2.31}$$

where $\boldsymbol{\xi}_i$ corresponds to the i^{th} quadrature point in the *global* finite element mesh and α represents the argument of the max operator in Equation (3.2.15), namely,

$$\alpha(\boldsymbol{\xi}_i) = \frac{\psi_e^+|_{\boldsymbol{\xi}_i}}{\eta_{ks}} \ln\left[1 + \exp\left(\eta_{ks}\left(1 - \frac{\psi_c}{\psi_e^+|_{\boldsymbol{\xi}_i}}\right)\right)\right] \tag{3.2.32}$$

where the superscript $(\cdot)^n$ implies the quantity corresponds to pseudo-time, t_n. Note that Equation (3.2.31) essentially replaces the max operator in the history function (e.g. if the current value of α is smaller than the previous, set the history function value equal to the previous, otherwise update the history function with the current value). This updated form makes the residual equations at time step (i) dependent on only the solution at time step (i) and $(i-1)$ rather than all previous increments as previously mentioned. As a result, a less complex structure may be used during the sensitivity analysis since the residual at step (i) has the form $\boldsymbol{R}^{(i)} = \boldsymbol{R}^{(i)}(\boldsymbol{\rho}, \boldsymbol{z}^{(i)}, \boldsymbol{z}^{(i-1)})$ with $\boldsymbol{z}$ being the augmented solution vector defined below. Clearly this form requires far fewer derivatives than the form used during the forward analyses since the original residual equations depend on all previous solution states due to the maximum over all previous time present in Equation (3.2.15). We form a monolithic system consisting of the displacement and phase field residual equations, augmented with the additional gauss point equations, $\boldsymbol{H_h} = \left[H^{n+1}(\boldsymbol{\xi}_1), \ldots, H^{n+1}(\boldsymbol{\xi}_{N_{gp}})\right]$ (where

N_{gp} is the total number of quadrature points in the finite element model) which results in

$$\boldsymbol{R} = \begin{pmatrix} \boldsymbol{R}_{\bar{u}} \\ \boldsymbol{R}_{\bar{d}} \\ \boldsymbol{H}_h \end{pmatrix} \tag{3.2.33}$$

Note that the history function, $\mathcal{H}_s$, in $\boldsymbol{R}_{\bar{d}}$ (Equation (3.2.22)) is replaced with the independent variable, $h(\boldsymbol{\xi}_i)$, when the integrand is evaluated at the corresponding quadrature point. The new jacobian of this augmented system then takes on the following block structure

$$\frac{\partial \boldsymbol{R}}{\partial \boldsymbol{z}} = \begin{bmatrix} \frac{\partial \boldsymbol{R}_{\bar{u}}}{\partial \bar{u}} & \frac{\partial \boldsymbol{R}_{\bar{u}}}{\partial \bar{d}} & \mathbf{0} \\ \mathbf{0} & \frac{\partial \boldsymbol{R}_{\bar{d}}}{\partial \bar{d}} & \frac{\partial \boldsymbol{R}_{\bar{d}}}{\partial h} \\ \frac{\partial \boldsymbol{H}_h}{\partial \bar{u}} & \mathbf{0} & \frac{\partial \boldsymbol{H}_h}{\partial h} \end{bmatrix} \tag{3.2.34}$$

where $\boldsymbol{z}$ represents the augmented solution vector,

$$\boldsymbol{z} = \begin{pmatrix} \bar{\boldsymbol{u}} \\ \bar{\boldsymbol{d}} \\ \boldsymbol{h} \end{pmatrix} \tag{3.2.35}$$

As previously mentioned, this new system structure will allow a less complex algorithm to be constructed and used for computing analytical sensitivities of the functions used in the optimization problem definition. This algorithm is presented later in Section 3.3.4.

3.3 Topology optimization formulation

In this section, the density-based design parameterization is first presented. Subsequently, the optimization problem is clearly defined and the selection of the objective and constraint functions is motivated. The filtering and projection schemes used in this chapter are presented and the analytical,

path-dependent sensitivities for each of the relevant functions are derived. Finally, we draw a comparison between the sensitivities of the functions used in this chapter and the previous in order to further justify our selection.

3.3.1 Design parameterization

Consistent with the well-known SIMP formulation (Solid Isotropic Material with Penalization [162, 163]), each finite element within the discretized domain is parameterized with a pseudo-density, ρ_e, which is allowed to vary continuously in the range $[0, 1]$. A pseudo-density of 1 corresponds to an element completely filled with material, while a value of 0 approximates the effect of a void in the domain. The pseudo-density for an element typically enters the constitutive relation through the computation of effective material properties which we compute using the relations,

$$E = \left(\epsilon_e + (1 - \epsilon_e)\, \rho_e^{p_1}\right)\ E_0 \tag{3.3.1}$$

$$\psi_c = \left(\epsilon_d + (1 - \epsilon_d)\, \rho_e^{p_2}\right)\ \psi_{c_0} \tag{3.3.2}$$

where E_0 and ψ_{c_0} represent the properties corresponding to the solid material. The ersatz parameters ϵ_e and ϵ_d are taken to be 10^{-8} and 10^{-4}, respectively. In order to prevent spurious cracks in low density regions we take $p_2 < p_1$ beginning initially with $p_1 = 3$ and $p_2 = 1.5$, and gradually increasing these parameters over the course of the optimization process to $p_1 = 4.5$ and $p_2 = 3$. Additionally, as detailed in Section 3.3.3, the design variables ($\boldsymbol{\theta}$) are filtered and projected. Therefore the element pseudo-density (ρ_e) in the material interpolations above is actually a composite function

$$\rho_e = \rho_e\left(\hat{\rho}_e\left(\boldsymbol{\theta}\right)\right) \tag{3.3.3}$$

where $\boldsymbol{\theta}$ is controlled by the optimizer, $\{\hat{\rho}_e\}$ are the filtered design variables, and $\{\rho_e\}$ are the projection of the filtered design variables.

3.3.2 Optimization problem statement

Qualitatively, we seek low weight structures that have a significantly increased resistance to fracture when compared with designs obtained from classical weight minimization problems modeled with only linear elastic physics. Our mathematical optimization approach to achieve this is outlined below.

An aggregate objective function, which consists of the material volume fraction, $\Lambda(\boldsymbol{\rho})$, and a new function, referred to as the integrated fracture energy, $\Xi(\boldsymbol{\rho}, d)$, is minimized. Minimization of the volume fraction is equivalent to weight minimization since we consider only a single material with uniform weight density, while penalization of the integrated fracture energy provides the desired fracture resistance. Consequently, we search for Pareto optimal designs with a tradeoff between structural weight and fracture resistance. Due to the use of a displacement-controlled loading scheme, a lower bound constraint is placed on the total work, $W(\boldsymbol{\rho}, \boldsymbol{u}, d)$. The resulting mathematical optimization problem statement is expressed as

$$
\begin{aligned}
\underset{\boldsymbol{\theta}}{\text{minimize}} \quad & \Lambda(\boldsymbol{\rho}) + \omega \cdot \Xi(\boldsymbol{\rho}, d) \\
\text{subject to} \quad & 0 \leq \theta_e \leq 1, \ e = 1, \ldots, N_{elem} \\
& W_{min} \leq W(\boldsymbol{\rho}, \boldsymbol{u}, d) \\
& \boldsymbol{R}^{(i)} = \boldsymbol{0}, \ i = 1, \ldots, N_{steps}
\end{aligned}
$$

where ω is a user-specified weighting factor, which may be regarded as a penalty parameter, penalizing the creation of fracture surfaces. Each of the relevant functions is defined below along with its numerically integrated form. Note that Ξ and W are integrated in pseudo-time using the trapezoidal rule and in space using a standard 4-point (i.e. $N_{quad} = 4$) Gauss quadrature rule. The subscript $(\cdot)_{e_q}$ implies the quantity is evaluated at the q^{th} quadrature point of element e and a

superscript $(\cdot)^{(i)}$ signifies the quantity is evaluated at the i^{th} pseudo-time increment.

$$\Lambda(\boldsymbol{\rho}) = \frac{1}{\int_{\hat{\Omega}} dV} \int_{\hat{\Omega}} \rho \; dV = \frac{1}{\sum_{e=1}^{N_{elem}} V_e} \sum_{e=1}^{N_{elem}} \rho_e \; V_e \tag{3.3.4}$$

$$\Xi(\boldsymbol{\rho}, d) = \int_0^t \hat{W}_{frac} \; d\tau \approx \sum_{i=1}^{N_{steps}} \frac{1}{2} \left(\hat{W}_{frac}^{(i)} + \hat{W}_{frac}^{(i-1)} \right) \Delta\tau^{(i)} \tag{3.3.5}$$

$$\begin{aligned} W(\boldsymbol{\rho}, \boldsymbol{u}, d) &= \int_0^t \int_{\hat{\Omega}} \boldsymbol{\sigma} : \dot{\boldsymbol{\varepsilon}} \; dV \; d\tau \\ &\approx \sum_{i=1}^{N_{steps}} \sum_{e=1}^{N_{elem}} \sum_{q=1}^{N_{quad}} \frac{1}{2} \left(\boldsymbol{\sigma}_{e_q}^{(i)} + \boldsymbol{\sigma}_{e_q}^{(i-1)} \right) : \left(\boldsymbol{\varepsilon}_{e_q}^{(i)} - \boldsymbol{\varepsilon}_{e_q}^{(i-1)} \right) \; w_{e_q} \end{aligned} \tag{3.3.6}$$

Note that w_{e_q} represents the quadrature weight multiplied by the jacobian of the isoparametric mapping, V_e represents the volume of element e, $\dot{\boldsymbol{\varepsilon}}$ is the derivative of the strain tensor with respect to pseudo-time, and $\hat{W}_{frac}$ is numerically computed as follows,

$$\hat{W}_{frac}^{(i)} \approx \sum_{e=1}^{N_{elem}} \sum_{q=1}^{N_{quad}} 2\psi_c \left(d_{e_q} + 2l_0^2 \nabla d_{e_q} \cdot \nabla d_{e_q} \right) \cdot w_{e_q} \tag{3.3.7}$$

The final set of constraint equations involving the augmented residual vectors, $\{\boldsymbol{R}^{(i)}\}$, are enforced during the forward analyses and represent quasi-static equilibrium requirements and history variable evolution at each load step. A flowchart of the optimization solution procedure is provided below in Figure 3.4.

It is important to note that the work, W, and integrated fracture energy, Ξ, were selected for a specific reason which will become more apparent in Section 3.3.4. The compliance function that is typically used in classical weight minimization problems with assumed linear elasticity (i.e. $\boldsymbol{f}^T\boldsymbol{u}$ with external force vector, $\boldsymbol{f}$) is only a function of the system state at the end of the forward analyses and, consequently, is avoided for reasons described below. In contrast to this, the external work is a function of the state throughout the entire solution path. Work quantities have been exploited in

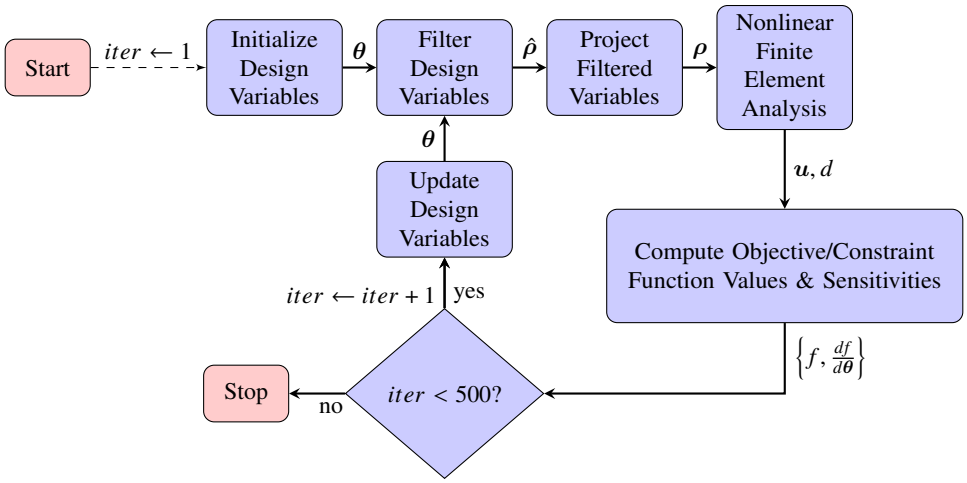

Figure 3.4: Flow chart illustrating the optimization procedure

many previous works ([45, 181, 18] to name only a few).

In the context of brittle fracture, functions of only the end state will almost certainly be discontinuous in the design variables. This presents a difficulty for gradient-based optimizers which rely on smoothness of the objective and constraint functions. Here we make an effort to explain this concept with the end-compliance and fracture energy functions used in previous chapter, motivating a clearer justification for the work and integrated fracture energy functions chosen herein. For example, take a given structural topology, which we refer to as Design A, that does not satisfy a minimum stiffness constraint (either work or end-compliance). Assume that Design A does not fracture under the applied load. The optimizer will attempt to increase the stiffness at the next design iteration and we refer to this updated topology as Design B. The increase in stiffness may result in fracture for the given applied load. This situation is illustrated in Figure 3.5a. The end-compliance of Design B is almost negligible due to the energy dissipated by fracture, while the compliance of Design A is comparatively large. However, the work corresponding to Design B is larger than that of Design A, which better reflects the increase in stiffness. Although the work function may still be discontinuous in the design variables, the jump in value is almost certainly smaller than the associated jump in the compliance due to the contribution of the pre-fracture load history. Additionally, the end-compliance contains very little information with regard to the structural state prior to fracture. This will be briefly explored in Section 3.3.4 via a comparison of the function

sensitivities.

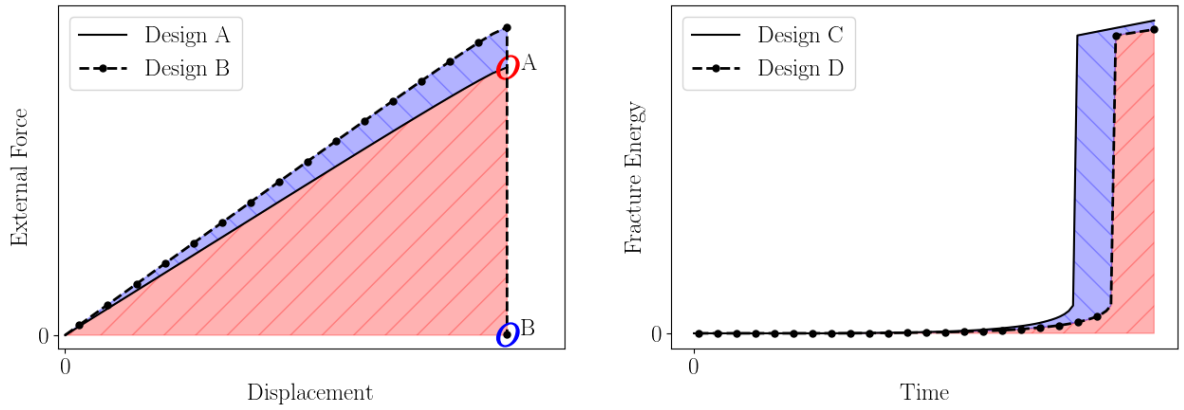

(a) (b)

Figure 3.5: (a) Example force vs. displacement curves for two similar topologies. The end state of Design A corresponds to point A, and the end state of Design B corresponds to point B. Design A clearly has a higher end-compliance than Design B, which has fractured. However, this comparison does not reflect the additional work over the load history required to impart the same displacement load on Design B. This additional work corresponds to the blue-shaded region. (b) Example fracture energy vs. time curves illustrating the additional area under the curve resulting from a fracture occuring sooner in time for a particular topology (Design C) versus a topology which fractures later in time (Design D). The additional area is shaded in blue and corresponds to the increase in the integrated fracture energy function.

In light of these ideas, we propose to minimize the integrated fracture energy, Ξ, in place of the crack surface functional in Equation (3.2.2). Although the integrated fracture energy does *not* have a physical meaning, it has two nice properties: (1) It is a function of the system state at each increment in time and, consequently, provides additional path information to the optimizer through the function sensitivities (this is explored in Section 3.3.4). (2) A decrease in the function value corresponds to a decrease in the crack length and/or a delay in the time at which fracture occurs, both of which are desirable for fracture resistance. An increase in the fracture energy corresponds to an increase in the crack length which results in a larger area under the fracture energy vs. time curve. Additionally, a delay in the time at which fracture occurs also corresponds to a decrease in total area under the curve since the fracture energy is nondecreasing in time due to irreversibility requirements. This additional area is illustrated in Figure 3.5b. Design C fractures earlier in time

than Design D which generates additional area under the curve, corresponding to an increase in the integrated fracture energy function equal to the area of the blue-shaded region.

Finally, we detail a continuation scheme that is used in which the lower bound on the work function, W_{min}, is relaxed during the first few optimization iterations. Due to the nonlinearity of a brittle fracture process, it can be difficult for the optimizer to satisfy the work constraint initially due to the presence of cracks. Since the drive to enter the feasible region is often stronger than the drive to lower the objective function value, we relax the constraint lower bound according to Algorithm 2 below, where α_r is the relaxation coefficient in the new constraint equation provided in Equation (3.3.8). Note that α_r is a parameter between 0 and 1 that is gradually increased to 1 over the first 20 iterations in the subsequent numerical examples.

$$\alpha_r \cdot W_{min} \leq W(\boldsymbol{\rho}, \boldsymbol{u}, d) \tag{3.3.8}$$

Algorithm 2 Constraint relaxation coefficient, α_r, continuation scheme

1. **for** $iter = 1$ to N_{iters} **do**
2. **if** $(iter \leq 10)$ **then**
3. $\alpha_r \leftarrow 0.5$
4. **else if** $(iter \leq 20)$ **then**
5. $\alpha_r \leftarrow 0.5 + \frac{1}{20}\,(iter - 10)$
6. **else**
7. $\alpha_r \leftarrow 1$
8. **end if**
9. **end for**

3.3.3 Density filter and projection

In order to alleviate checkerboard patterns and other numerical instabilities, a density filter may be applied which also provides a necessary regularization for mesh-independence as discussed in Sigmund and Petersson [164]. The filtering scheme proposed in Bruns and Tortorelli [165], based on a gaussian-type weighting function is used in this chapter. This procedure introduces a

topological length-scale, r_{min}, which regularizes the problem, provided that a mesh with sufficiently fine discretization is used. The design variables may be filtered utilizing a pre-constructed filter matrix of weighting coefficients, W_{ej},

$$\hat{\rho}_e = \sum_{j=1}^{N_{elem}} W_{ej}\theta_j \tag{3.3.9}$$

in which the components of the matrix are

$$W_{ej} = \frac{w_{ej}}{\sum_{i=1}^{N_{elem}} w_{ei}} \tag{3.3.10}$$

$$w_{ej} = \begin{cases} \exp\left(-\frac{r_{ej}^2}{r_{min}^2}\right), & \text{if } r_{ej} \leq r_{min} \\ 0, & \text{otherwise} \end{cases} \tag{3.3.11}$$

where $r_{ej} = ||\boldsymbol{X}_e - \boldsymbol{X}_j||_2$ is the distance between the centroids of elements e and j.

Although increasing the SIMP penalization parameters, p_1 and p_2, tends to produce structures with pseudo-densities closer to 0 or 1, the filtering scheme inevitably creates a transition region with intermediate pseudo-density values. In order to eliminate much of this transition region we employ a projection scheme based on the work of Guest et al. [166] and Wang et al. [167].

$$\rho_e = \frac{\tanh(\beta\eta) + \tanh(\beta(\hat{\rho}_e - \eta))}{\tanh(\beta\eta) + \tanh(\beta(1 - \eta))} \tag{3.3.12}$$

Note here that η governs the density threshold at which the projection takes place and β governs the strength of the projection operation. In all subsequent analyses η is fixed at 0.5 while a continuation scheme is used to update β as described in Algorithm 3 below, where β is progressively increased in increments of 0.75 until a maximum value of 20 is reached. Note that β is restricted to 1 during the first 100 optimization iterations in order to avoid additional unnecessary nonlinearity and local minima.

Algorithm 3 Continuation scheme applied to projection parameter, β

1. $\beta \leftarrow 1$
2. **for** $iter = 1$ to N_{iters} **do**
3. **if** ($iter > 100$) and ($iter$ divisible by 15) **then**
4. $\beta \leftarrow \beta + 0.75$
5. $\beta \leftarrow \min(\beta, 20)$
6. **end if**
7. **end for**

3.3.4 Derivation of analytical sensitivities

Due primarily to the large number of design variables in most topology optimization problems, along with computationally expensive finite element simulations, gradient based optimization methods are clearly preferred. Here we compute the analytical gradients using a computationally efficient, path-dependent adjoint method, based on the work of Michaleris et al. [49].

As a result of the expanded form of the governing equations provided in Section 3.2.3, the augmented residual (Equation (3.2.33)) evaluated at pseudo-time t_n, only depends on the pseudo-densities and the augmented solution vector at pseudo-time t_{n-1} and t_n.

$$\boldsymbol{R}^n = \boldsymbol{R}^n \left(\boldsymbol{\rho}, \boldsymbol{z}^n, \boldsymbol{z}^{n-1} \right), \text{ where } n = 1, \ldots, N_{steps} \tag{3.3.13}$$

The objective and constraint functions given in Section 3.3.2 may all be represented as a general function of the design variables and the solution vector at the each time increment, $f(\boldsymbol{\rho}, \boldsymbol{z}^N, \ldots, \boldsymbol{z}^1)$, where we have used the short-hand notation, $N = N_{steps}$. Augmenting this function with the sum of the inner product of the residual at each time increment (Equation (3.3.13)) and an unknown vector, $\boldsymbol{\psi}^n$ (referred to as an adjoint vector hereafter), we have

$$\hat{f}(\boldsymbol{\rho}, \boldsymbol{z}^N, \ldots, \boldsymbol{z}^1) = f(\boldsymbol{\rho}, \boldsymbol{z}^N, \ldots, \boldsymbol{z}^1) + \sum_{n=1}^{N} \boldsymbol{\psi}^{n^T} \boldsymbol{R}^n \left(\boldsymbol{\rho}, \boldsymbol{z}^n, \boldsymbol{z}^{n-1} \right) \tag{3.3.14}$$

where the value of the function and its derivative remain unchanged since the residual must vanish for any given set of pseudo-densities. Taking the derivative of this augmented function with respect

to a single element density, ρ_e, results in the following expression

$$\begin{aligned}\frac{d\hat{f}}{d\rho_e} =& \frac{\partial f}{\partial \rho_e} + \sum_{n=1}^{N} \frac{\partial f}{\partial \boldsymbol{z}^n} \frac{d\boldsymbol{z}^n}{d\rho_e} + \\ & \sum_{n=1}^{N} \boldsymbol{\psi}^{n^T} \left(\frac{\partial \boldsymbol{R}^n}{\partial \rho_e} + \frac{\partial \boldsymbol{R}^n}{\partial \boldsymbol{z}^n} \frac{d\boldsymbol{z}^n}{d\rho_e} + \frac{\partial \boldsymbol{R}^n}{\partial \boldsymbol{z}^{n-1}} \frac{d\boldsymbol{z}^{n-1}}{d\rho_e} \right)\end{aligned} \tag{3.3.15}$$

where, upon grouping terms, we obtain

$$\begin{aligned}\frac{d\hat{f}}{d\rho_e} =& \frac{\partial f}{\partial \rho_e} + \sum_{n=1}^{N} \boldsymbol{\psi}^{n^T} \frac{\partial \boldsymbol{R}^n}{\partial \rho_e} + \left(\frac{\partial f}{\partial \boldsymbol{z}^N} + \boldsymbol{\psi}^{N^T} \frac{\partial \boldsymbol{R}^N}{\partial \boldsymbol{z}^N} \right) \frac{d\boldsymbol{z}^N}{d\rho_e} + \\ & \sum_{n=1}^{N-1} \left(\boldsymbol{\psi}^{(n+1)^T} \frac{\partial \boldsymbol{R}^{n+1}}{\partial \boldsymbol{z}^n} + \boldsymbol{\psi}^{n^T} \frac{\partial \boldsymbol{R}^n}{\partial \boldsymbol{z}^n} + \frac{\partial f}{\partial \boldsymbol{z}^n} \right) \frac{d\boldsymbol{z}^n}{d\rho_e}\end{aligned} \tag{3.3.16}$$

Choosing the adjoint vectors $\boldsymbol{\psi}^n,\ n = 1, \ldots, N$, such that the terms in parentheses disappear, we avoid the costly derivatives of the finite element fields with respect to the design variables. The adjoint vectors are then obtained beginning with $\boldsymbol{\psi}^N$ and cycling backwards through the load increments via the solutions of the linear systems below.

$$\left[\frac{\partial \boldsymbol{R}^N}{\partial \boldsymbol{z}^N} \right]^T \boldsymbol{\psi}^N = - \frac{\partial f}{\partial \boldsymbol{z}^N}^T \tag{3.3.17}$$

$$\left[\frac{\partial \boldsymbol{R}^n}{\partial \boldsymbol{z}^n} \right]^T \boldsymbol{\psi}^n = - \left[\frac{\partial \boldsymbol{R}^{n+1}}{\partial \boldsymbol{z}^n} \right]^T \boldsymbol{\psi}^{n+1} - \frac{\partial f}{\partial \boldsymbol{z}^n}^T,\ n = N-1, \ldots, 1 \tag{3.3.18}$$

Since the quadrature point degrees of freedom are independent of one another we employ the same adjoint vector solution technique presented in Russ and Waisman [182], in which these degrees of freedom are condensed out of the system at the element level. Once the adjoint vectors are obtained, the derivative in Equation (3.3.16) simplifies to

$$\frac{d\hat{f}}{d\rho_e} = \frac{\partial f}{\partial \rho_e} + \sum_{n=1}^{N} \boldsymbol{\psi}^{n^T} \frac{\partial \boldsymbol{R}^n}{\partial \rho_e} \tag{3.3.19}$$

where $\frac{\partial \boldsymbol{R}^n}{\partial \rho_e}$ is a quick computation, performed at the element level.

The derivative computation in this section is performed with respect to a pseudo-density, ρ_e. However, the optimizer requires the derivative of the relevant functions with respect to the design variables, $\boldsymbol{\theta}$. Therefore we employ the chain rule due to Equation (3.3.3), which results in the final derivatives

$$\frac{d\hat{f}}{d\theta_j} = \sum_{i=1}^{N_{elem}} \frac{d\hat{f}}{d\rho_i}\frac{d\rho_i}{d\hat{\rho}_i}\frac{d\hat{\rho}_i}{d\theta_j} \tag{3.3.20}$$

$$= \sum_{i=1}^{N_{elem}} \frac{d\hat{f}}{d\rho_i}\frac{d\rho_i}{d\hat{\rho}_i}W_{ij} \tag{3.3.21}$$

where W_{ij} is the filter matrix presented in Section 3.3.3.

Work function explicit derivatives

In order to complete the derivation of the analytical sensitivities of the work function in Equation (3.3.6) we provide the unspecified derivatives $\frac{\partial f}{\partial \rho_e}$ and $\frac{\partial f}{\partial \boldsymbol{z}}$ in Equations (3.3.17), (3.3.18), and (3.3.19). Note that the work function may be re-written in the following form

$$W(\boldsymbol{\rho}, \boldsymbol{z}^N, \ldots, \boldsymbol{z}^1) = \frac{1}{2}\int_{\hat{\Omega}} \boldsymbol{\sigma}^{(N)} : \left(\boldsymbol{\varepsilon}^{(N)} - \boldsymbol{\varepsilon}^{(N-1)}\right) dV \tag{3.3.22}$$

$$+ \frac{1}{2}\sum_{i=1}^{N-1}\int_{\hat{\Omega}} \boldsymbol{\sigma}^{(i)} : \left(\boldsymbol{\varepsilon}^{(i+1)} - \boldsymbol{\varepsilon}^{(i-1)}\right) dV \tag{3.3.23}$$

where we assume that the body is initially unloaded so that $\boldsymbol{\varepsilon}^{(0)} = \mathbf{0}$. Note that we have switched back to continuous integration in space in the derivation in order to simplify the notation by avoiding the subscripts associated with element and quadrature point numbers. We may compute the partial derivative with respect to an element pseudo-density with the following expression

$$\frac{\partial W}{\partial \rho_e} = \frac{1}{2}\int_{\hat{\Omega}} \frac{\partial \boldsymbol{\sigma}^{(i)}}{\partial \rho_e} : \left(\boldsymbol{\varepsilon}^{(N)} - \boldsymbol{\varepsilon}^{(N-1)}\right) dV \tag{3.3.24}$$

$$+ \frac{1}{2}\sum_{i=1}^{N-1}\int_{\hat{\Omega}} \frac{\partial \boldsymbol{\sigma}^{(i)}}{\partial \rho_e} : \left(\boldsymbol{\varepsilon}^{(i+1)} - \boldsymbol{\varepsilon}^{(i-1)}\right) dV \tag{3.3.25}$$

Recall that ρ_e enters the expression for the stress tensor through the effective elastic modulus, E (Equation (3.3.1)). Since the stress is linear in E, we simply replace E with the partial derivative, $\frac{\partial E}{\partial \rho_e} = (1 - \epsilon_e)\ p_1\ \rho_e^{p_1 - 1}\ E_0$, in the stress computation in order to obtain the necessary derivative, $\frac{\partial \boldsymbol{\sigma}}{\partial \rho_e}$, above.

Next we compute each of the components of the second required partial derivative, $\frac{\partial W}{\partial \boldsymbol{z}} = \left[\frac{\partial W}{\partial \bar{\boldsymbol{u}}}, \frac{\partial W}{\partial \bar{\boldsymbol{d}}}, \frac{\partial W}{\partial \boldsymbol{h}}\right]$, separately. The derivative with respect to the displacement degrees of freedom may be computed using index notation and the Einstein summation convention.

Final (N^{th}) pseudo-time increment:

$$\begin{aligned}\frac{\partial W}{\partial \bar{\boldsymbol{u}}^{(N)}} = \frac{1}{2}\int_{\hat{\Omega}} \frac{\partial \sigma_{ij}^{(N)}}{\partial \bar{\boldsymbol{u}}^{(N)}} \left(\varepsilon_{ij}^{(N)} - \varepsilon_{ij}^{(N-1)}\right) dV \\ + \frac{1}{2}\int_{\hat{\Omega}} \sigma_{ij}^{(N)}\ \frac{\partial \varepsilon_{ij}^{(N)}}{\partial \bar{\boldsymbol{u}}^{(N)}} dV\end{aligned} \tag{3.3.26}$$

All other pseudo-time increments ($i = N - 1, \ldots, 1$):

$$\begin{aligned}\frac{\partial W}{\partial \bar{\boldsymbol{u}}^{(i)}} = \frac{1}{2}\int_{\hat{\Omega}} \frac{\partial \sigma_{ij}^{(i)}}{\partial \bar{\boldsymbol{u}}^{(i)}} \left(\varepsilon_{ij}^{(i+1)} - \varepsilon_{ij}^{(i-1)}\right) dV \\ + \frac{1}{2}\int_{\hat{\Omega}} \left(\sigma_{ij}^{(i-1)} - \sigma_{ij}^{(i+1)}\right)\ \frac{\partial \varepsilon_{ij}^{(i)}}{\partial \bar{\boldsymbol{u}}^{(i)}}\ dV\end{aligned} \tag{3.3.27}$$

Note that the required partial derivatives above can be expressed simply using the matrix notation from Section 3.2.2, in which $\frac{\partial \hat{\boldsymbol{\sigma}}}{\partial \bar{\boldsymbol{u}}} = \boldsymbol{D} \cdot \boldsymbol{B}_{\bar{\boldsymbol{u}}}$ and $\frac{\partial \hat{\boldsymbol{\varepsilon}}}{\partial \bar{\boldsymbol{u}}} = \boldsymbol{B}_{\bar{\boldsymbol{u}}}$. Similarly we may compute the derivative with respect to the phase field degrees of freedom.

Final (N^{th}) pseudo-time increment:

$$\frac{\partial W}{\partial \bar{\boldsymbol{d}}^{(N)}} = \frac{1}{2}\int_{\hat{\Omega}} \frac{\partial \sigma_{ij}^{(N)}}{\partial \bar{\boldsymbol{d}}^{(N)}} \left(\varepsilon_{ij}^{(N)} - \varepsilon_{ij}^{(N-1)}\right) dV \tag{3.3.28}$$

All other pseudo-time increments ($i = N-1, \ldots, 1$):

$$\frac{\partial W}{\partial \bar{\boldsymbol{d}}^{(i)}} = \frac{1}{2}\int_{\hat{\Omega}} \frac{\partial \sigma_{ij}^{(i)}}{\partial \bar{\boldsymbol{d}}^{(i)}} \left(\varepsilon_{ij}^{(i+1)} - \varepsilon_{ij}^{(i-1)}\right) dV \tag{3.3.29}$$

Note that this partial derivative may be computed with the expression, $\frac{\partial \sigma_{ij}}{\partial \bar{\boldsymbol{d}}} = -2(1 - \boldsymbol{N}_d \bar{\boldsymbol{d}})\sigma_{ij}^{+}\boldsymbol{N}_d$. Additionally, the work function does not depend explicitly on the quadrature point degree of freedom, h. Therefore, $\frac{\partial W}{\partial \boldsymbol{h}} = \boldsymbol{0}$.

Integrated fracture energy function explicit derivatives

The required derivatives of the integrated fracture energy function, Ξ, (Equation (3.3.5)) are less complex to compute. Since this function does not have any explicit dependence on $\bar{\boldsymbol{u}}$ or $\boldsymbol{h}$ we have $\frac{\partial \Xi}{\partial \bar{\boldsymbol{u}}} = \boldsymbol{0}$ and $\frac{\partial \Xi}{\partial \boldsymbol{h}} = \boldsymbol{0}$, leaving only the derivative with respect to the phase field, $\frac{\partial \Xi}{\partial \bar{\boldsymbol{d}}}$, and pseudo-densities, $\frac{\partial \Xi}{\partial \rho_e}$, to be computed. Beginning with the pseudo-density derivative, we have

$$\frac{\partial \Xi}{\partial \rho_e} = \sum_{i=1}^{N_{steps}} \frac{1}{2}\left(\frac{\partial \hat{W}_{frac}^{(i)}}{\partial \rho_e} + \frac{\partial \hat{W}_{frac}^{(i-1)}}{\partial \rho_e}\right)\Delta\tau^{(i)} \tag{3.3.30}$$

where,

$$\frac{\partial \hat{W}_{frac}^{(i)}}{\partial \rho_e} \approx \sum_{e=1}^{N_{elem}} \sum_{q=1}^{N_{quad}} 2\frac{\partial \psi_c}{\partial \rho_e}\left(d_{e_q} + 2l_0^2 \nabla d_{e_q} \cdot \nabla d_{e_q}\right) \cdot w_{e_q} \tag{3.3.31}$$

and the derivative $\frac{\partial \psi_c}{\partial \rho_e} = (1 - \epsilon_d) p_2 \, \rho_e^{p_2 - 1} \, \psi_{c_0}$ due to Equation (3.3.2). The derivative with respect to the phase field may be expressed as,

Final (N^{th}) pseudo-time increment:

$$\frac{\partial \Xi}{\partial \bar{\boldsymbol{d}}^{(N)}} = \left(\frac{\Delta t^{(N)}}{2}\right) \frac{\partial \hat{W}_{frac}^{(N)}}{\partial \bar{\boldsymbol{d}}^{(i)}} \tag{3.3.32}$$

All other pseudo-time increments ($i = N-1, \ldots, 1$):

$$\frac{\partial \Xi}{\partial \bar{\boldsymbol{d}}^{(i)}} = \left(\frac{\Delta t^{(i-1)} + \Delta t^{(i)}}{2} \right) \frac{\partial \hat{W}_{frac}^{(i)}}{\partial \bar{\boldsymbol{d}}^{(i)}} \tag{3.3.33}$$

where the required derivative is with respect to the phase field and may be expressed as

$$\frac{\partial \hat{W}_{frac}^{(i)}}{\partial \bar{\boldsymbol{d}}^{(i)}} = \int_{\hat{\Omega}} 2\psi_c \left(\boldsymbol{N}_d + 2l_0^2 \, \bar{\boldsymbol{d}}^{(i)^T} \boldsymbol{B}_d^T \boldsymbol{B}_d \right) dV \tag{3.3.34}$$

completing the expressions.

Sensitivity verification

The path-dependent work and integrated fracture energy function sensitivities are numerically verified in this section for the portal frame example problem with geometry and boundary conditions as shown in Figure 3.6. Note that a symmetry boundary condition is used to decrease the number of elements. A prescribed downward displacement is linearly increased to a value of 10mm and then linearly decreased to a value of 5mm in order to trigger the path-dependence due to irreversibility. The inhomogeneous pseudo-density field, mesh, and phase field distribution are illustrated in Figure 3.7. Relevant material and numerical parameters are provided in Table 3.1 in which the material properties correspond to a mild steel [168].

Table 3.1: Material and numerical parameters

E_0 [GPa]	ν	ψ_c $[GJ/m^3]$	l_0 $[m]$	β	r_{min} $[m]$	η_{ks}	Δt $[s]$	$\Delta\rho_e$
200	0.29	306	0.1	3	0.3	30	0.05	10^{-6}

The finite element mesh consists of 572 4-node quadrilateral elements. A central difference approximation of the sensitivities is used such that for a function, $f(\boldsymbol{\rho})$, the sensitivity is numerically approximated by

$$\frac{df}{d\rho_e} \approx \frac{f(\rho_1, \ldots, \rho_e + \Delta\rho_e, \ldots, \rho_{N_{elem}}) - f(\rho_1, \ldots, \rho_e - \Delta\rho_e, \ldots, \rho_{N_{elem}})}{2\Delta\rho_e} \tag{3.3.35}$$

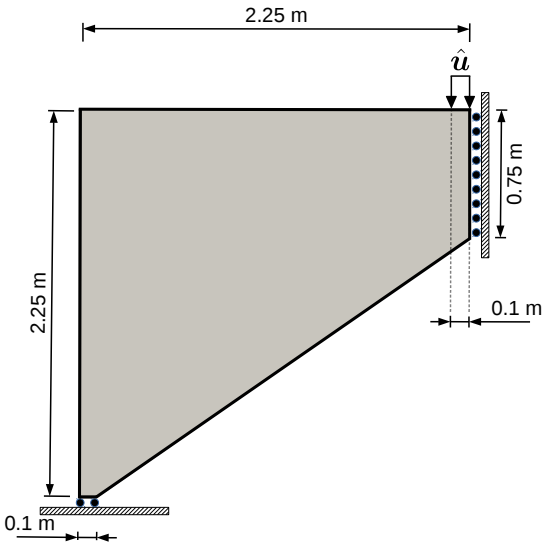

Figure 3.6: Sensitivity verification problem geometry / boundary conditions

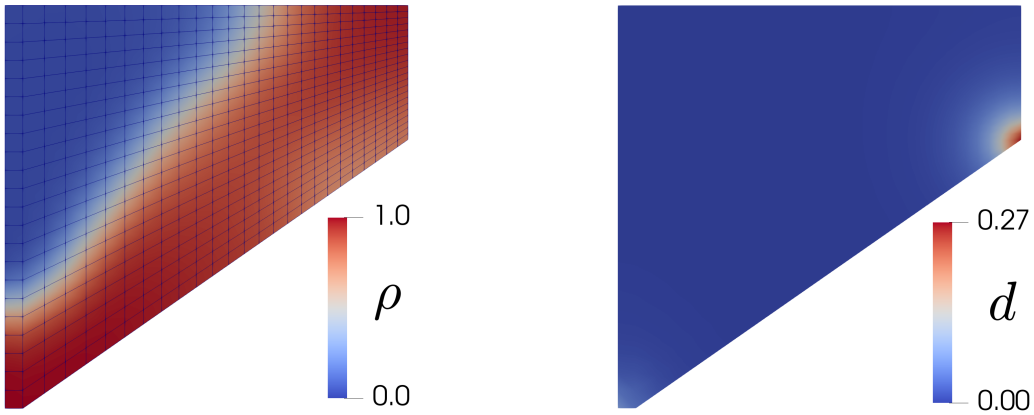

(a) Inhomogeneous pseudo-density field

(b) Phase field

Figure 3.7: Sensitivity verification problem densities and phase field

where a full, nonlinear finite element analysis is required for each element density perturbation.

Both, the work and integrated fracture energy sensitivities are verified and the results are illustrated in Figure 3.8. Note that the sensitivities have been sorted consistently from smallest to largest value for clarity. It can be seen that numerical differentiation and the analytical calculation presented previously give nearly identical results.

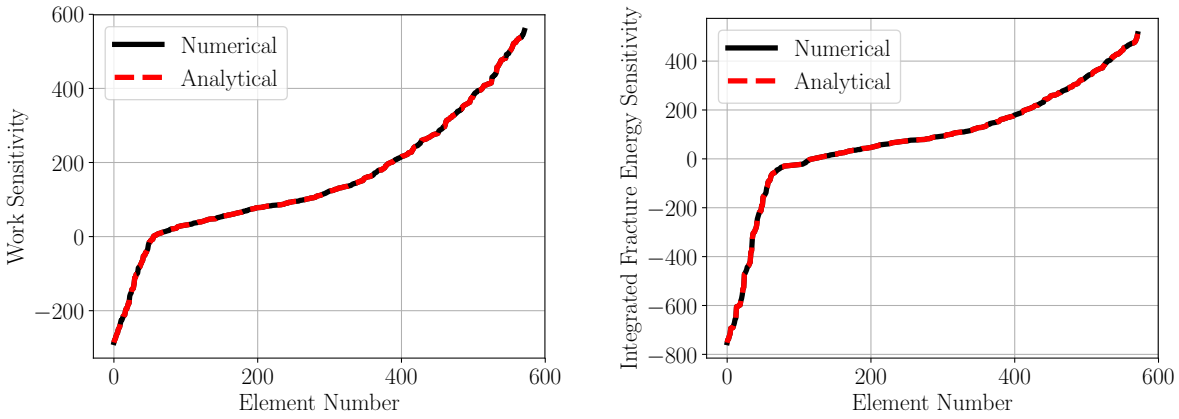

(a) Work

(b) Integrated fracture energy

Figure 3.8: Numerical verification of the analytical sensitivities

Sensitivity comparison

As mentioned previously, the work and integrated fracture energy functions used in the optimization problem definition contain information about the system state at each incremental step of the load history. This is in contrast to functions of only the end state of the system, like the compliance and fracture energy functional which were used in the previous chapter. These two functions are provided below in Equations (3.3.36) and (3.3.37), respectively, in which $\boldsymbol{f}_{ext}$ represents the global external force vector and G_c represents the critical energy release rate.

$$C(\boldsymbol{\rho}, \bar{\boldsymbol{u}}, \bar{\boldsymbol{d}}) = \boldsymbol{f}_{ext}^T \bar{\boldsymbol{u}} \tag{3.3.36}$$

$$\hat{\psi}_f(d) = G_c \int_{\hat{\Omega}} \left(\frac{1}{4l_0} d^2 + l_0 \left\| \nabla d \right\|_2^2 \right) dV \tag{3.3.37}$$

Here we briefly examine this idea for a single example problem via a comparison of the function sensitivities. The portal frame example with geometry described in Figure 3.6 is used with a discretization of 11,454 quadrilateral elements. A peak downward displacement of $\hat{u} = 10$mm is applied and the projection parameter, β, along with all of the pseudo-densities are set to 1. The parameters used in this section are provided in Table 3.2.

Figure 3.9 illustrates the phase field fracture at the end state of the simulation. For this specific

Table 3.2: Sensitivity comparison problem material and numerical parameters

E_0 [GPa]	ν	ψ_c $[GJ/m^3]$	l_0 $[m]$	r_{min} $[m]$	η_{ks}	Δt $[s]$	t_{final} $[s]$
200	0.29	306	0.05	0.1	30	0.01	1

loading, we provide the analytical sensitivity contours for the work and compliance in Figure 3.10 and the integrated fracture energy and fracture energy in Figure 3.11.

It is clear from Figure 3.10 that the work function contains more information from the solution path than the compliance, as is evidenced by the additional sensitivity corresponding to elements near the re-entrant corner and throughout the crack path. A similar situation is observed when comparing the integrated fracture energy and fracture energy sensitivities in Figure 3.11. In Figure 3.11a one can see a region of positive sensitivity just below the re-entrant corner due to the function dependence on the pre-cracked state. When the integrated fracture energy is minimized, this small region of positive sensitivity drives the removal of those elements from the design. This results in the eventual elimination of the re-entrant corner even when the loading induces fracture and allows the optimizer to eventually find a topology which does not fail completely under the applied load.

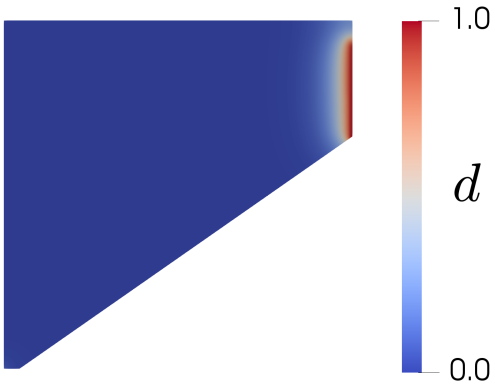

Figure 3.9: Fractured state for sensitivity comparison

It is also instructive to look at the magnitude of the sensitivities relative to the peak value across all elements on a line plot. This is provided for both pairs of functions in Figure 3.12. The magnitude of each sensitivity vector is normalized by the l_∞-norm in order to facilitate a comparison of relative magnitudes across all elements in the domain. It is clear from the figures that the work and integrated fracture energy functions are more sensitive throughout the domain than their counterparts.

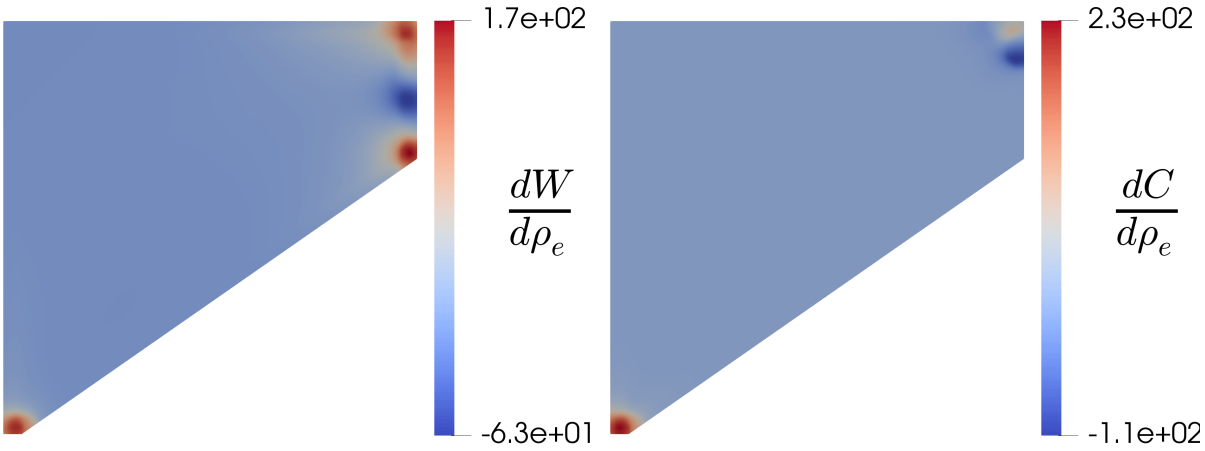

(a) Work (b) Compliance

Figure 3.10: Comparison of work and compliance sensitivities (note that the compliance function was used in the previous chapter)

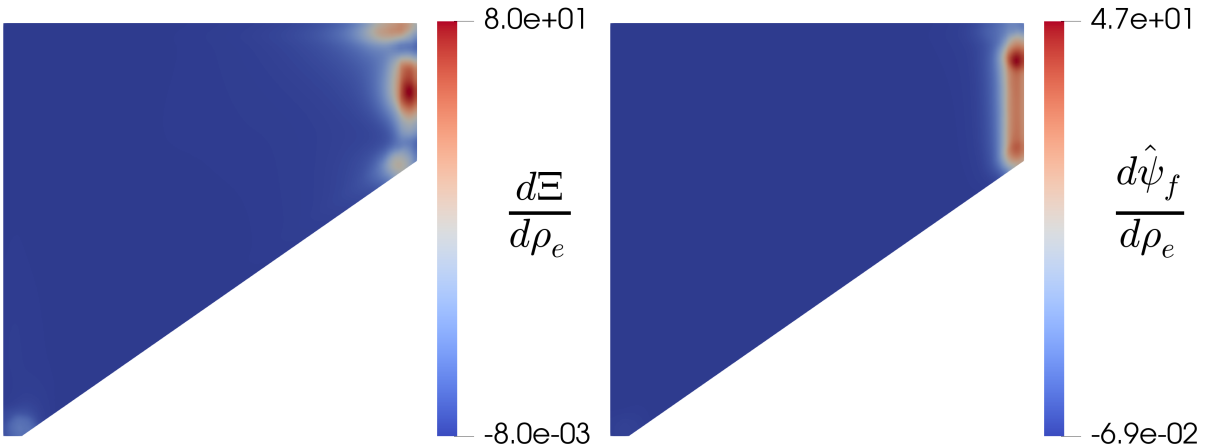

(a) Integrated Fracture Energy (b) Fracture Energy

Figure 3.11: Comparison of integrated fracture energy and fracture energy sensitivities (note that the fracture energy function was used in the previous chapter)

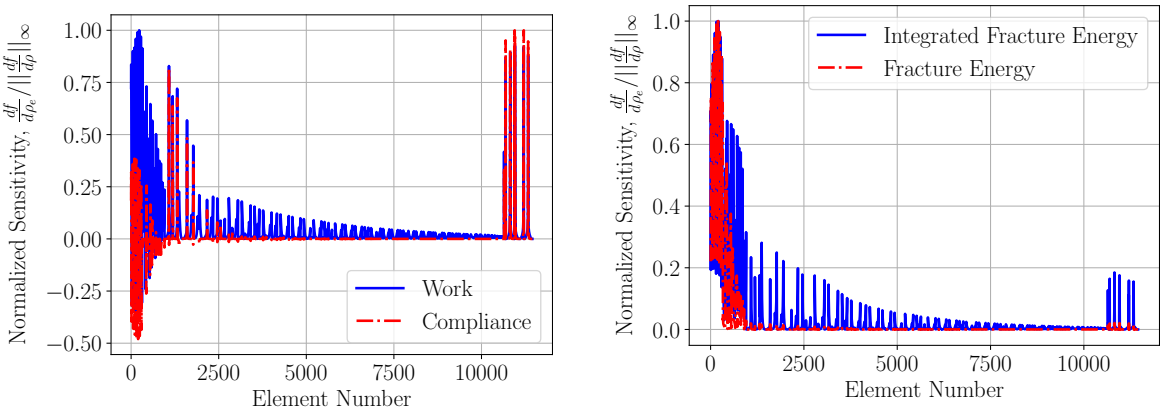

(a) $\frac{dW}{d\rho_e}$ and $\frac{dC}{d\rho_e}$

(b) $\frac{d\Xi}{d\rho_e}$ and $\frac{d\hat{\psi}_f}{d\rho_e}$

Figure 3.12: Comparison of normalized sensitivities

3.4 Numerical examples

In this section we present the numerical results for two benchmark problems; the Portal Frame and the L-bracket. The finite element solution is implemented in FEAP [169], which leverages the PETSc library for parallel, sparse linear algebra [170]. The optimization problem is solved using the method of moving asymptotes (MMA) [183], with default optimization parameters. The final pseudo-time, t_{final}, is set to $1s$. Since we are interested in minimum weight designs with higher strength, we provide the efficiency measure given by Equation (3.4.1), which represents the percent increase in the strength-to-weight ratio with respect to the design obtained with only linear elastic physics, minimizing the volume fraction subject to only the work constraint (note that we refer to this metric as the "gain"). In this equation P refers to the peak load (or strength) while Λ refers to the volume fraction. Quantities with the $base$ subscript correspond to the base design obtained using linear elasticity.

$$Gain(P, \Lambda) = \left(\frac{P}{\Lambda} \cdot \frac{\Lambda_{base}}{P_{base}} - 1 \right) \cdot 100\% \tag{3.4.1}$$

3.4.1 Portal frame

In this example the portal frame geometry in Figure 3.6 is discretized with 11,454 quadrilateral elements. The numerical parameters used are presented in Table 3.3. A peak downward displacement of $\hat{u} = 10$mm is applied to a small portion of the top of the frame (location shown in Figure 3.6).

Table 3.3: Portal frame material and numerical parameters

E_0 [GPa]	ν	ψ_c $[GJ/m^3]$	l_0 $[m]$	r_{min} $[m]$	η_{ks}	Δt $[s]$	W_{min} $[kJ]$
200	0.29	306	0.05	0.1	30	0.04	80

The optimized topologies for five (5) different cases are presented in Figure 3.13. The first is obtained using only linear elastic physics and minimizing the volume fraction subject to the work constraint (i.e. the aggregate objective weight, ω, is set to 0 since Ξ is not defined). Next the stress minimization result is provided using the formulation of Le et al. [6] briefly summarized in A.3.

Finally, we include the phase field fracture physics and minimize the aggregate objective function previously presented in Section 3.3.2 with three different values of the weighting parameter, ω, each varying by two orders of magnitude. The upper bound on the volume fraction used in the stress minimization formulation is selected to exactly match the volume fraction resulting from including the fracture physics and setting the weighting parameter, $\omega = 1e4$. The same force and finite element mesh are used, along with identical density projection and SIMP exponent continuation schemes. It is clear from the figure that the re-entrant corner is removed from all three topologies with nonzero weighting parameter, ω. This behavior is in sharp contrast to the behavior observed in the previous chapter. Additionally we obtain the expected behavior from the stress minimization algorithm which also removes the re-entrant corner from the design.

Since the phase field only increases in regions of the domain which exceed the tensile energy threshold, the locality of the topological change is provided by the integrated fracture energy function without the use of special aggregation techniques. This feature bears similarity to other works with a threshold including [36, 13] for example. In Figure 3.14 a plot of the phase field is provided at the final optimization iteration. As shown in the figure, no fully developed cracks are present however the phase field is still nonzero at multiple places in the domain, behaving as an indicator of potential fracture. Additionally, we provide a few illustrations of fracturing topologies at the beginning of the optimization process in Figure 3.15 for the example with $\omega = 1e0$. The optimizer decreases the densities just below the re-entrant corner and places a hole at the crack tip which is slowly moved toward the fracture initiation point until it is eliminated.

The optimized topologies are then loaded until failure and the corresponding numerical results are provided in Table 3.4. The associated force and fracture energy vs. displacement curves are provided in Figure 3.16 with the corresponding fractured topologies shown in Figure 3.17. The design corresponding to stress minimization with linear elasticity performs very well with respect to the design imposing only the work constraint. In fact, although the peak load is lower than the peak load considering fracture in the optimization process, it is of comparable magnitude. However, this increase in strength comes at the cost of larger volume fraction, which negatively impacts the

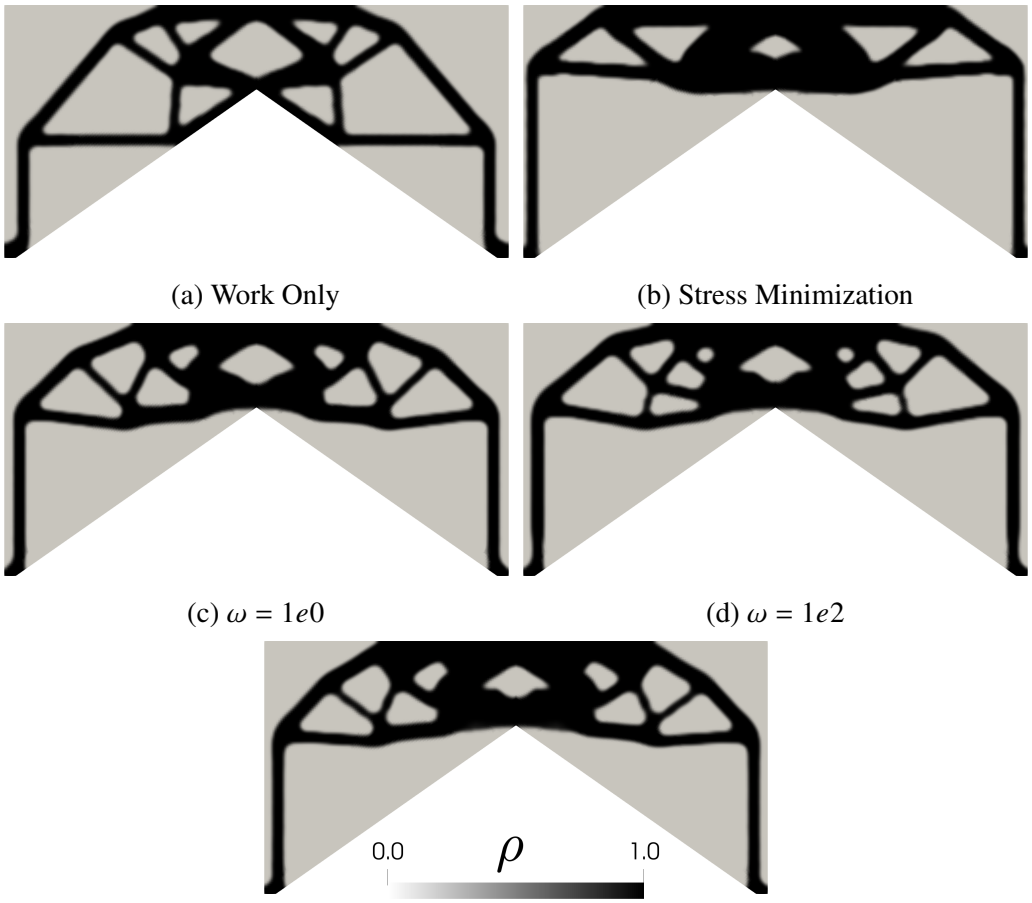

(a) Work Only

(b) Stress Minimization

(c) $\omega = 1e0$

(d) $\omega = 1e2$

(e) $\omega = 1e4$

Figure 3.13: Optimized portal frame topologies

strength-to-weight ratio. This is evidenced by the difference in gain (Equation (3.4.1)) presented in Table 3.4 in which we were able to achieve a 67.5% increase in strength-to-weight ratio versus the 54.7% increase provided by the stress-minimization algorithm.

Table 3.4: Portal frame numerical results. The peak load is provided in units of MN and the integrated fracture energy, Ξ, is provided in units of $J \cdot s$. Note that the gain is computed via Equation (3.4.1).

	Volume Fraction	Peak Load	Ξ	Gain
Work Only	0.301	10.6	–	–
Stress Min.	0.369	20.1	–	54.7%
Weight, $\omega = 1e0$	0.346	20.2	7.3e-4	65.8%
Weight, $\omega = 1e2$	0.356	21.0	6.5e-5	67.5%
Weight, $\omega = 1e4$	0.369	21.4	1.7e-6	64.7%

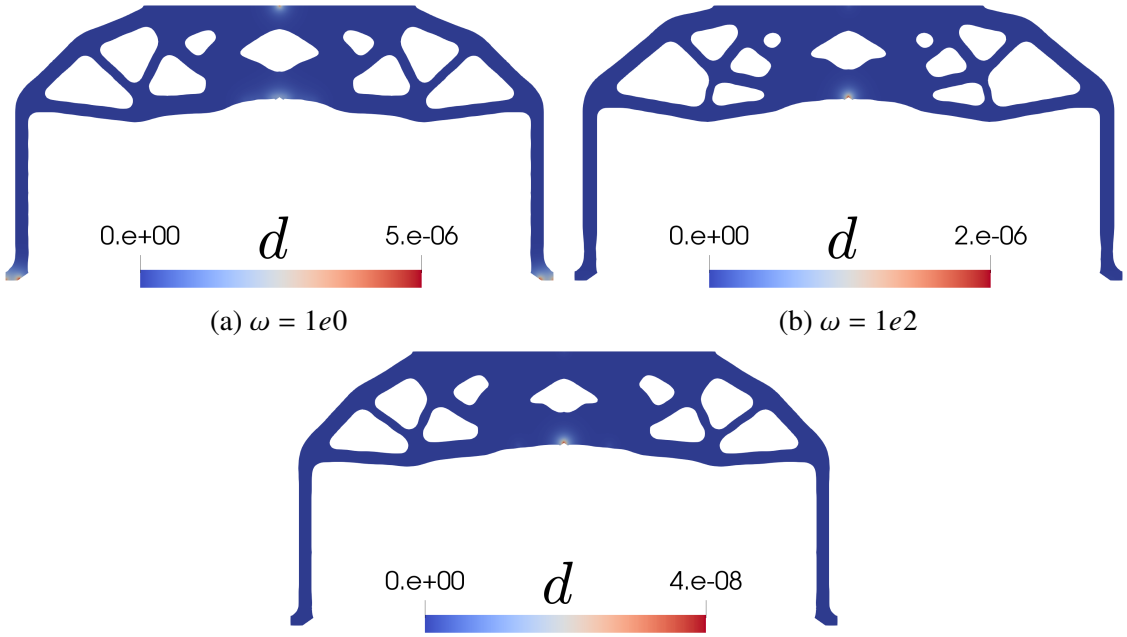

(a) $\omega = 1e0$ (b) $\omega = 1e2$

(c) $\omega = 1e4$

Figure 3.14: Phase field plot at the final design iteration for each of the three portal frame topologies obtained including the fracture physics

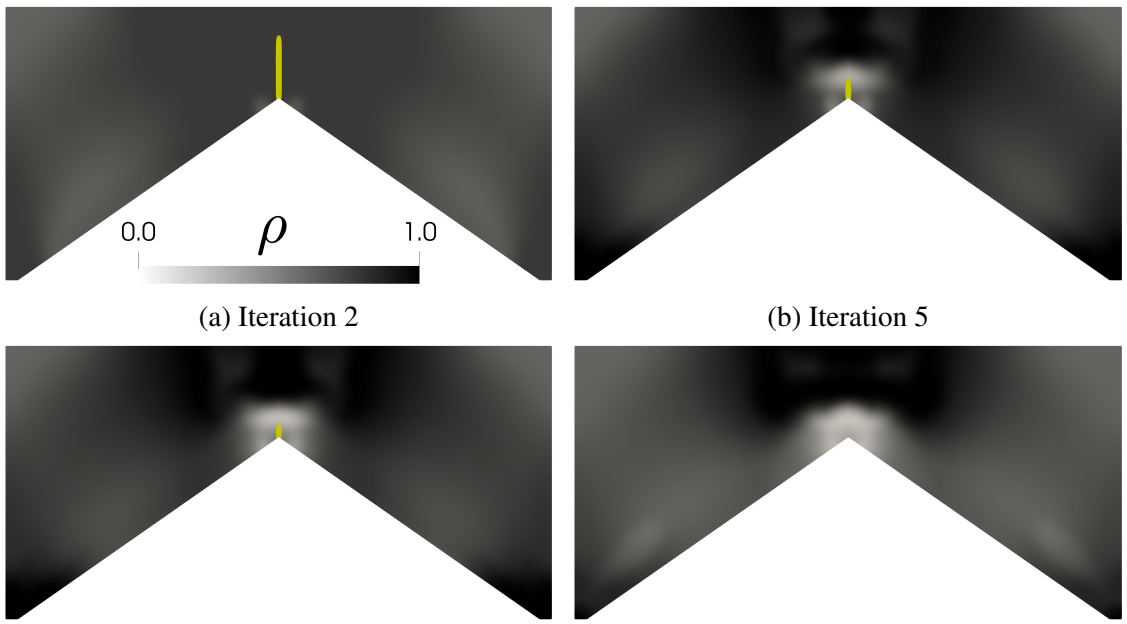

(a) Iteration 2 (b) Iteration 5

(c) Iteration 6 (d) Iteration 7

Figure 3.15: Optimizer design changes during the first few optimization iterations with $\omega = 1e0$. The phase field fracture is illustrated in yellow using a lower cutoff of 0.9

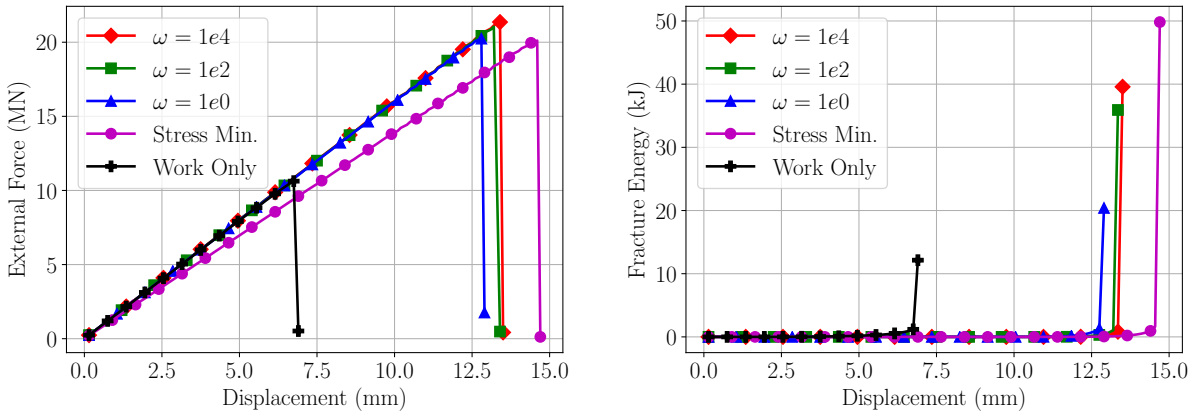

(a) (b)

Figure 3.16: Portal frame (a) force vs. displacement and (b) fracture energy ($\hat{W}_{frac}$) vs. displacement curves.

Clearly, the higher strength-to-weight ratio comes at a higher computational cost when compared with the designs based on linear elasticity with stress minimization. The bulk of the computational effort takes place during the forward problem in which fracture surfaces are initiating and propagating. However, since cracks generally do not form in the later optimization iterations most of the effort is expended during approximately 10-15 of the total 500 iterations with the remainder requiring far less computational effort. Finally, we complete this example with the optimizer convergence plots for each of the three relevant functions in Figure 3.18.

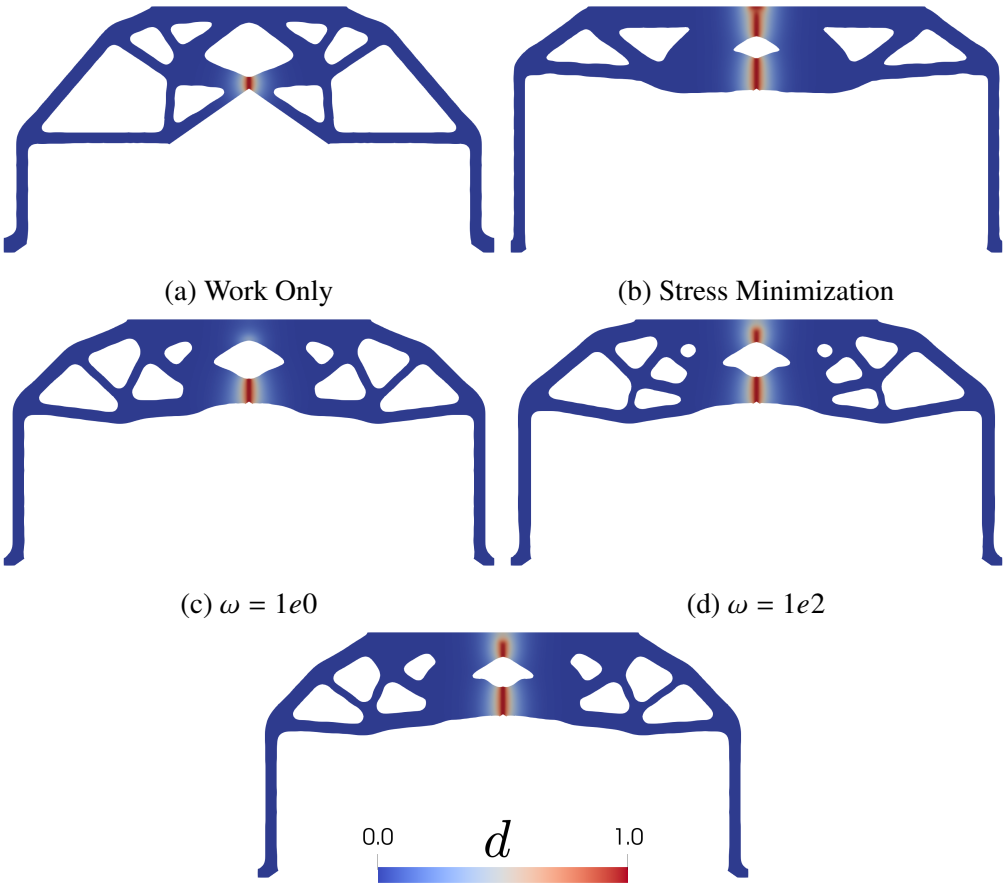

(a) Work Only

(b) Stress Minimization

(c) $\omega = 1e0$

(d) $\omega = 1e2$

(e) $\omega = 1e4$

Figure 3.17: Optimized portal frame topologies loaded until failure

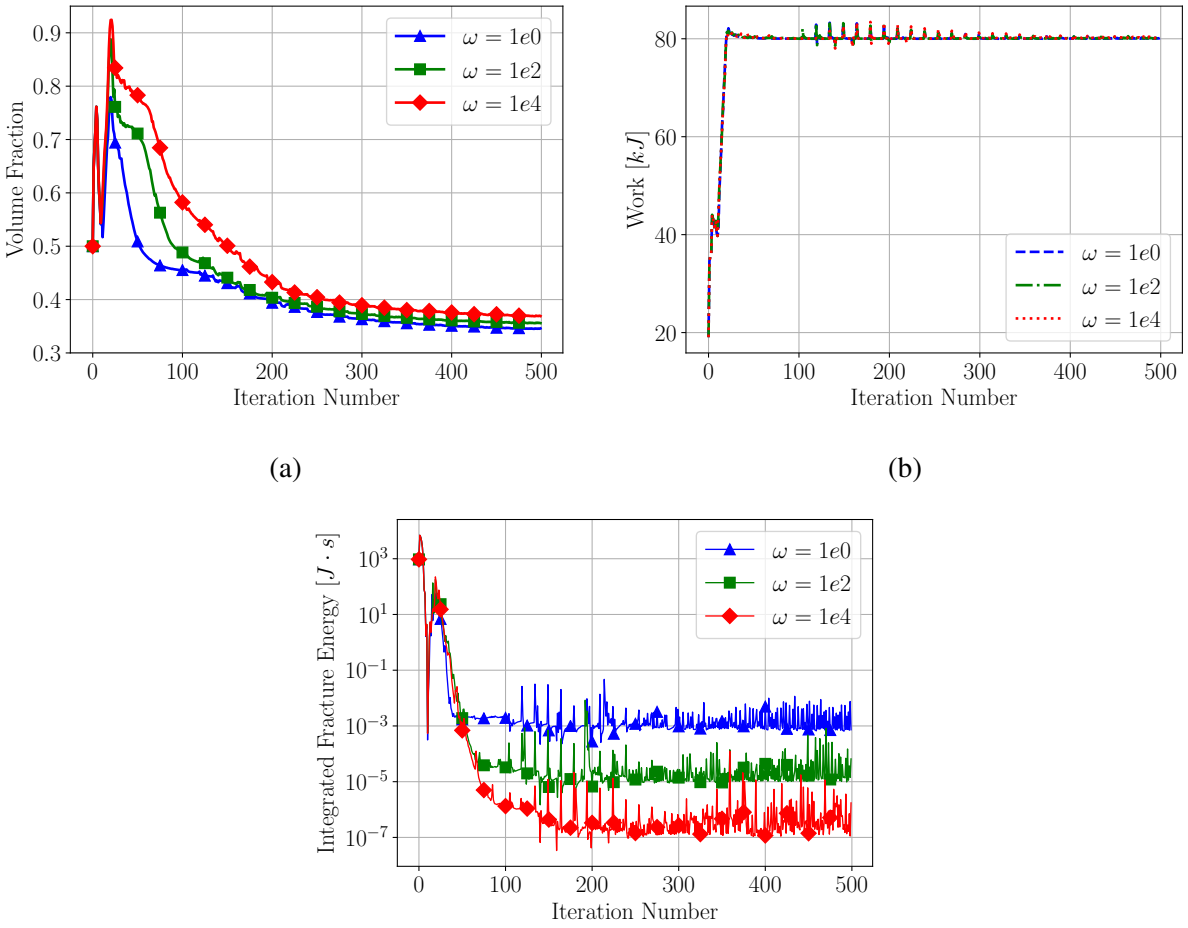

Figure 3.18: Portal frame optimizer convergence history for the (a) volume fraction, (b) work, and (c) integrated fracture energy. Note that the work constraint is active for each design.

3.4.2 L-bracket

Next, the L-bracket geometry presented in Figure 3.19 is discretized into 13,337 quadrilateral elements. The numerical parameters used are presented in Table 3.5. A peak downward displacement of $\hat{u} = 0.6$mm is applied to the right-most edge of the bracket.

Table 3.5: L-bracket material and numerical parameters

E_0 [GPa]	ν	ψ_c $[GJ/m^3]$	l_0 $[mm]$	r_{min} $[mm]$	η_{ks}	Δt $[s]$	W_{min} $[J]$
200	0.29	306	1	2	30	0.04	125

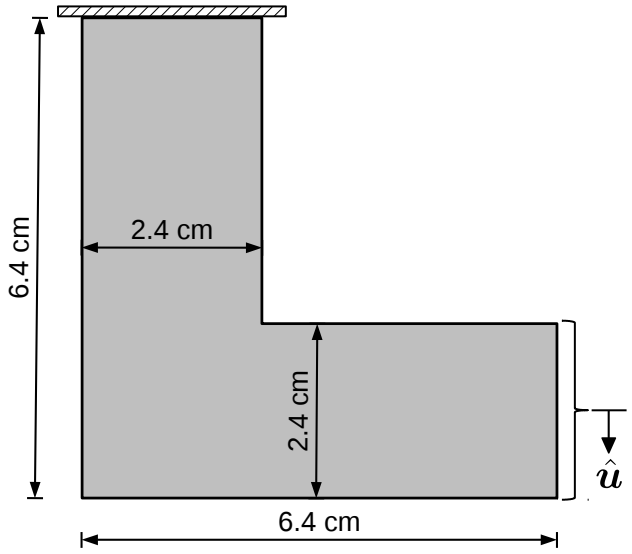

Figure 3.19: L-bracket geometry / boundary conditions

The optimized topologies for five (5) different cases are presented in Figure 3.20. The first is obtained using only linear elastic physics and minimizing the volume fraction subject to the work constraint while the second corresponds to the stress minimization result with the formulation outlined in A.3. In the three remaining cases we include the phase field fracture physics and minimize the aggregate objective function previously presented in Section 3.3.2 with the same three values of the weighting parameter, ω, used in the previous example. Similar to the case of the portal frame structure, we see from the figure that the re-entrant corner is removed from all three topologies with nonzero weighting parameter, ω. A plot of the phase field at the final optimization iteration is provided in Figure 3.21 , showing the absence of cracks in the final designs, but also the presence of nonzero phase field values behaving as indications of potential crack initiation points. A few fractured topologies during the initial iterations are provided in Figure 3.22. The optimizer places holes in the density field in order to arrest the crack in addition to decreasing the densities above and below the re-entrant corner in order to ultimately eliminate the fracture initiation.

Note that the stress minimization design also removes the re-entrant corner as expected. We set the volume fraction limit equal to that of the design obtained with the fracture physics setting $\omega = 1e4$ and apply an identical load just as in the previous example. Unlike the case of the portal

frame which performs well with a p-norm parameter of $p = 10$, the L-bracket is more challenging to obtain a well-performing result. In order to remedy this we use a continuation scheme, initially setting $p = 10$ for the first 100 iterations and increasing it by 2 every 20 iterations up to a maximum value of 30. Finally we also decrease the MMA optimizer “move" limit to 0.1 to abate some of the nonlinearity.

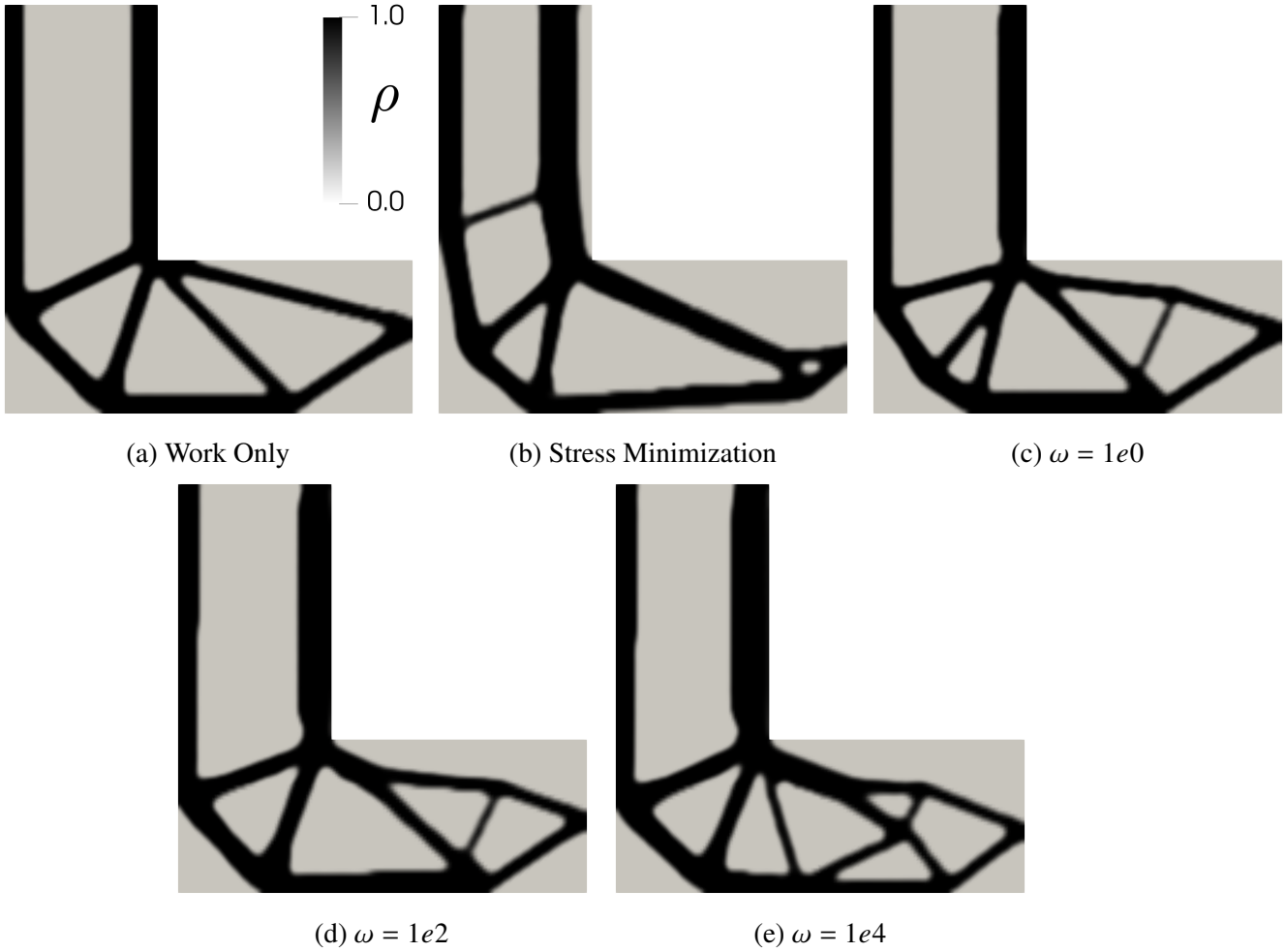

(a) Work Only (b) Stress Minimization (c) $\omega = 1e0$

(d) $\omega = 1e2$ (e) $\omega = 1e4$

Figure 3.20: Optimized L-bracket topologies

The optimized topologies are then loaded until failure and the numerical results are provided in Table 3.6 with the corresponding fractured topologies illustrated in Figure 3.24. Note that the topologies which have removed the re-entrant corner fail in other regions of the structure as expected since the stress concentration is no longer present. The associated force and fracture energy versus displacement curves are provided in Figure 3.23.

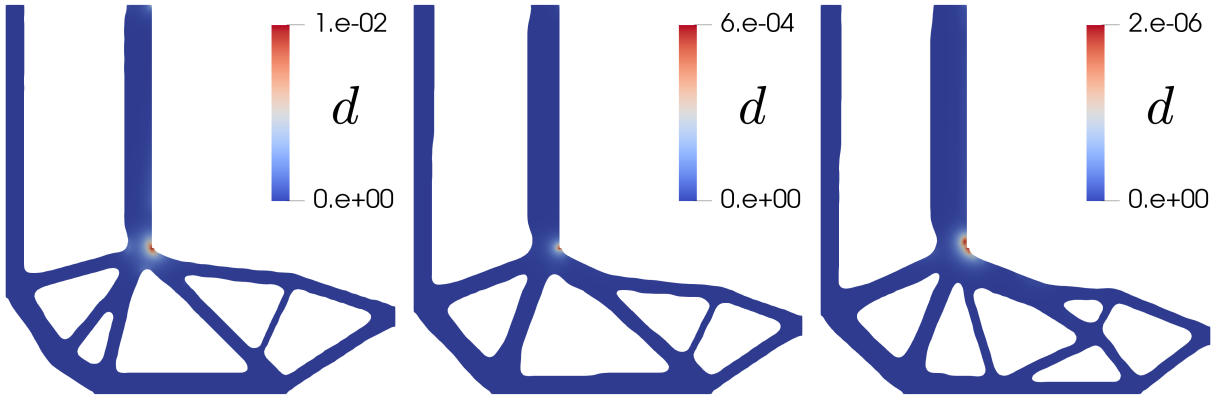

(a) $\omega = 1e0$ (b) $\omega = 1e2$ (c) $\omega = 1e4$

Figure 3.21: Phase field plot at the final design iteration for each of the three L-bracket topologies obtained including the fracture physics

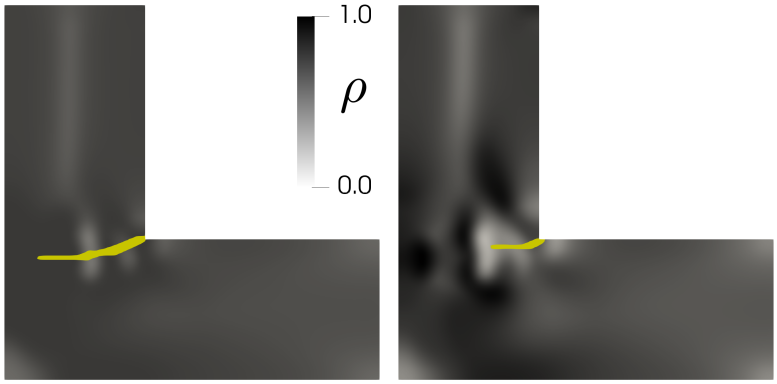

(a) Iteration 2 (b) Iteration 4

(c) Iteration 5 (d) Iteration 8

Figure 3.22: Optimizer topology changes during the first few optimization iterations with $\omega = 1e0$. The phase field fracture is illustrated in yellow using a lower cutoff of 0.9

Table 3.6: L-bracket numerical results. The peak load is provided in units of kN and the integrated fracture energy, Ξ, is provided in units of $J \cdot s$. Note that the gain is computed via Equation (3.4.1).

	Volume Fraction	Peak Load	Ξ	Gain
Work Only	0.314	254	–	–
Stress Min.	0.373	474	–	57.1%
Weight, $\omega = 1e0$	0.336	439	$2.1e$-3	61.5%
Weight, $\omega = 1e2$	0.354	484	$3.3e$-5	69.0%
Weight, $\omega = 1e4$	0.373	509	$2.2e$-7	68.7%

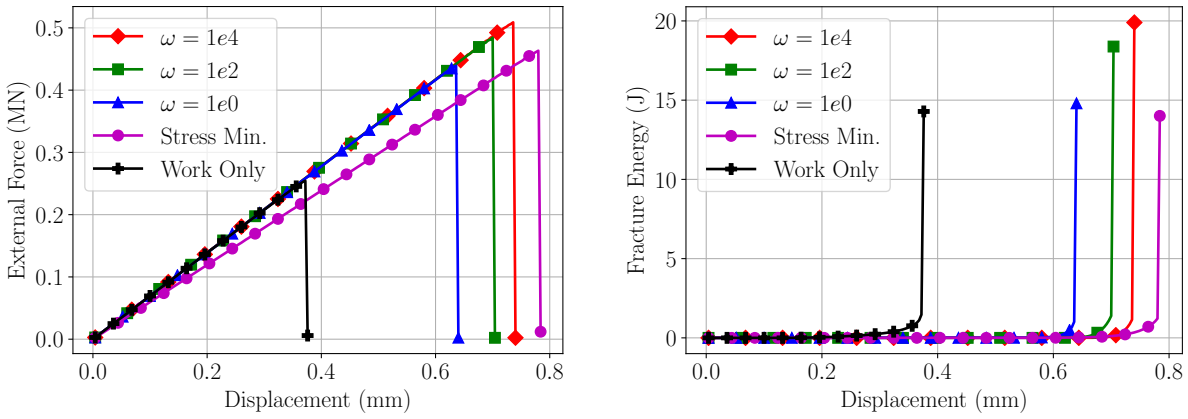

(a) (b)

Figure 3.23: L-bracket (a) force vs. displacement and (b) fracture energy ($\hat{W}_{frac}$) vs. displacement curves.

Note that while all of the topologies are quite different from one another, a similar trend has emerged in terms of the gain (Equation (3.4.1)) presented in Table 3.6. The stress minimization formulation results in a large increase in the structural strength at the cost of increased volume/weight, which yields a gain of 57.1%. In contrast the formulation presented herein is able to produce a result with a 69.0% gain, which is a considerably large increase, even compared to the result using stress minimization. Additionally we note that while the strength is larger for the stress minimization formulation than the corresponding strength obtained using $\omega = 1e0$, the volume is also considerably higher. Finally, we provide the optimizer convergence history plots for the three relevant functions in Figure 3.25.

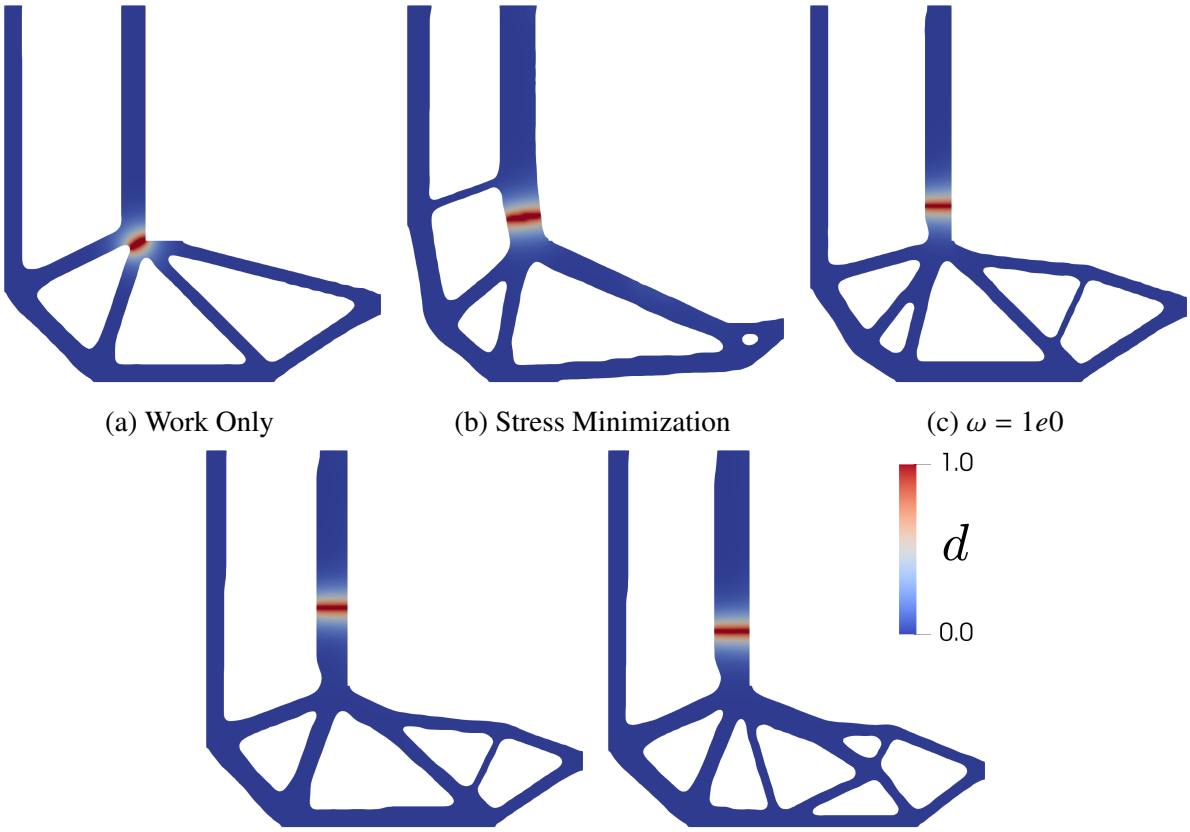

(a) Work Only (b) Stress Minimization (c) $\omega = 1e0$

(d) $\omega = 1e2$ (e) $\omega = 1e4$

Figure 3.24: Optimized L-bracket topologies loaded until failure

3.5 Conclusion

A new method for obtaining structures with an increased resistance to brittle fracture was presented and tested on two benchmark numerical examples. It is demonstrated that the phase field fracture method with a smooth energetic threshold, along with a new aggregate function of the phase field parameter, provides an effective driver for topological changes that result in enhanced fracture resistance. Additionally, this new formulation allows the gradient based MMA optimizer to find and converge to designs which do not fracture under the prescribed loading conditions, even though the brittle fracture physics produce strong discontinuities in most functions of the system state when a loading that induces fracture is applied during the optimization process. This is in clear and sharp contrast to the formulation presented in the previous chapter in which fracture

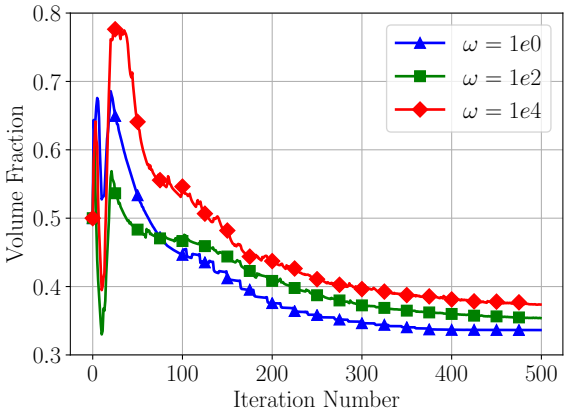

(a)

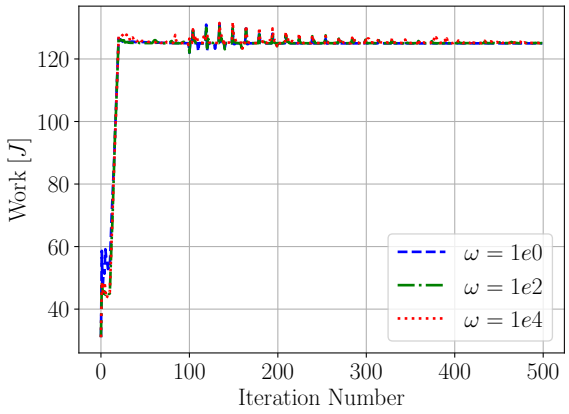

(b)

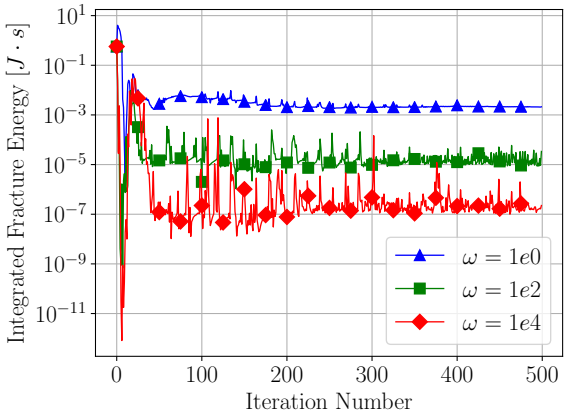

(c)

Figure 3.25: L-bracket optimizer convergence history for the (a) volume fraction, (b) work, and (c) integrated fracture energy

was not allowed to take place during the optimization iterations due to the convergence difficulties resulting from the very nonlinear physics and lack of sufficiently effective information in the function sensitivities. A judicious selection of objective and constraint functions is essential to obtaining better design performance when the brittle fracture physics are explicitly modeled during optimization. It is shown that this new formulation allows the optimizer to effectively update the design in order to reduce and ultimately remove cracks which have formed during the optimization process. Additionally, we have shown that the proposed formulation produces designs which remove re-entrant corners, consistent with intuition and also in contrast with our previous results. The numerical results provided are compared to the those obtained using linear elasticity; one in which

the volume is minimized subject to only a work constraint and a second formulation for stress minimization subject to a volume constraint as proposed by Le et al. [6]. It is demonstrated for the examples provided that the stress-formulation does a noteworthy job of producing structures with comparable strength. However, in terms of the provided gain in strength-to-weight ratio, the formulation proposed in this chapter produces designs with significant increases in performance. While the produced topologies bear some similar characteristics to the stress minimization result, such as the removal of re-entrant corners, the designs created by the proposed formulation are actually shown to be quite different. Additionally, we note the convenience of avoiding the use of aggregation functions and clustering techniques in the current formulation due to the naturally local nature of phase field formation which provides the desired local topological control.

Chapter 4

An optimization formulation for ductile failure and buckling resistance

This chapter is published as a journal article in: J. B. Russ and H. Waisman, "A novel elastoplastic topology optimization formulation for enhanced failure resistance via local ductile failure constraints and linear buckling analysis," Computer Methods in Applied Mechanics and Engineering, vol. 373, p. 113478, 2020, doi: 10.1016/j.cma.2020.113478.

4.1 Introduction

In this chapter we demonstrate an efficient and robust framework to increase a structure's peak load capacity and the total external work required to achieve the peak load, by including elastoplastic material behavior and failure resistance with respect to both ductile fracture and buckling. Since most structures are typically loaded in "force-control" rather than in "displacement-control", once a structure's peak load capacity is exceeded it is typical for the structure to either undergo fracture or buckling of structural members. If the load is not decreased past this point, further unstable structural behavior can result, potentially including structural collapse. Therefore we wish to not only increase the peak load capacity, but also the external work required to ultimately achieve this peak load. This may be viewed as a desired increase in the structural toughness, which is not only accompanied by an increase in strength but also an increase in the structural ductility.

To this end, we concentrate our efforts on structures consisting primarily of metals or other materials with relatively stiff elastic regions such that small deformation plasticity models may be used along with a separate linear elastic buckling analysis. At each optimization iteration two analyses are conducted with the same candidate topology. One incremental elastoplastic analysis in which a small strain J_2-plasticity model is employed in order to compute the total work and

uncoupled ductile failure indicators, and a separate linear elastic analysis in which the linear elastic buckling load factors are calculated. The results from the two analyses (which include the total work from the elastoplastic analysis and an aggregation function of the buckling load factors from the linear buckling analysis) are then combined into new aggregate objective function in which the local ductile failure constraints are handled via an adaptation of the Augmented Lagrangian framework of Senhora et al. [184, 7] . In addition to using the strain energy buckling mode filter introduced by [64], we also propose an additional buckling mode filter for highly localized modes in high density regions which we have encountered in the examples we tested. Finally, the large deformation phase field fracture formulation of Borden et al. [90] is used in order to evaluate the post-optimized topologies in lieu of desired experimental verification. Both the nonlinear elastoplastic hardening function, the ductile failure criterion used in this study, and particular parameters of the failure model are calibrated to available test data for Aluminum 2024-T351 presented in Bao and Wierzbicki [185, 186] in a genuine effort to demonstrate realistic performance gains. Additionally, we provide the external work computed at the load applied during the optimization procedure for the optimized topologies using both the small strain formulation and the large strain formulation. This provides an interesting metric for determining whether the small strain kinematics assumed during the optimization procedure adequately captured the structural response for the numerical examples explored herein.

The sections of this chapter may be summarized as follows. In Section 4.2 we briefly describe the standard small deformation J_2-plasticity model used in this chapter, along with the finite element implementation and the mean-dilatation method chosen to alleviate volumetric locking effects. Additionally we provide the details of the local ductile failure criterion selected for use during the optimization procedure. Section 4.3 provides a brief summary of the linear buckling analysis used herein. The details of the density based design parameterization are presented in Section 4.4, along with the optimization problem definition, sensitivity analyses, an overview of the optimization procedure, and other important details. These include the local constraint enforcement methodology along with an additional procedure used to identify and remove other pseudo buckling modes from

consideration. Section 4.5 summarizes the large deformation ductile phase field model implemented and used for verification of optimized design performance where key aspects of the model are briefly summarized. The results from three numerical examples are shown in Section 4.6 which demonstrate the performance improvements one might observe in practice. Section 4.7 provides a short summary of results, concluding remarks, and suggestions for future improvements.

4.2 Nonlinear finite element analysis used during optimization

In this section we provide a brief summary of the classical associative J_2-plasticity model and the finite element formulation. A small strain formulation, rather than one based on large strain kinematics, is used for numerical robustness and efficiency during the optimization procedure, along with a nonlinear Voce-type hardening law [187]. The justification for using small strain kinematics during the optimization procedure is addressed in the numerical results section. The small strain tensor, $\boldsymbol{\varepsilon}$, is assumed to be additively decomposed into elastic and plastic parts, namely $\boldsymbol{\varepsilon} = \boldsymbol{\varepsilon}^e + \boldsymbol{\varepsilon}^p$.

The Cauchy stress tensor, $\boldsymbol{\sigma}$, is split into its volumetric and deviatoric components according to $\boldsymbol{\sigma} = p\boldsymbol{I} + \boldsymbol{s}$, where p is the pressure or hydrostatic stress, $\boldsymbol{s}$ is the deviatoric stress, and $\boldsymbol{I}$ is the second order identity tensor. The local equations for associative J_2-plasticity with isotropic hardening are summarized below (de Souza Neto et al. [188]),

$$\boldsymbol{s} = 2\mu\mathbb{P}^{dev} : (\boldsymbol{\varepsilon} - \boldsymbol{\varepsilon}^p) \tag{4.2.1}$$

$$\Phi(\boldsymbol{\sigma}, \alpha) = \sigma_{vm} - \sigma_y(\alpha) \tag{4.2.2}$$

$$\boldsymbol{\varepsilon}^p = \dot{\gamma}\,\frac{\partial\Phi}{\partial\boldsymbol{\sigma}} = \dot{\gamma}\,\boldsymbol{N} \tag{4.2.3}$$

$$\dot{\alpha} = \dot{\gamma} \tag{4.2.4}$$

with yield function, Φ, along with the KKT conditions ($\Phi(\boldsymbol{\sigma}, \alpha) \leq 0$, $\dot{\gamma}\Phi(\boldsymbol{\sigma}, \alpha) = 0$, $\dot{\gamma} \geq 0$) and the complementarity condition ($\dot{\gamma}\dot{\Phi} = 0$). Note that $\sigma_{vm} = \sqrt{\frac{3}{2}\boldsymbol{s} : \boldsymbol{s}}$, is the von Mises stress measure and the elasticity is assumed to be linear where μ represents the classical shear modulus, which is related to elastic modulus (E) and Poisson's ratio (ν) via $\mu = E/(2\,(1+\nu))$ for an isotropic material.

Also note the use of ":" indicates the typical tensorial double contraction operator. The fourth order deviatoric projection tensor, $\mathbb{P}^{dev}_{ijkl} = \mathbb{I}^{s}_{ijkl} - \frac{1}{3}\delta_{ij}\delta_{kl}$, is used where $\mathbb{I}^{s}_{ijkl} = \frac{1}{2}\left(\delta_{ik}\delta_{jl} + \delta_{il}\delta_{jk}\right)$ is the fourth order symmetric identity tensor and δ_{ij} is the Kronecker delta. Additionally, we have used the notation γ for the plastic multiplier and $\boldsymbol{N} \equiv \frac{\partial \Phi}{\partial \boldsymbol{\sigma}} = \sqrt{\frac{3}{2}}\frac{\boldsymbol{s}}{||\boldsymbol{s}||}$ for the normal to yield surface. The yield stress (σ_y) is a function of the equivalent plastic strain (α) and is defined through the Voce-type hardening expression,

$$\sigma_y(\alpha) = \sigma_{y_0} + H\alpha + Y_\infty\left(1 - \exp\left(-\delta\alpha\right)\right) \tag{4.2.5}$$

where σ_{y_0} is the initial yield stress, H is the linear hardening modulus, and both Y_∞ and δ control the saturation portion of the hardening curve. This hardening function adequately describes the hardening of the Aluminum 2024-T351 plate material considered herein.

Global equilibrium for the continuum body, Ω, must then be obtained for a set of prescribed displacements ($\boldsymbol{u} = \bar{\boldsymbol{u}}$ on the Dirichlet boundary $\partial\Omega_d$) and surface tractions ($\boldsymbol{t}$ on the Neumann boundary $\partial\Omega_n$). Here we use the mean dilatation approach [189, 190] which is usually obtained via a three-field variational principle with potential, $\Pi = \Pi\left(\boldsymbol{u}_{n+1}, \Theta_{n+1}, p_{n+1}\right)$,

$$\begin{aligned}\Pi = \int_\Omega \left[\frac{1}{2}\kappa\Theta^2_{n+1} + \mu\boldsymbol{\varepsilon}^{\boldsymbol{e^{dev}}}_{\boldsymbol{n+1}} : \boldsymbol{\varepsilon}^{\boldsymbol{e^{dev}}}_{\boldsymbol{n+1}} + p_{n+1}\left(\nabla\cdot\boldsymbol{u}_{n+1} - \Theta_{n+1}\right)\right] dV \\ - \int_{\partial\Omega_n} \boldsymbol{t}_{n+1}\cdot\boldsymbol{u}_{n+1}\, dS\end{aligned} \tag{4.2.6}$$

where Θ is a volume-like independent variable, κ is the bulk modulus, and quantities with the $(\cdot)_{n+1}$ subscript correspond to pseudo-time, t_{n+1}, using the standard backward Euler time integration. Note that due to the small strain formulation we have not distinguished between the reference and current configurations of the body, Ω. Additionally we define relevant strain quantities below.

$$\boldsymbol{\varepsilon}_{n+1} = \mathbb{P}^{dev} : \nabla^s\boldsymbol{u}_{n+1} + \frac{1}{3}\Theta_{n+1}\boldsymbol{I} \tag{4.2.7}$$

$$\boldsymbol{\varepsilon}^{e^{dev}}_{n+1} = \mathbb{P}^{dev} : \left(\boldsymbol{\varepsilon}_{n+1} - \boldsymbol{\varepsilon}^{p}_{n+1}\right) \tag{4.2.8}$$

The variational equations of this energy functional may then be expressed as

$$\int_{\Omega} \left[\boldsymbol{s}_{n+1} : \nabla \delta \boldsymbol{u} + p_{n+1} \nabla \cdot \delta \boldsymbol{u} \right] \, dV - \int_{\partial \Omega_n} \boldsymbol{t}_{n+1} \cdot \delta \boldsymbol{u} \, dS = 0 \tag{4.2.9}$$

$$\int_{\Omega} \delta p \left(\nabla \cdot \boldsymbol{u}_{n+1} - \Theta_{n+1} \right) \, dV = 0 \tag{4.2.10}$$

$$\int_{\Omega} \delta \Theta \left(\kappa \Theta_{n+1} - p_{n+1} \right) \, dV = 0 \tag{4.2.11}$$

in which the divergence theorem has been used where appropriate. Next, we introduce the standard bilinear approximation within a given finite element for $(\boldsymbol{u}_{n+1}, \delta \boldsymbol{u})$ with shape function matrix, $\boldsymbol{N}^u$, shape function gradient matrix, $\boldsymbol{B}^u$, and shape function divergence matrix, $\boldsymbol{B}^u_{div}$,

$$\begin{aligned} \boldsymbol{u}_{n+1} &\approx \boldsymbol{N}^u \bar{\boldsymbol{u}}_{n+1} & \delta \boldsymbol{u} &\approx \boldsymbol{N}^u \delta \bar{\boldsymbol{u}} \\ \nabla \boldsymbol{u}_{n+1} &\approx \boldsymbol{B}^u \bar{\boldsymbol{u}}_{n+1} & \nabla \delta \boldsymbol{u} &\approx \boldsymbol{B}^u \delta \bar{\boldsymbol{u}} \\ \nabla \cdot \boldsymbol{u}_{n+1} &\approx \boldsymbol{B}^u_{div} \bar{\boldsymbol{u}}_{n+1} & \nabla \cdot \delta \boldsymbol{u} &\approx \boldsymbol{B}^u_{div} \delta \bar{\boldsymbol{u}} \end{aligned} \tag{4.2.12}$$

where $\bar{\boldsymbol{u}}_{n+1}$ and $\delta \bar{\boldsymbol{u}}$ represent the nodal displacement vector and nodal test function values, respectively. Using piecewise constant interpolations for $(\Theta_{n+1}, \delta\Theta, p_{n+1}, \delta p)$ over a given finite element (Ω_e), and using standard arguments regarding the nodal test function values, the equations are reduced to the following

$$\boldsymbol{R}^e_{n+1} = \int_{\Omega_e} \boldsymbol{B}^{u^T} : \boldsymbol{s}_{n+1} \, dV + p_{n+1} \int_{\Omega_e} \boldsymbol{B}^{u^T}_{div} \, dV - \int_{\partial \Omega_{e_n}} \boldsymbol{N}^{u^T} \boldsymbol{t}_{n+1} \, dS \tag{4.2.13}$$

$$\Theta_{n+1} = \frac{1}{V_e} \int_{\Omega_e} \boldsymbol{B}^u_{div} \bar{\boldsymbol{u}}_{n+1} \, dV \tag{4.2.14}$$

$$p_{n+1} = \kappa \Theta_{n+1} \tag{4.2.15}$$

where we have labeled the elemental residual vector. For a given displacement field, the values of Θ_{n+1} and p_{n+1} are known and can be substituted into the residual expression, resulting in a single set of equations to be solved for the displacement field. The elemental residual vectors are then assembled into their global counterpart, $\boldsymbol{R}$, via standard finite element assembly operations. Global

equilibrium is then obtained iteratively using Newton's method over a given time increment via the standard update of the form

$$\bar{\boldsymbol{u}}_{n+1}^{(k+1)} = \bar{\boldsymbol{u}}_{n+1}^{(k)} - \boldsymbol{J}_{n+1}^{(k)^{-1}} \boldsymbol{R}_{n+1}^{(k)} \tag{4.2.16}$$

for a given Newton iteration, k. The global Jacobian matrix, $\boldsymbol{J}$, is assembled from the elemental Jacobian matrices,

$$\boldsymbol{J}_{n+1}^{e} = \int_{\Omega_e} \boldsymbol{B}^{u^T} : \mathbb{C}_{n+1}^{dev} : \boldsymbol{B}^{u} \, dV + \frac{\kappa}{V_e} \left(\int_{\Omega_e} \boldsymbol{B}_{div}^{u^T} \, dV \right) \left(\int_{\Omega_e} \boldsymbol{B}_{div}^{u} \, dV \right) \tag{4.2.17}$$

where $\mathbb{C}_{n+1}^{dev}$ is the deviatoric part of the algorithmic consistent tangent operator arising from the common backward Euler time integration of the constitutive response. This is provided in B.1 along with the standard return mapping algorithm. The local residual equations governing the local material constitutive response are based upon the return mapping algorithm and, therefore, differ between elastic and plastic loading. For elastic loading we have the local residual expressions for quadrature point q of element e,

$$\boldsymbol{H}_{n}^{e_q} = \begin{bmatrix} \alpha_n - \alpha_{n-1} \\ \Delta\gamma_n \\ \boldsymbol{\varepsilon}_n^p - \boldsymbol{\varepsilon}_{n-1}^p \end{bmatrix} = \begin{bmatrix} 0 \\ 0 \\ \boldsymbol{0} \end{bmatrix} \tag{4.2.18}$$

whereas for plastic loading we have the following expressions.

$$\boldsymbol{H}_{n}^{e_q} = \begin{bmatrix} \alpha_n - \alpha_{n-1} - \Delta\gamma_n \\ \sqrt{\frac{3}{2}\boldsymbol{s}_n : \boldsymbol{s}_n} - \sigma_y(\alpha_n) \\ \boldsymbol{\varepsilon}_n^p - \boldsymbol{\varepsilon}_{n-1}^p - \Delta\gamma_n \boldsymbol{N}_n \end{bmatrix} = \begin{bmatrix} 0 \\ 0 \\ \boldsymbol{0} \end{bmatrix} \tag{4.2.19}$$

In our subsequent treatment the local residual equations are notationally grouped into a single vector, $\boldsymbol{H}$, analogous to the global residual, $\boldsymbol{R}$, such that $\boldsymbol{H}$ contains all of the local residual equations

corresponding to every quadrature point in the global finite element mesh. A standard 4-point Gauss quadrature rule is used within each element to perform the numerical integration. The Newton iteration procedure is carried out in each time increment until the relative residual achieves the desired tolerance (i.e. $||\boldsymbol{R}_{n+1}^{(k)}||/||\boldsymbol{R}_{n+1}^{(0)}|| < 10^{-8}$).

4.2.1 Ductile failure indicators

As previously mentioned in the introduction, rather than explicitly including the failure physics in the forward analyses used during the optimization problem, we use a ductile failure indicator that is uncoupled from the forward analyses (i.e. it does not have any effect on the forward problem, but rather serves as an indication of where ductile failure may occur at some location in the domain). This value may then be locally constrained during the optimization procedure in order to provide the desired resistance to ductile failure. While there have been a great number of uncoupled ductile failure criteria that have been proposed and examined (see [186, 191, 192] for instance) and also used within the context of elastoplastic response in topology optimization [44, 45, 46], here we choose a single failure criterion to demonstrate the idea.

The ductile failure criteria used in the aforementioned topology optimization works include the CrachFEM criteria of [193] and also the more classical Johnson-Cook failure criterion [194]. Since many of the criteria predict a certain equivalent plastic strain at failure (α_f) as a function of particular stress/strain measures, it is typical to use an integral approximation due to the generally nonlinear strain path that a material point will be subjected to over a load history [195, 193],

$$D_f = \int_0^{\alpha_{final}} \frac{1}{\alpha_f(\eta)} d\alpha \tag{4.2.20}$$

where we have introduced the stress triaxiality, $\eta = \frac{p}{\sigma_{vm}}$. While this is generally only applicable to monotonically loaded structures (e.g. no stress reversals) it provides an adequate approximation for use herein. The criteria can then be calibrated such that its value equals 1 when failure is predicted at a material point. It is well known that ductile failure of metals is clearly influenced by the stress

triaxiality as was previously shown extensively in other works [196, 186, 191]. Although more recent work has shown additional dependence on the Lode's angle [197, 198], we choose not to incorporate these effects here for simplicity. To this end we have chosen to use the Johnson-Cook failure criterion (which has also been used in [46]),

$$\alpha_f(\eta) = \hat{d}_1 + \hat{d}_2 \exp\left(\hat{d}_3 \eta\right) \tag{4.2.21}$$

with three material parameters ($\hat{d}_1$, $\hat{d}_2$, and $\hat{d}_3$) in this study. The calibration of these three parameters is briefly discussed in B.2.1, which resulted in the parameter set ($\hat{d}_1 = 0.0728$, $\hat{d}_2 = 1.1355$, $\hat{d}_3 = -2.8013$). As will be explained in more detail later, this ductile fracture criterion is used during the optimization process and is constrained to be some number less than 1 at every quadrature point, in a manner similar to how the stress might be constrained to be less than some fraction of the yield strength in a typical stress-based topology optimization problem. Again, this is done in order to drive creation of designs with some level of ductile failure resistance in a more computationally efficient manner than the alternative method of *explicitly simulating* ductile failure during the optimization process.

4.3 Linear buckling analysis

The linear elastic buckling analysis presented in Ferrari and Sigmund [65] is used in this chapter and is briefly summarized here, while the handling of pseudo-buckling modes and sensitivity analysis will be presented later. We start by assuming the structure is comprised of a material with a purely linear elastic constitutive response, subject the model to the same fixed displacement boundary conditions and apply a surface traction in the same direction and at the same location as the displacement loading in the elastoplastic forward analysis. Identical material parameters for the linear elastic part of the elastoplastic model are used in these analyses. The initial stress results

from the solution of the classical static equilibrium problem of linear elasticity,

$$\boldsymbol{K}_L \bar{\boldsymbol{u}}_L = \boldsymbol{f}_0 \tag{4.3.1}$$

where we use $\boldsymbol{K}_L$ to describe the standard linear elastic stiffness matrix, and $\bar{\boldsymbol{u}}_L$ to distinguish the nodal displacements obtained via this solution from the elastoplastic solution presented in Section 4.2. The external force vector, $\boldsymbol{f}_0$, arises due to the reference applied traction load. The critical load factor, λ_1, which predicts buckling if the load $\boldsymbol{f}_0$ were amplified by its magnitude, may then be estimated by means of an eigenvalue problem,

$$\boldsymbol{K}_L \boldsymbol{\phi}_i = -\lambda_i \boldsymbol{K}_\sigma \boldsymbol{\phi}_i \tag{4.3.2}$$

where $\boldsymbol{\phi}_i$ corresponds to the buckling mode shape, and $\boldsymbol{K}_\sigma$ represents the geometric or initial stress matrix which may be computed according to de Borst et al. [199]. As some authors have suggested [65], it may be better from a computational standpoint to solve the eigenproblem,

$$\boldsymbol{K}_\sigma \boldsymbol{\phi}_i = \mu_i \boldsymbol{K}_L \boldsymbol{\phi}_i \tag{4.3.3}$$

where $\lambda_i = -1/\mu_i$ due to the indefinite nature of the matrix $\boldsymbol{K}_\sigma$. In this case one is interested in the largest algebraic eigenvalues of the system. While this did work with more reliability, we have found that the formulation presented in [55] was more robust when solved using the standard Krylov-Schur eigensolver in the large scale parallel eigenanalysis package, SLEPc [200]. Finally, we also use the KS-aggregation function (in order to place more weight on the lowest buckling load factor). This is important since oftentimes multiple buckling modes must be considered due to mode swapping and it additionally renders the gradient unique in the case of eigenvalues which are not simple [201]. The final buckling function used in the optimization problem is the following,

$$B_{KS} = \frac{1}{\xi_{ks}} \ln \left(\sum_{i \in \mathcal{B}} \exp \left(\xi_{ks} \mu_i \right) \right) \tag{4.3.4}$$

where ξ_{ks} is the aggregation parameter that controls the degree to which the function approximates the eigenvalue corresponding to the smallest load factor. Note that $\mathcal{B}$ represents a set of computed eigenvalues and ultimately only includes the set of eigenvalues, $\{\mu_i\}$, corresponding to buckling modes which are not deemed to be pseudo-modes that have developed in low density or highly localized regions. These issues are addressed in Section 4.4.4.

4.4 Density-based topology optimization formulation

In this section we first outline the proposed density-based design parameterization used for the elastoplastic and structural buckling analyses performed during the topology optimization procedure. Our goal is to increase the structural strength including the amount of external work required to reach this state (after which any external load increase may be subsequently accompanied by structural softening in the form of either buckling or ductile fracture). We formulate the multiobjective optimization problem and briefly discuss the PDE-based filter and projection scheme used in this chapter. Additionally, the local constraint enforcement method is presented, along with an additional filtering scheme for highly-localized pseudo buckling modes that often arise during the linear elastic buckling analyses. The complete optimization procedure is then summarized with a flow diagram for clarity. In the final subsection, we provide the analytical, adjoint-based derivation of the relevant function sensitivities.

4.4.1 Density-based design parameterization

Elastoplasticity model design parameterization

The geometry is parameterized using a SIMP formulation [162, 163] with an ersatz material stiffness parameter used in the elastoplastic forward analyses as follows,

$$E = (\epsilon_e + (1 - \epsilon_e)\rho_e^p)E^{solid} \tag{4.4.1}$$

$$H = (\epsilon_p + (1 - \epsilon_p)\rho_e^q)H^{solid} \tag{4.4.2}$$

$$\sigma_{y_0} = (\epsilon_p + (1 - \epsilon_p)\rho_e^q)\sigma_{y_0}^{solid} \tag{4.4.3}$$

$$Y_\infty = (\epsilon_p + (1 - \epsilon_p)\rho_e^q)Y_\infty^{solid} \tag{4.4.4}$$

The elastic ersatz material parameter, ϵ_e, is set to 10^{-8} while the plastic ersatz material parameter, ϵ_p, is set to 10^{-4} for all examples in this chapter. In a manner similar to Amir [36] we apply continuation on the penalization exponents as follows. Initially the exponents are set to ($p = 1$, $q = 0.5$) for the first 10 iterations and subsequently increased by 0.1 every 10 subsequent iterations up to a maximum value of ($p = 4$, $q = 3.5$). This strategy, combined with the projection technique detailed in a subsequent subsection, proved to be effective for arriving at 0/1 designs and provided a smoother optimization process.

Linear buckling model design parameterization

Consistent with [62] we choose different elastic modulus interpolations for the linear elastic stiffness matrix, $\boldsymbol{K}_L$, and the initial stress matrix, $\boldsymbol{K}_\sigma$. As discussed in [62], this is in order to hinder the appearance of many pseudo-buckling modes in low density regions. Here the same interpolation strategy is used.

$$E_L = (10^{-6} + (1 - 10^{-6})\rho_e^p)E^{solid} \tag{4.4.5}$$

$$E_\sigma = \rho_e^p E^{solid} \tag{4.4.6}$$

While this strategy does generally decrease the number of pseudo-buckling modes which appear, in our experience there are many examples in which a great number of pseudo modes are still present. Perhaps the ersatz stiffness, 10^{-6}, in Equation (4.4.5) should also be adjusted along with the continuation scheme imposed on the density exponent, p. Rather than exploring this strategy, a different method is imposed which will be discussed in Section 4.4.4. Also, we note that the SIMP exponent, p, is the same as the exponent, p, presented in the previous subsection for the elastoplastic parameterization. The same continuation scheme mentioned there also applies.

4.4.2 Density filter and projection schemes

PDE-based density filter

In order to alleviate checkerboard patterns and other numerical instabilities, a density filter is applied to the design variables, $\boldsymbol{\theta} = [\theta_1, \ldots, \theta_{N_{elem}}]$, which are controlled by the optimizer. This also provides an effective strategy for dealing with issues of mesh-dependence as discussed in Sigmund and Petersson [164]. Here we use a PDE-based filter based on the work of Lazarov and Sigmund [202] which allows the algorithm to be easily parallelized using an existing finite element framework and the same design mesh discretization. The filtering scheme introduces a design length scale, r_{min}, which helps alleviate the problem of mesh-dependence [62]. The filtered design variables, $\hat{\rho}$, are obtained from the solution of the following boundary value problem,

$$-r^2\nabla^2\hat{\rho} + \hat{\rho} = \theta \text{ , in the domain, } \Omega \tag{4.4.7}$$

$$\nabla\hat{\rho} \cdot \boldsymbol{n} = 0 \text{ , on the boundary, } \partial\Omega, \text{ with outward normal } \boldsymbol{n} \tag{4.4.8}$$

where the parameter r controls the length scale of features in the final topology (i.e. $r = r_{min}/(2\sqrt{3})$ where r_{min} is related to the classical filter radius shown in [165] as discussed in [202]), and θ again represents the design variables controlled by the optimizer. The numerical solution of this PDE is obtained using the Galerkin finite element method with piece-wise continuous bilinear basis functions to discretize the filtered density field in the manner discussed in [202].

Filtered density projection

While it is true that increasing the SIMP penalization parameters, (p, q), tends to produce structures with pseudo-densities closer to 0 or 1, the filtering scheme inevitably creates a transition region with intermediate density values. In order to eliminate much of this transition region we employ a projection scheme beginning with the work of Guest et al. [166] and subsequently modified in Wang et al. [167].

$$\rho_e(\hat{\rho}_e(\boldsymbol{\theta})) = \frac{\tanh(\beta\eta) + \tanh(\beta(\hat{\rho}_e - \eta))}{\tanh(\beta\eta) + \tanh(\beta(1 - \eta))} \tag{4.4.9}$$

Note here that η governs the density threshold at which the projection takes place and β governs the strength of the projection operation. In all subsequent analyses η is fixed at 0.5 while a continuation scheme is used to update β during the optimization procedure. The parameter β is progressively increased in increments of 0.5 every 20 iterations from an initial value of 1 to a maximum value of 10. The value of $\beta = 1$ is kept constant, however, for the first 300 iterations in order to prevent unnecessary nonlinearity before a well-defined topology emerges (analogous to the strategy of Amir [36]).

4.4.3 Optimization problem statement/formulation

The goal of the formulation we propose is to maximize the peak load carrying capacity of the structure and the external work required to reach this state, by increasing not only the resistance to ductile fracture through the imposition of local failure constraints, but also the resistance to buckling of structural members by including the buckling load factors obtained from a linear buckling analysis in the objective function itself. Compared with previous work on elastoplastic topology optimization several novel features are presented. The first being that the total work is included in an *aggregate* objective function along with the KS-function of the buckling load factors from the linear elastic analysis. Including Equation (4.3.4) in the objective function is intended to provide additional support for members that are in compression and may be more sensitive to buckling.

The second feature includes the manner in which the local ductile failure constraints are imposed. Namely, the Augmented Lagrangian method that is used in place of traditional aggregation functions and is outfitted with suggested improvements for the ductile failure constraints imposed herein. This will be further discussed later in this section. Finally, the optimal results are verified using a more realistic finite deformation analysis with ductile failure predicted via the phase field fracture method. This model is briefly outlined in Section 4.5. Formally, we write the final mathematical optimization problem we wish to solve,

$$
\begin{aligned}
\underset{\boldsymbol{\theta}=[\theta_1,\ldots,\theta_{N_{elem}}]}{\text{minimize}} \quad & -\omega_1 \frac{W(\boldsymbol{\theta},\{\bar{\boldsymbol{u}}_i\},\{\boldsymbol{c}_i\})}{W^{scale}} + \omega_2 \frac{B_{KS}(\boldsymbol{\theta},\bar{\boldsymbol{u}}_L)}{B_{KS}^{scale}} + \omega_3\, AL(\boldsymbol{\theta},\{\bar{\boldsymbol{u}}_i\},\{\boldsymbol{c}_i\}) \\
\text{subject to} \quad & 0 \le \theta_e \le 1,\ e = 1,\ldots,N_{elem} \\
& \Lambda(\boldsymbol{\theta}) \le \Lambda_{max} \\
& \boldsymbol{R}^{(i)}(\boldsymbol{\theta},\{\bar{\boldsymbol{u}}_i\},\{\boldsymbol{c}_i\}) = \boldsymbol{0},\ i = 1,\ldots,N_{steps} \\
& \boldsymbol{H}^{(i)}(\boldsymbol{\theta},\{\bar{\boldsymbol{u}}_i\},\{\boldsymbol{c}_i\}) = \boldsymbol{0},\ i = 1,\ldots,N_{steps} \\
& \boldsymbol{K}_L(\boldsymbol{\theta})\bar{\boldsymbol{u}}_L = \boldsymbol{f}_0 \\
& \boldsymbol{K}_\sigma(\boldsymbol{\theta},\bar{\boldsymbol{u}}_L)\phi_i = \mu_i \boldsymbol{K}_L(\boldsymbol{\theta})\phi_i \text{ for } i \in \mathcal{B}
\end{aligned}
\tag{4.4.10}
$$

where we introduce the user-defined weighting factors $\{\omega_i \mid i \in \{1,2,3\}\ \&\ \omega_i \ge 0\}$, $(W^{scale}, B_{KS}^{scale})$ are scale factors for the corresponding functions, and we use the notation $\{\bar{\boldsymbol{u}}_i\}$ and $\{\boldsymbol{c}_i\}$ to describe the set of nodal displacement and local state variables at each increment, $i = 1,\ldots,N_{steps}$, where N_{steps} is the number of increments employed during the elastoplastic forward analysis. Note that the local state variables we have used are the equivalent plastic strain, plastic multiplier increment, and plastic strain tensor ($\boldsymbol{c} = \{\alpha, \Delta\gamma, \boldsymbol{\varepsilon}^p\}$) which will be important during the sensitivity analysis. Each function will be briefly described in more detail below. The buckling function, $B_{KS}(\boldsymbol{\theta},\bar{\boldsymbol{u}}_L)$, was previously provided in Equation (4.3.4).

Additionally, an upper bound (Λ_{max}) constraint is placed on the volume fraction, denoted by Λ

and defined in Equation (4.4.11) where V_{total} represents the design domain volume.

$$\Lambda(\boldsymbol{\theta}) = \frac{1}{\int_\Omega dV} \int_\Omega \rho(\boldsymbol{\theta})\, dV = \frac{1}{V_{total}} \sum_{e=1}^{N_{elem}} \rho_e V_e \tag{4.4.11}$$

Finally, we briefly provide the rationale for the scale factors (W^{scale}, B_{KS}^{scale}) and how they are updated. Due to aggregated nature of the objective function, it is important for the individual functions to be normalized in some manner. Over the course of the optimization problem, the magnitudes of the functions are changing, sometimes by orders of magnitude. This is due to multiple factors, including the continuation scheme on the SIMP penalty exponents (p and q), which are updated every 10 optimization iterations. In order for the *fixed* weights ω_1, ω_2, and ω_3 to have a consistent effect, we set the scaling parameters $W^{scale} = W$ and $B_{KS}^{scale} = B_{KS}$ every 10 optimization iterations, at the same iteration as the update of the SIMP penalization parameters p and q. This strategy has proven to be very effective for the examples we have encountered. Additionally, since they are not updated every iteration, we have experienced no stability or oscillatory issues with the optimization process.

Remark. The linear buckling analysis problem presented in Section 4.3 is a *pseudo*-problem that is not intended to accurately capture the physics of the physical problem. Rather the elastoplastic problem is intended for this purpose. The linear buckling analysis is significantly unphysical due largely to its constitutive assumption of linear elasticity in which the material stiffness is generally much higher than the same material which has been loaded beyond its elastic limit. Therefore, although one might use the same displacement-based loading in the buckling analysis as is used in the elastoplastic analysis, the two loadings are still not equivalent since the imparted loads depend on the constitutive response. Since this is the case, we use the force-based loading scheme for the linear buckling problem, in accordance with the existing literature, and apply the load in a direction consistent with the elastoplastic problem. The linear elastic buckling problem is only exploited for its capability to produce a function in which the sensitivities drive structural support for members that are in compression. This provides our desired resistance to buckling failure.

Remark. The B_{KS} function is minimized rather than constrained for a specific reason. Since the linear buckling analysis is a pseudo-problem that is weakly connected to the physical problem, it is not clear a-priori what upper bound one should place on this function. Thus, it is beneficial from a practical perspective to minimize it rather than constrain it, although there is no theoretical argument against constraining this function if a designer wishes to do so. Similarly, while one could constrain the part of the Augmented Lagrangian corresponding to the local failure constraints, we do not do so for two primary reasons. The first is simply to be consistent with the optimization theory, which is discussed in Nocedal and Wright [203]. The second, more practical reason, is that this part of the Augmented Lagrangian tends to be quite nonlinear in the design variables. Since most optimizers drive strongly toward the feasible region when a constraint is not satisfied, constraining this function may result in large design changes over few iterations. In order to avoid this, it is beneficial to include it in the objective function rather than directly constrain it.

Total work function

The total work function may be written in its typical integral form in addition to the numerically integrated form using the trapezoid rule,

$$\begin{aligned} W(\boldsymbol{\theta}, \{\bar{\boldsymbol{u}}_i\}, \{\boldsymbol{c}_i\}) &= \int_0^{t_{final}} \int_\Omega \boldsymbol{\sigma} : \dot{\boldsymbol{\varepsilon}} \, dV \, dt \\ &\approx \sum_{n=1}^{N_{steps}} \sum_{e=1}^{N_{elem}} \sum_{q=1}^{N_{quad}} \frac{1}{2} \left(\boldsymbol{\sigma}_{e_q}^{(n)} + \boldsymbol{\sigma}_{e_q}^{(n-1)} \right) : \left(\boldsymbol{\varepsilon}_{e_q}^{(n)} - \boldsymbol{\varepsilon}_{e_q}^{(n-1)} \right) w_{e_q} \end{aligned} \tag{4.4.12}$$

where the notation $(\cdot)_{e_q}$ implies the quantity corresponds to the q-th quadrature point of element e and w_{e_q} is the Jacobian of the elemental mapping multiplied by the corresponding quadrature weight.

Local ductile failure constraint enforcement

In order to increase resistance to ductile fracture, we enforce the local ductile failure constraints at each quadrature point in the finite element mesh. To this end we employ a new strategy based

on the work of Senhora et al. [184, 7] for stress constraints. This strategy removes the need for aggregation functions and clustering strategies as the number of local constraints increases. Given a local inequality constraint, $g_q(\boldsymbol{\theta}, \{\bar{\boldsymbol{u}}_i\}, \{\boldsymbol{c}_i\}) \leq 0$, a common Augmented Lagrangian strategy [203] may be used to enforce it, resulting in a function of the following form appended to the original objective.

$$AL(\boldsymbol{\theta}, \{\bar{\boldsymbol{u}}_i\}, \{\boldsymbol{c}_i\}) = \sum_{q=1}^{N_{quad}} \left(\lambda_q g_q(\boldsymbol{\theta}, \{\bar{\boldsymbol{u}}_i\}, \{\boldsymbol{c}_i\}) + \frac{\mu_q}{2} g_q(\boldsymbol{\theta}, \{\bar{\boldsymbol{u}}_i\}, \{\boldsymbol{c}_i\})^2 \right) \tag{4.4.13}$$

Note (λ_q, μ_q, $g_q(\boldsymbol{\theta}, \{\bar{\boldsymbol{u}}_i\}, \{\boldsymbol{c}_i\})$) represent the Lagrange multiplier, penalty parameter, and local ductile fracture constraint function at each quadrature point, q, all to be discussed later in more detail.

The local constraint function previously proposed in the context of stress-constrained linear elastic problems takes the following form for a stress measure ($\sigma_q = \sigma_q(\boldsymbol{\theta}, \bar{\boldsymbol{u}}_L)$) within a given finite element e, at quadrature point q,

$$g_q(\sigma_q) = \begin{cases} \rho_e^3 \left(\frac{\sigma_q}{\sigma_{max}} - 1 \right)^2, & \text{if } \sigma_q > \sigma_{max} \\ 0, & \text{otherwise} \end{cases} \tag{4.4.14}$$

where σ_{max} is the desired upper bound. The authors have found this method to work well in the context of linear elastic response but suggest a few modifications in order to potentially enhance its performance, particularly for the ductile failure constraints imposed in this chapter.

Before moving further we remind the reader that our local constraint to be enforced at each quadrature point is $D_f \leq D_{max}$ where D_f is computed using the Equations (4.4.15) and (4.4.16) below, and D_{max} is the user specified upper bound. As previously explained in Section 4.2, the local ductile failure indicator D_f is calibrated such that a value greater than or equal to 1 signifies a prediction of ductile failure of the material locally. Enforcing an upper bound, D_{max}, on this quantity which is less than 1 everywhere in the domain for a given external load then provides the

ductile failure resistance we desire.

$$D_{f_q}(\boldsymbol{\theta}, \{\bar{\boldsymbol{u}}_i\}, \{\boldsymbol{c}_i\}) = \int_0^{\alpha_q^{final}} \frac{1}{\hat{d}_1 + \hat{d}_2 \exp\left(\hat{d}_3 \eta_q\right)} d\alpha_q \approx \frac{1}{2} \sum_{n=1}^{N_{steps}} \left(f_q^{(n)} + f_q^{(n-1)}\right)\left(\alpha_q^{(n)} - \alpha_q^{(n-1)}\right) \tag{4.4.15}$$

$$\text{where } f_q^{(n)} \equiv \frac{1}{\hat{d}_1 + \hat{d}_2 \exp\left(\hat{d}_3 \eta_q^{(n)}\right)} \tag{4.4.16}$$

Note that this function is always positive for $\hat{d}_1, \hat{d}_2 \geq 0$. An analogous form to Equation (4.4.14) would result in a local constraint function,

$$g_q(D_{f_q}) = \begin{cases} \rho_e^3 \left(\frac{D_{fq}}{D_{max}} - 1\right)^2, & \text{if } D_{f_q} > D_{max} \\ 0, & \text{otherwise} \end{cases} \tag{4.4.17}$$

where the arguments, $D_{f_q} = D_{f_q}(\boldsymbol{\theta}, \{\bar{\boldsymbol{u}}_i\}, \{\boldsymbol{c}_i\})$, have been dropped for clarity. Empirically, we have found this form to be quite nonlinear in the design variables. This is due in part to the density exponent, the curvature of the function, and the zero derivative of the function when the constraint is satisfied. To this end, the functional form we propose may be expressed as,

$$g_q(D_{f_q}) = \begin{cases} \rho_e^{0.5} \left(\zeta_1 \left(\frac{D_{fq}}{D_{max}}\right)^2 + (\zeta_2 - 2\zeta_1)\frac{D_{fq}}{D_{max}} + \zeta_1\right), & \text{if } D_{f_q} > D_{max} \\ \rho_e^{0.5} \zeta_2 \left(\frac{D_{fq}}{D_{max}}\right), & \text{otherwise} \end{cases} \tag{4.4.18}$$

where $\zeta_1 > 0$ and $\zeta_2 \geq 0$ are two additional parameters we have introduced. Note that the function is C^1 in D_{f_q} and that the parameter selection $\zeta_1 = 1$ and $\zeta_2 = 0$ recovers the original function of Equation (4.4.17) with the exception of the density exponent replacement from 3 to 0.5. The density exponent has been reduced to 0.5 similar to the qp-relaxation of Bruggi [204], which also helps to reduce the nonlinearity of the function in the design variables. The parameter $\zeta_1 > 0$ controls the second derivative of the function when the constraint is not satisfied. Herein we set $\zeta_1 = 0.5$ which

makes the second derivative of the function half that of the function in Equation (4.4.17), further reducing the nonlinearity.

Additionally, we have included the parameter ζ_2 which provides the designer the option of allowing a nonzero function sensitivity when the constraint is satisfied. For the numerical examples presented herein we have set $\zeta_2 = 10^{-8}$ which has little effect on the resulting designs for the examples provided in Section 4.6. Later, larger values might be explored in order to determine whether the nonzero derivative has a positive impact on optimizer performance. Continuation schemes might also be employed for one or both parameters which make the function less nonlinear and help smooth the function sensitivities during the initial design iterations, while subsequently gently changing their values in later iterations so that the function is ultimately similar to Equation (4.4.17). We leave these exercises for future research and improvement but do not dwell on them further herein. The effects of the parameters are graphically shown in Figure 4.1.

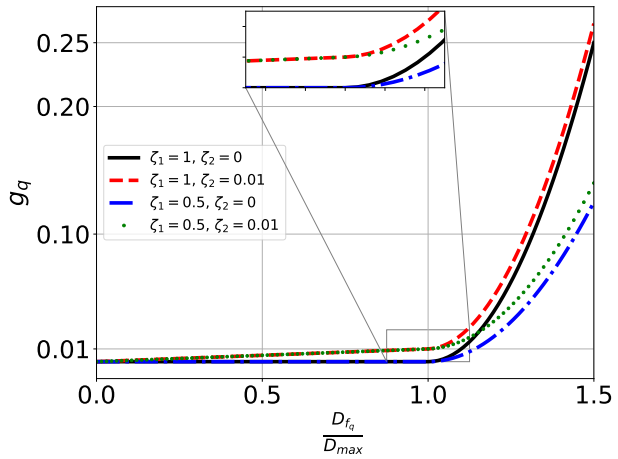

Figure 4.1: Demonstration of the effect of the new parameters ζ_1 and ζ_2 on Equation (4.4.18) for $\rho_e = 1$.

Finally we update the Lagrange multipliers and penalties in the following manner. For the first 50 optimization iterations the values are held fixed. Subsequently, every 5 optimization iterations, the values are updated according to the following equations at every quadrature point in the finite element mesh. Note also that the parameters, μ_q, are updated independently at every quadrature

point, rather than using a single penalty parameter, μ.

$$\lambda_q = \begin{cases} \max\left(\lambda_q + \mu_q \cdot g_q, 0\right) & \text{, if } D_{f_q} > D_{max} \\ \lambda_q & \text{, otherwise} \end{cases} \tag{4.4.19}$$

$$\mu_q = \begin{cases} 1.05 \cdot \mu_q & \text{, if } D_{f_q} > D_{max} \\ \mu_q & \text{, otherwise} \end{cases} \tag{4.4.20}$$

4.4.4 Buckling mode filters

We employ the strain energy buckling mode filter of Gao et al. [64] which is based upon an elemental criterion rather than the nodal criterion presented earlier in Gao and Ma [63]. While Ferrari and Sigmund [65] mention they did not see this issue for the example that they tested, we have seen the issue in both the portal frame example and the cantilever beam example explored in this chapter. However, we remark the L-bracket example did not have much issue with pseudo-buckling modes, although there were some pseudo modes occasionally detected and removed via this criterion. The standard parameters that are outlined in [64] to identify pseudo modes are used and we do not elaborate further on this point.

However, a different issue was also experienced that the strain energy filter mentioned above did not resolve. For examples such as the portal frame and cantilever beam, highly localized, clearly spurious buckling modes were observed in regions of high density which were under compression. Figure 4.2 illustrates one such example, and highlights the region where the downward traction is applied for the portal frame. In an effort to remove these spurious modes, we have implemented the following method which is efficient, parallelizable, and seemed to be effective for the examples we tested. This approach is briefly described below.

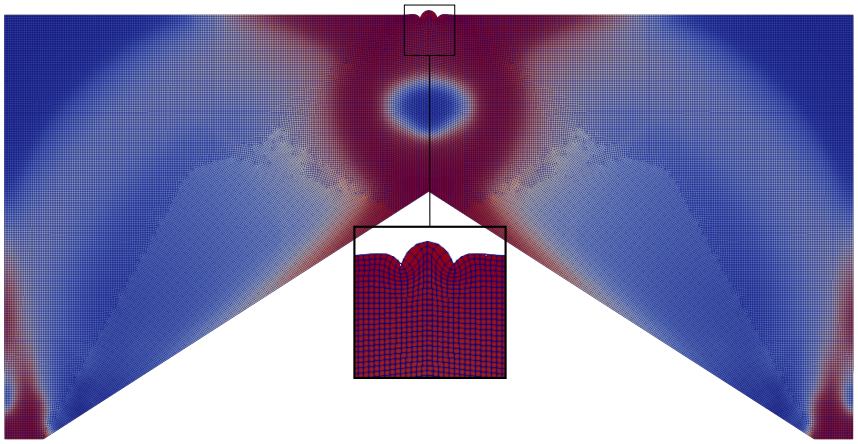

Figure 4.2: Portal frame localized pseudo-buckling mode at an intermediate optimization iteration. Pseudo-density field contours are depicted ($\rho_e = 0$ (blue), $\rho_e = 1$ (red)).

Take for example a single buckling mode, ϕ_i, which we normalize according to the l_∞-norm and refer to this normalized vector as $\boldsymbol{v} \equiv \frac{\phi_i}{||\phi_i||_\infty}$. The most active parts of the vector, $\boldsymbol{v}$, now have components with absolute values closer to 1 (note that another approach might be to normalize the vector such that the node with the largest norm of its vector displacement is 1 rather than our component-wise strategy). Therefore, if more than a large percentage, ξ_v%, of the vector components consists of absolute values less than $v_{thresh} \ll 1$ then regardless of the element density field, one might conclude that this vector is a highly localized pseudo-buckling mode of the type shown in Figure 4.2. In this chapter we use very conservative values for these parameters ($\xi_v = 90\%$, $v_{thresh} = 0.02$). Put in a different way, we do not consider any buckling modes for which 90% or more of the vector contains values less than 2% of the largest value. A relatively high (90%) threshold is used in order to ensure real buckling modes are not unintentionally removed, even though this has prevented the removal of several localized buckling modes in some cases. However, as the optimization procedure progresses towards a 0/1 solution, this becomes much less of an issue in our experience. We compute between 50 and 100 buckling modes (depending on the problem and the number of pseudo modes we observe) which are then passed through both filter algorithms. The first 6 of the filtered buckling modes are then included in the set $\mathcal{B}$, although this number could easily be changed if needed for some specific problem.

4.4.5 Optimization process and methodology

Here we provide a clear diagram illustrating the flow of information and a macroscopic view of the entire optimization procedure. This is illustrated in Figure 4.3.

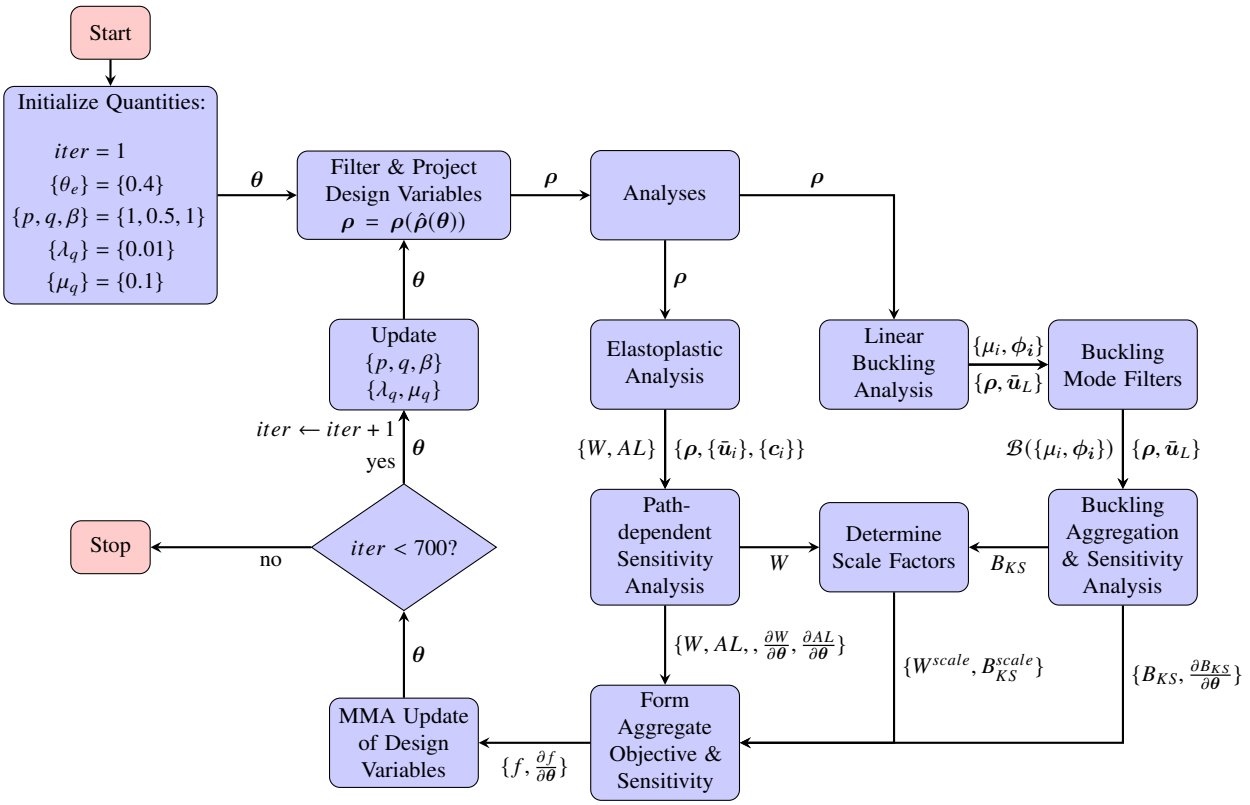

Figure 4.3: Flow chart illustrating the optimization procedure

Initially, the SIMP exponents, projection parameter (β), and Lagrange multipliers with associated penalty parameters are all initialized, along with the design variables, $\boldsymbol{\theta}$. The design variables are then filtered and projected as described in Section 4.4.2 to obtain the physical density variables, $\boldsymbol{\rho}$, used in the forward analyses. Subsequently, two separate forward analyses are conducted with the same density variables, $\boldsymbol{\rho}$. The first is the elastoplastic analysis in which the total work and local ductile failure indicators are computed. The second is the linear elastic buckling analysis, in which the aggregated form of the buckling load factors is computed after employing the pseudo-buckling mode filters described in Section 4.4.4. The sensitivities of the functions are then determined separately as is outlined in the following subsection and scale factors for the total work and buckling

aggregation function are determined as outlined previously. Subsequently, the aggregate objective function and its sensitivity is formed. We perform a fixed number of 700 iterations (unless otherwise noted) for each optimization problem. Note that this could also be replaced by a convergence check based on whichever convergence criteria is desired. Finally, the optimizer updates the design variables and the SIMP penalty exponents, projection parameter (β), Lagrange multipliers, and penalties are potentially updated as previously described in Sections 4.4.1, 4.4.2, and 4.4.3, respectively.

4.4.6 Sensitivity analysis

Since the elastoplastic analysis and the linear buckling analysis are treated separately, two sensitivity analyses corresponding to each solution are performed. The buckling sensitivity analysis ultimately reduces to

$$\frac{\partial B_{KS}}{\partial \rho_e} = \frac{1}{\sum_{i\in\mathcal{B}} \exp\left(\xi_{ks}\mu_i\right)} \sum_{i\in\mathcal{B}} \exp\left(\xi_{ks}\mu_i\right) \frac{\partial \mu_i}{\partial \rho_e} \tag{4.4.21}$$

where,

$$\frac{\partial \mu_i}{\partial \rho_e} = \boldsymbol{\phi}_i^T \left(\frac{\partial \boldsymbol{K}_\sigma}{\partial \rho_e} - \mu_i \frac{\partial \boldsymbol{K}_L}{\partial \rho_e} \right) \boldsymbol{\phi}_i - \boldsymbol{v}_i^T \frac{\partial \boldsymbol{K}_L}{\partial \rho_e} \bar{\boldsymbol{u}}_L \tag{4.4.22}$$

and the adjoint vector $\boldsymbol{v}_i$ is obtained via the solution of the adjoint problem [205],

$$\boldsymbol{K}_L \boldsymbol{v}_i = \boldsymbol{\phi}_i^T \frac{\partial \boldsymbol{K}_\sigma}{\partial \bar{\boldsymbol{u}}_L} \boldsymbol{\phi}_i \tag{4.4.23}$$

which completes the sensitivity analysis for the B_{KS} function. Note that these results are contingent upon the buckling mode shapes being normalized such that $\boldsymbol{\phi}_i^T \boldsymbol{K}_L \boldsymbol{\phi}_i = 1$.

The work and failure constraint function sensitivities take significantly more effort compute, primarily due to the path dependent, incremental nature of the problem. We begin with a general function (f) of the global state ($\{\bar{\boldsymbol{u}}_i\}$), local state ($\{\boldsymbol{c}_i\}$), and element densities $\boldsymbol{\rho} \equiv \{\rho_e,\ e =$

$1...N_{elem}\}$, and subsequently augment the function (to form $\hat{f}$) with the summation of inner products between the global/local equilibrium vectors at every load step and corresponding unknown adjoint vectors, $\boldsymbol{\lambda_R^n}$ and $\boldsymbol{\lambda_H^n}$.

$$\begin{aligned}\hat{f}(\boldsymbol{\rho}, \{\bar{\boldsymbol{u}}_i\}, \{\boldsymbol{c}_i\}) &= f(\boldsymbol{\rho}, \{\bar{\boldsymbol{u}}_i\}, \{\boldsymbol{c}_i\}) \\ &+ \sum_{n=1}^{N_{steps}} \boldsymbol{\lambda}_R^{n^T} \boldsymbol{R}_n(\boldsymbol{\rho}, \bar{\boldsymbol{u}}_n, \bar{\boldsymbol{u}}_{n-1}, \boldsymbol{c}_n, \boldsymbol{c}_{n-1}) \\ &+ \sum_{n=1}^{N_{steps}} \boldsymbol{\lambda}_H^{n^T} \boldsymbol{H}_n(\boldsymbol{\rho}, \bar{\boldsymbol{u}}_n, \bar{\boldsymbol{u}}_{n-1}, \boldsymbol{c}_n, \boldsymbol{c}_{n-1})\end{aligned} \tag{4.4.24}$$

Taking the total derivative of this function with respect to ρ_e, regrouping terms, and applying typical arguments one arrives at a system of equations which may be solved to determine the unknown adjoint vectors and decrease the overall computational expense of the sensitivity analysis when the number of design variables is large.

For the final time increment, $n = N_{steps}$, we have,

$$\frac{\partial \boldsymbol{R}_n}{\partial \bar{\boldsymbol{u}}_n}^T \boldsymbol{\lambda}_R^n + \frac{\partial \boldsymbol{H}_n}{\partial \bar{\boldsymbol{u}}_n}^T \boldsymbol{\lambda}_H^n = -\frac{\partial f}{\partial \bar{\boldsymbol{u}}_n}^T \tag{4.4.25}$$

$$\frac{\partial \boldsymbol{R}_n}{\partial \boldsymbol{c}_n}^T \boldsymbol{\lambda}_R^n + \frac{\partial \boldsymbol{H}_n}{\partial \boldsymbol{c}_n}^T \boldsymbol{\lambda}_H^n = -\frac{\partial f}{\partial \boldsymbol{c}_n}^T \tag{4.4.26}$$

while for $n < N_{steps}$ one must solve the system,

$$\frac{\partial \boldsymbol{R}_n}{\partial \bar{\boldsymbol{u}}_n}^T \boldsymbol{\lambda}_R^n + \frac{\partial \boldsymbol{H}_n}{\partial \bar{\boldsymbol{u}}_n}^T \boldsymbol{\lambda}_H^n = -\frac{\partial f}{\partial \bar{\boldsymbol{u}}_n}^T - \frac{\partial \boldsymbol{R}_{n+1}}{\partial \bar{\boldsymbol{u}}_n}^T \boldsymbol{\lambda}_R^{n+1} - \frac{\partial \boldsymbol{H}_{n+1}}{\partial \bar{\boldsymbol{u}}_n}^T \boldsymbol{\lambda}_H^{n+1} \tag{4.4.27}$$

$$\frac{\partial \boldsymbol{R}_n}{\partial \boldsymbol{c}_n}^T \boldsymbol{\lambda}_R^n + \frac{\partial \boldsymbol{H}_n}{\partial \boldsymbol{c}_n}^T \boldsymbol{\lambda}_H^n = -\frac{\partial f}{\partial \boldsymbol{c}_n}^T - \frac{\partial \boldsymbol{R}_{n+1}}{\partial \boldsymbol{c}_n}^T \boldsymbol{\lambda}_R^{n+1} - \frac{\partial \boldsymbol{H}_{n+1}}{\partial \boldsymbol{c}_n}^T \boldsymbol{\lambda}_H^{n+1} \tag{4.4.28}$$

for the unknown adjoint vectors. Labeling the right hand side of Equations (4.4.25) and (4.4.27) with $\boldsymbol{F_u}$ and Equations (4.4.26) and (4.4.28) with $\boldsymbol{F_c}$ for conciseness, the equations may be re-arranged

such that,

$$\left(\frac{\partial \boldsymbol{R}_n}{\partial \bar{\boldsymbol{u}}_n} - \frac{\partial \boldsymbol{R}_n}{\partial \boldsymbol{c}_n}\frac{\partial \boldsymbol{H}_n}{\partial \boldsymbol{c}_n}^{-1}\frac{\partial \boldsymbol{H}_n}{\partial \bar{\boldsymbol{u}}_n}\right)^T \boldsymbol{\lambda}_R^n = \boldsymbol{F_u} + \frac{\partial \boldsymbol{R}_n}{\partial \boldsymbol{c}_n}\frac{\partial \boldsymbol{H}_n}{\partial \boldsymbol{c}_n}^{-1}\boldsymbol{F_c} \tag{4.4.29}$$

$$\boldsymbol{\lambda}_H^n = \frac{\partial \boldsymbol{H}_n}{\partial \boldsymbol{c}_n}^{-1}\left(\boldsymbol{F_c} - \frac{\partial \boldsymbol{H}_n}{\partial \bar{\boldsymbol{u}}_n}\boldsymbol{\lambda}_R^n\right) \tag{4.4.30}$$

which facilitates the formation of both the left and right hand side of Equation (4.4.29) at the element level prior to global assembly since all of the gauss point local variables are independent of one another (as mentioned and used in [182, 206]). Therefore the matrix inverse in the equations is much cheaper to compute than that of the original system, which need never be explicitly formed or solved (eliminating the need for constructing the new sparsity pattern and larger matrix structures as well). Once the adjoint vector, $\boldsymbol{\lambda}_R^n$, is known, the calculation of $\boldsymbol{\lambda}_H^n$ can be locally performed very rapidly at the element level. With the set of adjoint vectors known, the sensitivity of the original function may then be computed via

$$\frac{df}{d\rho_e} = \frac{d\hat{f}}{d\rho_e} = \frac{\partial f}{\partial \rho_e} + \sum_{n=1}^{N_{steps}} \boldsymbol{\lambda}_R^{n^T}\frac{\partial \boldsymbol{R}_n}{\partial \rho_e} + \sum_{n=1}^{N_{steps}} \boldsymbol{\lambda}_H^{n^T}\frac{\partial \boldsymbol{H}_n}{\partial \rho_e} \tag{4.4.31}$$

which consists of simple explicit derivatives to compute within each element.

Global residual derivatives

In the absence of tractions applied during the elastoplastic analyses, the elemental residual vectors take the form,

$$\boldsymbol{R}_n^e = \int_{\Omega_e} \boldsymbol{B}^{u^T} : \boldsymbol{s}_n \, dV + p_n \int_{\Omega_e} \boldsymbol{B}_{div}^{u^T} \, dV \tag{4.4.32}$$

as previously presented in Section 4.2. The following explicit derivatives may then be defined.

$$\frac{\partial \boldsymbol{R}_n^e}{\partial \rho_e} = \int_{\Omega_e} 2\frac{d\mu}{d\rho_e}\boldsymbol{B}^{u^T} : \mathbb{P}_{dev} : \left(\boldsymbol{\varepsilon}_n - \boldsymbol{\varepsilon}_n^p\right)\, dV + \frac{d\kappa}{d\rho_e}\Theta_{n+1}\int_{\Omega_e} \boldsymbol{B}_{div}^{u^T}\, dV$$

$$\frac{\partial \boldsymbol{R}_n^e}{\partial \bar{\boldsymbol{u}}_n} = \int_{\Omega_e} 2\mu\boldsymbol{B}^{u^T} : \mathbb{P}_{dev} : \boldsymbol{B}^u\, dV + \frac{\kappa}{V_e}\left(\int_{\Omega_e} \boldsymbol{B}_{div}^{u^T}\, dV\right)\left(\int_{\Omega_e} \boldsymbol{B}_{div}^{u}\, dV\right)$$

$$\frac{\partial \boldsymbol{R}_n^e}{\partial \boldsymbol{\varepsilon}_n^p} = \int_{\Omega_e} -2\mu\boldsymbol{B}^{u^T} : \mathbb{P}_{dev}\, dV$$

$$\frac{\partial \boldsymbol{R}_n^e}{\partial \alpha_n} = \frac{\partial \boldsymbol{R}_n^e}{\partial \Delta\gamma_n} = \frac{\partial \boldsymbol{R}_{n+1}^e}{\partial \bar{\boldsymbol{u}}_n} = \frac{\partial \boldsymbol{R}_{n+1}^e}{\partial \boldsymbol{\varepsilon}_n^p} = \frac{\partial \boldsymbol{R}_{n+1}^e}{\partial \alpha_n} = \frac{\partial \boldsymbol{R}_{n+1}^e}{\partial \Delta\gamma_n} = \boldsymbol{0}$$

Local residual derivatives

The explicit derivatives of the local residual equations previously defined in Equation (4.2.18) and (4.2.19) are provided in this section. In the case of elastic loading the required derivatives are,

$$\frac{\partial \boldsymbol{H}_n^{e_q}}{\partial \rho_e} = \begin{bmatrix} 0 \\ 0 \\ \boldsymbol{0} \end{bmatrix} \qquad \frac{\partial \boldsymbol{H}_n^{e_q}}{\partial \bar{\boldsymbol{u}}_n} = \begin{bmatrix} 0 \\ 0 \\ \boldsymbol{0} \end{bmatrix} \qquad \frac{\partial \boldsymbol{H}_{n+1}^{e_q}}{\partial \bar{\boldsymbol{u}}_n} = \begin{bmatrix} 0 \\ 0 \\ \boldsymbol{0} \end{bmatrix}$$

$$\frac{\partial \boldsymbol{H}_n^{e_q}}{\partial \alpha_n} = \begin{bmatrix} 1 \\ 0 \\ \boldsymbol{0} \end{bmatrix} \qquad \frac{\partial \boldsymbol{H}_n^{e_q}}{\partial \Delta\gamma_n} = \begin{bmatrix} 0 \\ 1 \\ \boldsymbol{0} \end{bmatrix} \qquad \frac{\partial \boldsymbol{H}_n^{e_q}}{\partial \boldsymbol{\varepsilon}_n^p} = \begin{bmatrix} 0 \\ 0 \\ \mathbb{I}^s \end{bmatrix}$$

$$\frac{\partial \boldsymbol{H}_{n+1}^{e_q}}{\partial \alpha_n} = \begin{bmatrix} -1 \\ 0 \\ \boldsymbol{0} \end{bmatrix} \qquad \frac{\partial \boldsymbol{H}_{n+1}^{e_q}}{\partial \Delta\gamma_n} = \begin{bmatrix} 0 \\ 0 \\ \boldsymbol{0} \end{bmatrix} \qquad \frac{\partial \boldsymbol{H}_{n+1}^{e_q}}{\partial \boldsymbol{\varepsilon}_n^p} = \begin{bmatrix} 0 \\ 0 \\ -\mathbb{I}^s \end{bmatrix}$$

while for plastic loading the derivatives become more complex and are provided below.

$$\frac{\partial \boldsymbol{H}_n^{e_q}}{\partial \rho_e} = \begin{bmatrix} 0 \\ a_n \\ 0 \end{bmatrix} \qquad \frac{\partial \boldsymbol{H}_n^{e_q}}{\partial \bar{\boldsymbol{u}}_n} = \begin{bmatrix} \boldsymbol{0} \\ \boldsymbol{A}_n : \boldsymbol{B}^u \\ \mathbb{A}_n : \boldsymbol{B}^u \end{bmatrix} \qquad \frac{\partial \boldsymbol{H}_{n+1}^{e_q}}{\partial \bar{\boldsymbol{u}}_n} = \begin{bmatrix} \boldsymbol{0} \\ \boldsymbol{0} \\ \boldsymbol{0} \end{bmatrix}$$

$$\frac{\partial \boldsymbol{H}_n^{e_q}}{\partial \alpha_n} = \begin{bmatrix} 1 \\ -\frac{d\sigma_y}{d\alpha}\big|_{\alpha_n} \\ \boldsymbol{0} \end{bmatrix} \qquad \frac{\partial \boldsymbol{H}_n^{e_q}}{\partial \Delta\gamma_n} = \begin{bmatrix} -1 \\ 0 \\ \sqrt{\frac{3}{2}} \frac{\boldsymbol{s_n}}{||\boldsymbol{s}_n||} \end{bmatrix} \qquad \frac{\partial \boldsymbol{H}_n^{e_q}}{\partial \boldsymbol{\varepsilon}_n^p} = \begin{bmatrix} \boldsymbol{0} \\ -\boldsymbol{A}_n \\ \mathbb{I}^s + \mathbb{A}_n \end{bmatrix}$$

$$\frac{\partial \boldsymbol{H}_{n+1}^{e_q}}{\partial \alpha_n} = \begin{bmatrix} -1 \\ 0 \\ \boldsymbol{0} \end{bmatrix} \qquad \frac{\partial \boldsymbol{H}_{n+1}^{e_q}}{\partial \Delta\gamma_n} = \begin{bmatrix} 0 \\ 0 \\ \boldsymbol{0} \end{bmatrix} \qquad \frac{\partial \boldsymbol{H}_{n+1}^{e_q}}{\partial \boldsymbol{\varepsilon}_n^p} = \begin{bmatrix} 0 \\ 0 \\ -\mathbb{I}^s \end{bmatrix}$$

Note that the notation $\frac{d\sigma_y}{d\alpha}\big|_{\alpha_n}$ refers to the derivative $\frac{d\sigma_y}{d\alpha}$ evaluated at α_n. We have used the following definitions to simplify the above expressions.

$$a_n \equiv \frac{d\mu}{d\rho_e} \frac{\sqrt{6}}{||\boldsymbol{s}_n||} \boldsymbol{s}_n : \left(\boldsymbol{\varepsilon}_n - \boldsymbol{\varepsilon}_n^p\right) - \left(\frac{d\sigma_{y_0}}{d\rho_e} + \frac{dH}{d\rho_e}\alpha_n + \frac{dY_\infty}{d\rho_e}\left(1 - \exp\left(-\delta\alpha_n\right)\right)\right)$$

$$\boldsymbol{A}_n \equiv \sqrt{6}\mu \frac{\boldsymbol{s}_n}{||\boldsymbol{s}_n||}$$

$$\mathbb{A}_n \equiv \frac{\mu\sqrt{6}\Delta\gamma_n}{||\boldsymbol{s}_n||}\left(\mathbb{P}_{dev} - \frac{\boldsymbol{s}_n}{||\boldsymbol{s}_n||} \otimes \frac{\boldsymbol{s}_n}{||\boldsymbol{s}_n||}\right)$$

The work and AL functions both depend on the element pseudo-densities and the global/local state variables. The derivatives $\frac{\partial f}{\partial \rho_e}$, $\frac{\partial f}{\partial \bar{\boldsymbol{u}}_n}$, and $\frac{\partial f}{\partial \boldsymbol{c}_n}$ appear in Equations (4.4.25), (4.4.26), (4.4.27), (4.4.28), and (4.4.31) and must therefore be provided in order to complete the sensitivity analysis for a given function. These explicit derivatives are provided in the next subsection. Finally, due to the filtering and projection schemes presented in Section 4.4.2, the chain rule must be employed in order to obtain the final required derivatives of the functions with respect to the design variables, $\boldsymbol{\theta}$. This is performed as discussed in [202].

Work function explicit derivatives

Note that the work function may be re-written in the following form where we use the shorter notation, $N \equiv N_{steps}$, for clarity

$$W(\boldsymbol{\rho}, \{\bar{\boldsymbol{u}}_i\}, \{\boldsymbol{c}_i\}) = \frac{1}{2}\int_\Omega \boldsymbol{\sigma}_N : (\boldsymbol{\varepsilon}_N - \boldsymbol{\varepsilon}_{N-1})\, dV + \frac{1}{2}\sum_{n=1}^{N-1}\int_\Omega \boldsymbol{\sigma}_n : (\boldsymbol{\varepsilon}_{n+1} - \boldsymbol{\varepsilon}_{n-1})\, dV$$

and where we assume that the body is initially unloaded so that $\boldsymbol{\varepsilon}_0 = \boldsymbol{0}$. We may compute the partial derivative with respect to an element pseudo-density with the following expression

$$\frac{\partial W}{\partial \rho_e} = \frac{1}{2}\int_\Omega \frac{\partial \boldsymbol{\sigma}_N}{\partial \rho_e} : (\boldsymbol{\varepsilon}_N - \boldsymbol{\varepsilon}_{N-1})\, dV + \frac{1}{2}\sum_{n=1}^{N-1}\int_\Omega \frac{\partial \boldsymbol{\sigma}_n}{\partial \rho_e} : (\boldsymbol{\varepsilon}_{n+1} - \boldsymbol{\varepsilon}_{n-1})\, dV \tag{4.4.33}$$

$$\frac{\partial \boldsymbol{\sigma}_n}{\partial \rho_e} = \frac{d\kappa}{d\rho_e}\Theta_n \boldsymbol{I} + 2\frac{d\mu}{d\rho_e}\mathbb{P}_{dev} : \left(\boldsymbol{\varepsilon}_n - \boldsymbol{\varepsilon}_n^p\right) \tag{4.4.34}$$

The derivatives with respect to global and local state variables at particular time steps are slightly more tedious to compute and are grouped according to those corresponding to the state at the final time increment and those of previous increments.

Final (N^{th}) pseudo-time increment:

$$\begin{aligned}\frac{\partial W}{\partial \bar{\boldsymbol{u}}_N} &= \frac{1}{2}\int_\Omega (\boldsymbol{\varepsilon}_N - \boldsymbol{\varepsilon}_{N-1}) : (2\mu\mathbb{P}_{dev}) : \boldsymbol{B}^u dV \\ &+ \frac{1}{2}\left(\int_\Omega (\boldsymbol{\varepsilon}_N - \boldsymbol{\varepsilon}_{N-1}) : \boldsymbol{I}\, dV\right)\left(\frac{\kappa}{V_e}\int_\Omega \boldsymbol{B}^u_{div} dV\right) \\ &+ \frac{1}{2}\int_\Omega (\boldsymbol{\sigma}_N + \boldsymbol{\sigma}_{N-1}) : \boldsymbol{B}^u dV\end{aligned} \tag{4.4.35}$$

$$\frac{\partial W}{\partial \boldsymbol{\varepsilon}_N^p} = \frac{1}{2}\int_\Omega (\boldsymbol{\varepsilon}_N - \boldsymbol{\varepsilon}_{N-1}) : (-2\mu\mathbb{P}_{dev})\, dV \tag{4.4.36}$$

$$\frac{\partial W}{\partial \alpha_N} = \frac{\partial W}{\partial \Delta\gamma_N} = 0 \tag{4.4.37}$$

All other pseudo-time increments ($n = N-1, \ldots, 1$):

$$\begin{aligned}\frac{\partial W}{\partial \bar{\boldsymbol{u}}_n} &= \frac{1}{2}\int_\Omega (\boldsymbol{\varepsilon}_{n+1} - \boldsymbol{\varepsilon}_{n-1}) : (2\mu\mathbb{P}_{dev}) : \boldsymbol{B}^u dV \\ &+ \frac{1}{2}\left(\int_\Omega (\boldsymbol{\varepsilon}_{n+1} - \boldsymbol{\varepsilon}_{n-1}) : \boldsymbol{I}\, dV\right)\left(\frac{\kappa}{V_e}\int_\Omega \boldsymbol{B}^u_{div} dV\right) \\ &+ \frac{1}{2}\int_\Omega (\boldsymbol{\sigma}_{n-1} - \boldsymbol{\sigma}_{n+1}) : \boldsymbol{B}^u dV\end{aligned} \tag{4.4.38}$$

$$\frac{\partial W}{\partial \boldsymbol{\varepsilon}^p_n} = \frac{1}{2}\int_\Omega (\boldsymbol{\varepsilon}_{n+1} - \boldsymbol{\varepsilon}_{n-1}) : (-2\mu\mathbb{P}_{dev})\, dV \tag{4.4.39}$$

$$\frac{\partial W}{\partial \alpha_n} = \frac{\partial W}{\partial \Delta\gamma_n} = 0 \tag{4.4.40}$$

AL function explicit derivatives

The AL function is a summation of terms which are each related to a unique gauss quadrature point. Therefore, we only need to provide the derivatives for a general quadrature point, q, in an element, e, whose piece of the function in Equation (4.4.13) may be abbreviated as

$$f_q = \lambda_q g_q(\rho_e, D_{f_q}) + \frac{\mu_q}{2} g_q(\rho_e, D_{f_q})^2 \tag{4.4.41}$$

where over a given optimization iteration λ_q and μ_q are constant and we have made a notational substitution where g_q is now a function of the integrated damage criterion ($D_{f_q} = D_{f_q}(\{\bar{\boldsymbol{u}}_i\}, \{\boldsymbol{c}_i\})$) at the corresponding quadrature point for convenience. We start with the derivative of this function with respect to ρ_e.

$$\frac{\partial f_q}{\partial \rho_e} = \left(\lambda_q \frac{\partial g_q}{\partial \rho_e} + \mu_q g_q(\rho_e, D_{f_q})\frac{\partial g_q}{\partial \rho_e}\right) \tag{4.4.42}$$

$$\frac{\partial g_q}{\partial \rho_e} = \begin{cases} \frac{1}{2}\rho_e^{-0.5}\left(\zeta_1\left(\frac{D_{fq}}{D_{max}}\right)^2 + (\zeta_2 - 2\zeta_1)\frac{D_{fq}}{D_{max}} + \zeta_1\right), & \text{if } D_{f_q} > D_{max} \\ \frac{1}{2}\rho_e^{-0.5}\zeta_2\left(\frac{D_{fq}}{D_{max}}\right), & \text{otherwise} \end{cases} \tag{4.4.43}$$

The derivatives with respect to the state variables may be written more concisely by taking the derivative with respect to a general state variable, χ,

$$\frac{\partial f_q}{\partial \chi} = \left(\lambda_q \frac{\partial g_q}{\partial D_{f_q}} + \mu_q g_q(\rho_e, D_{f_q}) \frac{\partial g_q}{\partial D_{f_q}} \right) \frac{\partial D_{f_q}}{\partial \chi} \tag{4.4.44}$$

where,

$$\frac{\partial g_q}{\partial D_{f_q}} = \begin{cases} \rho_e^{0.5} \left(\frac{2\zeta_1 D_{f_q}}{(D_{max})^2} + \frac{\zeta_2 - 2\zeta_1}{D_{max}} \right), & \text{if } D_{f_q} > D_{max} \\ \rho_e^{0.5} \left(\frac{\zeta_2}{D_{max}} \right), & \text{otherwise} \end{cases} \tag{4.4.45}$$

and now it remains only to determine the derivatives, $\frac{\partial D_{f_q}}{\partial \chi}$ for $\chi \in \{\{\bar{\boldsymbol{u}}_i\}, \{\boldsymbol{c}_i\}\}$. For convenience we make the following definition, $h_n(\eta_n) \equiv \frac{1}{\hat{d}_1 + \hat{d}_2 \exp\left(\hat{d}_3 \eta_n\right)}$, to again further simplify notation.

Final (N^{th}) pseudo-time increment:

$$\frac{\partial D_{f_q}}{\partial \bar{\boldsymbol{u}}_N} = \frac{1}{2} \left(\alpha_N - \alpha_{N-1} \right) \frac{\partial h_N}{\partial \bar{\boldsymbol{u}}_N} \tag{4.4.46}$$

$$\frac{\partial D_{f_q}}{\partial \alpha_N} = \frac{1}{2} \left(h_N + h_{N-1} \right) \tag{4.4.47}$$

$$\frac{\partial D_{f_q}}{\partial \varepsilon_N^p} = \frac{1}{2} \left(\alpha_N - \alpha_{N-1} \right) \frac{\partial h_N}{\partial \varepsilon_N^p} \tag{4.4.48}$$

$$\frac{\partial D_{f_q}}{\partial \Delta\gamma_N} = 0 \tag{4.4.49}$$

All other pseudo-time increments ($n = N-1, \ldots, 1$):

$$\frac{\partial D_{f_q}}{\partial \bar{\boldsymbol{u}}_n} = \frac{1}{2} \left(\alpha_{n+1} - \alpha_{n-1} \right) \frac{\partial h_n}{\partial \bar{\boldsymbol{u}}_n} \tag{4.4.50}$$

$$\frac{\partial D_{f_q}}{\partial \alpha_n} = \frac{1}{2} \left(h_{n-1} - h_{n+1} \right) \tag{4.4.51}$$

$$\frac{\partial D_{f_q}}{\partial \varepsilon_n^p} = \frac{1}{2} \left(\alpha_{n+1} - \alpha_{n-1} \right) \frac{\partial h_n}{\partial \varepsilon_n^p} \tag{4.4.52}$$

$$\frac{\partial D_{f_q}}{\partial \Delta\gamma_n} = 0 \tag{4.4.53}$$

With the final required derivatives,

$$\frac{\partial h_n}{\partial \bar{\boldsymbol{u}}_n} = \frac{-\hat{d}_2\hat{d}_3 \exp\left(\hat{d}_3\eta_n\right)}{\left(\hat{d}_1 + \hat{d}_2 \exp\left(\hat{d}_3\eta_n\right)\right)^2}\left(\frac{\kappa}{V_e\sigma_{vm}}\left(\int_{\Omega_e} \boldsymbol{B}^u_{div}\, dV\right) - \frac{p_n\sqrt{6}\mu}{\sigma^2_{vm}}\frac{\boldsymbol{s}_n}{||\boldsymbol{s}_n||} : \boldsymbol{B}^u\right) \tag{4.4.54}$$

$$\frac{\partial h_n}{\partial \boldsymbol{\varepsilon}^p_n} = \frac{-\hat{d}_2\hat{d}_3 \exp\left(\hat{d}_3\eta_n\right)}{\left(\hat{d}_1 + \hat{d}_2 \exp\left(\hat{d}_3\eta_n\right)\right)^2}\left(\frac{p_n\sqrt{6}\mu}{\sigma^2_{vm}}\frac{\boldsymbol{s}_n}{||\boldsymbol{s}_n||}\right) \tag{4.4.55}$$

$$\tag{4.4.56}$$

Sensitivity verification

In order to verify the sensitivity calculation previously outlined, we employ the portal frame geometry with dimensions and boundary conditions illustrated in Figure 4.6. Figure 4.4 illustrates the non-uniform density field and element numbering scheme. The finite element mesh consists of 880 quadrilateral elements and a filter radius of 2.75mm ($r_{min} = 2.75mm$, approximately 3 times the element size). The elastoplastic analysis consisted of a prescribed downward displacement of 1.0mm (i.e. $L_y \rightarrow \bar{u}_y = -1.0mm$), while the linear elastic buckling analysis was carried out with a downward traction load of $1000\frac{N}{mm}$ with assumed unit thickness (i.e. $L_y \rightarrow \boldsymbol{t} = [0, -1000]\frac{N}{mm}$). The SIMP penalization parameters are set to $p = 2$ and $q = 1.5$, while the projection parameter β is set to 2.0. We set D_{max} equal to 0.1 and take 50 equally spaced time-increments in the elastoplastic forward analysis.

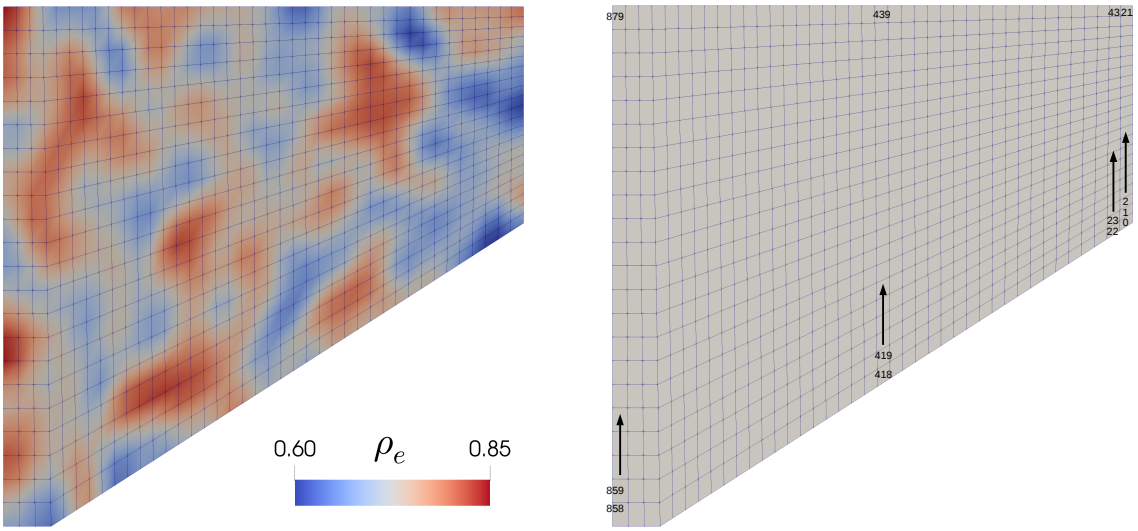

(a) (b)

Figure 4.4: Sensitivity verification problem (a) non-uniform density field and (b) element numbering.

The sensitivities are verified via a typical central difference approximation for each of the 4 functions used during the optimization procedure. Namely, for a function, $f(\rho_1, \ldots, \rho_e, \ldots, \rho_N)$, we have,

$$\frac{\partial f}{\partial \rho_e} \approx \frac{f(\rho_1, \ldots, \rho_e + \Delta\rho, \ldots, \rho_N) - f(\rho_1, \ldots, \rho_e - \Delta\rho, \ldots, \rho_N)}{2\Delta\rho} \tag{4.4.57}$$

where we have used $\Delta\rho = 10^{-5}$. The comparison is made in Figure 4.5 via numerical and analytical sensitivities computed for all 880 elements in the finite element mesh. The subplots of the relative error demonstrate the accuracy of the sensitivity analysis.

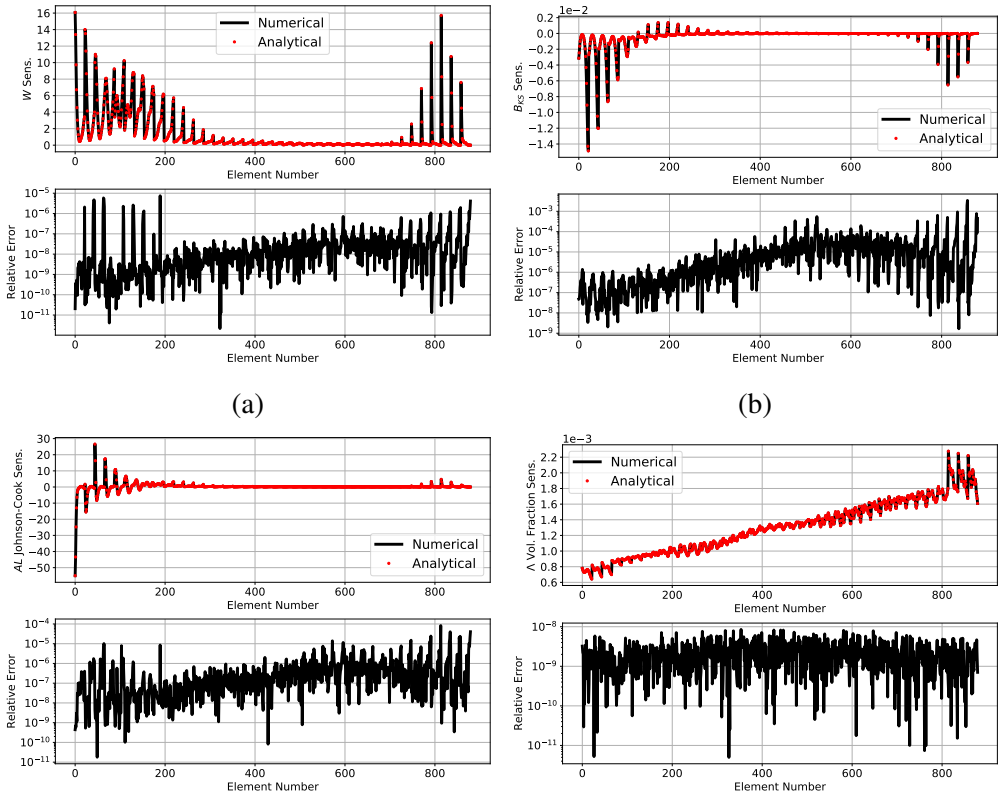

Figure 4.5: Analytical vs. numerical sensitivity verification for all 4 relevant functions.

4.5 Ductile phase field fracture model used for design verification

A verification step is completed after optimization in order to more accurately approximate the performance of the optimized structures. Since a small strain formulation without explicit failure modeling is used during the optimization procedure, we employ a large deformation, ductile phase field fracture model in order to better predict the actual structural responses and compare their characteristics. A similar formulation to the one proposed in Borden et al. [90] is employed herein, where we have omitted inertial forces and used a mean-dilatation technique for volumetric locking in place of the higher-order basis functions used the aforementioned work. This particular model is chosen for the post-optimization verification evaluation since it incorporates the stress triaxiality in the fracture driving force (which is critical in the context of ductile failure as was shown in [196]).

In this section we provide a very brief summary of the formulation and detail a few minor

changes to the model that we have employed. For the sake of brevity, the reader is referred to [90] for details regarding the return mapping algorithm and the derivation of the governing equations while we provide a few highlights below for convenience.

Starting from the multiplicative split of the deformation gradient into elastic and plastic parts (i.e. $\boldsymbol{F} = \boldsymbol{F}^e \boldsymbol{F}^p$), the hyperelastic response is governed by a stored elastic energy per unit volume of the form, $W(\Theta, \bar{\boldsymbol{C}}, \boldsymbol{C}^p) = U(\Theta) + \bar{W}(\bar{\boldsymbol{C}}, \boldsymbol{C}^p)$. The volumetric strain energy density is defined as

$$U(\Theta) = \frac{\kappa}{2}\left(\frac{1}{2}\left(\Theta^2 - 1\right) - \ln\left(\Theta\right)\right) \tag{4.5.1}$$

where κ is the bulk modulus and Θ is the volume-like independent variable used in the mean dilatation formulation [190]. The isochoric component of the strain energy density is

$$\bar{W}(\bar{\boldsymbol{C}}, \boldsymbol{C}^p) = \frac{\mu}{2}\left(\bar{\boldsymbol{C}} : \boldsymbol{C}^{p^{-1}} - 3\right) \tag{4.5.2}$$

where μ is the shear modulus, $\bar{\boldsymbol{C}} = J^{-2/3}\boldsymbol{F}^T\boldsymbol{F}$ is the isochoric right Cauchy-Green tensor, and $\boldsymbol{C}^p = \boldsymbol{F}^{p^T}\boldsymbol{F}^p$ is the plastic right Cauchy-Green tensor. We represent the phase field by the variable $c \in [0, 1]$ in which $c = 0$ corresponds to undamaged material and $c = 1$ corresponds to fully damaged material. Consistent with the aforementioned work, we use the cubic degradation function,

$$g(c) = (1 - k_e)\left((s-2)(1-c)^3 + (3-s)(1-c)^2\right) + k_e \tag{4.5.3}$$

where k_e is a small residual stiffness parameter for the fully broken (i.e. $c = 1$) material and s controls the initial slope of the degradation function. A value of $s = 10^{-4}$ is used along with $k_e = 10^{-6}$. The degradation function is used to form the damaged strain energy density, $\hat{W}$, which

is split into parts corresponding to tensile and compressive components.

$$\hat{W}(\Theta, \bar{\boldsymbol{C}}, \boldsymbol{C}^p) = g(c)W^+(\Theta, \bar{\boldsymbol{C}}, \boldsymbol{C}^p) + W^-(\Theta) \tag{4.5.4}$$

$$W^+(\Theta, \bar{\boldsymbol{C}}, \boldsymbol{C}^p) = \begin{cases} U(\Theta) + \bar{W}(\bar{\boldsymbol{C}}, \boldsymbol{C}^p) & \text{if } \Theta \geq 1 \\ \bar{W}(\bar{\boldsymbol{C}}, \boldsymbol{C}^p) & \text{otherwise} \end{cases} \tag{4.5.5}$$

$$W^-(\Theta) = \begin{cases} 0 & \text{if } \Theta \geq 1 \\ U(\Theta) & \text{otherwise} \end{cases} \tag{4.5.6}$$

The Kirchoff stress may then be obtained via derivatives of the energy density expressions and appropriate push-forward operations to obtain,

$$\boldsymbol{\tau}^+_{vol} = \begin{cases} J^e p \boldsymbol{I} & \text{if } \Theta \geq 1 \\ \boldsymbol{0} & \text{otherwise} \end{cases} \tag{4.5.7}$$

$$\boldsymbol{\tau}^+_{dev} = \mu \mathbb{P}_{dev} : \bar{\boldsymbol{b}}^e \tag{4.5.8}$$

$$\boldsymbol{\tau}^- = \begin{cases} \boldsymbol{0} & \text{if } \Theta \geq 1 \\ J^e p \boldsymbol{I} & \text{otherwise} \end{cases} \tag{4.5.9}$$

$$\boldsymbol{\tau} = \overline{g(c)}\boldsymbol{\tau}^+_{vol} + g(c)\boldsymbol{\tau}^+_{dev} + \boldsymbol{\tau}^- \tag{4.5.10}$$

where $J^e = \det \boldsymbol{F}^e$, p is the pressure stress, $\bar{\boldsymbol{b}}^e = J^{e^{-2/3}} \boldsymbol{F}^e \boldsymbol{F}^{e^T}$ is the isochoric elastic left Cauchy-Green tensor, and $\overline{g(c)}$ is the volume average of the degradation function within a given finite element, Ω^e_0, in the reference configuration (note this arises due to the use of the mean dilatation formulation). In an analogous manner to the small strain mean dilatation method outlined in Section

4.2, the pressure (p) and volume-like variable (Θ) are ultimately computed using

$$\Theta = \frac{1}{V_0^e} \int_{\Omega_0^e} J \, dV_0 \tag{4.5.11}$$

$$p = U'(\Theta) = \frac{\kappa}{2}\left(\Theta - \frac{1}{\Theta}\right) \tag{4.5.12}$$

$$\overline{g(c)} = \frac{1}{V_0^e} \int_{\Omega_0^e} g(c) \, dV_0 \tag{4.5.13}$$

since $J = \det \boldsymbol{F} = J^e$ due to isochoric plastic flow (i.e. $\det \boldsymbol{F}^p = 1$). Note we have distinguished the volume of finite element Ω_0^e in the reference configuration with the notation V_0^e.

The weak form of the governing equations over a single element, neglecting inertial effects and surface tractions, and using a standard backward Euler incremental integration scheme with the increment number indicated by the subscript $(\cdot)_n$, may be expressed as,

$$\int_{\Omega_0^e} \boldsymbol{\tau}_n : \left(\nabla_0 \delta \boldsymbol{u} \cdot \boldsymbol{F}_n^{-1}\right) \, dV_0 = 0 \tag{4.5.14}$$

$$\begin{aligned} &\int_{\Omega_0^e} \left(\eta_v \frac{c_n - c_{n-1}}{\Delta t} + \frac{G_c}{2l_0} c_n \, \delta c + 2G_c l_0 \nabla_0 c_n \cdot \nabla_0 \delta c\right) \, dV_0 = \\ &\qquad \int_{\Omega_0^e} \left(g'(c_n) W^+ + g_p'(c_n) \left\langle W_p - W_0 \right\rangle\right) \delta c \, dV_0 \end{aligned} \tag{4.5.15}$$

where the artificial numerical viscosity of Miehe [22] is included in the phase field equation. Note that a few key parameters have been introduced and ∇_0 refers to the gradient with respect to the reference configuration. The parameter η_v represents the artificial viscosity, G_c is the critical fracture energy, l_0 is the phase field length scale parameter which governs the width of the diffuse approximation of the sharp crack surface, δc is the test function associated with the phase field equation, and W_p is the effective plastic work contributing to fracture with a threshold parameter, W_0. Note we have also used the notation $\langle x \rangle = (x + |x|)/2$.

There are two additional key features of the formulation that we should mention here. The first is the existence of the plastic degradation function, $g_p(c)$, which degrades the radius of the yield

surface with yield function,

$$f\left(\boldsymbol{s},\alpha\right) = ||\boldsymbol{s}|| - g_p(c)\sqrt{\frac{2}{3}}\sigma_y \tag{4.5.16}$$

where the yield stress, σ_y, takes the same form introduced in Section 4.2. We take the same cubic degradation function for $g_p(c)$ as the one defined in Equation (4.5.3) with the exception that k_e is set to 10^{-3} in order to mitigate excessive mesh distortion in near completely degraded elements (i.e. elements with $c \approx 1$) by allowing the pseudo-deformation to be compressible hyperelasticity rather than isochoric plasticity.

The second key feature of the model is the definition of the effective plastic work density rate which is modified to include the effect of the stress triaxiality,

$$\dot{W}_p = \dot{\gamma}\frac{||\boldsymbol{s}||}{\phi} \tag{4.5.17}$$

$$\phi(p,\boldsymbol{s}) = d_1 + d_2\exp\left(d_3\frac{p}{||\boldsymbol{s}||}\right) \tag{4.5.18}$$

where the pressure (p) was previously defined in Equation (4.5.12), $\dot{\gamma}$ is the plastic multiplier rate for the model, and the variables (d_1,d_2,d_3) are parameters to be calibrated to the specific material behavior. Also notice that with respect to the parameters in Equation (4.2.21), the hat, $\hat{(\cdot)}$, has been removed to emphasize that they are distinct.

Finally, we provide the material parameters used for all subsequent examples in this chapter. The elastoplastic parameters provided in Table 4.1 are used in both the small strain formulation during the optimization procedure and in the large strain ductile failure model outlined in this section. The parameters associated with the phase-field fracture formulation are provided in Table 4.2. The selection of these parameters is briefly discussed in B.2.2.

Table 4.1: Elastoplasticity model parameters

$E\ [MPa]$	ν	$\sigma_{y_0}\ [MPa]$	$H\ [MPa]$	$Y_\infty\ [MPa]$	δ
74633.0	0.3	344	95.42	268.8	9.996

Table 4.2: Fracture model parameters

η_v	$G_c\ \left[kJ/mm^2\right]$	$l_0\ [mm]$	$W_0\ \left[\frac{N \cdot mm}{mm^3}\right]$	d_1	d_2	d_3
$5(10^{-3})$	108	0.25	200	0.193	8.592	-4.630

4.6 Numerical examples

Three numerical examples demonstrating an array of different results are presented. The forward analyses and sensitivity computations were implemented in an in-house code, developed using the deal.II [207] C++ finite element library in a massively parallel framework. The parallel linear algebra is carried out using Trilinos [208] for the analyses involving elastoplasticity and phase field fracture, while PETSc [209] is used along with SLEPc [210] in order to perform the linear elastic solution and subsequent buckling eigenanalysis. Once the sensitivities are obtained, an in-house developed C++ code is used to perform the update of the design variables using the method of moving asymptotes (MMA) [183] , in which the subproblem is solved efficiently using IPOPT [171]. Default MMA parameters are used with the exception of the *move* limit which is set to 0.1 [211].

For each example, four different optimized geometries are obtained for comparison where we describe the notation used to refer to each design in Table 4.3. When buckling analysis is not included in an optimization problem, the linear elastic equilibrium and eigenvalue problem constraints present in Equation (4.4.10) are omitted. The values of the weights ($\{\omega_i\}$) in Equation (4.4.10) are kept constant across examples. Note that these values have been empirically found to

work well for the examples studied herein, however they may need to be adjusted for other problems. We elaborate further on our selection rationale for the interested reader in Remark 4.6 below.

Table 4.3: Short hand notation for each optimized geometry detailing what is included in the objective function with ω weights corresponding to those shown in Equation (4.4.10).

Design	Work (W)	Buckling (B_{KS})	Local Failure Constraints (AL)
W	YES ($\omega_1 = 100$)	NO ($\omega_2 = 0$)	NO ($\omega_3 = 0$)
WF	YES ($\omega_1 = 100$)	NO ($\omega_2 = 0$)	YES ($\omega_3 = 1$)
WB	YES ($\omega_1 = 100$)	YES ($\omega_2 = 20$)	NO ($\omega_3 = 0$)
WBF	YES ($\omega_1 = 100$)	YES ($\omega_2 = 20$)	YES ($\omega_3 = 1$)

In addition to these items, it is important to explicitly mention that, as with most topology optimization problems, the designs are load dependent. This of course makes sense for a nonlinear problem, but also is valid for linear elastic topology optimization with stress constraints. Briefly, we have selected a strategy for determining both the displacement load in the elastoplastic analyses and the traction load applied at the same location for the linear analyses regarding buckling. In the case of the displacement loading used during the elastoplastic analyses, we apply a total displacement load such that the failure measure, D_f, is approximately a value of 1 at some location in the domain (i.e. indicating failure) for the **W** design. This provides a direct method for selecting a displacement-based loading. Additionally, it allows us to limit our scope to observe the effect of the ductile failure constraints with a single upper bound for all examples presented. In other words, when activating the local ductile failure constraints, we only consider a single upper bound $D_{max} = 0.3$ in all cases. Due to this, it is important to have a standard method of selecting the applied displacement loading. Also, note that while we allow adaptive time-stepping to take place, typically 50 evenly spaced time-increments are sufficient for the elastoplastic analyses. This minimum number of steps is enforced in order to ensure the total work and failure measures are integrated with sufficient accuracy. Additionally, the design variables of elements with nodes that are subject to the external loading are fixed at 1 and are not optimized.

The traction loading applied in the linear elastic analyses is evenly distributed over the same

boundary as the aforementioned displacement-based loading in the elastoplastic analyses. We select a traction magnitude such that the first eigenvalue μ_1, is roughly on the order of 0.1-1.0 at the beginning of the optimization procedure. This selection keeps the magnitude of the B_{KS} function comparable across examples. Lastly, we set the aggregation parameter $\xi_{ks} = 50$ since more weight is placed on the lower buckling load factors as is usually desired. Finally we define a few quantities in Table 4.4 that are subsequently used as comparative metrics.

Table 4.4: Notation and explanations of metrics provided in the results tables for each numerical example. LSPFM stands for the large strain phase field fracture model detailed in Section 4.5, while SSM refers to the small strain model described in Section 4.2 and used during the optimization procedure. Note that "optimization load" refers to the displacement applied during the elastoplastic analyses of the optimization problem.

Notation	**Explanation**
$W^S_{\bar{\boldsymbol{u}}}$	Work predicted up to optimization load ($\bar{\boldsymbol{u}}$) using SSM
$W^L_{\bar{\boldsymbol{u}}}$	Work predicted up to optimization load ($\bar{\boldsymbol{u}}$) using LSPFM
F^L_{max}	Peak load predicted using LSPFM
$W^L_{F_{max}}$	Work predicted up to peak load F^L_{max} using LSPFM
Failure Mode	Structural failure mode predicted using LSPFM (either *Fracture* or *Buckling*)

Remark. There are likely many strategies for choosing the weighting parameters $\{\omega_i\}$, however here we briefly mention our own rationale. The part of the Augmented Lagrangian function associated with the failure constraints eventually has a magnitude less than 1 when the constraints are nearly satisfied. Fixing this weight (ω_3) to be 1, we examine the other two. Since the work is the physical objective, we place a relatively high weight (e.g. $\omega_1 = 100$) on this function in order to increase its importance to the optimizer. Selecting a weight that is too large, however, would diminish the drive to satisfy the failure constraints. We have empirically found a value of 100 to strike an effective balance for the examples we have studied. With regard to buckling, only enough resistance is

needed to prevent structural buckling from preceding ductile failure. Selecting ω_2 too low may not provide any substantial structural modification for compressive members, whereas selecting a value too high could make buckling resistance "more important" than the work objective. We achieve an effective balance by setting ω_2 equal to 20% of ω_1.

4.6.1 Portal frame

The first example is the portal frame geometry with dimensions and boundary conditions illustrated in Figure 4.6. Note that symmetry is employed to decrease the mesh size. In general this should be done with care since some buckling modes might not be captured, although we have not encountered this issue in this particular example. The finite element mesh consists of 41,839 quadrilateral elements, 42,272 nodes, and a filter radius of 1mm is used ($r_{min} = 1mm$, approximately 6 times the average element size). The elastoplastic analysis includes a prescribed downward displacement of 1mm (i.e. $L_y \rightarrow \bar{u}_y = -1.0mm$), while the linear elastic buckling analysis is carried out with a downward traction load of $1000\frac{N}{mm}$ with assumed unit thickness (i.e. $L_y \rightarrow \boldsymbol{t} = [0, -1000]\frac{N}{mm}$). The four optimization problems summarized in Table 4.3 are then

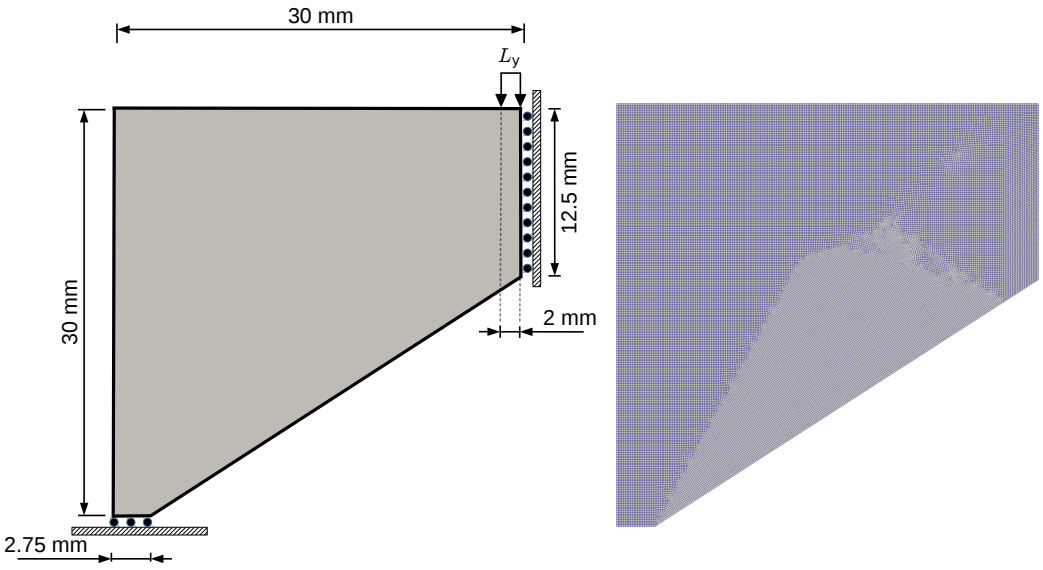

(a) (b)

Figure 4.6: Portal frame geometry, boundary conditions, and finite element mesh. The applied load is distributed over 15 elements.

performed with an upper bound on the volume fraction of $\Lambda_{max} = 0.4$. As mentioned previously, although during the optimization the local ductile failure constraints were imposed for the **WF** and **WBF** designs in order to provide the ductile failure resistance, the large deformation ductile phase field fracture formulation outlined in Section 4.5 is used to simulate failure for all of the optimized topologies. These simulations are conducted via extraction of the resulting topology via the $\rho = 0.5$ level set using a part of the PLATO code, maintained and developed by Sandia National Laboratories [212]. This can also be achieved using the open source software described in [2]. The resulting STL file is remeshed with a mesh density such that the average element size (h) is smaller than the phase field length scale parameter (l_0) divided by 3. Care is also taken to ensure a sufficient number of elements through the thickness of thin members in order to accurately capture buckling behavior.

The resulting topologies and failure simulation results are provided in Figure 4.8. The data described in Table 4.4 is provided for this example in Table 4.5 with the associated force versus displacement curves shown in Figure 4.7. While there are many interesting features of the designs and their performance, here we highlight a few key results. First we notice that the **W** and **WF** designs both buckle at roughly the same loading point with subsequent load capacity decrease. Additionally, they follow roughly the same subsequent load path. However, while the **WB** design does not buckle, it does experience a clear ductile fracture at the re-entrant corner of the design at a relatively low level of applied displacement. This is accompanied by a modest increase in load carrying capacity but a noticeable decrease in the work required to achieve the peak load. In stark contrast, the **WBF** design does not only withstand the largest peak load, but also requires a much higher level of work to reach the peak load than the other three designs. This clearly demonstrates that for some boundary value problems, it is important to consider both buckling and ductile failure constraints in the design procedure. With regard to load carrying capacity, it is interesting to note that for this structure, using the calibrated elastoplastic model for Aluminum 2024-T351, the peak load capacity does not increase by a large percentage in any case (i.e. we predict a peak load increase of approximately 5.2%). Larger gains might be expected for a material

with more significant hardening characteristics as the plastic strain increases. For the aluminum material employed, the hardening modulus decreases by a factor of 20 with increased plastic strain which results in a loss of stiffness in heavily loaded regions. The same trend is obviously not observed for the work required achieve the peak load which is greatly affected by the formulation for this example with a maximum increase of approximately 270%. It is also notable that both the peak load and external work required are largest for the design resulting from the **WBF** formulation which included both the buckling function and failure constraints during optimization.

Additionally, the total work at the load used during the optimization is also provided in Table 4.5 using both the small and large deformation formulations to demonstrate the appropriateness of using the small deformation formulation during the optimization procedure. The work is generally over-estimated by the small strain formulation due to the under-prediction of plastic strains but appears to be within reasonable limits.

Table 4.5: Portal frame results. Force units (N). Work units ($N \cdot mm$). The metrics presented are defined in Table 4.4.

Design	$W^S_{\tilde{\boldsymbol{u}}}$	$W^L_{\tilde{\boldsymbol{u}}}$	F^L_{max}	% Increase	$W^L_{F_{max}}$	% Increase	Failure Mode
W	1076	1030	1447	0.98	772	8.73	Buckling
WF	1071	1022	1433	-	710	-	Buckling
WB	1033	1009	1462	2.02	1393	96.20	Fracture
WBF	1020	998	1508	5.23	2631	270.56	Fracture

Finally, we provide the optimization function histories in Figure 4.9 to highlight the associated changes in magnitude of particular functions due in part to the continuation schemes employed. It is clear from the plots that the volume fraction constraint is active ($\Lambda = 0.4$ for every design) and that the AL function value at the end of the optimization is very small in magnitude, indicating that the local ductile failure constraints are satisfied when included in the optimization formulation ($\max D_{f_q} = 0.307$ for **WF** and $\max D_{f_q} = 0.303$ for **WBF**). The aggregate objective function history is also shown with constant scale factors, W^{scale} and B^{scale}_{KS}, set equal to their final values for each design. Lastly, we note that the computational cost for this example ranged from 13.2 hours

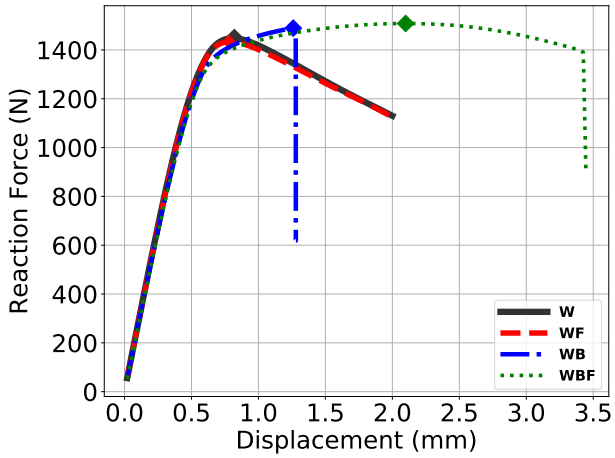

Figure 4.7: Portal frame force vs. displacement curves. Note that a diamond marker signifies the peak load point for each design.

(500 iterations for the **W** design) to 22.5 hours (700 iterations for the **WBF** design) running on 8 processor cores of a 2019 MacBook Pro laptop with an Intel Core i9 processor and 32 GB of RAM.

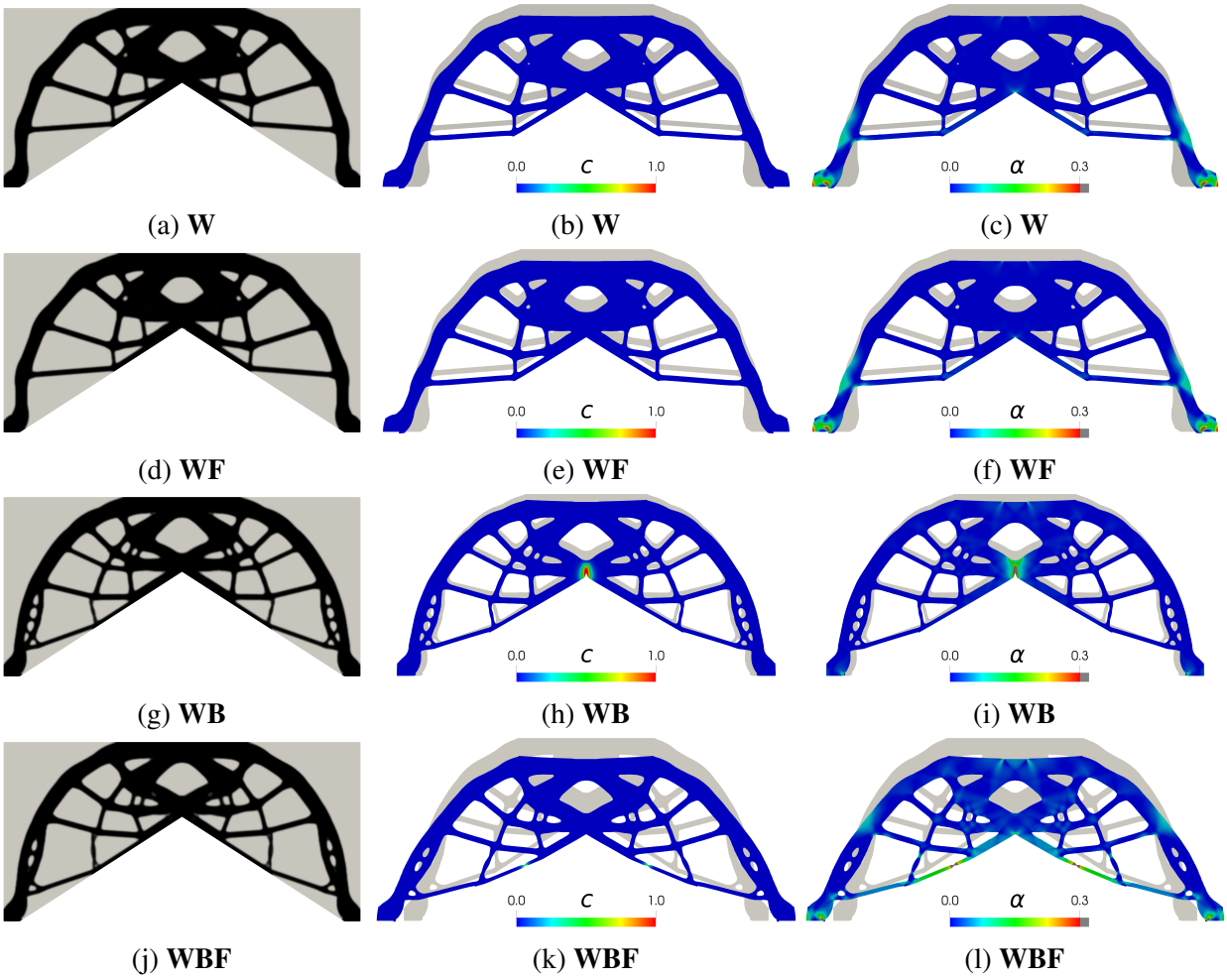

(a) **W** (b) **W** (c) **W**

(d) **WF** (e) **WF** (f) **WF**

(g) **WB** (h) **WB** (i) **WB**

(j) **WBF** (k) **WBF** (l) **WBF**

Figure 4.8: Portal frame results. Left column illustrates the topology, middle column illustrates the phase field contours on the final deformed configuration with the undeformed configuration placed in light gray behind it for reference. A similar set of plots is provided in the last column with the contours of the equivalent plastic strain.

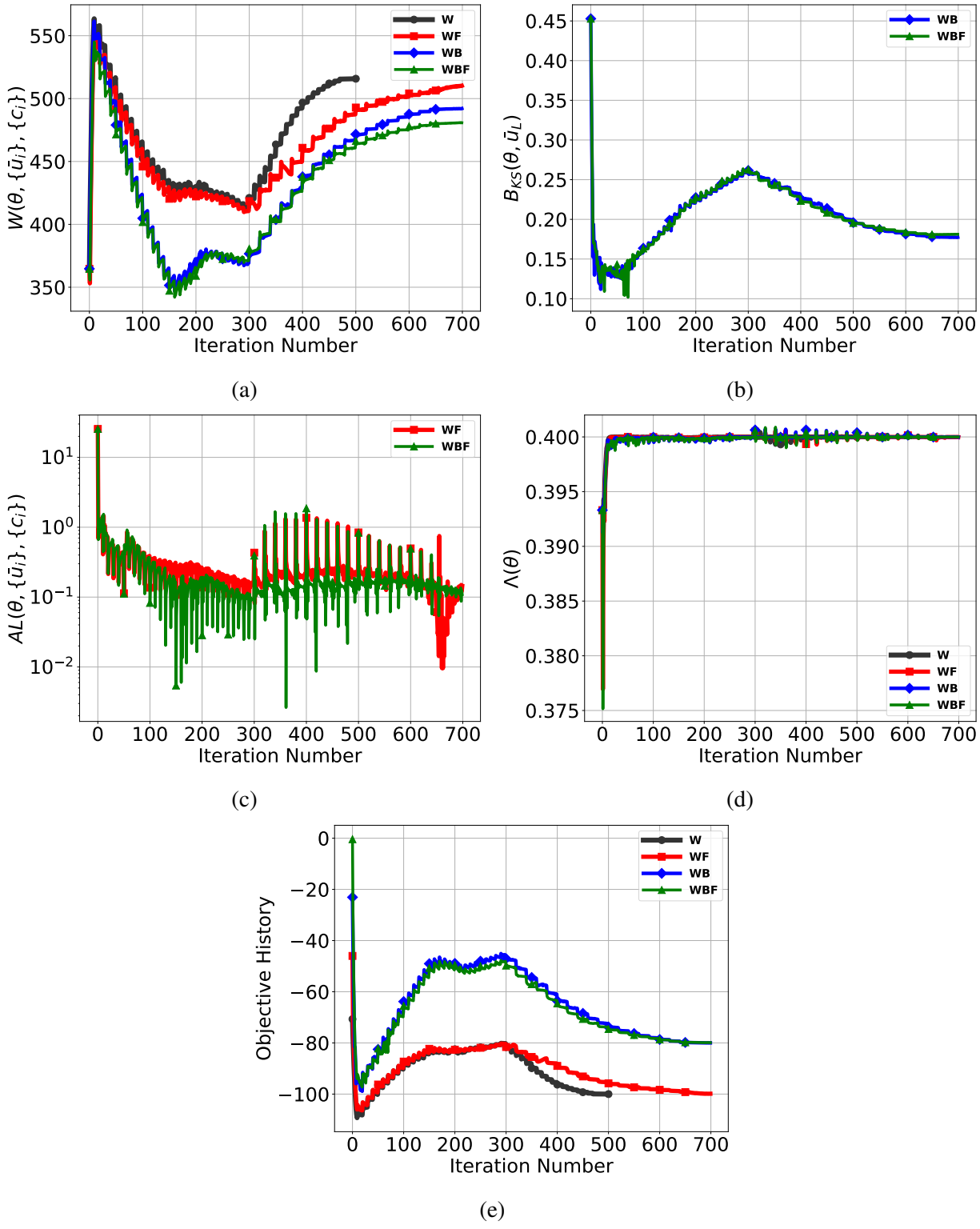

Figure 4.9: Portal frame optimizer convergence history. Note that the **W** design is stopped at 500 iterations due to rapid convergence.

4.6.2 Cantilever beam

Next we study the cantilever geometry with dimensions and boundary conditions illustrated in Figure 4.10. The finite element mesh consists of 35,511 quadrilateral elements, 35,912 nodes, and a filter radius of 0.5mm is used ($r_{min} = 0.5mm$, approximately 6 times the element size). The elastoplastic analysis consists of a prescribed downward displacement of 1mm (i.e. $L_y \rightarrow \bar{u}_y = -1.0mm$), while the linear elastic buckling analysis is carried out with a downward traction load of $3000\frac{N}{mm}$ with assumed unit thickness (i.e. $L_y \rightarrow \boldsymbol{t} = [0, -3000]\frac{N}{mm}$). Similar to the previous

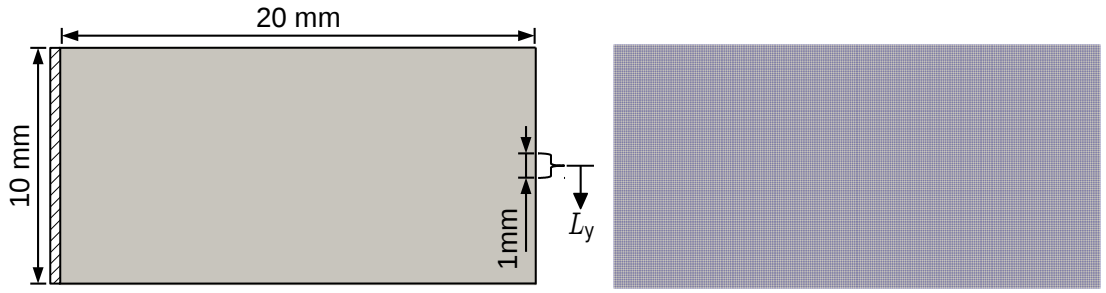

(a) (b)

Figure 4.10: Cantilever beam geometry, boundary conditions, and finite element mesh. The applied load is distributed over 13 elements.

example, after all four designs are obtained, they are extracted via the 0.5 density level-set, re-meshed, and analyzed using the large deformation ductile phase field fracture model. The optimized topologies, failure configurations, and plastic strain fields are illustrated in Figure 4.11, while the previously computed metrics are provided in Table 4.6. The associated force versus displacement curves are illustrated in Figure 4.12. Again, the total work computed up to the displacement load imposed during the optimization iterations is comparable between small and large deformation formulations as evidenced by the data in Table 4.6. With regard to load carrying capacity, we note the peak load capacity increase of approximately 15.4% for the **WBF** design. The increase in the external work to reach the peak load results in an incredible maximum percent increase of 899% with the largest being that of the **WBF** design and the smallest being that of the **WF** design. It is very interesting that simply including only the ductile failure constraints (i.e. the **WF** design) can result in such a drop in performance with respect to the **W** design, which only maximizes the work.

Table 4.6: Cantilever beam results. Force units (N). Work units ($N \cdot mm$). The metrics presented are defined in Table 4.4.

Design	$W^S_{\tilde{\boldsymbol{u}}}$	$W^L_{\tilde{\boldsymbol{u}}}$	F^L_{max}	% Increase	$W^L_{F_{max}}$	% Increase	Failure Mode
W	326	322	425	8.97	575	266.24	Buckling
WF	322	309	390	-	157	-	Buckling
WB	316	312	429	10.00	990	530.57	Fracture
WBF	303	301	450	15.38	1568	898.73	Fracture

This is quite a critical observation for practicing designers.

Finally, we provide the optimization function histories in Figure 4.13. Again, the volume fraction constraint is active ($\Lambda = 0.4$ for every design) and the AL function value at the end of the optimization is very small in magnitude, indicating sufficient satisfaction of the local ductile failure constraints ($\max D_{f_q} = 0.309$ for **WF** and $\max D_{f_q} = 0.284$ for **WBF**). Consistent with the previous example, the aggregate objective function history is also illustrated with constant scale factors, W^{scale} and B^{scale}_{KS}, set equal to their final values for each design. The computational cost for this example ranged from 10.7 hours (500 iterations for the **W** design) to 18.8 hours (700 iterations for the **WBF** design) running on 8 processor cores of a 2019 MacBook Pro laptop with an Intel Core i9 processor and 32 GB of RAM.

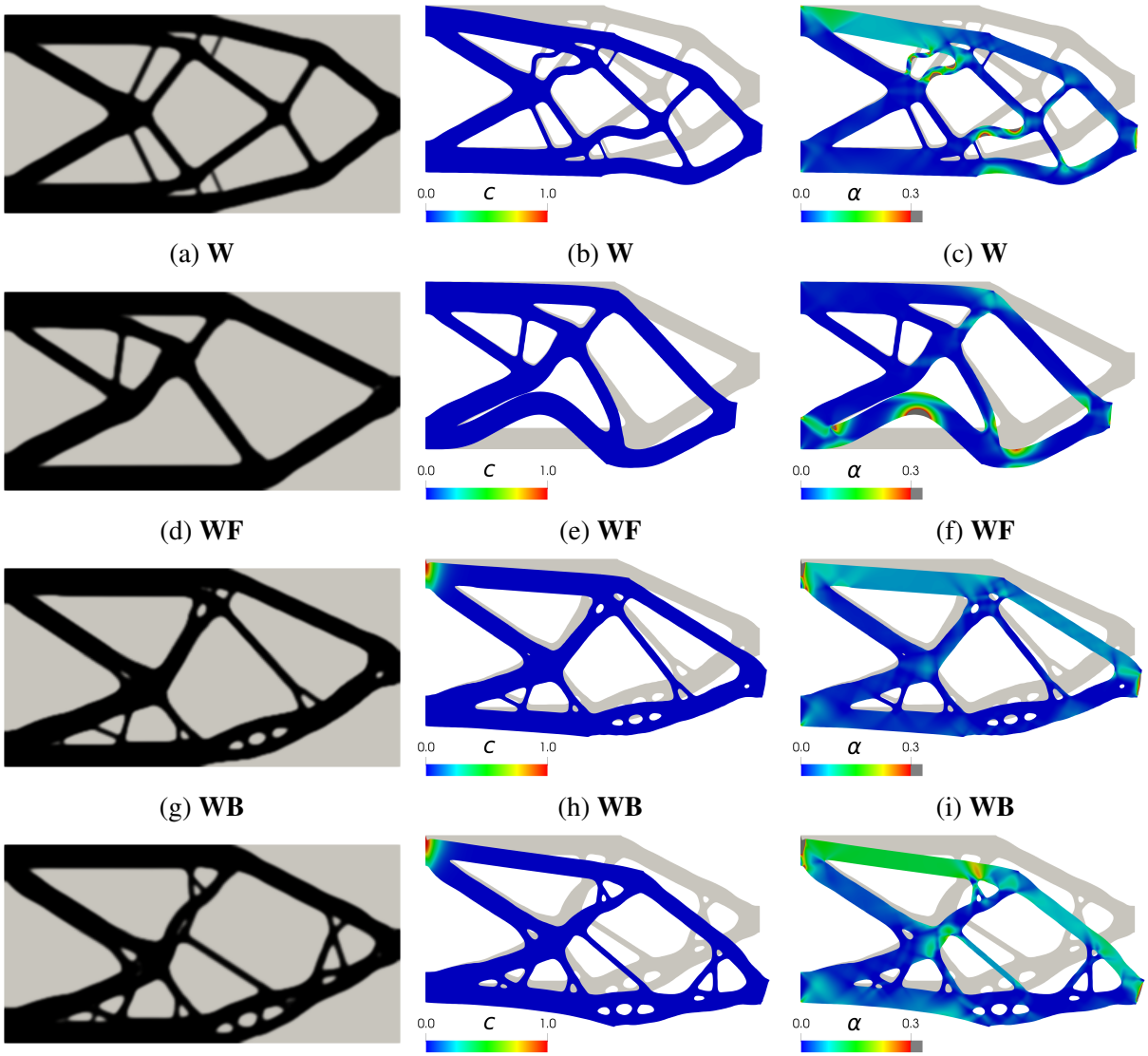

(a) **W** (b) **W** (c) **W**

(d) **WF** (e) **WF** (f) **WF**

(g) **WB** (h) **WB** (i) **WB**

(j) **WBF** (k) **WBF** (l) **WBF**

Figure 4.11: Cantilever beam results. Left column illustrates the topology, middle column illustrates the phase field contours on the final deformed configuration with the undeformed configuration placed in light gray behind it for reference. A similar set of plots is provided in the last column with the contours of the equivalent plastic strain.

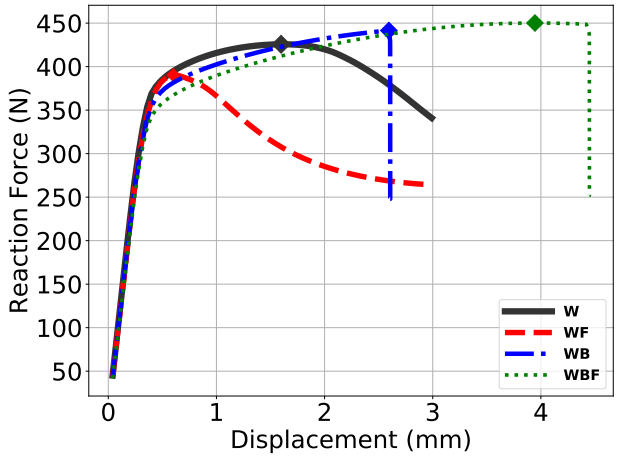

Figure 4.12: Cantilever force vs. displacement curves. Note that a diamond marker signifies the peak load point for each design.

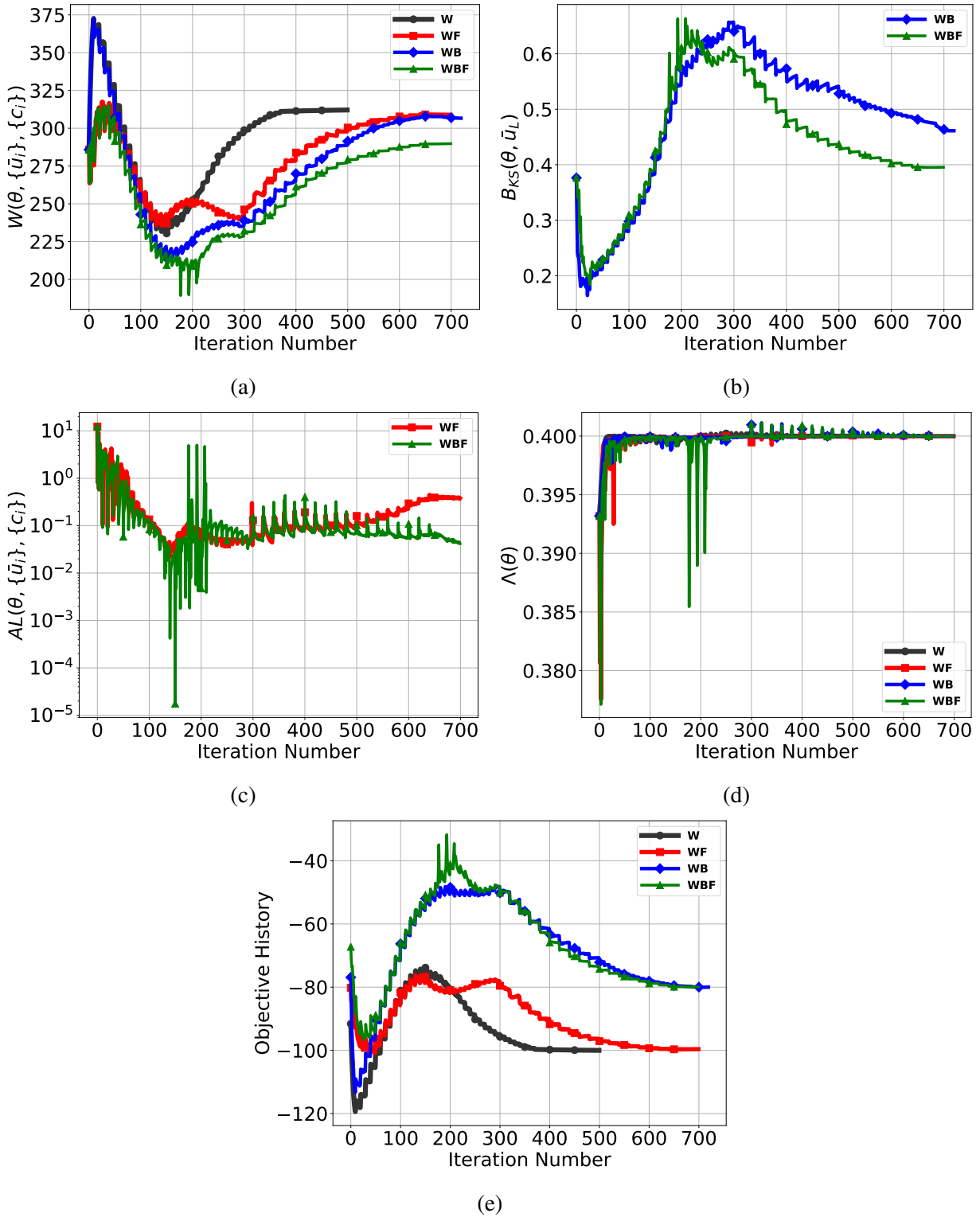

Figure 4.13: Cantilever optimizer convergence history. Note that the **W** design is stopped at 500 iterations due to rapid convergence, and we allow 20 additional iterations for the **WB** design to ensure convergence.

4.6.3 L-bracket

Finally, the L-bracket geometry with dimensions and boundary conditions illustrated in Figure 4.14 is studied. The finite element mesh consists of 27,680 quadrilateral elements, 28,107 nodes, and a filter radius of 0.75mm is used ($r_{min} = 0.75mm$, approximately 4 times the element size). The elastoplastic analysis consists of a prescribed downward displacement of 4mm (i.e. $L_y \rightarrow \bar{u}_y = -4.0mm$), while the linear elastic buckling analysis is carried out with a downward traction load of $2000\frac{N}{mm}$ with assumed unit thickness (i.e. $L_y \rightarrow \boldsymbol{t} = [0, -2000]\frac{N}{mm}$). An identical

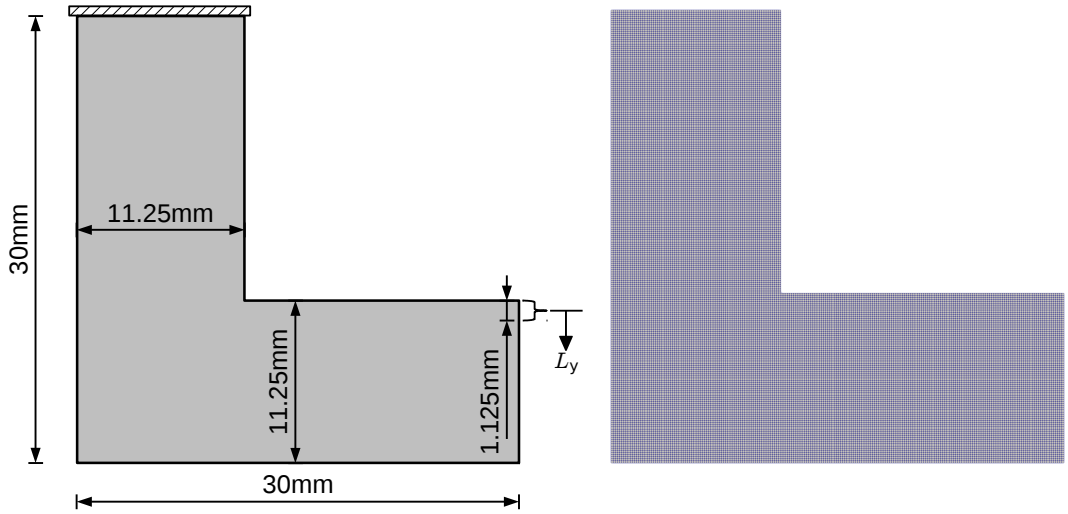

Figure 4.14: L-bracket geometry, boundary conditions, and finite element mesh. The applied load is distributed over 8 elements.

verification procedure was followed similar to the two previously outlined examples with optimized topologies, deformed shapes, and plastic strain distributions provided in Figure 4.16. The work done by the displacement load applied during the optimization problem between the small and large displacement formulations is usually similar but differs slightly more than typical for two cases studied herein. This is due primarily to buckling which occurs for designs **W** and **WF** earlier in the loading history. With regard to load carrying capacity, we note the peak load capacity increase of approximately 6.5% including buckling only (i.e. the **WB** design). Additionally, a very considerable 491% increase was also observed in the work to failure of the **WB** design with respect to the **WF**

Table 4.7: L-bracket results. Force units (N). Work units ($N \cdot mm$). The metrics presented are defined in Table 4.4.

Design	$W^S_{\tilde{\boldsymbol{u}}}$	$W^L_{\tilde{\boldsymbol{u}}}$	F^L_{max}	% Increase	$W^L_{F_{max}}$	% Increase	Failure Mode
W	1266	1014	336	0.48	250	0.08	Buckling
WF	1261	990	334	-	250	-	Buckling
WB	1191	1157	356	6.52	1480	490.58	Fracture
WBF	1196	1163	353	5.56	1205	380.85	Fracture

design.

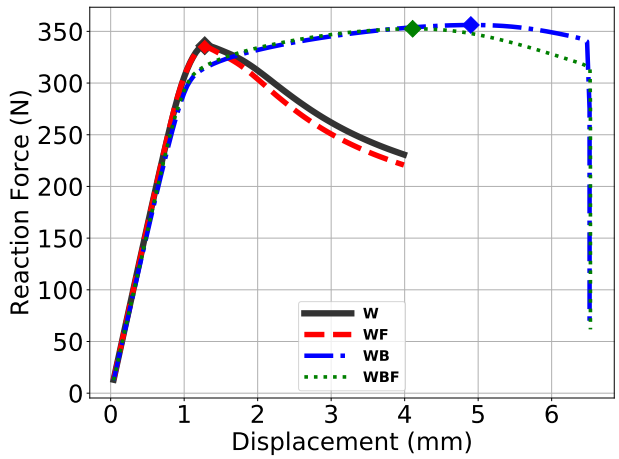

Figure 4.15: L-bracket force vs. displacement curves. Note that a diamond marker signifies the peak load point for each design.

We note also that the small deformation formulation is incapable of capturing the necking behavior which precedes failure for both the **WB** and **WBF** designs. While the **WBF** design has used additional material to support the re-entrant corner, this decision has resulted in a slightly thinner member which ultimately fails, leading to the load capacity performance increase of the **WB** design with respect to that of **WBF**. This occurs when members are subject to significant straining which may result in localization of plastic strains and/or necking. In this situation it may be possible to further improve our results by incorporating the large deformation kinematics during the optimization procedure. However, the large 491% gain in external work up to the peak load along with the 6.5% gain in the peak load observed with the **WB** design, highlights the potential

of this formulation in practical applications, even with the small strain kinematics used during the optimization process. Therefore, even in this example, our formulation has once again demonstrated the importance of including buckling resistance in the design procedure. Large strain kinematics may have allowed an improvement of the capacity of design **WBF** with respect to the **WB** design, but we will delay further exploration of these possibilities to future work.

Finally, we provide the optimization histories in Figure 4.17 for this example. It is clear from the plots that the volume fraction constraint is active ($\Lambda = 0.4$ for every design) and that the AL function value at the end of the optimization is very small in magnitude, indicating that the local ductile failure constraints are satisfied ($\max D_{f_q} = 0.273$ for **WF** and $\max D_{f_q} = 0.294$ for **WBF**). The aggregate objective function history is also shown with constant scale factors, W^{scale} and B_{KS}^{scale}, set equal to their final values for each design. The computational cost for this example ranged from 7.7 hours (500 iterations for the **W** design) to 14.2 hours (700 iterations for the **WBF** design) running on 8 processor cores of a 2019 MacBook Pro laptop with an Intel Core i9 processor and 32 GB of RAM.

4.7 Conclusion

An efficient framework for both ductile failure and buckling resistance in the context of structures subject to extreme loads inducing elastoplastic response was proposed and examples demonstrating its effectiveness were provided. This includes a new aggregate objective function, where local ductile failure constraints are enforced via an adaptation of the aggregation-free Augmented Lagrangian method. Additionally, buckling resistance was obtained via inclusion of an aggregation function of load factors resulting from a linear elastic buckling analysis in the aggregate objective function. All relevant function sensitivities were derived explicitly and verified numerically. The sensitivities of the aggregation function of load factors were used to provide the desired structural buckling resistance while only incurring the computational expense of an additional linear elastic problem with an associated eigenanalysis. Additionally, a new filter was proposed to remove highly localized pseudo-buckling modes in high density regions. Finally, the results obtained were evaluated using

a large deformation phase field fracture model in lieu of desired experimental testing of the final topologies. This served as a verification step which provided a more accurate estimate of the structural failure response, including both geometric and material nonlinearity with the important triaxiality effects accounted for in the failure analysis of metals. The model parameters were calibrated in a good-faith effort using the test data provided by other researchers for Aluminum 2024-T351, including the observed nonlinear hardening.

Three numerical examples were presented which demonstrate that the proposed formulation may not only result in increased structural strength (predicted percent increases between 5.2 and 15.4%), but also greatly increased structural toughness, as demonstrated by the large percent increases in the external work required to reach the peak load carrying capacity of the structure (predicted percent increases between 270 and 899%). As mentioned in Section 4.6.1, the authors also believe that larger gains in performance may be expected when constitutive properties for other metals with more significant hardening characteristics are employed.

Finally, we note our procedure highlights the importance of the verification step used herein with more complex failure and constitutive models. This is especially true when significantly simplified physics such as small strain kinematics and linear elasticity are used during the optimization process as is often the case in the literature.

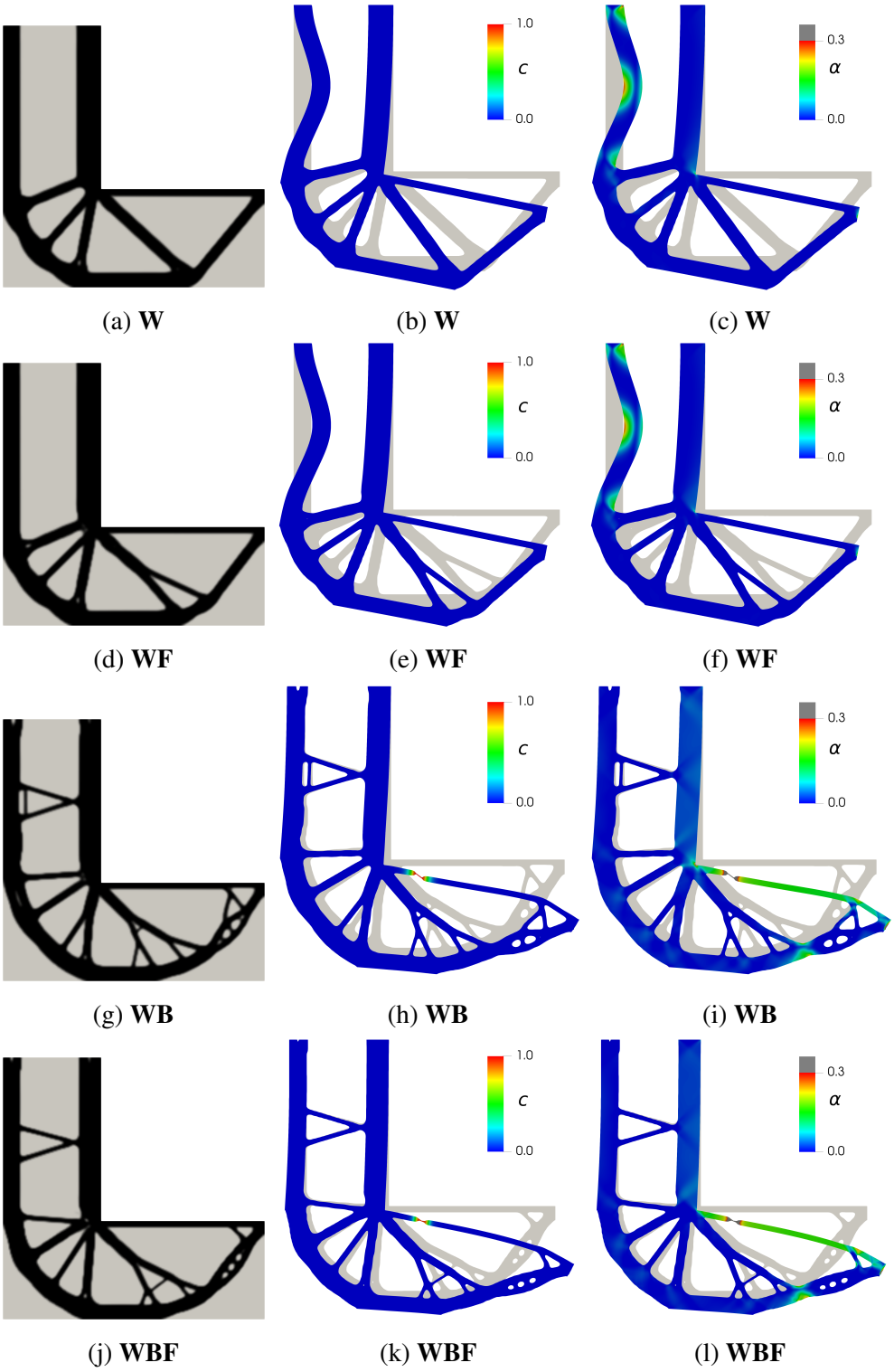

(a) **W** (b) **W** (c) **W**

(d) **WF** (e) **WF** (f) **WF**

(g) **WB** (h) **WB** (i) **WB**

(j) **WBF** (k) **WBF** (l) **WBF**

Figure 4.16: L-bracket results. Left column illustrates the topology, middle column illustrates the phase field contours on the final deformed configuration with the undeformed configuration placed in light gray behind it for reference. A similar set of plots is provided in the last column with the contours of the equivalent plastic strain.

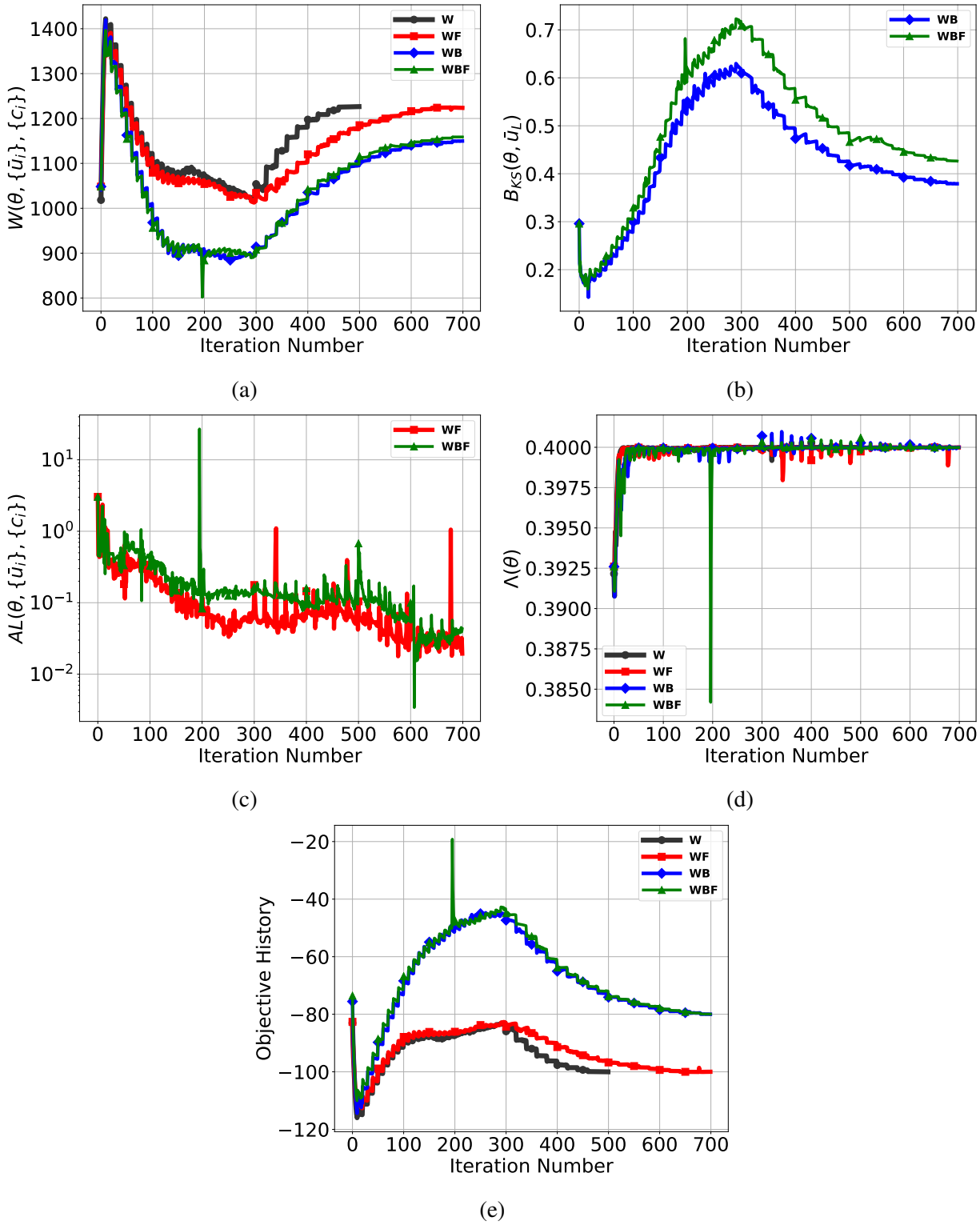

Figure 4.17: L-bracket optimizer convergence history. Note that the **W** design is stopped at 500 iterations due to rapid convergence.

Chapter 5

Fracture of 3D-printed hyperelastic composites

This chapter is published as a journal article in: J. Russ, V. Slesarenko, S. Rudykh, and H. Waisman, "Rupture of 3D-printed hyperelastic composites: Experiments and phase field fracture modeling," Journal of the Mechanics and Physics of Solids, vol. 140, p. 103941, Jul. 2020, doi: 10.1016/j.jmps.2020.103941.

5.1 Introduction

In this chapter we study the failure behavior of 3D-printed polymer composites undergoing large deformation through experiments and numerical modeling. A simple parameterized geometry with three rigid circular inclusions embedded into a soft hyperelastic matrix is proposed for a test study. By adjusting the distances between inclusions and introducing notches of various lengths we alter the failure pattern in the specimens. A non-standard phase field fracture method with energetic threshold is employed for the numerical study assuming plane stress conditions. Remarkably, the derived and implemented reduced plane stress formulation coupled with phase field fracture agrees well with the experimental data, capturing both crack arrest and secondary crack initiation in the bulk material.

We remark that the material fabrication technique employed in this study does not result in weak interphase regions between the matrix and inclusion phases, and, for various composite systems [213, 214, 215, 216, 217, 218, 219], failure in this region has not been observed. We note, however, that the composite fabrication method produces the interphase mixing zone (see, for example, Arora et al. [220] that studied the influence of the inhomogeneous interphase region on mechanical stability). Our experimental observations indicate that the matrix is weaker than the interphase

material. Nevertheless, the numerical formulation could potentially be extended to the class of composites with weak interphase regions by adopting a framework appropriately capturing the relevant physics (see, for example, Nguyen et al. [86]).

This chapter is organized as follows: In Section 5.2 we provide the details of the phase field fracture model employed herein and the corresponding finite element implementation. In Section 5.3 the composite structures are detailed and the experimental/numerical methods used to study their failure behavior are outlined. Finally the numerical and experimental results are provided in Section 5.4 in which both qualitative and quantitative features are compared. Furthermore, the numerical model is also used in place of additional experimental data to remark on the physical implications of the results obtained, followed by a concluding summary.

5.2 Large deformation phase field fracture model with energetic threshold

In this section we provide the derivation of the non-standard phase field formulation with an energetic threshold as presented in Miehe et al. [24] in order to prevent energy degradation at low stress levels. We note that the same phenomenon could also be partially mitigated by judicious selection of the degradation function as presented by Borden [160]. Experimentally applied loading rates are low enough to permit the use of quasi-static numerical analyses and for reasons of computational efficiency we perform the numerical simulations in two space dimensions under an assumed state of plane stress. In C.1 the plane stress assumption is justified for the geometry used herein via numerical comparison with a plane strain assumption and a full three-dimensional formulation. Additionally, since the plane stress assumption results in a constraint that is not trivially satisfied, we also derive the reduced in-plane relations, including the nonlinear equation to be solved for the out-of-plane stretch and the analytical reduced consistent tangent tensor.

5.2.1 Phase field fracture formulation

The phase field fracture formulation used in this chapter is obtained from an energy minimization problem for a continuum body, Ω_0 (where the $(\cdot)_0$ subscript signifies the reference configuration) in

a manner similar to that described in Section 3.2. Here we let $\boldsymbol{F}$ represent the deformation gradient and Γ_0 represents the crack surface. Neglecting the potential associated with external forces, the total potential energy of the solid may be expressed as

$$\Pi(\boldsymbol{F}, \Gamma_0) = W_{elas}(\boldsymbol{F}) + W_{frac}(\Gamma_0) \tag{5.2.1}$$

in which the stored elastic energy, W_{elas}, is a function of the deformation gradient ($\boldsymbol{F}$), and the fracture surface energy, W_{frac}, depends on the crack surface. In a manner similar to the presentation in Section 3.2, we use the phase field approximation of the fracture surface energy outlined in Miehe et al. [24], in order to prevent degradation of the elastic energy at low stress levels. This updated model is used in this chapter where the fracture surface energy approximation may be expressed as

$$\hat{W}_{frac}(d) = \int_{\Omega_0} 2\Psi_c \left(d + \frac{l_0^2}{2} \nabla_0 d \cdot \nabla_0 d \right) dV \tag{5.2.2}$$

in which Ψ_c represents a critical fracture energy per unit reference volume. In this chapter we use Ψ_c as a material parameter for calibration of the model with the experimental data.

Stored elastic energy approximation

The undamaged elastic energy density employed in this chapter consists of a standard decomposition into volumetric and isochoric components as shown below. The isochoric function is a simple neo-Hookean model with shear modulus, μ, while the volumetric function is another common form with bulk modulus, κ. Here we define the elastic energy density function per unit undeformed volume,

$$\Psi_e(\boldsymbol{F}) = \Psi_e(\bar{I}_1, J) = \underbrace{\frac{\kappa}{2} (\log J)^2}_{\Psi_e^{vol}} + \underbrace{\frac{\mu}{2} \left(\bar{I}_1 - 3 \right)}_{\Psi_e^{iso}} \tag{5.2.3}$$

where $J = \det \boldsymbol{F}$ and $\bar{I}_1 = J^{-2/3} I_1$ which is the first invariant of the isochoric right Cauchy-Green deformation tensor and $I_1 = F_{ij} F_{ij}$ is the unmodified first invariant. This elastic energy density adequately describes the elastic response of the material and may be naturally decomposed into compressive and tensile components via a volumetric/isochoric energy split similar to that of Amor et al. [161]. Here we define this tensile/compressive (Ψ_e^+/Ψ_e^-) energy decomposition in the following way based upon the determinant of the deformation gradient similar to Wu et al. [100].

$$\Psi_e^+(\bar{I}_1, J) = \begin{cases} \frac{\kappa}{2} (\log J)^2 + \frac{\mu}{2} \left(\bar{I}_1 - 3 \right) & \text{, if } J \geq 1 \\ \frac{\mu}{2} \left(\bar{I}_1 - 3 \right) & \text{, otherwise} \end{cases} \tag{5.2.4}$$

$$\Psi_e^-(\bar{I}_1, J) = \Psi_e(\bar{I}_1, J) - \Psi_e^+(\bar{I}_1, J) \tag{5.2.5}$$

Note that other splits of the elastic energy are possible, including one based on a multiplicative split of the deformation gradient [221], one based on principal invariants of the Cauchy-Green deformation tensor [222], and a more recent split based on principal stretches [223].

This yields a damaged elastic energy density in which only the tensile energy is degraded according to [23],

$$\Psi_e(\bar{I}_1, J, d) = \Psi_e^-(\bar{I}_1, J) + (g(d) + k) \Psi_e^+(\bar{I}_1, J) \tag{5.2.6}$$

where the total stored elastic energy approximation is obtained via integration over the reference volume.

$$\hat{W}_{elas}(\bar{I}_1, J, d) = \int_{\Omega_0} \Psi_e(\bar{I}_1, J, d) dV \tag{5.2.7}$$

The phase field parameter, d, affects the stored elastic energy via the action of the so-called degradation function, $g(d)$. Although a cubic degradation function has previously been proposed [160], we employ the more common quadratic degradation function in this chapter, defined as $g(d) = (1 - d)^2$. Additionally, we include the small constant parameter, k, in order to ensure the

problem remains well-posed [22]. In all subsequent examples in this chapter k is set to 10^{-6}.

The damaged first Piola-Kirchoff stress may then be obtained directly from the damaged elastic energy density via the following relation,

$$\boldsymbol{P} = \underbrace{\frac{\partial \Psi_e^-}{\partial \boldsymbol{F}}}_{\boldsymbol{P}^-} + (g(d) + k) \underbrace{\frac{\partial \Psi_e^+}{\partial \boldsymbol{F}}}_{\boldsymbol{P}^+} \tag{5.2.8}$$

where $\boldsymbol{P}$ is now the damaged first Piola-Kirchoff stress tensor and $\boldsymbol{P}^-/\boldsymbol{P}^+$ are the undamaged, compressive and tensile first Piola-Kirchoff stress tensors, respectively.

Approximate total potential energy

Substituting the above approximations into the total potential energy in Equation 5.2.1 we obtain the approximate form ($\tilde{\Pi}$) as

$$\begin{aligned} \tilde{\Pi}(\boldsymbol{u}, d) &= \hat{W}_{elas}(\boldsymbol{F}, d) + \hat{W}_{frac}(d) \\ &= \int_{\Omega_0} \left(\Psi_e^-(\boldsymbol{F}) + (g(d) + k)\Psi_e^+(\boldsymbol{F}) \right) dV \\ &+ \int_{\Omega_0} 2\Psi_c \left(d + \frac{l_0^2}{2} \nabla_0 d \cdot \nabla_0 d \right) dV \end{aligned} \tag{5.2.9}$$

Note that the hat notation, $\hat{(\cdot)}$, in Equation 5.2.9 signifies the previously introduced approximation of the quantity. At a minimum, the first variation of the total potential with respect to the displacement and phase field must vanish, i.e. $\delta\tilde{\Pi} = 0$. Application of this principle, the divergence theorem, and the standard variational argument yields the Euler-Lagrange equations,

$$\nabla_0 \cdot \boldsymbol{P} = \boldsymbol{0} \quad \text{in } \Omega_0 \tag{5.2.10}$$

$$\Psi_c \left(d - l_0^2 \nabla_0 \cdot \nabla_0 d \right) - (1 - d)(\Psi_e^+ - \Psi_c) = 0 \quad \text{in } \Omega_0 \tag{5.2.11}$$

$$\boldsymbol{u} = \hat{\boldsymbol{u}} \quad \text{on } \partial\Omega_0^u \tag{5.2.12}$$

$$\boldsymbol{n} \cdot \nabla_0 d = 0 \quad \text{on } \partial\Omega_0 \tag{5.2.13}$$

where the additional Dirichlet and Neumann boundary conditions have been added (i.e. Equation 5.2.12 and 5.2.13). Note that the Equation 5.2.13 implies that there is no damage flux out of the domain. Equation 5.2.10 represents quasi-static equilibrium in the absence of body forces while Equation 5.2.11 governs the evolution of the phase field. Note that using the tensile energy density as a crack driving force for rubber is quite consistent with existing experimental evidence. Using the strain energy density as a failure criterion was demonstrated by Hocine et al. [224] in which failure of natural rubber was investigated and the strain energy density along the crack trajectory was found to be independent of the crack length and specimen geometry (see also Volokh [225]).

Finally, Equation 5.2.11 is modified in order to enforce irreversibility of crack growth. The local history field, $\mathcal{H}$, proposed in Miehe et al. [23], is used in order to ensure the local crack driving force is nondecreasing. Note that in the equation below, t, is a pseudo-time variable related to the incremental external loading. Additionally, we employ the purely numerical viscous regularization with viscosity parameter, η, phase field at the previous time increment, d_n, and time increment, Δt, presented by Miehe et al. [23, 24]. The reader is referred to these works for additional details regarding this numerical regularization. This viscous term is included in the quasi-static setting in order to prevent large jumps in the crack length over a given time increment. In the context large deformations, this is particularly important since large jumps in crack length are also typically accompanied by large changes in the displacement field which may result in inverted elements during the displacement update and potential failure of the simulation. The final equation governing the evolution of the phase field is provided below.

$$\eta \frac{d - d_n}{\Delta t} + \Psi_c \left(d - l_0^2 \nabla_0 \cdot \nabla_0 d \right) - (1 - d)\mathcal{H} = 0 \tag{5.2.14}$$

$$\text{where } \mathcal{H}(\boldsymbol{X}, t) = \max_{\tau \in [0,t]} \left\langle \Psi_e^+(\boldsymbol{X}, \tau) - \Psi_c \right\rangle_+ \tag{5.2.15}$$

Note that the Macaulay brackets are defined such that $\langle \cdot \rangle_+ = \max(\cdot, 0)$.

Plane stress enforcement

The experiments presented herein are generally well-represented by a state of plane stress. Due to the large computational burden of the three-dimensional formulation, we reduce the equations to a two-dimensional plane stress state. The derivation of the reduced first Piola-Kirchoff stress and the associated analytical consistent tangent are provided in this section.

We begin with the specific three-dimensional first Piola-Kirchoff stress as obtained from the undamaged stored elastic energy density provided in Equation 5.2.3.

$$\boldsymbol{P} = \frac{\partial \Psi_e(\bar{I}_1, J)}{\partial \boldsymbol{F}} = \kappa \log(J) \boldsymbol{F}^{-T} + \mu J^{-2/3} \left(\boldsymbol{F} - \frac{I_1}{3} \boldsymbol{F}^{-T} \right) \tag{5.2.16}$$

The Kirchoff stress may then be obtained via right multiplication of the deformation gradient transpose, resulting in

$$\boldsymbol{\tau} = \boldsymbol{P} \cdot \boldsymbol{F}^T = \kappa \log(J) \boldsymbol{I} + \mu J^{-2/3} \left(\boldsymbol{B} - \frac{I_1}{3} \boldsymbol{I} \right) \tag{5.2.17}$$

in which $\boldsymbol{I}$ represents the second order identity tensor and $\boldsymbol{B} = \boldsymbol{F}\boldsymbol{F}^T$ signifies the left Cauchy-Green deformation tensor. For a state of plane stress we have the following constraints on the Kirchoff stress (equivalently, these represent constraints on the Cauchy stress since the two stress measures only differ by the positive scalar multiple, J),

$$\tau_{13} = \tau_{31} = 0 \implies B_{13} = B_{31} = 0 \tag{5.2.18}$$

$$\tau_{23} = \tau_{32} = 0 \implies B_{23} = B_{32} = 0 \tag{5.2.19}$$

$$\tau_{33} = \kappa \log(J) + \mu J^{-2/3} \left(B_{33} - \frac{I_1}{3} \right) = 0 \tag{5.2.20}$$

Assuming that the deformation gradient takes the following structure,

$$\boldsymbol{F} = \begin{bmatrix} F_{11} & F_{12} & 0 \\ F_{21} & F_{22} & 0 \\ 0 & 0 & \lambda \end{bmatrix} \tag{5.2.21}$$

where λ is the out-of-plane stretch, one sees that Equations 5.2.18 and 5.2.19 are automatically satisfied. Equation 5.2.20, however, cannot be trivially satisfied and reduces to the following nonlinear equation.

$$f \equiv \lambda^2 + \frac{\kappa}{\mu} J^{2/3} \log(J) + \frac{I_1}{3} = 0 \tag{5.2.22}$$

Subsequently, the constitutive equations are reduced by using indicial notation combined with Einstein's summation convention where Greek indices may vary from 1 to 2 only and represent the tensorial in-plane components. Defining the following reduced invariants,

$$i_1 = F_{\alpha\beta} F_{\alpha\beta} \tag{5.2.23}$$

$$j = F_{11} F_{22} - F_{12} F_{21} \tag{5.2.24}$$

we have $I_1 = i_1 + \lambda^2$ and $J = j\lambda$, reducing Equation 5.2.22 to

$$f \equiv \lambda^2 + \frac{3\kappa}{2\mu} (j\lambda)^{2/3} \log(j\lambda) - \frac{i_1}{2} = 0 \tag{5.2.25}$$

Due to our choice of elastic energy density, the above scalar equation is nonlinear in the out-of-plane stretch, λ, and is solved numerically with a local newton iteration.

Once λ is determined, the reduced first Piola-Kirchoff stress may be computed via substitution of the above expressions and differentiation of each component with respect to $F_{\alpha\beta}$ to obtain

$P_{\alpha\beta} = P^{vol}_{\alpha\beta} + P^{iso}_{\alpha\beta}$.

$$P^{vol}_{\alpha\beta} = \frac{\partial \Psi^{vol}_e}{\partial F_{\alpha\beta}} = \kappa \log(j\lambda) T_{\alpha\beta} \tag{5.2.26}$$

$$P^{iso}_{\alpha\beta} = \frac{\partial \Psi^{iso}_e}{\partial F_{\alpha\beta}} = \mu (j\lambda)^{-2/3} \left(E_{\alpha\beta} - \frac{i_1 + \lambda^2}{3} T_{\alpha\beta} \right) \tag{5.2.27}$$

where we have defined,

$$T_{\alpha\beta} \equiv F^{-T}_{\alpha\beta} + \frac{1}{\lambda} \frac{\partial \lambda}{\partial F_{\alpha\beta}} \tag{5.2.28}$$

$$E_{\alpha\beta} \equiv F_{\alpha\beta} + \lambda \frac{\partial \lambda}{\partial F_{\alpha\beta}} \tag{5.2.29}$$

The derivative $\frac{\partial \lambda}{\partial F_{\alpha\beta}}$ may be obtained by differentiating Equation 5.2.25 with respect to $F_{\alpha\beta}$. After some algebra, the following expression results,

$$\frac{\partial \lambda}{\partial F_{\alpha\beta}} = \frac{F_{\alpha\beta} - \frac{3\kappa}{2\mu} (j\lambda)^{2/3} \left(\frac{2}{3} \log(j\lambda) + 1 \right) F^{-T}_{\alpha\beta}}{2\lambda + \frac{3\kappa}{2\mu} j^{2/3} \lambda^{-1/3} \left(\frac{2}{3} \log(j\lambda) + 1 \right)} \tag{5.2.30}$$

In order to solve the global Newton system efficiently the analytical consistent tangent tensor is derived and used in computation of the global tangent stiffness matrices. Although this derivation is rather long and tedious, we believe that this is an essential component of the method in order to ensure some degree of robustness when coupled with phase field fracture since very large deformations often result.

We begin by defining each component of the consistent tangent separately as is done in Equations 5.2.26 and 5.2.27 above where the total consistent tangent may be written $\mathbb{C} = \mathbb{C}^{vol} + \mathbb{C}^{iso}$.

$$\mathbb{C}^{vol}_{\alpha\beta\gamma\delta} = \frac{\partial P^{vol}_{\alpha\beta}}{\partial F_{\gamma\delta}} = \kappa \log(j\lambda) \frac{\partial T_{\alpha\beta}}{\partial F_{\gamma\delta}} + \kappa T_{\alpha\beta} T_{\gamma\delta} \tag{5.2.31}$$

$$\mathbb{C}^{iso}_{\alpha\beta\gamma\delta} = \frac{\partial P^{iso}_{\alpha\beta}}{\partial F_{\gamma\delta}} = \mu\left(E_{\alpha\beta} - \frac{i_1+\lambda^2}{3}T_{\alpha\beta}\right)\frac{\partial (j\lambda)^{-2/3}}{\partial F_{\gamma\delta}} + \frac{\mu}{(j\lambda)^{2/3}}\left(\frac{\partial E_{\alpha\beta}}{\partial F_{\gamma\delta}} - \frac{1}{3}\left(\frac{\partial (i_1+\lambda^2)}{\partial F_{\gamma\delta}}T_{\alpha\beta} + (i_1+\lambda^2)\frac{\partial T_{\alpha\beta}}{\partial F_{\gamma\delta}}\right)\right) \tag{5.2.32}$$

The unspecified derivatives in the above expressions may then be expressed via the following relations.

$$\frac{\partial (j\lambda)^{-2/3}}{\partial F_{\gamma\delta}} = -\frac{2}{3}(j\lambda)^{-2/3}T_{\gamma\delta} \tag{5.2.33}$$

$$\frac{\partial (i_1+\lambda^2)}{\partial F_{\gamma\delta}} = 2F_{\gamma\delta} + 2\lambda\frac{\partial \lambda}{\partial F_{\gamma\delta}} \tag{5.2.34}$$

$$\frac{\partial T_{\alpha\beta}}{\partial F_{\gamma\delta}} = -F^{-1}_{\delta\alpha}F^{-1}_{\beta\gamma} + \frac{1}{\lambda}\frac{\partial^2 \lambda}{\partial F_{\alpha\beta}\partial F_{\gamma\delta}} - \frac{1}{\lambda^2}\frac{\partial \lambda}{\partial F_{\alpha\beta}}\frac{\partial \lambda}{\partial F_{\gamma\delta}} \tag{5.2.35}$$

$$\frac{\partial E_{\alpha\beta}}{\partial F_{\gamma\delta}} = \delta_{\alpha\gamma}\delta_{\beta\delta} + \lambda\frac{\partial^2 \lambda}{\partial F_{\alpha\beta}\partial F_{\gamma\delta}} + \frac{\partial \lambda}{\partial F_{\alpha\beta}}\frac{\partial \lambda}{\partial F_{\gamma\delta}} \tag{5.2.36}$$

The final unspecified derivative is the second derivative of the out-of-plane stretch with respect to the in-plane components of the deformation gradient. Labeling the numerator of Equation 5.2.30 $N_{\alpha\beta}$ and the denominator D we differentiate each expression and use the quotient rule to obtain the final expression.

$$\text{Let } c_1 \equiv (j\lambda)^{2/3}\left(\log(j\lambda) + \frac{3}{2}\right) \tag{5.2.37}$$

$$N_{\alpha\beta} \equiv F_{\alpha\beta} - c_1\frac{\kappa}{\mu}F^{-T}_{\alpha\beta} \tag{5.2.38}$$

$$D \equiv 2\lambda + \frac{\kappa c_1}{\mu\lambda} \tag{5.2.39}$$

Differentiating the numerator and the denominator of Equation 5.2.30 we obtain,

$$\frac{\partial N_{\alpha\beta}}{\partial F_{\gamma\delta}} = -\frac{\kappa}{\mu}\left(F^{-T}_{\alpha\beta}\frac{\partial c_1}{\partial F_{\gamma\delta}} - c_1 F^{-1}_{\delta\alpha}F^{-1}_{\beta\gamma}\right) + \delta_{\alpha\gamma}\delta_{\beta\delta} \tag{5.2.40}$$

$$\frac{\partial D}{\partial F_{\gamma\delta}} = 2\frac{\partial \lambda}{\partial F_{\gamma\delta}} + \frac{\kappa}{\mu}\left(-\frac{c_1}{\lambda^2}\frac{\partial \lambda}{\partial F_{\gamma\delta}} + \frac{1}{\lambda}\frac{\partial c_1}{\partial F_{\gamma\delta}}\right) \tag{5.2.41}$$

$$\frac{\partial c_1}{\partial F_{\gamma\delta}} = (j\lambda)^{2/3}\left(\frac{2}{3}\log(j\lambda) + 2\right)T_{\gamma\delta} \tag{5.2.42}$$

Combining these expressions we obtain the final required derivative.

$$\frac{\partial^2 \lambda}{\partial F_{\alpha\beta}\partial F_{\gamma\delta}} = \frac{D\frac{\partial N_{\alpha\beta}}{\partial F_{\gamma\delta}} - N_{\alpha\beta}\frac{\partial D}{\partial F_{\gamma\delta}}}{D^2} \tag{5.2.43}$$

5.2.2 Finite element discretization

The weak form of the governing equations is obtained in the usual manner by multiplication of the strong form equations with admissible test functions, integration over the domain, and application of the divergence theorem. The test functions are denoted $\boldsymbol{w}^u$ and w^d for the linear momentum and phase field equations, respectively. The residual form of the equations for the displacement field, R_u, and phase field, R_d, can then be written as follows where we have omitted any traction boundary conditions.

$$R_u = \int_{\Omega_0} \boldsymbol{P} : \nabla_0 \boldsymbol{w}^u \, dV = 0 \tag{5.2.44}$$

$$R_d = \int_{\Omega_0} \left(\frac{\eta}{\Delta t}(d - d_n)\, w^d + \Psi_c d\; w^d + \Psi_c l_0^2 \nabla_0 d \cdot \nabla_0 w^d - (1-d)\mathcal{H}\; w^d\right) dV = 0 \tag{5.2.45}$$

We search for $u_i \in \mathcal{S}_{u_i}$ and $d \in \mathcal{S}_d$ such that Equations 5.2.44 and 5.2.45 are satisfied $\forall w_i^u \in \mathcal{V}_{w_i^u}$ and $\forall w^d \in \mathcal{V}_{w^d}$ where these function spaces are defined below.

$$\mathcal{S}_{u_i} = \{u_i \mid u_i \in H^1 \ \& \ u_i = \hat{u}_i \text{ on } \partial\Omega_0^u\} \tag{5.2.46}$$

$$\mathcal{S}_d = \{d \mid d \in H^1\} \tag{5.2.47}$$

$$\mathcal{V}_{w_i^u} = \{w_i^u \mid w_i^u \in H^1 \ \& \ w_i^u = 0 \text{ on } \partial\Omega_0^u\} \tag{5.2.48}$$

$$\mathcal{V}_{w^d} = \{w^d \mid w^d \in H^1\} \tag{5.2.49}$$

Laying the groundwork for the staggered update of the displacement and phase field introduced later, we linearize Equation 5.2.44 with respect to $\boldsymbol{u}$ and Equation 5.2.45 with respect to d (note that although Equation 5.2.45 is already a linear equation in d we update the phase field incrementally in a Newton-like manner).

$$R_u(\boldsymbol{u}^{(k+1)}, d^{(k)}) \approx R_u(\boldsymbol{u}^{(k)}, d^{(k)}) + DR_u(\boldsymbol{u}^{(k)}, d^{(k)})[\delta\boldsymbol{u}] = 0 \tag{5.2.50}$$

$$R_d(\boldsymbol{u}^{(k+1)}, d^{(k+1)}) \approx R_d(\boldsymbol{u}^{(k)}, d^{(k)}) + DR_d(\boldsymbol{u}^{(k)}, d^{(k)})[\delta d] = 0 \tag{5.2.51}$$

The directional derivatives above may be expressed as

$$DR_u(\boldsymbol{u}^{(k)}, d^{(k)})[\delta\boldsymbol{u}] = \int_{\Omega_0} \nabla_0 \boldsymbol{w}^u : \mathbb{C} : \nabla_0 \delta\boldsymbol{u} \, dV \tag{5.2.52}$$

$$DR_d(\boldsymbol{u}^{(k)}, d^{(k)})[\delta d] = \int_{\Omega_0} \left(\left(\Psi_c + \mathcal{H} + \frac{\eta}{\Delta t} \right) \delta d \ w^d + \Psi_c l_0^2 \nabla_0 \delta d \cdot \nabla_0 w^d \right) dV \tag{5.2.53}$$

where $\mathbb{C}$ is the previously provided fourth order constitutive tensor.

The linearized equations above are then discretized and solved incrementally using the finite element method with appropriately chosen finite dimensional subspaces ($\mathcal{S}_{u_i}^h \subset \mathcal{S}_{u_i}$, $\mathcal{S}_d^h \subset \mathcal{S}_d$, $\mathcal{V}_{w_i^u}^h \subset \mathcal{V}_{w_i^u}$, $\mathcal{V}_{w^d}^h \subset \mathcal{V}_{w^d}$). The 2D domain is partitioned using 4-node quadrilateral elements and the typical bilinear Lagrange basis functions are used for the test and trial spaces, consistent with the standard Galerkin formulation. We represent these field approximations with the shape function

matrices, $\boldsymbol{N}^{\boldsymbol{u}}$ and $\boldsymbol{N}^{d}$, for the displacement and phase field, respectively. The corresponding matrices of shape function gradients are represented analogously by $\boldsymbol{B}^{\boldsymbol{u}}$ and $\boldsymbol{B}^{d}$.

$$\begin{aligned} \boldsymbol{u} &\approx \boldsymbol{u}^h = \boldsymbol{N}^{\boldsymbol{u}}\bar{\boldsymbol{u}} & d &\approx d^h = \boldsymbol{N}^{d}\bar{\boldsymbol{d}} \\ \delta\boldsymbol{u} &\approx \delta\boldsymbol{u}^h = \boldsymbol{N}^{\boldsymbol{u}}\delta\bar{\boldsymbol{u}} & \delta d &\approx \delta d^h = \boldsymbol{N}^{d}\delta\bar{\boldsymbol{d}} \\ \boldsymbol{w}^{u} &\approx \boldsymbol{w}^{u^h} = \boldsymbol{N}^{\boldsymbol{u}}\bar{\boldsymbol{w}}^{u} & w^{d} &\approx w^{d^h} = \boldsymbol{N}^{d}\bar{\boldsymbol{w}}^{d} \end{aligned}$$

Substituting these approximations along with their gradients into Equations 5.2.50 and 5.2.51, and invoking the arbitrariness of the vectors $\bar{\boldsymbol{w}}^{u}$ and $\bar{\boldsymbol{w}}^{d}$, we can identify the discrete elemental residual vectors and jacobian matrices,

$$\boldsymbol{R}^{e^{(k)}}_{\bar{\boldsymbol{u}}} = \int_{\Omega_0} \boldsymbol{P}^{(k)} : \boldsymbol{B}^{\boldsymbol{u}}\, dV = \boldsymbol{0} \tag{5.2.54}$$

$$\boldsymbol{J}^{e^{(k)}}_{\bar{\boldsymbol{u}}} = \int_{\Omega_0} \boldsymbol{B}^{\boldsymbol{u}} : \mathbb{C}^{(k)} : \boldsymbol{B}^{\boldsymbol{u}}\, dV \tag{5.2.55}$$

$$\begin{aligned} \boldsymbol{R}^{e^{(k)}}_{\bar{\boldsymbol{d}}} = &\int_{\Omega_0} \left(\Psi_c \left(\boldsymbol{N}^{d^T}\boldsymbol{N}^{d} + l_0^2 \boldsymbol{B}^{d^T}\boldsymbol{B}^{d}\right)\bar{\boldsymbol{d}}^{(k)}\right) dV \\ &+ \int_{\Omega_0} \frac{\eta}{\Delta t}\boldsymbol{N}^{d^T}\boldsymbol{N}^{d}\left(\bar{\boldsymbol{d}}^{(k)} - \bar{\boldsymbol{d}}_n\right) dV \\ &- \int_{\Omega_0} (1 - \boldsymbol{N}^{d}\bar{\boldsymbol{d}}^{(k)})\boldsymbol{N}^{d^T}\mathcal{H}\, dV = \boldsymbol{0} \end{aligned} \tag{5.2.56}$$

$$\boldsymbol{J}^{e^{(k)}}_{\bar{\boldsymbol{d}}} = \int_{\Omega_0} \left(\left(\Psi_c + \mathcal{H} + \frac{\eta}{\Delta t}\right)\boldsymbol{N}^{d^T}\boldsymbol{N}^{d} + \Psi_c l_0^2 \boldsymbol{B}^{d^T}\boldsymbol{B}^{d}\right) dV \tag{5.2.57}$$

where the e superscript signifies elemental quantities and the operation $\boldsymbol{A} : \boldsymbol{B}$ represents the double contraction of tensors $\boldsymbol{A}$ and $\boldsymbol{B}$. Additionally, the $(\cdot)^{(k)}$ notation implies that the quantity $(\cdot)$ is evaluated using the relevant field variables at iteration k. The elemental quantities are then assembled into the global residual vectors and jacobian matrices via the standard finite element assembly operators.

$$\boldsymbol{R}^{(k)}_{\bar{\boldsymbol{u}}} = \mathcal{A}_{e=1}^{N_{elem}}\, \boldsymbol{R}^{e^{(k)}}_{\bar{\boldsymbol{u}}} \qquad \boldsymbol{J}^{(k)}_{\bar{\boldsymbol{u}}} = \mathcal{A}_{e=1}^{N_{elem}}\, \boldsymbol{J}^{e^{(k)}}_{\bar{\boldsymbol{u}}} \tag{5.2.58}$$

$$\boldsymbol{R}^{(k)}_{\bar{\boldsymbol{d}}} = \mathcal{A}_{e=1}^{N_{elem}}\, \boldsymbol{R}^{e^{(k)}}_{\bar{\boldsymbol{d}}} \qquad \boldsymbol{J}^{(k)}_{\bar{\boldsymbol{d}}} = \mathcal{A}_{e=1}^{N_{elem}}\, \boldsymbol{J}^{e^{(k)}}_{\bar{\boldsymbol{d}}} \tag{5.2.59}$$

These global quantities are then used separately to compute the Newton-type correction of the

displacement and phase field nodal variables.

$$\bar{\boldsymbol{u}}^{(k+1)} = \bar{\boldsymbol{u}}^{(k)} - \boldsymbol{J}_{\bar{\boldsymbol{u}}}^{(k)^{-1}} \boldsymbol{R}_{\bar{\boldsymbol{u}}}^{(k)} \tag{5.2.60}$$

$$\bar{\boldsymbol{d}}^{(k+1)} = \bar{\boldsymbol{d}}^{(k)} - \boldsymbol{J}_{\bar{\boldsymbol{d}}}^{(k)^{-1}} \boldsymbol{R}_{\bar{\boldsymbol{d}}}^{(k)} \tag{5.2.61}$$

Algorithm 4 provides the details of the iterative staggered solution used herein. Note that this scheme is essentially identical to that of Miehe et al. [23]. Sufficiently small applied displacement increments are chosen such that the results are indistinguishable under further reduced load incrementation. During crack propagation the displacement increment is significantly reduced from an initial value of approximately 10^{-4} $[mm]$ to a value of 10^{-6} $[mm]$. We also note the use of a backtracking line search that is employed occasionally during the displacement update in order to ensure the determinant of the deformation gradient (J) is strictly positive at all quadrature points in the discretized domain. If this requirement is violated following an update of the displacement field, the newton increment, $\delta \boldsymbol{u}$, is reduced by a constant multiplier, $0 < \gamma < 1$, until the condition is satisfied. Subsequently, the displacement newton iteration is allowed to continue to convergence. Although this procedure is rarely required, it has proven to be an effective strategy for delaying failure of the numerical simulations in certain instances. The jacobian and residual equations are integrated using a standard 4-point Gauss quadrature rule for a quadrilateral element and the irreversibility requirement is enforced via a history variable stored at each quadrature point.

5.3 Numerical and experimental methods

5.3.1 Design of the composite samples

In this section we outline the process used to study the failure mechanism of 3D-printed polymer composites undergoing large deformation both experimentally and numerically. A specific parameterized geometry is proposed in order to study this behavior which consists of a soft matrix, within which three stiff circular inclusions are embedded as shown in Figure 5.1. Additionally, two

Algorithm 4 Staggered update of nodal degrees of freedom, $(\bar{\boldsymbol{u}}, \bar{\boldsymbol{d}})$

$t \leftarrow 0$
$\bar{\boldsymbol{u}}, \bar{\boldsymbol{d}} \leftarrow \boldsymbol{0}$
while $t < t_{final}$ **do**
  $t \leftarrow t + \Delta t$
  $\hat{\boldsymbol{u}} \leftarrow t \cdot \hat{\boldsymbol{u}}_{final}$ {Update prescribed displacements}
  $k \leftarrow 0$
  while $||\boldsymbol{R}^{(k)}_{\bar{\boldsymbol{u}}}||_2 \,/\, ||\boldsymbol{R}^{(0)}_{\bar{\boldsymbol{u}}}||_2 > 10^{-8}$ **do**
    $k \leftarrow k + 1$
    Update $\bar{\boldsymbol{u}}$ via Equation 5.2.60
  end while
  Update $\mathcal{H}$ with updated $\bar{\boldsymbol{u}}$
  $k \leftarrow 0$
  while $||\boldsymbol{R}^{(k)}_{\bar{\boldsymbol{d}}}||_2 \,/\, ||\boldsymbol{R}^{(0)}_{\bar{\boldsymbol{d}}}||_2 > 10^{-8}$ **do**
    $k \leftarrow k + 1$
    Update $\bar{\boldsymbol{d}}$ via Equation 5.2.61
  end while
end while

notches of various lengths are introduced in the middle of the specimen. By varying the distance between stiff inclusions and the notch lengths, we are able to alter the failure sequence.

In total, 9 different geometries (3 initial notch lengths and 3 distances between inclusions) are subjected to uniaxial tension until complete failure of the specimen. We adopt the short notation N__D__ to describe the geometry of the specimens that reflects the notch length as well as spacing between rigid inclusions. For instance, the notation N05D18 corresponds to a specimen with an 18 $[mm]$ distance between inclusion centers and an initial notch length corresponding to 5% of the total specimen width. This is illustrated graphically in Figure 5.1, below. Note that the out-of-plane thickness of all samples is 2.5 $[mm]$.

5.3.2 Experimental testing

The composite specimens with the selected geometries (see Figure 5.1) were produced by multimaterial PolyJet 3D-printing using a Stratasys Object Connex 3 printer that supports fabrication of specimens containing up to 3 materials simultaneously. The matrix of the composite was printed

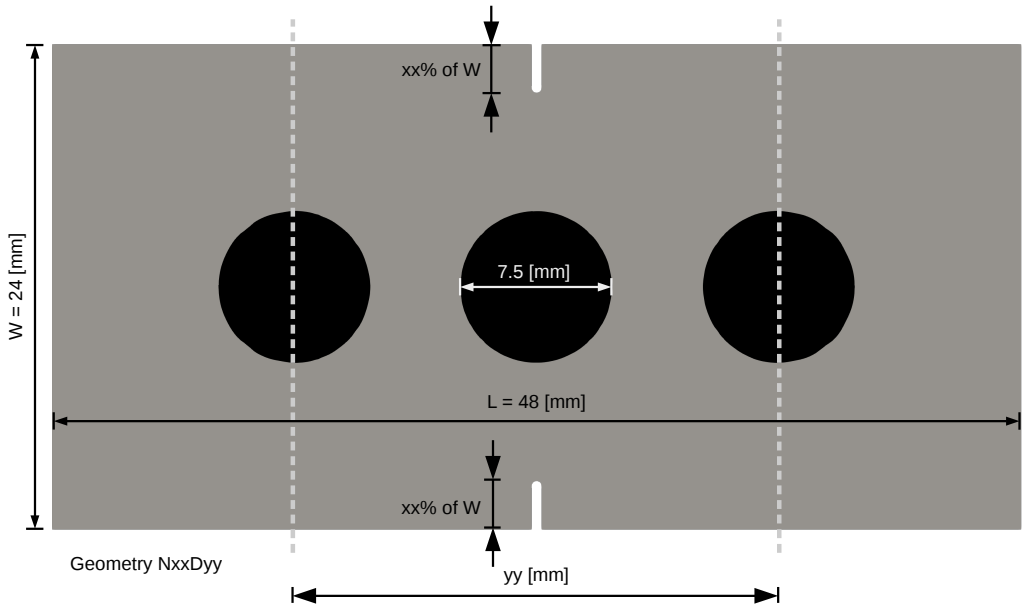

Figure 5.1: Geometric parameterization, NxxDyy, in which xx and yy are illustrated graphically.

using soft elastomeric TangoBlackPlus material (TP), while stiff VeroWhite (VW) material was selected for the inclusions. The printed specimens were subjected to uniaxial tension using the universal testing machine Shimadzu EZ-LX with a low strain rate of 10 mm/min to avoid dynamic effects and decrease the influence of rate-dependent TP material behavior. For consistency all samples were printed with the same orientation in the building tray, even though supplementary tests verified that the printing orientation has only minor effect on the failure behavior. The deformation process was captured using a CMOS camera, enabling the use of digital image correlation (DIC) to estimate the strain field within the soft matrix prior to crack initiation.

5.3.3 Numerical investigation

The numerical formulation was implemented using the open-source, C++ finite element library, deal.II [207], and PETSc [209] for parallel, sparse linear algebra. First, the elastic parameters for the soft TP material were estimated from select homogeneous uniaxial tension experiments. Near incompressibility was assumed and the bulk modulus was taken to be 100 times the calibrated shear modulus of 0.24 $[MPa]$, resulting in an initial Poisson's ratio of approximately 0.495. These

are consistent with previously reported material parameters [81]. The stiff VW inclusions may effectively be regarded as rigid due to their high stiffness relative to TP. The elastic modulus as reported on the manufacturer's data sheet [226] is in the range 2,000-3,000 $[MPa]$. For the purpose of the numerical studies presented herein, we assume the material has an approximate Poisson's ratio of 0.4. Using the lower bound on the elastic modulus from the manufacturer we estimate the shear modulus of the rigid material to be 714 $[MPa]$ and bulk modulus to be 3.33 $[GPa]$, based on the standard theory of isotropic, linear elasticity (i.e. $\mu = E/(2(1+\nu))$ and $\kappa = E/(3(1-2\nu))$). The finite element size is approximately $l_0/6$ in all regions in which cracks may nucleate or propagate and the boundary conditions are illustrated in Figure 5.2 below. Note that in order to obtain numerical predictions more consistent with experiments, we break the symmetry about the vertical axis by applying a small shift of the center inclusion (0.1% of the specimen width). This 0.024 $[mm]$ shift is less than the 0.1 $[mm]$ "accuracy" asserted by the manufacturer [227] and the 0.03 $[mm]$ layer thickness.

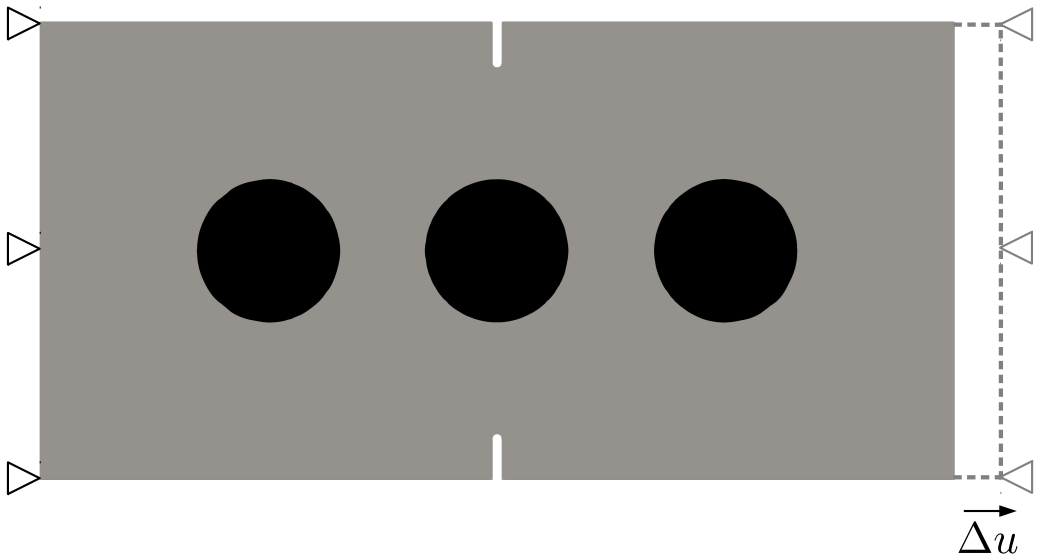

Figure 5.2: Boundary conditions imposed in numerical simulations. The left edge is fixed while a displacement is applied to the right edge.

The material parameters used in subsequent numerical analyses are provided in Table 5.1. In this chapter, rather than employing a complex calibration procedure for the phase field model parameters, we set the length scale parameter as small as possible based on computational limitations ($l_0 = 0.5$

mm similar to the 0.5504 mm obtained for a rubber material by Loew et al. [109]) and adjust the critical energy density ($\Psi_c = 0.34\ \frac{N}{mm^2}$) in order to approximately match the failure stretch of only one (i.e. the N10D24) experiment. The resulting parameter set gave reasonably predictive results for the other experiments with different geometries. The same length scale parameter is used for the stiff inclusions and the critical energy density is estimated using the approximation $\Psi_c = \sigma_c^2/(2E)$ with a critical stress of 65 MPa (corresponding to the tensile strength estimated by the manufacturer). Note that since the stiff inclusions are not directly loaded, the strain energy density of the inclusion material never exceeds the critical threshold and consequently has little to no effect on the numerical predictions. In the future, a more complex calibration procedure such as the one outlined in Loew et al. [109] may be employed. Furthermore, future studies introducing stochasticity may be conducted in order to identify the material parameters (see Rappel et al. [228] for example) and better understand the effect of uncertainty in their value (see Hauseux et al. [229] for an example regarding hyperelasticity).

Multiple simulations were performed corresponding to the experimentally tested geometric configurations. For particular combinations of the initial notch length and distance between inclusions, cracks initiate either between inclusions or at the notch tip as illustrated in Figure 5.3. Here we note that when cracks initiate near the rigid inclusion pole rather than at the notch tip, this is likely related to cavitation resulting from the stress triaxiality as is discussed in Volokh and Aboudi [230]. The relationship between this phenomenon and fracture has also been recently investigated by Raayai-Ardakani et al. [231]. Additionally, it should be mentioned that due to the large stretch ratios that soft materials generally exhibit prior to failure, stress concentrators such as notches are typically significantly blunted. This generally results in lower sensitivity to notches when compared with materials that are significantly stiffer. Nonetheless, our numerical/experimental results do indicate that a sufficiently large notch will indeed lead to crack initiation at the notch tip.

Table 5.1: Material parameters

	$\kappa\ [MPa]$	$\mu\ [MPa]$	$l_0\ [mm]$	$\Psi_c\ [\frac{N \cdot mm}{mm^3}]$
TangoBlackPlus	24	0.24	0.5	0.34
VeroWhite	3,330	714	0.5	1.05

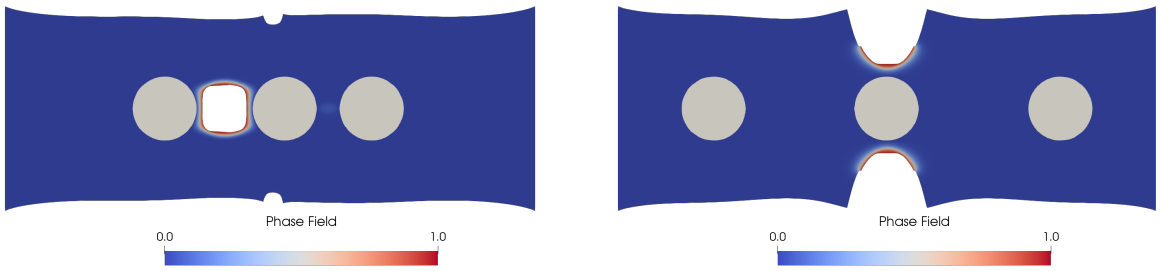

(a) (b)

Figure 5.3: Predicted crack initiation comparison for (a) N05D18 and (b) N20D30. Note that the plots are clipped at a phase field value of 0.95.

5.3.4 Pre-fracture strain field comparison

In order to validate the employed elastic strain energy density, we compare the calculated strain field in the specimen before fracture with the strain field observed experimentally using DIC. As illustrated in Figure 5.4 for specimen N20D30, the strain localization is observed between inclusions as well as near the initial notch tip, both numerically and experimentally. However, in specimen N05D18 the strain primarily localizes between inclusions rather than near the notch tip (Figure 5.5). A minor difference between the numerically-estimated and experimentally-observed strain fields occurs near the boundary of the rigid inclusions (compare Figure 5.5a and 5.5b). This phenomenon may be attributed to the actual non-uniform out-of-plane deformation near the rigid inclusions, which may not be accurately captured by the employed plane stress numerical approximation (see C.1). Note that we do not use the data obtained by DIC for model calibration. See Loew et al. [109] for an example where DIC data is used in conjunction with force-displacement results in order to calibrate the fracture parameters of the model.

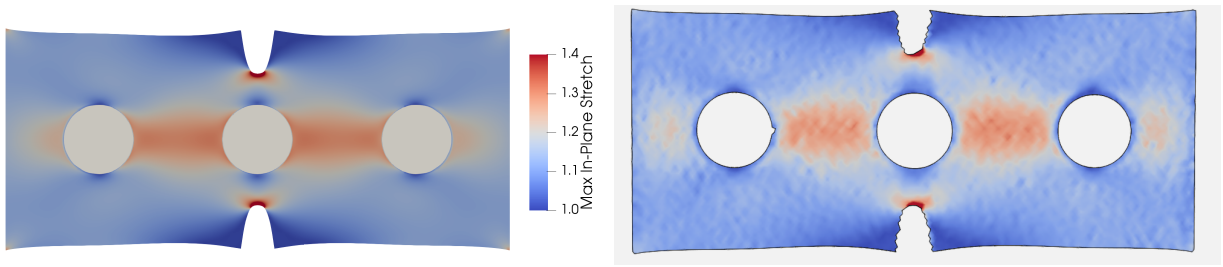

(a) Numerical prediction (b) Experimental result

Figure 5.4: Stretch comparison for N20D30 at a prescribed end-displacement of 6.6mm compared with DIC image.

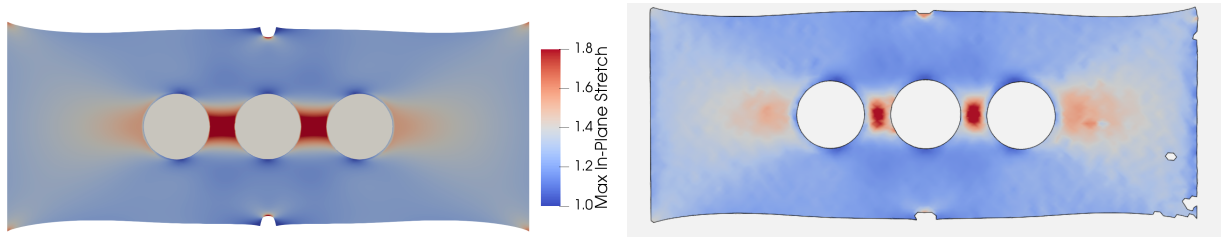

(a) Numerical prediction (b) Experimental result

Figure 5.5: Stretch comparison for N05D18 at a prescribed end-displacement of 11.8mm compared with DIC image.

5.4 Numerical and experimental studies

In this section we investigate the effects of the initial notch length and distance between inclusions on the failure pattern of the polymer composites, both numerically and experimentally. First, we compare the qualitative failure pattern via a side-by-side comparison of failure sequences for a few representative geometries in Section 5.4.1. Second, we provide the force versus displacement curves for comparison in Section 5.4.2, and an illustration of the numerically and experimentally computed external work to failure is provided in Section 5.4.3.

5.4.1 Failure sequence comparisons

First, we provide a qualitative comparison of the experimental and numerical failure patterns for a few representative geometries. For the samples with the largest distance between inclusions ($D = 30\ [mm]$) and both the smallest (N05D30 in Figure 5.6) and the largest (N20D30 in Figure 5.7) initial notch lengths, it is clear that the fracture nucleates at the notch tip. This indicates that the inclusions are a sufficient distance apart to prevent substantial elastic energy accumulation between inclusions with respect to the elastic energy accumulated near the notch tip. In both cases it is observed that once the initial crack is arrested by the center inclusion, a secondary fracture surface nucleates between inclusions. In the case of N05D30, it is observed that although the initial crack has begun propagating around the center inclusion, Figure 5.6f shows the nucleation of new fracture surface on both the left and right side of the inclusion. It is interesting that the initiation of new fracture surface on both sides of the center inclusion is also predicted numerically (see Figure 5.6e).

In the case of the larger initial notch length corresponding to the N20D30 geometry, Figure 5.7f shows a secondary crack initiation more clearly since we experimentally observe the initial cracks do not begin propagating around the center inclusion before the secondary crack initiates and propagates. In contrast with N05D30, Figure 5.7e shows secondary crack initiation on only one side of the center inclusion in somewhat remarkable correspondence with the experimental observation in Figure 5.7f. A very similar pattern is observed for the N20D24 geometry with the

same initial notch length and smaller distance between inclusions. Figure 5.8 illustrates the initial fracture surface nucleation and propagation from the notch tip, with subsequent nucleation and propagation of a secondary crack on only one side of the center inclusion.

Once the inclusions are sufficiently close together cracks typically initiate between the inclusions rather than at the initial notch tip. Figure 5.9 illustrates the failure sequence for the N10D18 geometry. It is interesting to note that the phase field formulation is capable of capturing not only the location of initiation of the first crack, but also the subsequent mild crack evolution at the notch tip as shown in Figures 5.9g and 5.9h. Note that this mild secondary initiation does not occur for the N05D18 geometry with smaller initial notch length as illustrated in Figure 5.10. Additionally, we note that while the sequences shown in Figures 5.6 and 5.9 generally exhibit failure at similar global stretch values ($\Lambda = \frac{\text{current length}}{\text{initial length}}$), for other samples we do not have ideal agreement between experiments and simulations with respect to the global stretch values (although we do have a nearly perfect qualitative match). In general, this discrepancy is expected due to the complexity of the TP material properties and/or inconsistency in the 3D-printing process (factors that may not be sufficient to describe using the single failure parameter of the employed numerical model). Nevertheless, very good agreement between the experimentally observed failure sequences and numerical predictions once again illustrates the promising capability of the proposed formulation to assess the overall fracture behavior of the 3D-printed composites undergoing large deformations.

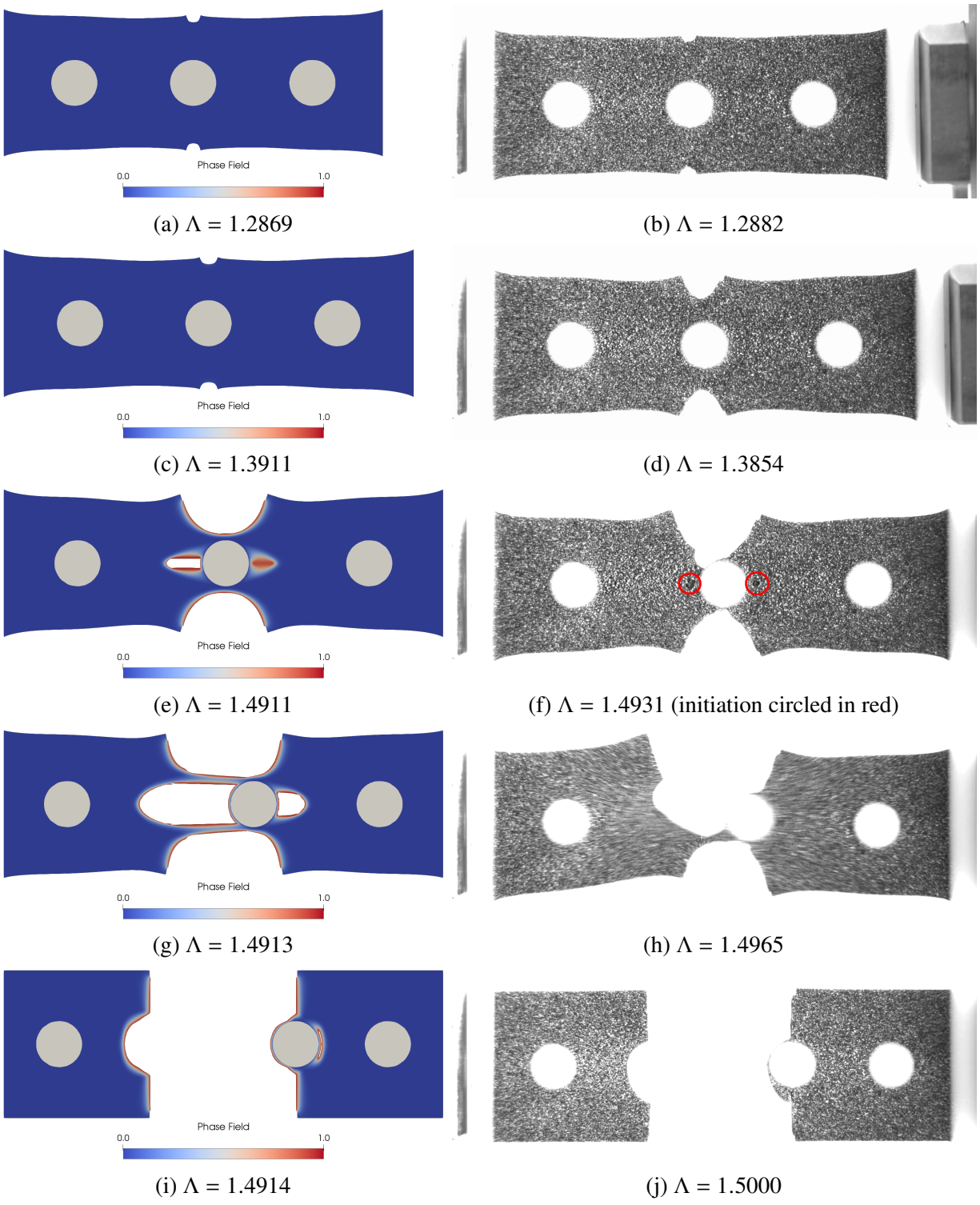

(a) $\Lambda = 1.2869$ (b) $\Lambda = 1.2882$

(c) $\Lambda = 1.3911$ (d) $\Lambda = 1.3854$

(e) $\Lambda = 1.4911$ (f) $\Lambda = 1.4931$ (initiation circled in red)

(g) $\Lambda = 1.4913$ (h) $\Lambda = 1.4965$

(i) $\Lambda = 1.4914$ (j) $\Lambda = 1.5000$

Figure 5.6: N05D30 crack initiation sequence at different values of global stretch, Λ. Numerical results (left column) and experimental results (right column).

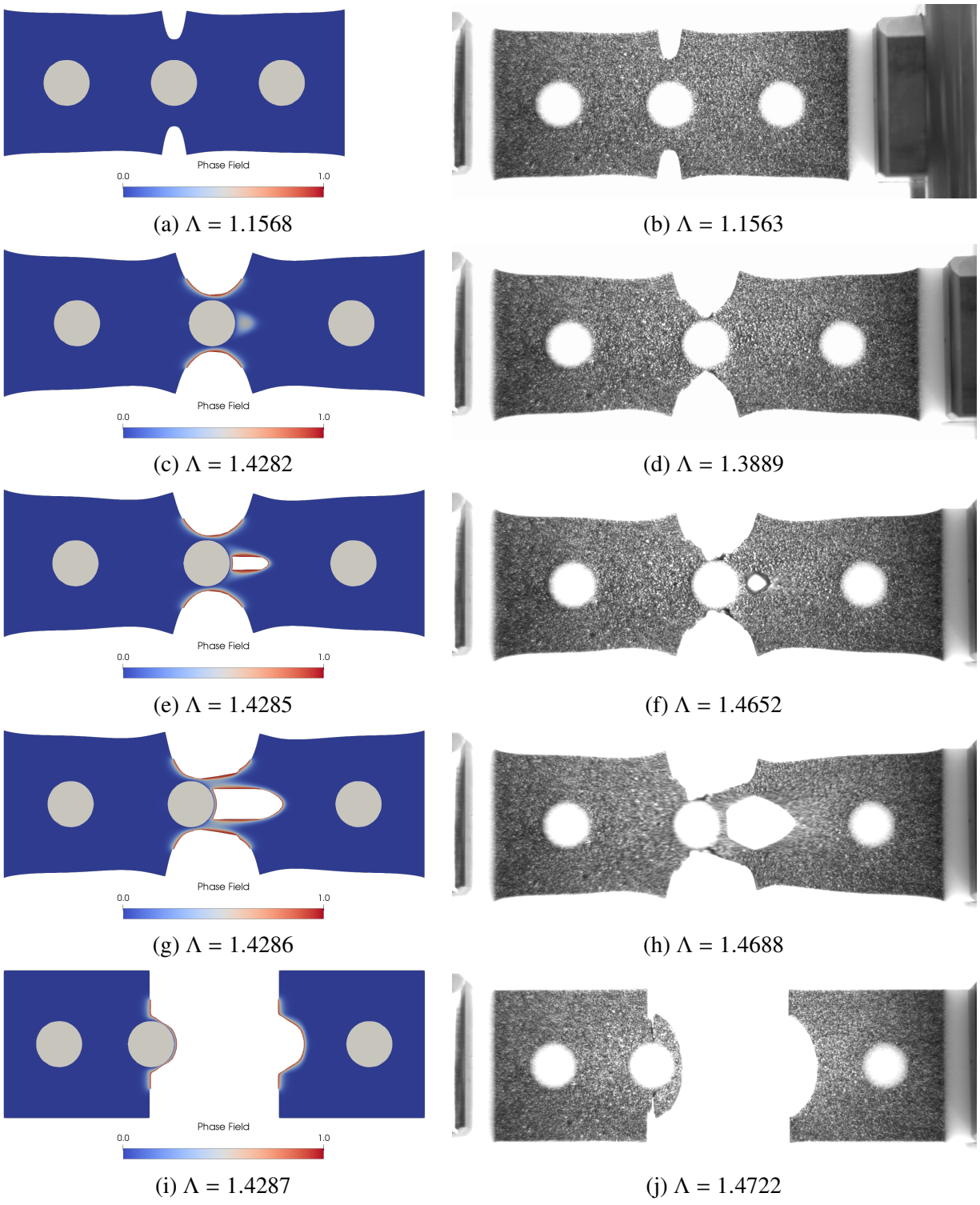

(a) $\Lambda = 1.1568$ (b) $\Lambda = 1.1563$

(c) $\Lambda = 1.4282$ (d) $\Lambda = 1.3889$

(e) $\Lambda = 1.4285$ (f) $\Lambda = 1.4652$

(g) $\Lambda = 1.4286$ (h) $\Lambda = 1.4688$

(i) $\Lambda = 1.4287$ (j) $\Lambda = 1.4722$

Figure 5.7: N20D30 crack initiation sequence at different values of global stretch, Λ. Numerical results (left column) and experimental results (right column).

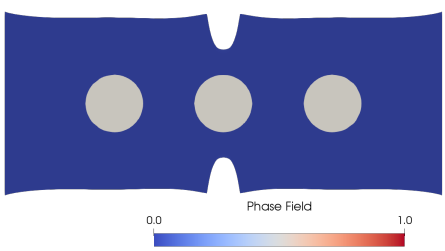

(a) $\Lambda = 1.1880$

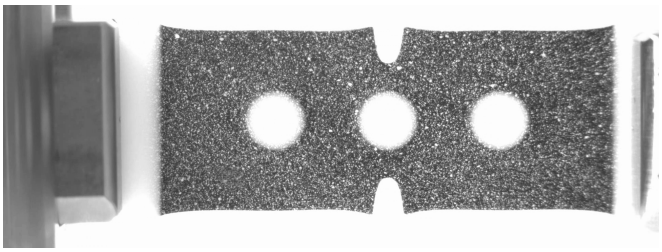

(b) $\Lambda = 1.1875$

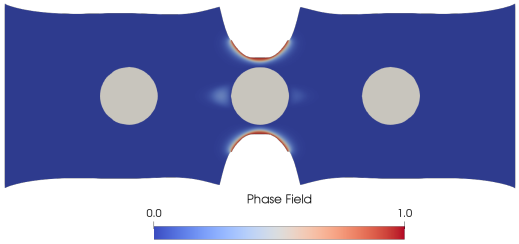

(c) $\Lambda = 1.3859$

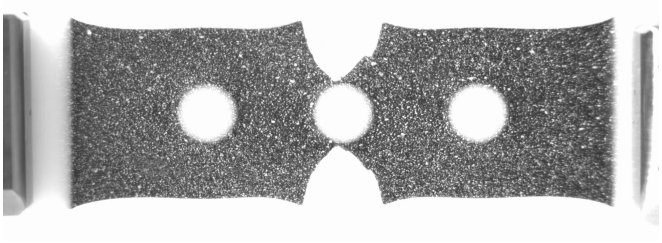

(d) $\Lambda = 1.4236$

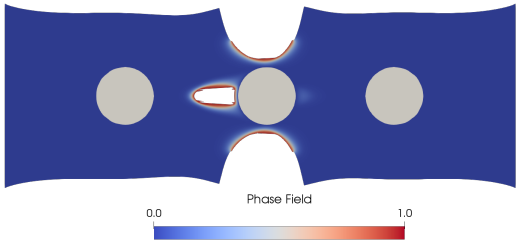

(e) $\Lambda = 1.3872$

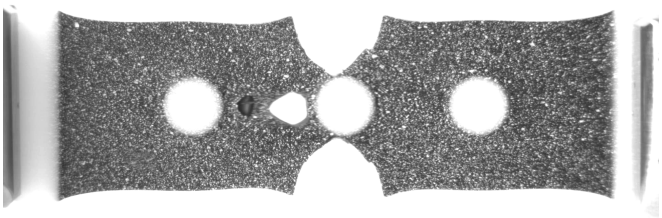

(f) $\Lambda = 1.4549$

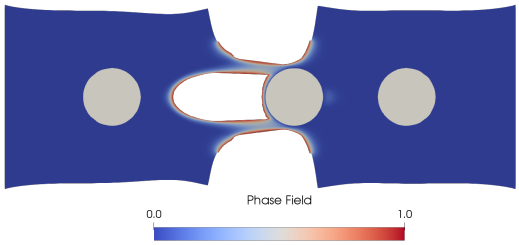

(g) $\Lambda = 1.3875$

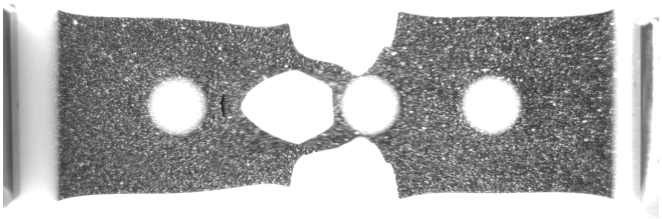

(h) $\Lambda = 1.4583$

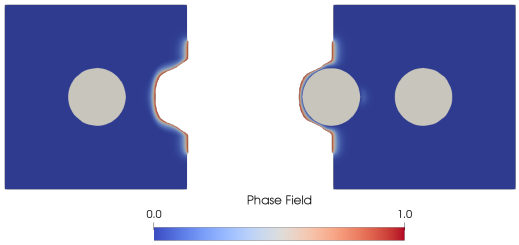

(i) $\Lambda = 1.3876$

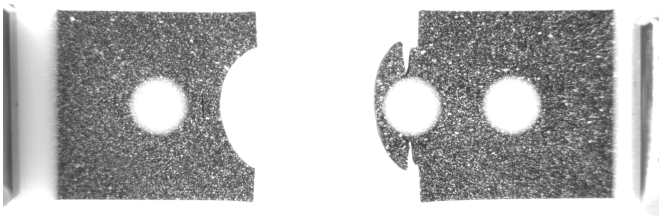

(j) $\Lambda = 1.4618$

Figure 5.8: N20D24 crack initiation sequence at different values of global stretch, Λ. Numerical results (left column) and experimental results (right column).

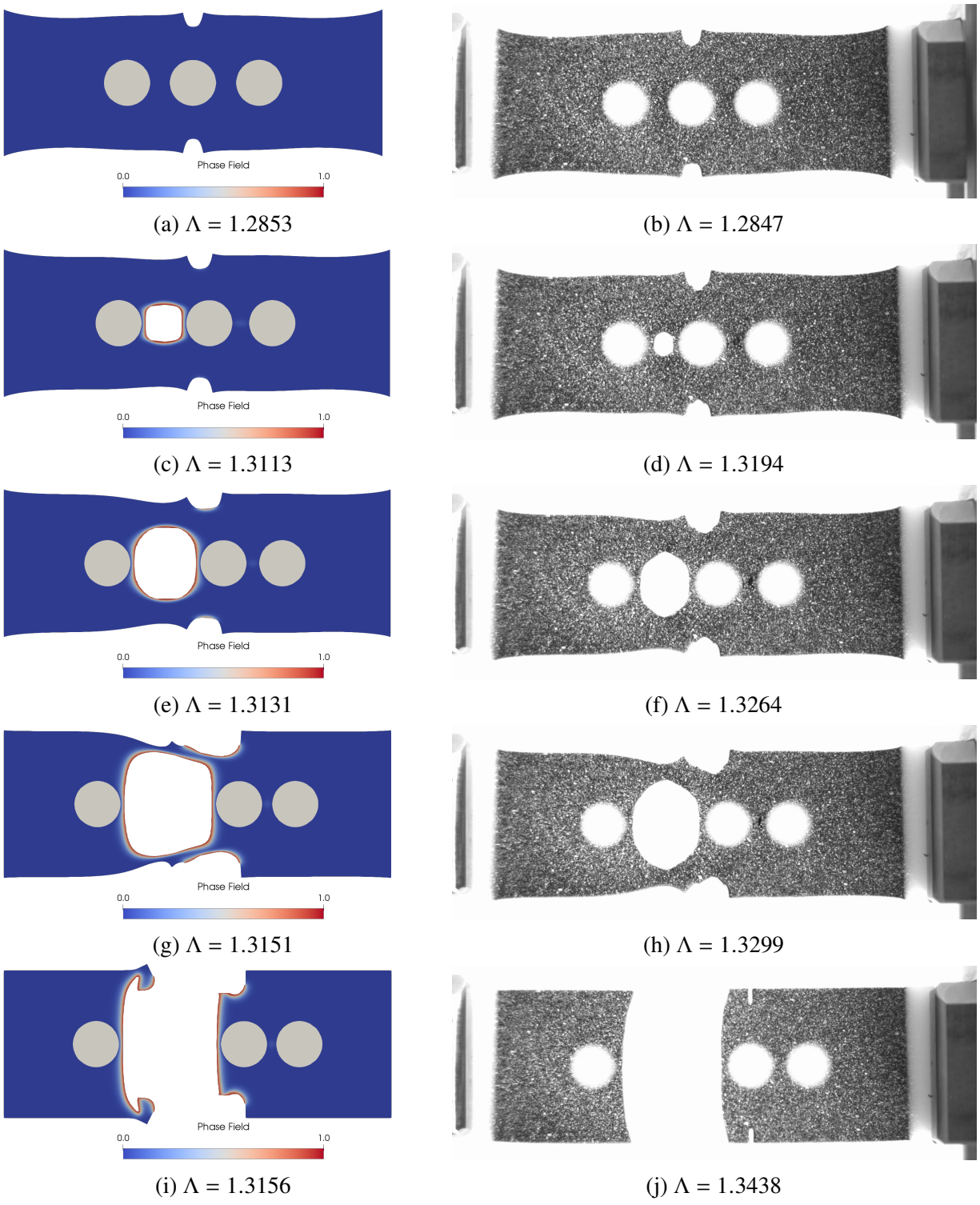

(a) $\Lambda = 1.2853$ (b) $\Lambda = 1.2847$

(c) $\Lambda = 1.3113$ (d) $\Lambda = 1.3194$

(e) $\Lambda = 1.3131$ (f) $\Lambda = 1.3264$

(g) $\Lambda = 1.3151$ (h) $\Lambda = 1.3299$

(i) $\Lambda = 1.3156$ (j) $\Lambda = 1.3438$

Figure 5.9: N10D18 crack initiation sequence at different values of global stretch, Λ. Numerical results (left column) and experimental results (right column).

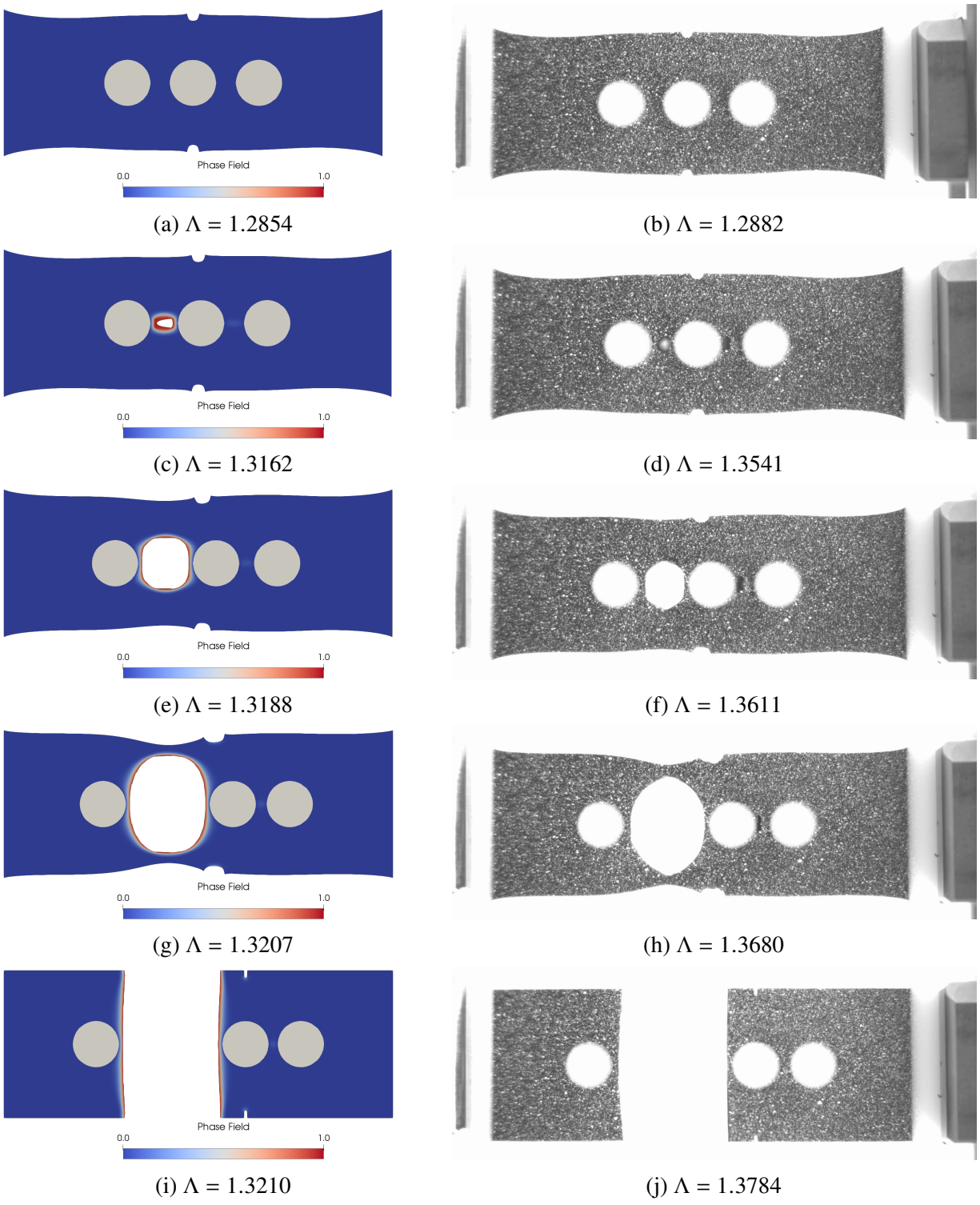

(a) $\Lambda = 1.2854$ (b) $\Lambda = 1.2882$

(c) $\Lambda = 1.3162$ (d) $\Lambda = 1.3541$

(e) $\Lambda = 1.3188$ (f) $\Lambda = 1.3611$

(g) $\Lambda = 1.3207$ (h) $\Lambda = 1.3680$

(i) $\Lambda = 1.3210$ (j) $\Lambda = 1.3784$

Figure 5.10: N05D18 crack initiation sequence at different values of global stretch, Λ. Numerical results (left column) and experimental results (right column).

5.4.2 Force versus displacement response

While in the previous section we focus on the qualitative failure behavior of the 3D-printed composites, here we examine the quantitative prediction via force-displacement curves. Figure 5.11 illustrates the experimental curves and corresponding numerical predictions (note that only one experiment for each geometry is shown for clarity). It is clear that an increase in the notch length leads to the slight decrease in the effective structural stiffness and a decrease in the critical strain at which crack initiation and subsequent catastrophic failure occur. This trend is also confirmed by the numerical simulations for all geometries irrespective of the distance between inclusions. Comparison between corresponding experimental and numerical data reveals very good agreement while the structures are loaded elastically, although minor under-prediction of the structural stiffness is observed when the inclusions are closest together (corresponding to $D = 18\ [mm]$). This can be explained by the absence of the out-of-plane stiffening effect near the rigid inclusions in the proposed plane stress formulation (see C.1).

Discrepancies are observed between experimental and numerical force-displacement curves only after crack initiation. As mentioned in the previous section, this is expected due to the very complex behavior of the soft 3D-printed material during failure. While the numerical prediction is not perfect, it is still fascinating that the numerical model with its simplifying assumptions (e.g. quasi-static, isotropic, rate-independent hyperelastic model in plane stress with a single numerical failure parameter, Ψ_c) is capable of qualitatively describing the failure behavior of the considered composite structures. For instance, we observe the force decrease due to crack initiation and subsequent force increase after crack arrest both numerically and experimentally when the inclusions are sufficiently far apart (e.g. $D = 30\ [mm]$). Furthermore, the specimens in which the inclusions are closest together ($D = 18\ [mm]$) fail catastrophically without crack arrest. Recall that in the former case cracks initially nucleate at the notch tip, while in the latter case cracks nucleate between the inclusions and exhibit fast subsequent crack propagation. These phenomena are illustrated briefly in C.2, while the numerically predicted crack initiation behavior at the notch tip is also briefly investigated in C.3 through comparison with contour integral calculations.

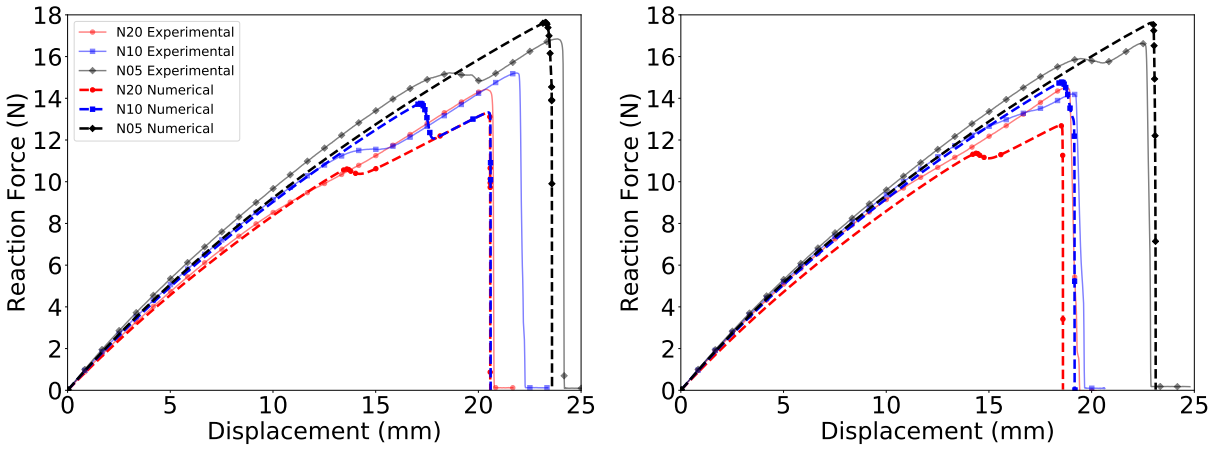

(a) $D = 30\ [mm]$ (b) $D = 24\ [mm]$

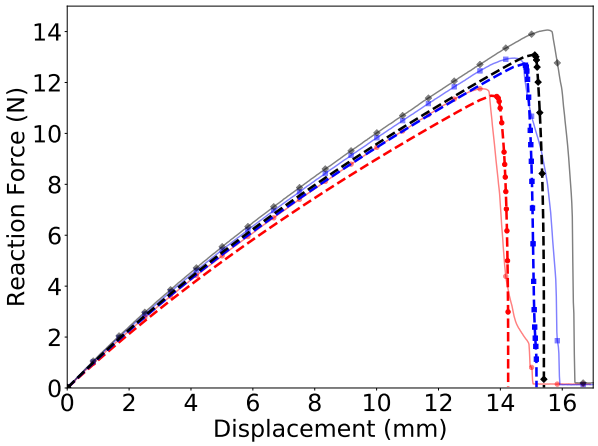

(c) $D = 18\ [mm]$

Figure 5.11: Experimental and numerical force versus displacement curves grouped by the geometric distance between inclusions (D).

In Figure 5.12 below, we present the numerically predicted force versus displacement curves grouped by notch length where we have included the numerical prediction for the homogeneous material without inclusions for comparison. For completeness, additional numerical simulations were performed using an initial notch length corresponding to 15% of the total width (i.e. N15D__), a distance between inclusions of 21 $[mm]$ (i.e. N__D21), and 27 $[mm]$ (i.e. N__D27) for a total of 20 numerically obtained values. In addition, the peak forces for each notch length are illustrated in Figure 5.13a along with the predicted results for the homogeneous case. It is clearly observed that for N10, N15, and N20 the inclusions provide a significant increase in strength (peak force) irrespective of the distances between the inclusions studied herein. However, the situation is quite

different for the shortest notch length N05 in which the inclusions must be sufficiently far apart in order to obtain an increase in strength when compared to the pure polymer case. We also note the presence of the local maximum for the N05 case which suggests that there is an optimal distance between inclusions that will maximize the strength. Spacing the inclusions closely together (e.g. $D = 18$) in this case clearly results in worse performance when compared to the homogeneous result. Finally, we highlight the fact that the addition of the rigid inclusions, when appropriately spaced, seem to also increase the structural failure stretch in all cases except for N05 where the is a marginal improvement when compared with N05D27. This is quite an interesting result since it is not unusual for the failure stretch to decrease with the addition of rigid particles (see [100] for instance).

5.4.3 External work comparison

While comparison between the failure sequences and force-displacement curves provides important insight into the behavior of proposed composite structures, we also provide the external work to failure as an additional quantitative measure for comparison. The external work to failure is computed via numerical integration of the force versus displacement curves presented in the previous section. Figure 5.14 below provides a simple visual comparison of the numerically and experimentally obtained external work.

Here we highlight the non-trivial appearance of a local maximum between N05D24 and N05D30. This likely occurs due to the approximate equality between the inclusion spacing and the space between outer inclusions and the rigid boundary for sample N05D27, which may contribute to the external work increase as a result of the more “uniform" load distribution in the soft matrix. We note this in addition to the peculiar shape of the surface near N10D21 where numerically we observe a deviation from the general trend. This deviation occurs during the transition between cracks nucleating at the initial notch tip and cracks initiating between inclusions. The N10D21 geometry results in predicted cracks initiating at both the initial notch tip and between inclusions, seemingly simultaneously. This simultaneous initiation of multiple cracks leads to the increase in

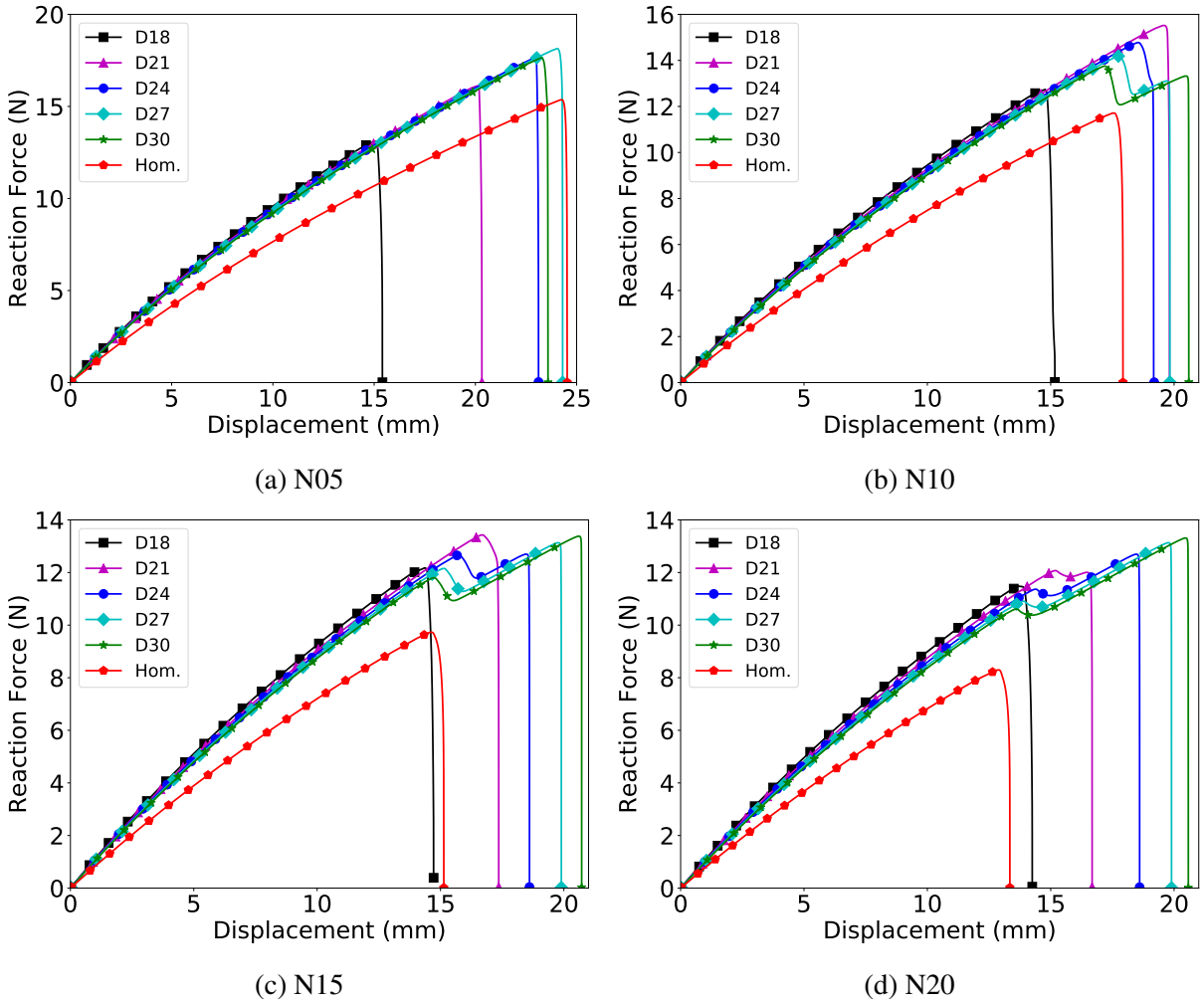

(a) N05

(b) N10

(c) N15

(d) N20

Figure 5.12: Numerical force versus displacement curves grouped by notch length along with the numerical prediction for the homogeneous case without inclusions for comparison.

the displacement required to finally separate the structure, which results in additional area under the force-displacement curve. Consistent with previously presented results, we see that the numerical model is capable of capturing the general trend of the experimental results.

The numerically predicted external work versus distance between inclusions is presented in Figure 5.13b along with the prediction for the homogeneous case without inclusions. In this figure we see the toughening effect explicitly associated with the addition of the rigid inclusions (i.e. the potential increase in external work required for complete structural failure resulting from the inclusion addition). However, for both the N05 and N10 cases the situation is not very straightforward since there appears to be a minimum distance between inclusions in order to improve this

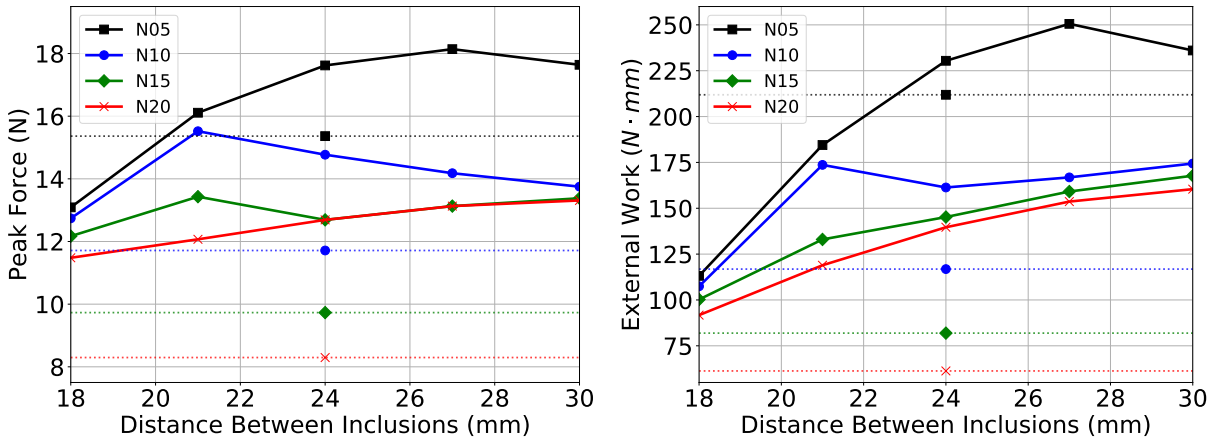

(a) (b)

Figure 5.13: Numerically predicted (a) peak forces and (b) external work versus distance between inclusions for each notch length. Additionally, a horizontal dotted line (with marker style of the corresponding notch length) signifies the predicted value for the homogeneous case without inclusions. Figure (b) is discussed in the following subsection but placed alongside (a) for ease of comparison.

measure of structural toughness. This is likely also true for the N15 and N20 cases but not for the range of distances between inclusions that we have studied herein (if one extrapolates the curves from $D = 18$ to $D = 16$ they would likely intersect the pure polymer case as well). Also, the appearance of the local maxima for the N05 and N10 cases clearly demonstrates that the optimal inclusion spacing for structural toughness is not a trivial matter. However, the curves do clearly show that spacing the inclusions too close together can certainly have a negative impact on the structure's mechanical performance.

5.5 Conclusion

In this chapter we investigate the failure of 3D-printed polymer composites comprised of a soft matrix with stiff inclusions. The composites are fabricated through multimaterial 3D-printing and uniaxial tests are performed to investigate their mechanical behavior and failure mechanisms. In order to obtain a more detailed picture of the underlying physics, we numerically simulate the failure of the composite structures using the phase field fracture method with an energetic threshold

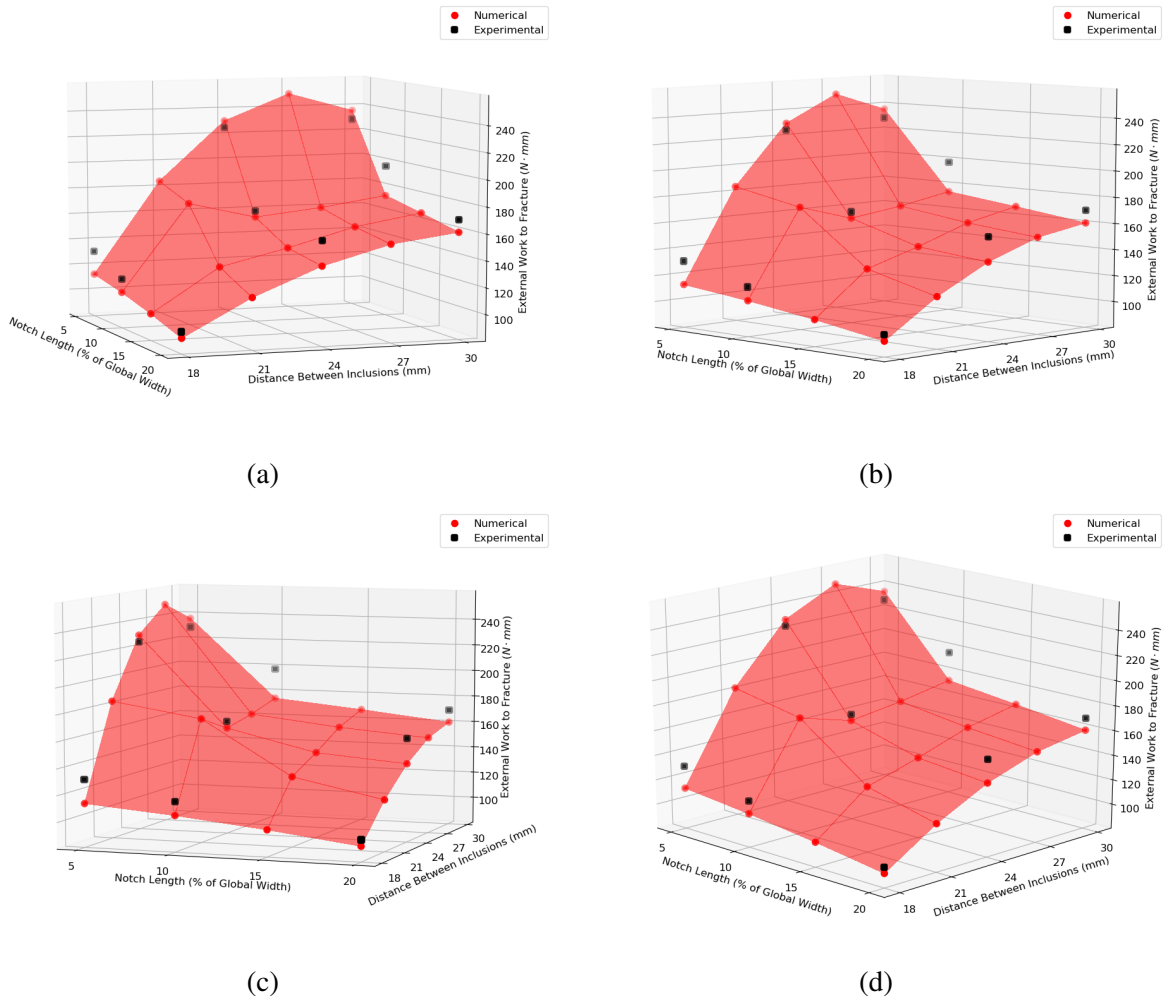

Figure 5.14: The numerically computed external work surface viewed from various angles along with the relevant experimentally computed data points.

using an efficient plane-stress formulation. The two-dimensional numerical formulation is provided and the reduced consistent tangent tensor is analytically derived.

It is demonstrated, both experimentally and numerically, that changes in particular geometric parameters (e.g. inclusion spacing and initial notch length) have a strong impact on the resulting failure sequence and overall structural resistance to failure. Although the numerical model is derived with several simplifying assumptions, the results demonstrate that it is capable of capturing the complex large deformation failure sequences of the 3D-printed composite structure presented herein. This includes a non-trivial secondary crack initiation and propagation in the bulk material consistent with the corresponding experimental observations.

Additionally we highlight an interesting behavior of the structures studied herein that is of practical interest. We have observed that the addition of stiff inclusions results in an expected improvement in the structure's mechanical properties (namely, the strength, toughness, and stiffness). However, the situation is not as obvious as one might expect. Spacing the inclusions too closely can clearly result in a degradation of structural strength and toughness. This has been demonstrated both experimentally and numerically. Not only does there appear to be a minimum inclusion spacing to be effective with respect to the homogeneous matrix case, but we have also numerically observed an optimal inclusion spacing which maximizes the structural strength and toughness (this is most clearly observed for the case with the shortest initial notch length).

Chapter 6

Cardiovascular stent design for an expandable valved conduit

6.1 Introduction

A cardiovascular stent design optimization method is proposed with application to a pediatric balloon-expandable prosthetic heart valve. Here we refer to a prosthetic replacement valved conduit which can be expanded to a larger permanent diameter *in vivo* via subsequent transcatheter balloon dilation procedures. While multiple expandable prosthetic heart valves are currently at different stages of development, in this chapter we focus on one particular design in which a stent is situated inside of an expandable polymeric valved conduit. Since the valve and conduit must be joined with a robust manufacturing technique, a polymeric glue layer is inserted between the two, which results in radial retraction of the conduit after expansion. We propose counteracting this phenomenon by designing an appropriate stent to maintain the desired permanent diameter throughout the device after a single non-compliant balloon dilation procedure.

The finite element method is used to compute performance metrics related to the permanent expansion diameter and required radial force. Additionally, failure due not only to high cycle fatigue but also due to ductile fracture is incorporated into the design study through the use of an existing ductile fracture criterion for metals. Surrogate models are constructed with the results of the high fidelity simulations and are subsequently used to numerically obtain a set of Pareto-optimal stent designs. Finally, a single design is identified by optimizing a normalized aggregate objective function with equal weighting of all design objectives. The ultimate goal is to design a device that may be permanently expanded from 12mm inner diameter (i.e. that of a neonate) to 24mm (approximately that of an adult). In this chapter we focus first on expansion from 12mm to 16mm

permanent inner diameter, which would effectively replace one open heart surgical procedure with a noninvasive transcatheter balloon dilation.

The remainder of this chapter is outlined as follows. The numerical approximation of the device geometry and stent parameterization are provided in Section 6.2, followed by the details of the numerical simulations in Section 6.3. Subsequently, the performance metrics that we consider in this study are provided in Section 6.4 and the surrogate-based multiobjective optimization procedure is summarized in Section 6.5. Finally, the numerical results are discussed in detail in Section 6.6 and concluding remarks are then provided.

6.2 Geometric parameterization

As mentioned briefly in the introduction, we examine the impact of 3 stent geometric parameters (i.e. the strut width, W, strut thickness, T, and number of circumferential patterns, NCP) on particular performance metrics, later presented in Section 6.4, along with two different stent materials (316L stainless steel and L605 cobalt chromium). The outer conduit is assumed to be constructed of e-PTFE (samples obtained from International Polymer Engineering [232]), while Carbothane^{TM} [233] is used as a polymeric glue. The geometry of a conceptual prototype is shown in Figure 6.1, along with a depiction of the fabrication procedure. The numerical approximation and parameterization of the stent geometry are illustrated in Figures 6.2 and 6.3, while in Figure 6.4 the numerical approximation of the assembly including the stent, conduit, and polymeric glue layers is shown. Note that the inner e-PTFE valve geometry has been omitted from the numerical analyses in an effort to decrease the computational complexity. This approximation is justified due to the low thickness and stiffness of the inner e-PTFE layer compared to the remainder of the structure, however it could also be considered in future studies. Creation of the stent CAD geometry is performed via the Python scripting interface of the CAD software, FreeCAD [234], while the conduit and glue layers are constructed via the Python scripting interface of Abaqus [235]. As shown in the next section, a non-compliant balloon (used for device expansion) is approximated in this chapter as a rigid, radially expanding cylindrical surface with an initial diameter of 12mm.

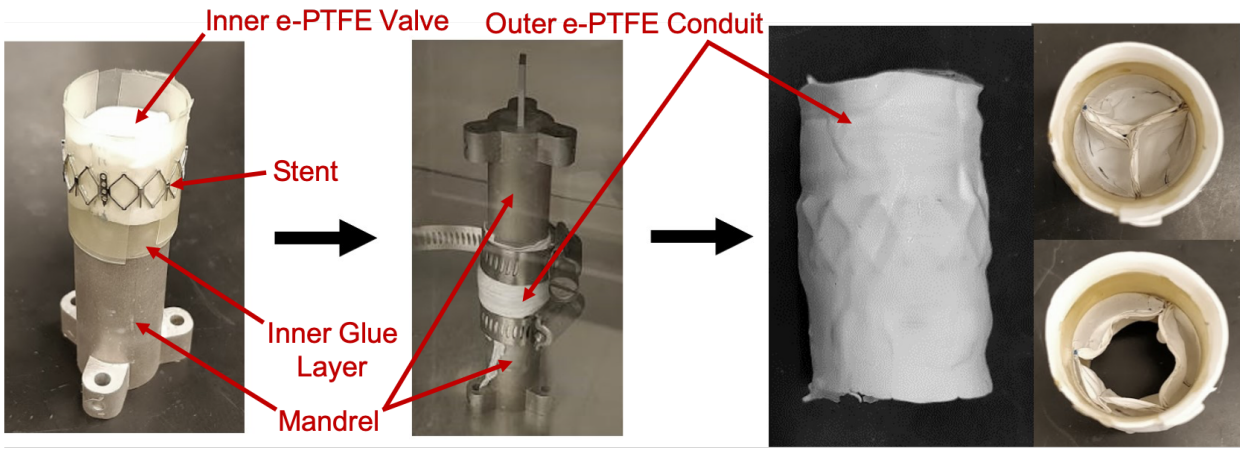

Figure 6.1: Valved conduit prototype fabrication illustration including depictions of the inner valve, polymeric glue layers, stent, and outer conduit.

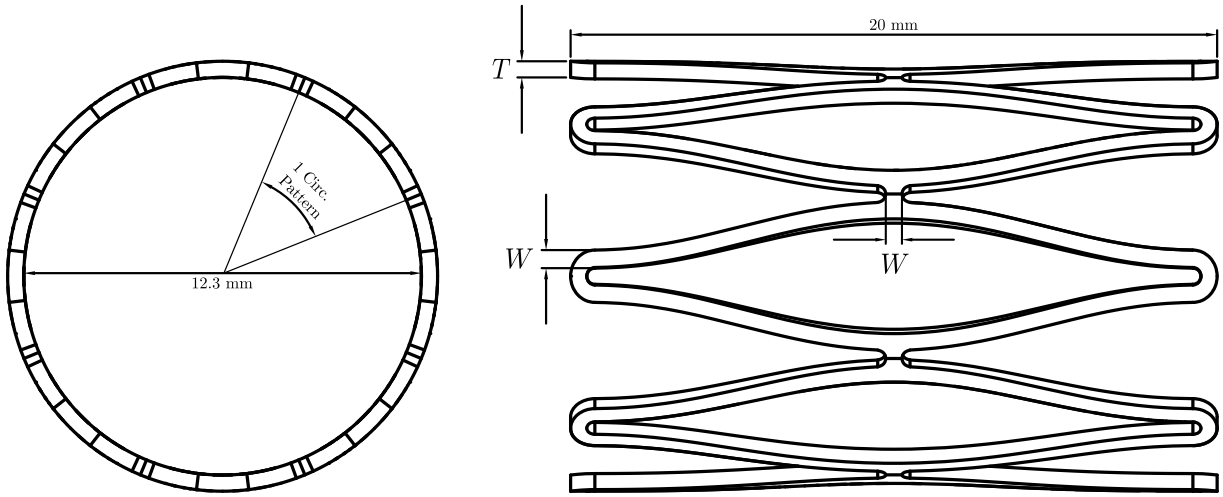

Figure 6.2: Stent geometry and parameterization where W and T represent the strut width and thickness, respectively. A single circumferential pattern is identified and the variable NCP is used to represent the total number of circumferential patterns.

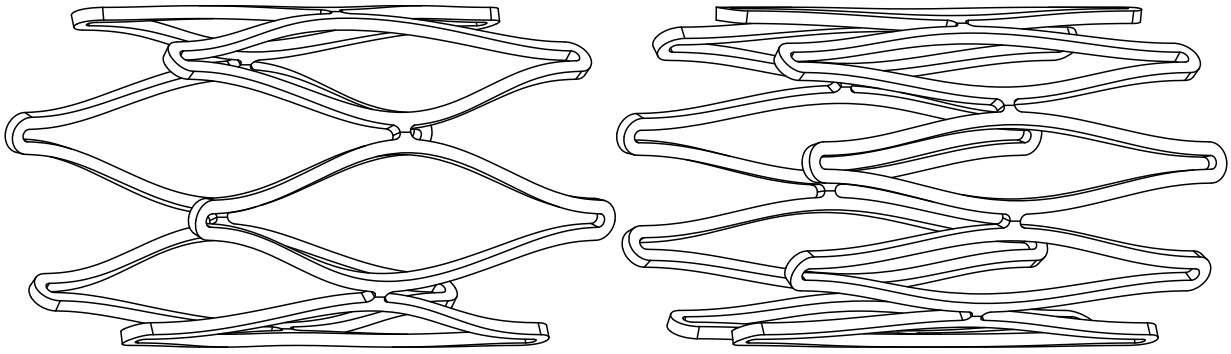

(a) (b)

Figure 6.3: Illustrations of stent realizations with (a) 6 NCP and (b) 9 NCP

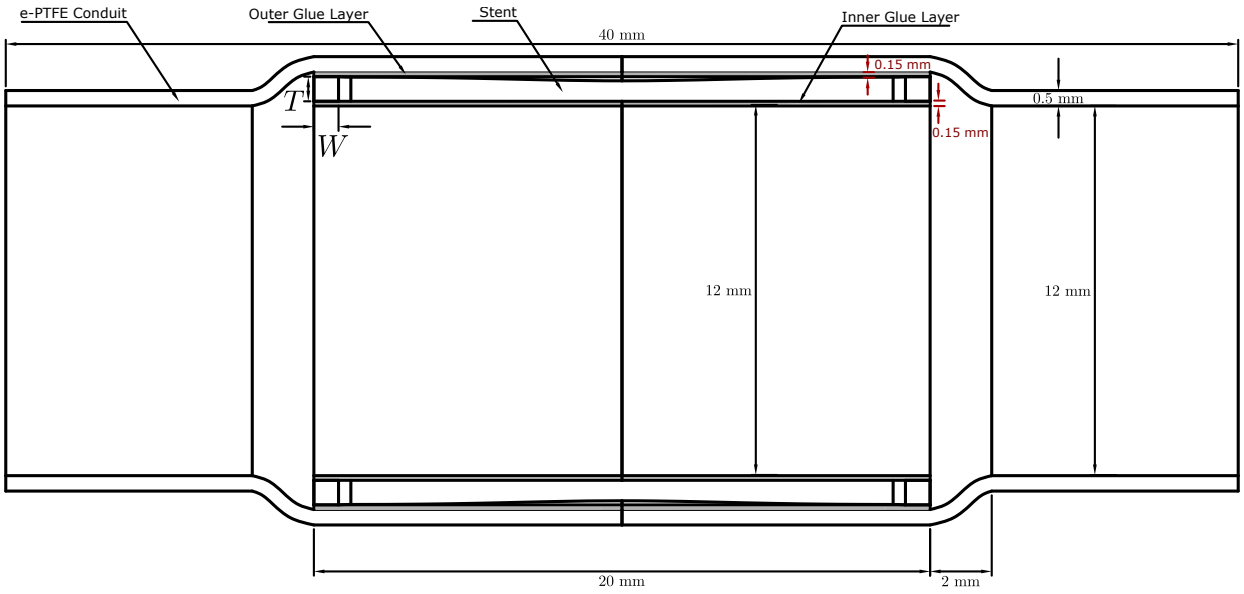

Figure 6.4: Cross-section drawing of the geometry used in the numerical simulations, including the outer conduit, stent, and inner/outer layers of polymeric glue.

6.3 Numerical simulation setup

The numerical models are created and executed using the Python interface to the commercial finite element software, Abaqus [235]. Symmetry boundary conditions are employed in a cylindrical coordinate system in order to significantly reduce the computational expense. This is illustrated along with the rigid balloon radial displacement boundary conditions and tie constraints between the stent and glue layers in Figure 6.5. Each geometry is partitioned in order to facilitate the creation

of a high quality hexahedral mesh, an example of which is shown in Figure 6.6. The volumetric components of the model (i.e. the conduit, polymeric glue, and stent) are all meshed with C3D20H hybrid finite elements, which interpolate the displacement field with nearly second order accuracy and also consist of a linear pressure field interpolation. Each element is fully integrated with a 27-point gauss quadrature rule. Although these elements require relatively high computational cost, they provide higher accuracy and alleviate any concern of volumetric or shear locking. In addition, the fully-integrated elements in the stent region ensure 9 to 12 integration points through the stent cross-section which provides the desired high accuracy for the ductile failure and fatigue metrics presented in the next section. A non-compliant balloon is approximated using a rigid cylindrical surface mesh consisting of reduced integration membrane elements (M3D4R) with fully specified nodal displacement/rotation boundary conditions. Hard contact is used between the outer balloon surface and the inner diameter of the device. The constitutive models and calibrated constants for each material (i.e. 316L stainless steel, L605 cobalt chromium, e-PTFE, and Carbothane^{TM} [233] polymeric glue) are presented in D.1.

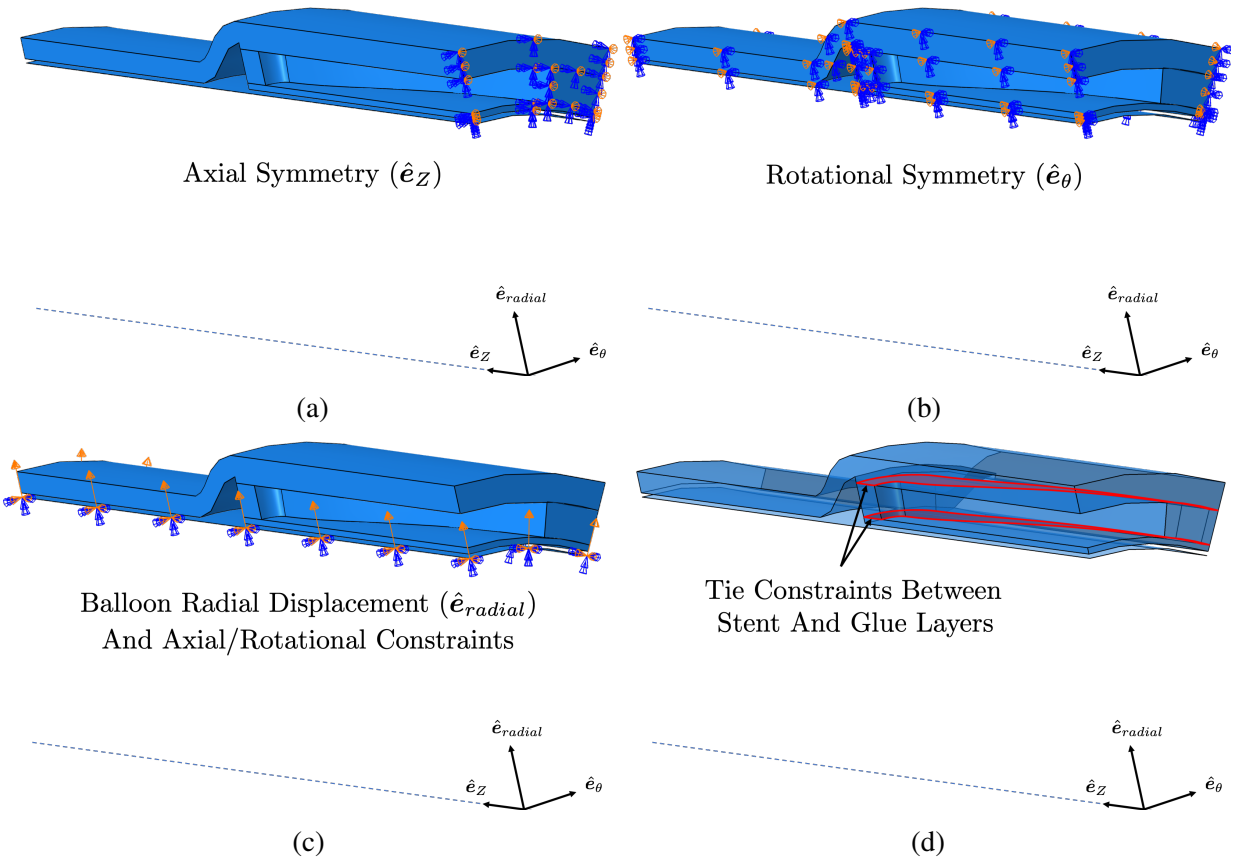

Figure 6.5: Boundary conditions in cylindrical coordinates (a-c) and tie constraints (d). The dashed-line marks the center axis of the device.

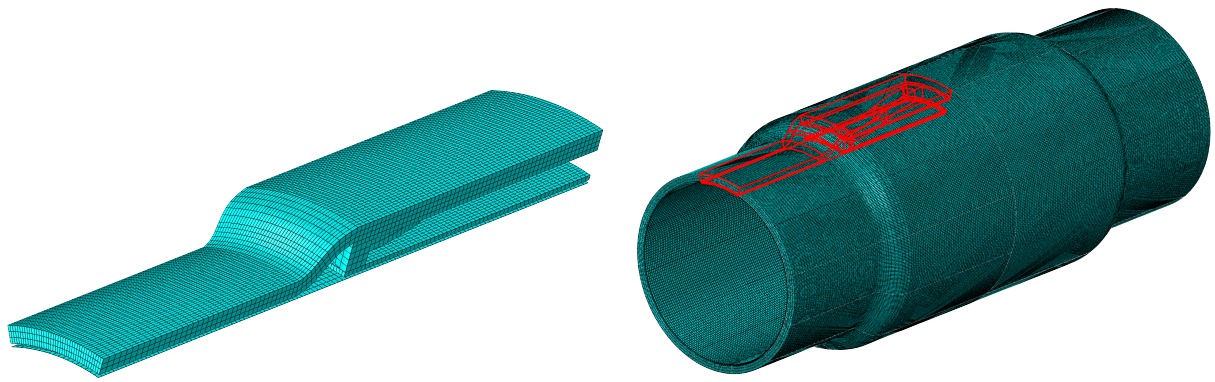

Figure 6.6: An example finite element mesh corresponding to one stent geometry realization. (a) Reduced model employing symmetry boundary conditions. (b) A full model illustrating the entire assembly and the location of the submodel shown in (a).

The rigid balloon is radially expanded from an initial diameter of 12mm to 22mm temporarily,

followed by radial retraction until the balloon is no longer in contact with the device. It is numerically predicted that the temporary 22mm expansion diameter would achieve the desired permanent expanded diameter of 16mm in a homogeneous e-PTFE conduit with 12mm initial inner diameter and 0.5mm thickness. Therefore, this is the basis for our design study. In other words, without the polymeric glue, the desired expanded diameter would be realized if the device is expanded temporarily to 22mm. The retractive behavior of the polymeric glue is illustrated in Figure 6.7 for the same geometry without a stent. It is shown that in the homogeneous e-PTFE conduit the 16mm diameter is realized while the polymeric glue limits the permanent diameter in the valved region to 14mm. On this basis we may then design the stent so as to counteract the retractive forces of the polymeric glue as previously mentioned. Once the balloon is removed, a typical pulmonary diastolic pressure loading of 10 mmHg is quasi-statically applied to the inner surfaces of the device, followed by an increase to a systolic pressure of 30 mmHg [236]. These two load states are used in a similar manner to much of the literature (e.g. [237, 238]) in order to estimate particular metrics associated with fatigue life, as further explained in the next section. Each model typically consists of 235-362k degrees of freedom and requires 3-5 hours of running time on a workstation with an Intel Xeon E3-1281 CPU and 16GB of RAM. For convenience, a typical numerical simulation sequence is illustrated in Figure 6.8.

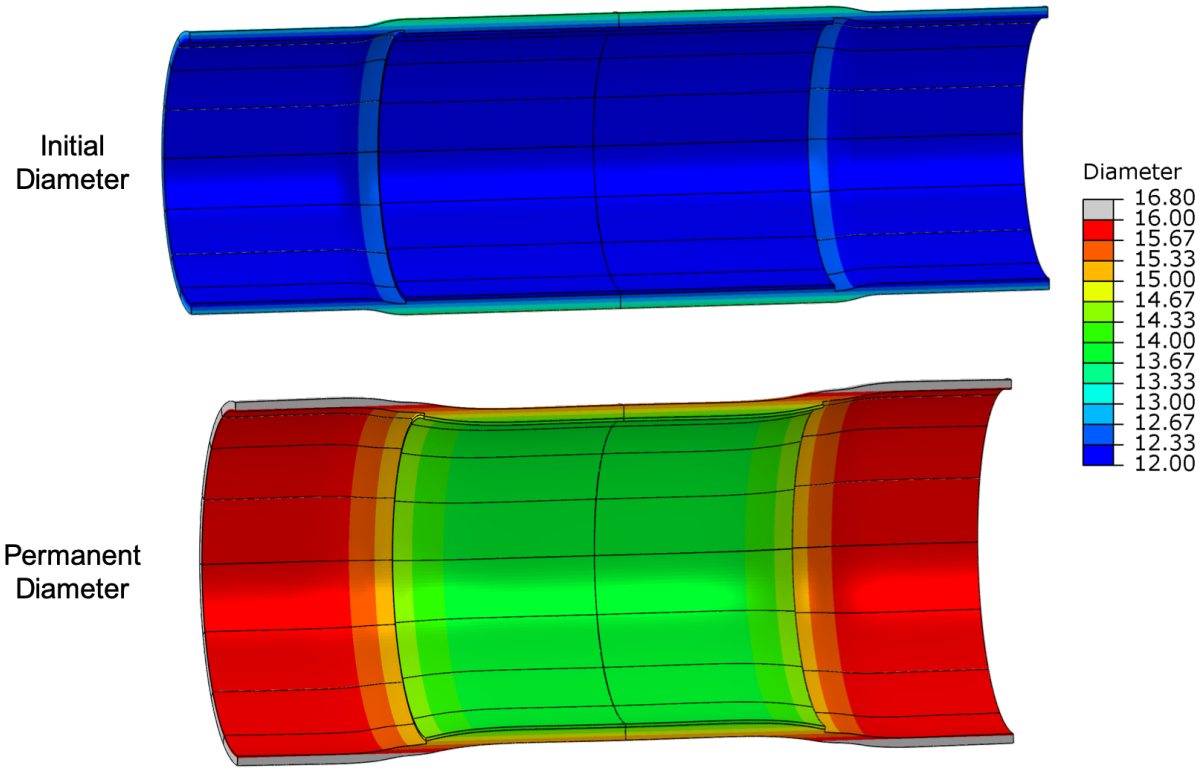

Figure 6.7: Cross-section of initial and predicted permanent configurations without a stent, illustrating the anticipated radial retraction in the central region due to the polymeric glue.

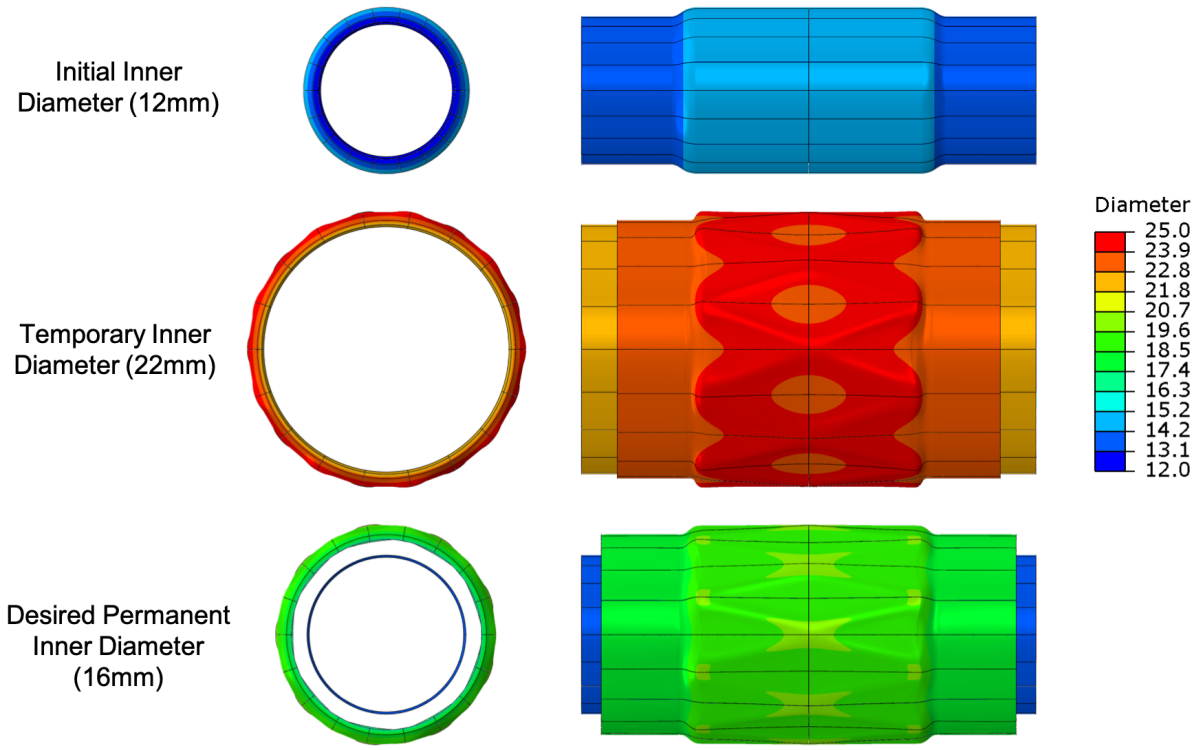

Figure 6.8: Simulation sequence from the initial state, to a temporary configuration during rigid balloon expansion, and finally to the desired permanent diameter at which the systolic and diastolic pressures are subsequently applied. Note that the geometry includes a stent.

6.4 Performance metrics

In this section we outline multiple response quantities of interest that can be numerically approximated. The relevant metrics used in this study include the mean and standard deviation of the predicted permanent inner diameter in the stented region, which we represent by the function notation $D_{\text{mean}}(\boldsymbol{\chi})/D_{\text{stddev}}(\boldsymbol{\chi})$, respectively. In other words, these functions represent the mean and standard deviation of the diameter computed over all of the inner-most glue layer's inner surface nodes in the permanently deformed configuration. Note that we use the shorthand symbol $\boldsymbol{\chi}$ to represent a realization of 3 geometric parameters and a selected stent material (i.e. $\boldsymbol{\chi} = \{W,\ T,\ NCP,\ \text{Stent Material}\}$). The goal is to design the stent so that it counteracts the retraction of the polymeric glue and helps achieve a permanent inner diameter in the valved region similar to that of the remainder of the conduit. We constrain the mean permanent diameter and minimize its

standard deviation in an effort to also provide some permanent diameter uniformity. Additionally, the peak radial force required to expand the stented region is of interest since the non-compliant balloon will be required to achieve this force during the expansion procedure. We represent this quantity with the notation $RF(\boldsymbol{\chi})$. Note that the peak radial force is computed via summation of the radial contact force over all inner surface nodes in this region.

Two additional metrics are used which are related to the durability of the stent itself. Design for fatigue resistance is one particularly important aspect of stent design that has been incorporated quite extensively in the literature. Due to the very large number of typical cardiac cycles, fatigue failure is a necessary component of any stent engineering analysis. The FDA [239] recommends a Goodman fatigue life analysis for stent design which has been incorporated into other works in the literature for stents constructed of both 316L stainless steel (e.g. [240, 141, 241]) and L605 cobalt chromium materials (e.g. [238, 237]), both of which are also explored herein. The Goodman criterion states that a fatigue failure may be expected when the stress amplitude ($\sigma_a \equiv |\sigma_{max} - \sigma_{min}|/2$) and mean stress ($\sigma_m \equiv |\sigma_{max} + \sigma_{min}|/2$) experienced during the pulsatile loading result in $\frac{\sigma_a}{\sigma_N} + \frac{\sigma_m}{\sigma_{UTS}} > 1$ at some location in the structure, where the maximum and minimum of a Cauchy stress invariant (here we use the von Mises stress, defined later) over a typical pulsatile load cycle is used for σ_{max} and σ_{min}, respectively. Note that σ_N and σ_{UTS} represent the fatigue limit and the ultimate tensile strength for the material, respectively. The relevant properties provided in [141] and [238] are used in this chapter for fatigue analysis (i.e. $\sigma_N = 115$ MPa, $\sigma_{UTS} = 580$ MPa for 316L, and $\sigma_N = 207$ MPa, $\sigma_{UTS} = 1449$ MPa for L605), however other values reported in the literature could also be employed. Although fatigue safety factors such as those in [238, 150] may be used, we have chosen the metric shown in Equation (6.4.1) since it is both dimensionless and directly provides a measure of constraint satisfaction for a particular stent design realization (i.e. $GF(\boldsymbol{\chi}) \leq 1$). Values greater than or equal to 1 indicate potential fatigue failure. Therefore we minimize this function, although it could also be formulated in a constraint with an upper bound equal to some fraction of 1.

$$GF(\boldsymbol{\chi}) = \max_{i \in [1,\ldots,N_{GP}^{\text{stent}}]} \frac{\sigma_a^i}{\sigma_N} + \frac{\sigma_m^i}{\sigma_{UTS}} \tag{6.4.1}$$

Note that N_{GP}^{stent} represents the total number of Gauss quadrature points in the stent finite element mesh.

While fatigue failure might be the governing failure mechanism, a stent intended to endure the very large temporary changes in diameter intended in this device may experience ductile failure during a balloon expansion procedure. Therefore, we incorporate a criterion for ductile failure into our design process, although ductile failure measures are generally not directly accounted for in the stent design literature. Many authors use the equivalent plastic strain or a particular stress invariant as a failure measure. However, since the work of Rice and Tracey [242], Gurson [243], and Bao and Wierzbicki [196] among many others, it has been known that ductile failure of metals likely depends quite strongly on the stress triaxiality, and potentially also on the Lode angle [197]. The work of Bao and Wierzbicki [186] demonstrated that the hydrostatic stress criterion worked quite well for predicting ductile failure in the range of high stress triaxiality. Although only the specific metal, aluminum 2024-T351, was investigated in their work, we also use this criterion as a predictive measure for ductile failure of the metals, 316L and L605, used herein. The calibration of the critical value of this criterion, DF_{crit}, for each of these materials is discussed in D.1 and the normalized ductile failure criterion used during the optimization process is expressed in Equation (6.4.2). The argument of max operator in the equation below represents the integral of the stress triaxiality over the equivalent plastic strain history at a material point.

$$DF(\boldsymbol{\chi}) = \frac{1}{DF_{crit}} \max_{i \in [1,\ldots,N_{GP}^{\text{stent}}]} \int_0^{\bar{\varepsilon}_p^i} \frac{p^i}{\sigma_{vm}^i} \, d\bar{\varepsilon}_p \tag{6.4.2}$$

Representing the Cauchy stress tensor with $\boldsymbol{\sigma}$, we note that $\bar{\varepsilon}_p = \int_0^t \sqrt{\frac{2}{3}\dot{\varepsilon}_{ij}^p \dot{\varepsilon}_{ij}^p} dt$ represents the equivalent plastic strain (with plastic strain rate tensor $\dot{\boldsymbol{\varepsilon}}^p$), $p = \frac{\sigma_{kk}}{3}$ is the pressure stress, and $\sigma_{vm} = \sqrt{\frac{3}{2} s_{ij} s_{ij}}$ is the von Mises stress, where $s_{ij} = \sigma_{ij} - p\delta_{ij}$ is the stress deviator. Note that Einstein summation convention is used and δ_{ij} is the Kronecker delta. Similar to the Goodman fatigue metric, ductile failure is predicted at some spatial point in the stent when $DF \geq 1$. Each of the parameters and performance metrics are summarized briefly in Table 6.1, below.

Table 6.1: Summary of design parameters and performance metrics

Design Parameter	Summary
W	Stent strut width $[mm]$
T	Stent strut thickness $[mm]$
NCP	Number of stent patterns around the circumference
Stent Material	Construction material of the stent (either 316L or L605)
Performance Metric	**Summary**
$D_{\text{mean}}(\boldsymbol{\chi})$	Mean permanent inner diameter in the stented region $[mm]$
$D_{\text{stddev}}(\boldsymbol{\chi})$	Standard deviation of permanent inner diameter in the stented region $[mm]$
$RF(\boldsymbol{\chi})$	Peak radial force exerted in the stented region during expansion $[N]$
$GF(\boldsymbol{\chi})$	Goodman metric for high cycle fatigue failure prediction of the stent
$DF(\boldsymbol{\chi})$	Hydrostatic criterion for ductile failure prediction of the stent

6.5 Surrogate-based multiobjective optimization procedure

Due to the relatively large computational expense associated with the high fidelity finite element simulations discussed in Section 6.3, surrogate models are constructed for each performance metric. The multiobjective optimization problem we wish to solve may be stated as follows.

$$\begin{aligned} \underset{\boldsymbol{\chi}}{\text{minimize}} \quad & GF(\boldsymbol{\chi}),\ DF(\boldsymbol{\chi}),\ RF(\boldsymbol{\chi}), D_{\text{stddev}}(\boldsymbol{\chi}) \\ \text{subject to} \quad & 0.4mm \leq W,\ T \leq 0.8mm \\ & 16.0mm \leq D_{\text{mean}}(\boldsymbol{\chi}) \end{aligned} \tag{6.5.1}$$

Note that while we notationally optimize over all parameters, χ, numerically we optimize over W and T, solving one multiobjective optimization problem for each fixed combination of NCP and stent material. Minimizing the Goodman fatigue and ductile failure metrics provide the desired failure resistance, while minimization of the peak radial force in the stented region is also desirable in order to improve the ease of device expansion with existing non-compliant balloons. In addition to these failure-type metrics we also minimize the standard deviation of the permanent diameter in the stented region in an effort to achieve some degree of permanent diameter uniformity. Bound constraints are placed on the stent strut width and thickness, while we also place a lower bound on the mean permanent diameter in the stented region equal to the target 16mm permanent expansion diameter. While one could also place an upper bound on the mean permanent diameter, we have found this to be unnecessary since the objective functions favor a decrease in D_{mean} (i.e. only the lower bound constraint is active).

Stent geometries with all combinations of five different strut widths ($W \in [0.4, 0.5, 0.6, 0.7, 0.8]$mm), five strut thicknesses ($T \in [0.4, 0.5, 0.6, 0.7, 0.8]$mm), and four different numbers of circumferential patterns ($NCP \in [6, 7, 8, 9]$) are created using the Python interface to FreeCAD as previously mentioned. The 100 resulting geometries are then imported into Abaqus and numerical models are created and executed as previously described in Section 6.3. A total of 200 high fidelity finite element simulations are completed (100 for each of two stent materials considered in this study). The performance metrics outlined in Section 6.4 are computed via an Abaqus Python post-processing script and the resulting data is tabulated into CSV files for subsequent analysis.

Since only the stent strut width, W, and thickness, T, are continuous parameters, C^1 cubic gridded interpolants are constructed in Matlab [244] for each performance metric shown with fixed combination of stent material and number of circumferential patterns, NCP. These surrogate models are then used to obtain 100 Pareto optimal points by replacing the high fidelity function evaluations in Equation 6.5.1 with their respective surrogates and using the Matlab built-in “paretosearch" function based on a direct multisearch algorithm for multiobjective optimization [245]. This surrogate-based multiobjective optimization problem is solved a total of eight times, once for each

unique combination of candidate stent material and number of circumferential patterns, NCP.

Subsequently, an equally weighted, normalized aggregate objective function is constructed in order to obtain a single optimal design candidate for each stent material. The performance metrics are normalized in the following manner. Minimum and maximum values of each performance metric (say a physical quantity Y and corresponding Y_{min}/Y_{max}) are computed over all results from the 200 high fidelity simulations. A single objective optimization problem may then be stated using an equally weighted, normalized aggregate objective function.

$$\begin{aligned} \underset{\chi}{\text{minimize}} \quad & \frac{GF(\boldsymbol{\chi}) - GF_{min}}{GF_{max} - GF_{min}} + \frac{DF(\boldsymbol{\chi}) - DF_{min}}{DF_{max} - DF_{min}} + \frac{RF(\boldsymbol{\chi}) - RF_{min}}{RF_{max} - RF_{min}} + \frac{D_{\text{stddev}}(\boldsymbol{\chi}) - D^{min}_{\text{stddev}}}{D^{max}_{\text{stddev}} - D^{min}_{\text{stddev}}} \\ \text{subject to} \quad & 0.4mm \leq W,\ T \leq 0.8mm \\ & 16.0mm \leq D_{\text{mean}}(\boldsymbol{\chi}) \end{aligned} \tag{6.5.2}$$

The solution of this single objective optimization problem is then obtained for each fixed combination of stent material and number of circumferential patterns as previously explained, using the constructed surrogate models. Aggregate objective values corresponding to optimized results are then used to further quantitatively compare the designs and provide a single result for a design candidate with good overall performance. An overview of this process is provided in Algorithm 5. This procedure results in not only the sets of Pareto-optimal designs from the solution of Equation (6.5.1), but also the identification of an optimized design with good performance via solution of Equation (6.5.2).

6.6 Numerical results

The cubic surrogate models for each function are illustrated in Figures 6.9 to 6.12 below. There are a few interesting things to note regarding the presented data. First, the nonlinearity of the Goodman fatigue metric is clear from Figure 6.9. The other performance metrics are also quite nonlinear in the design parameters. Additionally, it is interesting to see that while the normalized ductile failure criterion is generally lower for 316L with respect to L605, the Goodman fatigue metric indicates much better fatigue performance for L605. This is at least partially explained

Algorithm 5 Overview of the design optimization procedure

```
for Stent Material in [316L, L605] do
  for NCP in [6, 7, 8, 9] do
    for W in [0.4mm, 0.5mm, 0.6mm, 0.7mm, 0.8mm] do
      for T in [0.4mm, 0.5mm, 0.6mm, 0.7mm, 0.8mm] do
        Perform high fidelity simulation and compute (D_mean, D_stddev, RF, GF, DF)
      end for
    end for
    Construct cubic surrogate model for each performance metric
    Solve Equation (6.5.1) for a set of 100 Pareto-optimal (W, T) pairs and store
    Solve Equation (6.5.2) for a single optimal (W, T) pair and store
  end for
end for
Identify parameters producing lowest aggregate objective value in Equation (6.5.2)
```

by the seemingly high ultimate tensile strength stated in much of the literature for L605 [238, 237]. Additional test data should be obtained to validate the Goodman parameters for the material thickness range of interest. Also, note that most of the design region places the Goodman metric above 1 for the 316L stent, indicating a potential fatigue failure. Figure 6.11 illustrates that the peak radial force required to expand the stented region of the device generally increases with the number of circumferential patterns, NCP, although this observation is reversed for large enough strut width (W) and thickness (T). The other metrics (GF,DF,D_{stddev}) all increase with a decrease in NCP for fixed W and T, showing a clear benefit to including a larger number of circumferential patterns.

As mentioned in the previous section, these surrogate models were then used to obtain a set of 100 Pareto-optimal points for the multiobjective optimization problem stated in Equation (6.5.1). Two dimensional trade-off plots for every unique combination of the 4 objective functions (6 in total) are provided in Figures 6.13 to 6.18. The results shown in Figure 6.13 are particularly interesting since they illustrate the conflicting trade-off between ductile failure resistance during expansion and the subsequent resistance to high cycle fatigue failure. Although larger values of the normalized ductile failure criterion are predicted for the L605 stent, the values are still quite low (a value greater than 1 would represent a ductile failure prediction). However, subsequent future expansions (not currently considered in this chapter) may result in ductile failure for the L605 material, while 316L

might generally be safer. This highlights the difficulty of the design problem since 316L may be better for large diameter expansions, but it also might be subject to higher risk of fatigue failure. Additionally we note that in each case, with the exception of the peak radial force (RF), increasing the number of circumferential patterns (NCP) is beneficial. The peak radial force clearly increases more rapidly with increasing strut width (W) as opposed to strut thickness (T) as expected, but the values for fixed W and T do not seem to vary greatly with the number of circumferential patterns (NCP). The opposite effect is observed for the standard deviation of the permanent diameter (D_{stddev}), which appears to be overwhelmingly most sensitive to NCP.

Plots of the normalized aggregate objective function in Equation (6.5.2) are provided in Figure 6.19, along with the Pareto-optimal points and the result of solving the single objective optimization problem. Equation (6.5.2) is solved using the gradient-based “fmincon" optimizer with an initial guess equal to the Pareto-optimal point which produced the lowest normalized aggregate objective function value. The CAD geometry corresponding to the optimized designs for both 316L and L605 were created and high fidelity numerical analyses were completed for each. Table 6.2 provides the values of the objective functions at the corresponding optimized parameter set for each material and NCP. The surrogate function values are provided alongside the results from additional high fidelity simulations with the optimized parameters in order to partially demonstrate the very high accuracy of the surrogate models. As expected, the L605 material allows generally thinner stent struts to be used. The optimized geometric design parameters obtained for 316L are (0.46mm W, 0.8mm T, 9 NCP) and (0.5mm W, 0.4mm T, 9 NCP) for L605. The spatial distribution of the permanent diameter in the stented region, the normalized ductile failure criterion, and the Goodman fatigue metric are also illustrated in Figures 6.20, 6.21, and 6.22, respectively. As anticipated, the largest ductile failure and fatigue measures are concentrated on the inner radii of the stent members. The Goodman diagrams for each optimized design are also provided in Figure 6.23, illustrating the proximity of each integration point’s fatigue measure in the stent to the Goodman limit. This again demonstrates the relative superiority of L605 over 316L. Pending verification of the material parameters and constitutive models employed, one can conclude that the optimized L605 stent with

aforementioned parameters is best suited to achieve our goal as stated mathematically in Equation (6.5.2). It is also clear from Figure 6.19h that the L605 material may allow for a better performing design with a stent strut thickness below the 0.4mm lower bound assigned in this study. Based on Figure 6.19g, a similar observation is noted for 316L if strut thicknesses greater than 0.8mm were allowed. Finally, although we do not optimize these quantities directly, the spatial distributions of the peak von Mises stress and the equivalent plastic strain are also provided in Figures 6.24 and 6.25, respectively.

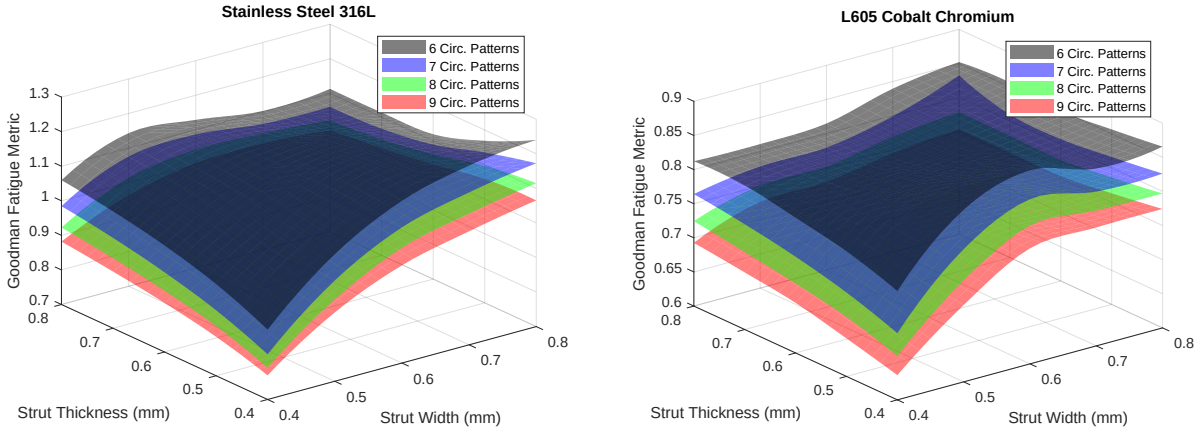

(a) (b)

Figure 6.9: Illustrations of the GF surrogate models created for each stent material and number of circumferential patterns, NCP.

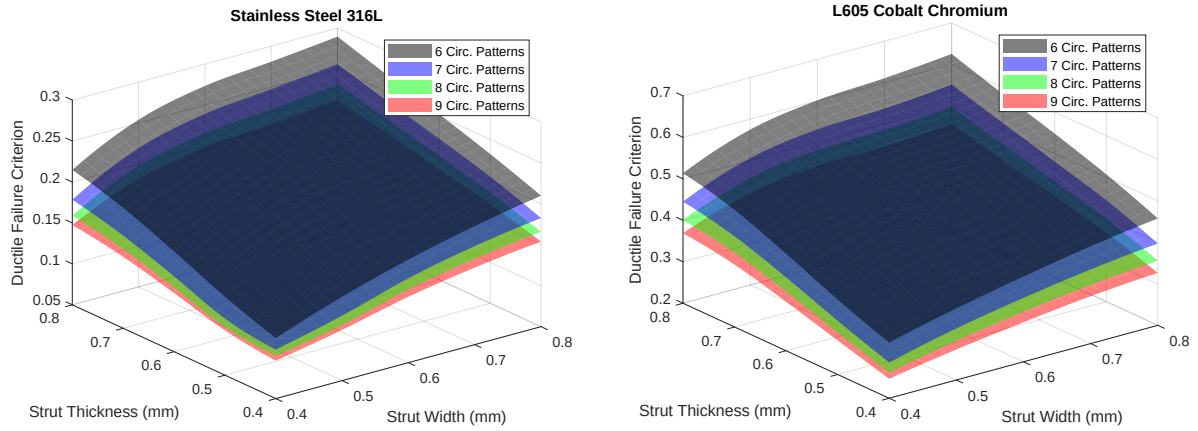

(a) (b)

Figure 6.10: Illustrations of the DF surrogate models created for each stent material and number of circumferential patterns, NCP.

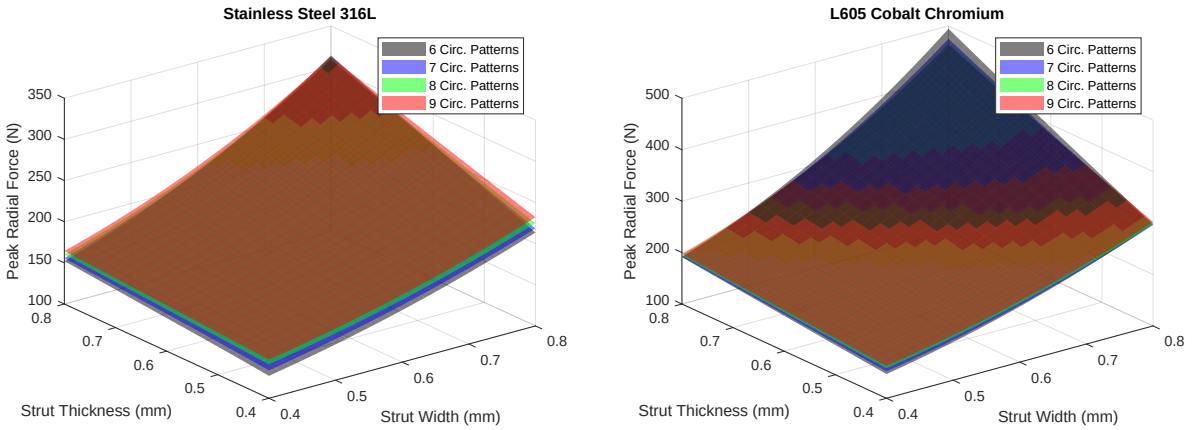

(a) (b)

Figure 6.11: Illustrations of the RF surrogate models created for each stent material and number of circumferential patterns, NCP.

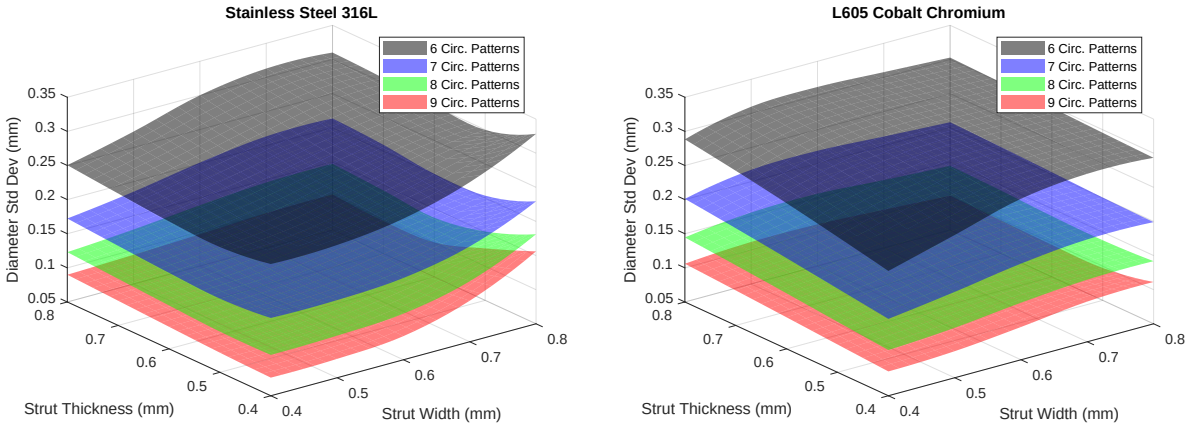

(a) (b)

Figure 6.12: Illustrations of the D_{stddev} surrogate models created for each stent material and number of circumferential patterns, NCP.

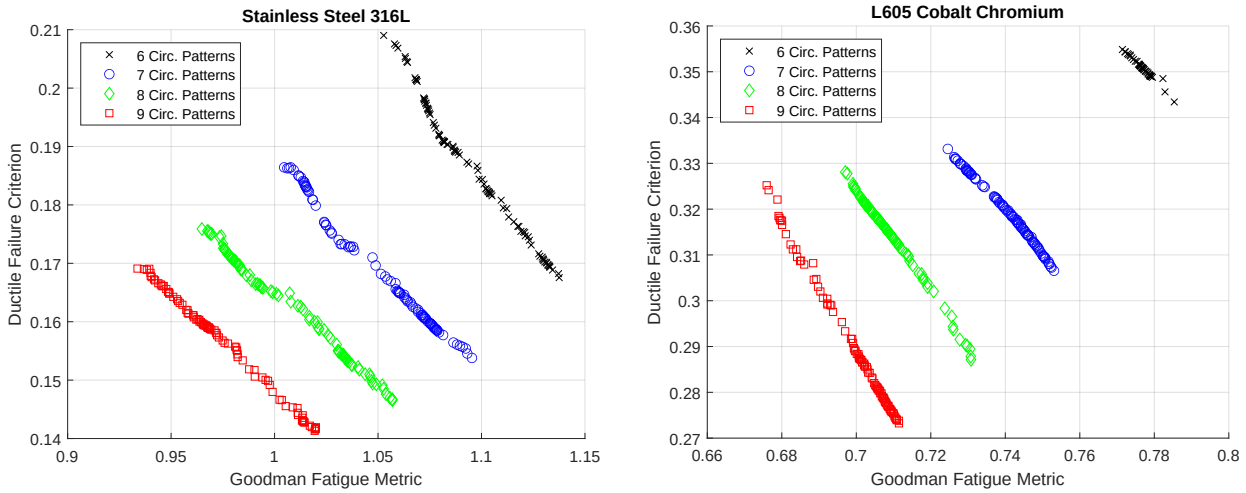

(a) (b)

Figure 6.13: Pareto-optimal points illustrating the trade-off between GF and DF for (a) 316L and (b) L605 stent materials

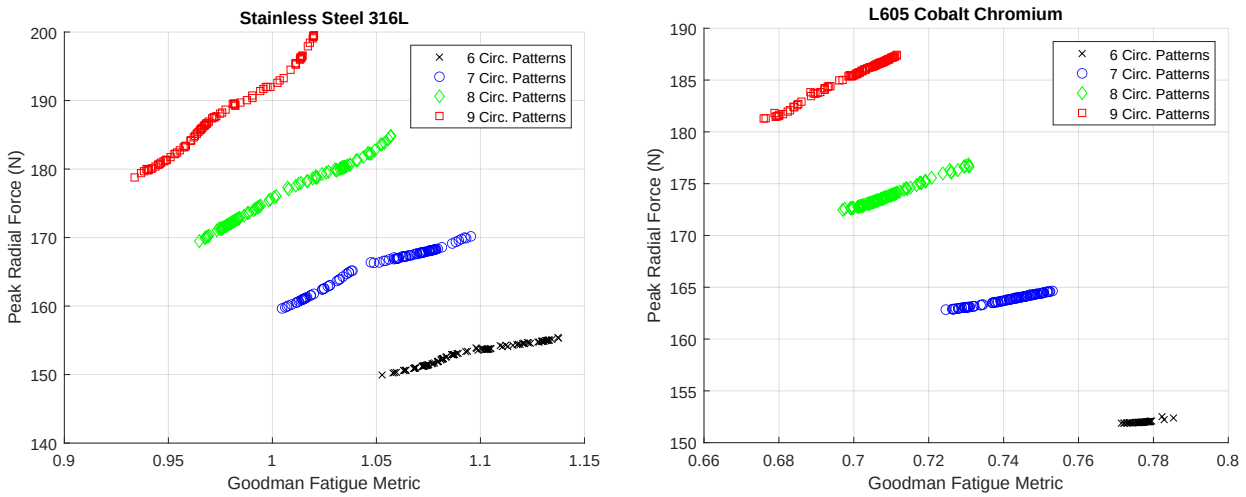

(a) (b)

Figure 6.14: Pareto-optimal points illustrating the trade-off between GF and RF for (a) 316L and (b) L605 stent materials

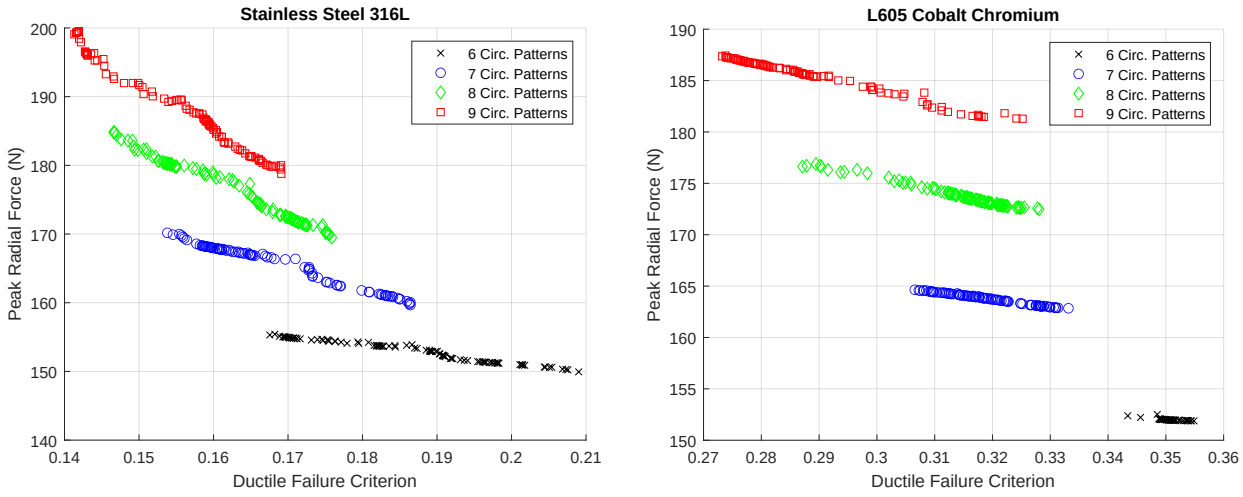

(a) (b)

Figure 6.15: Pareto-optimal points illustrating the trade-off between DF and RF for (a) 316L and (b) L605 stent materials

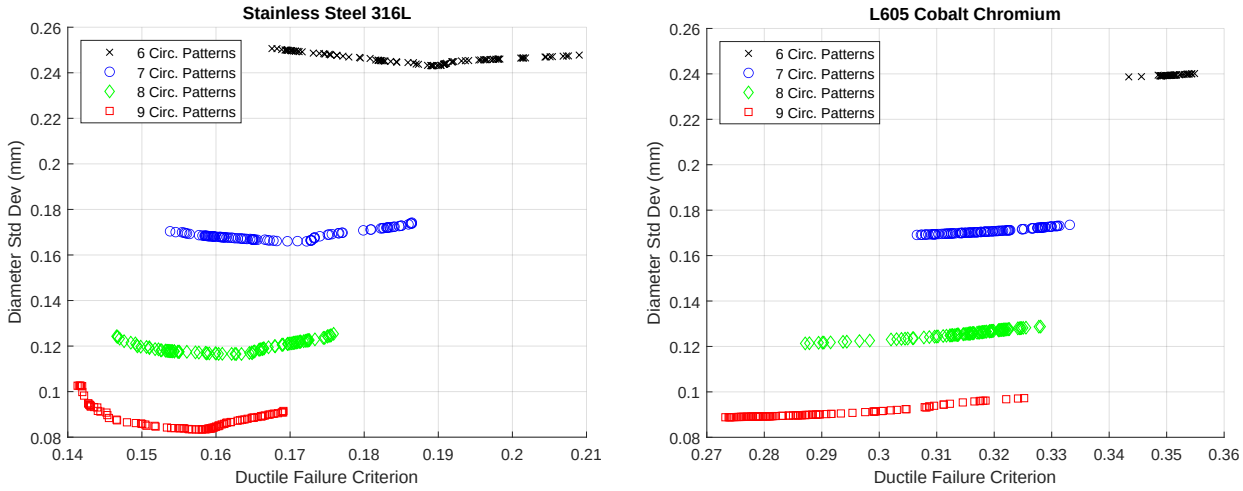

(a) (b)

Figure 6.16: Pareto-optimal points illustrating the trade-off between DF and D_{stddev} for (a) 316L and (b) L605 stent materials

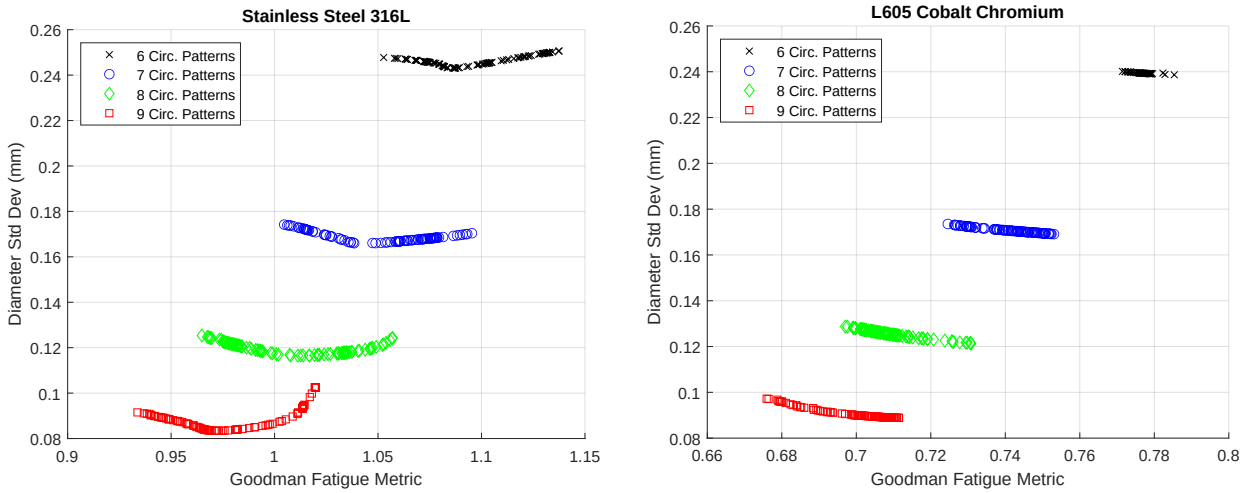

(a) (b)

Figure 6.17: Pareto-optimal points illustrating the trade-off between GF and D_{stddev} for (a) 316L and (b) L605 stent materials

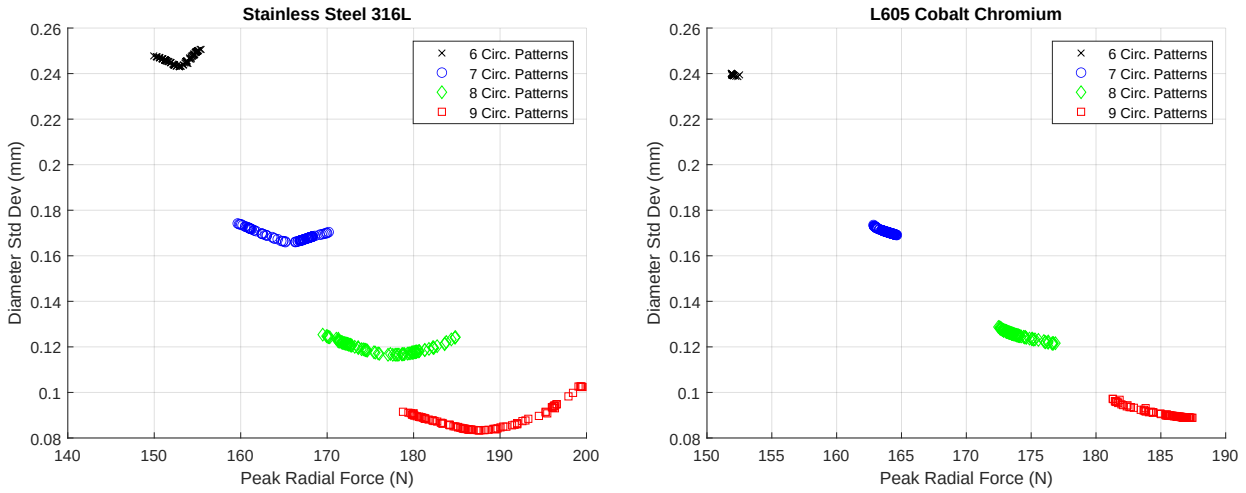

(a) (b)

Figure 6.18: Pareto-optimal points illustrating the trade-off between RF and D_{stddev} for (a) 316L and (b) L605 stent materials

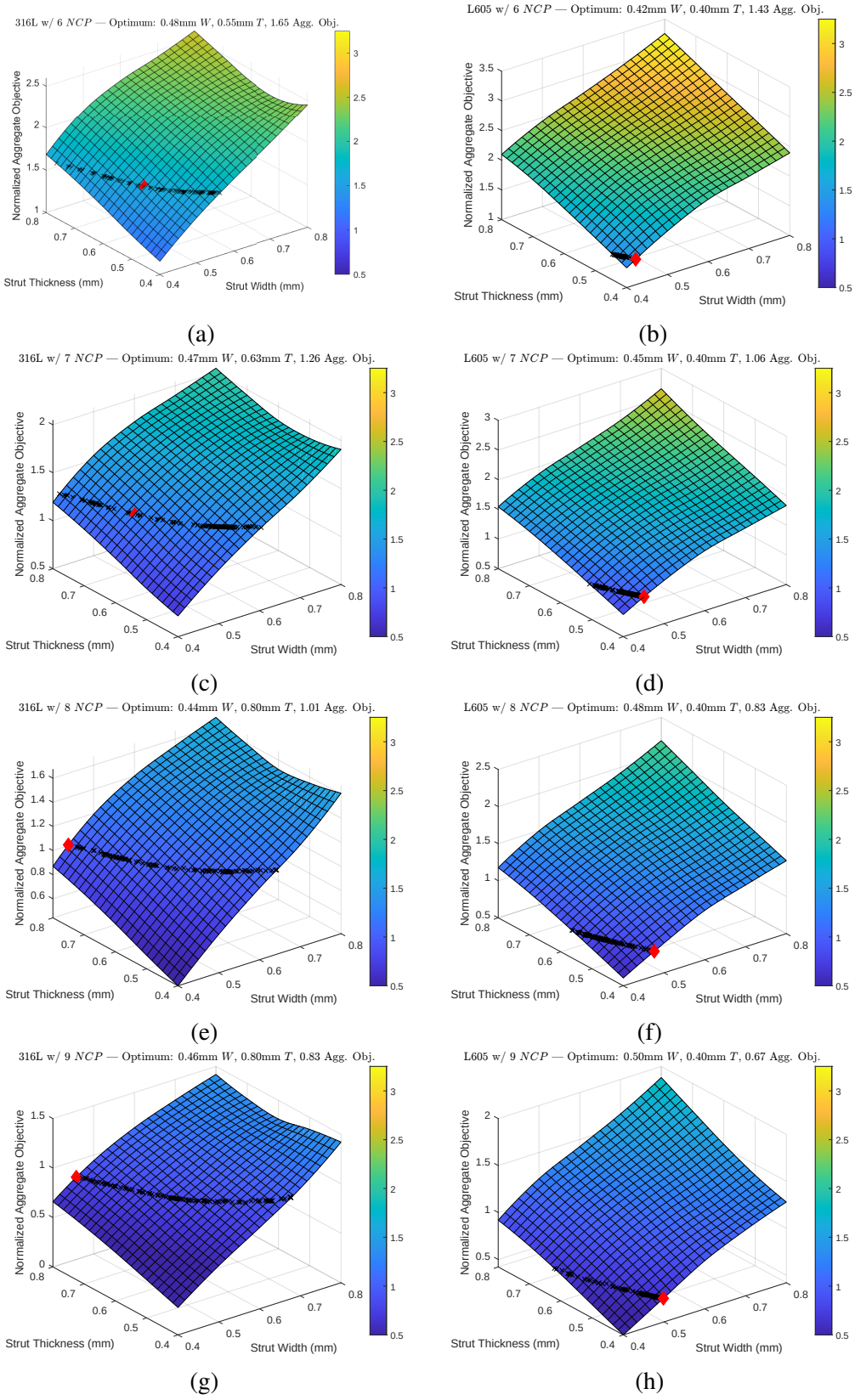

Figure 6.19: Aggregate objective function surfaces for each combination of NCP and stent material. Pareto-optimal points are illustrated with black x markers. The optimal point of Equation (6.5.2) is marked by a red diamond.

Table 6.2: Performance metric values corresponding to the optimized designs obtained by solving the single objective optimization problem in Equation (6.5.2). Note that W^* and T^* refer to the optimized values of W and T, respectively, "Mat." represents the stent material, and "A.Obj." signifies the value of the aggregate objective function in Equation (6.5.2) evaluated with the corresponding optimized parameters. Note that D_{mean} is not reported since the constraint is active and the value is equal to 16mm in all cases. For each objective function high fidelity verification simulations were completed with the optimized parameters in order to validate the results, partially demonstrating very high accuracy of the surrogate models. The high fidelity responses are provided in parentheses.

Mat.	NCP	W^*	T^*	GF	DF	RF $[N]$	D_{stddev} $[mm]$	A.Obj.
316L	6	0.48	0.55	1.080 (1.088)	0.191 (0.189)	152 (153)	0.244 (0.245)	1.65
316L	7	0.47	0.63	1.030 (1.021)	0.176 (0.175)	163 (162)	0.169 (0.169)	1.26
316L	8	0.44	0.80	0.965 (0.966)	0.176 (0.178)	169 (171)	0.125 (0.125)	1.01
316L	9	0.46	0.80	0.934 (0.934)	0.169 (0.171)	179 (179)	0.092 (0.091)	**0.83**
L605	6	0.42	0.40	0.785 (0.780)	0.343 (0.346)	152 (152)	0.239 (0.238)	1.43
L605	7	0.45	0.40	0.753 (0.744)	0.307 (0.315)	165 (164)	0.169 (0.169)	1.06
L605	8	0.48	0.40	0.731 (0.735)	0.287 (0.288)	177 (178)	0.121 (0.122)	0.83
L605	9	0.50	0.40	0.711 (0.713)	0.273 (0.274)	187 (188)	0.089 (0.089)	**0.67**

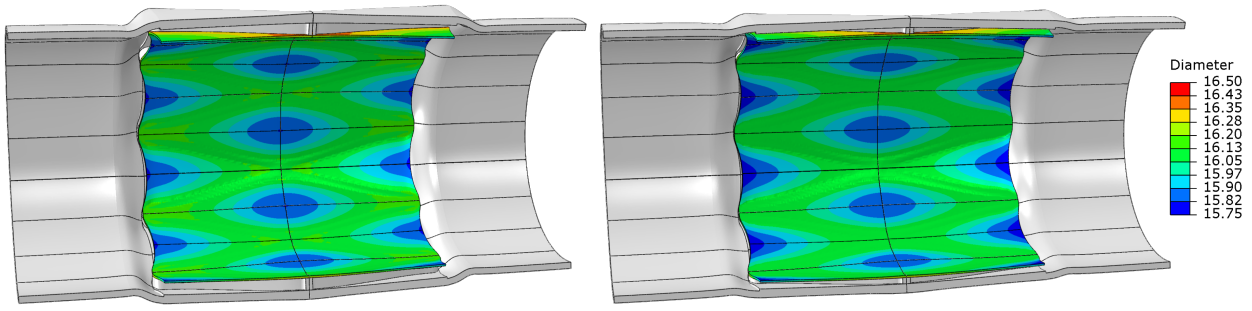

(a) (b)

Figure 6.20: Spatial variation of the permanent diameter in the stented region for (a) 316L and (b) L605 stent materials with optimized stent parameters.

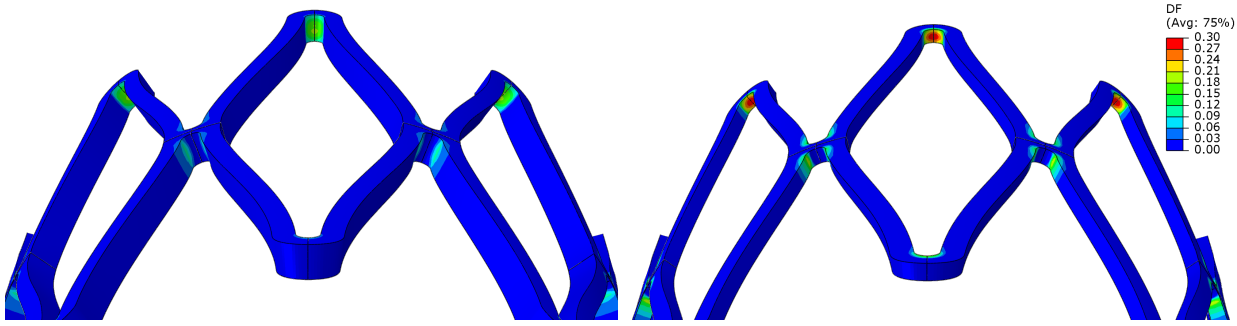

(a) (b)

Figure 6.21: Spatial variation of the normalized ductile failure criterion (DF) for (a) 316L and (b) L605 stent materials with optimized stent parameters.

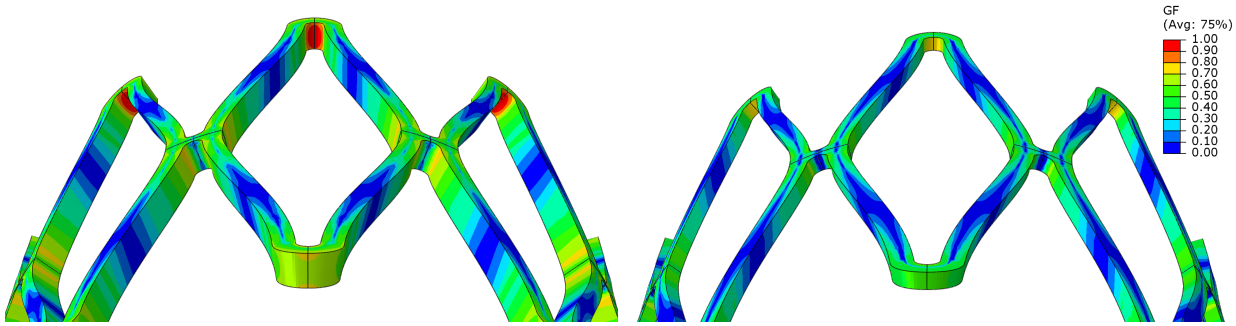

(a) (b)

Figure 6.22: Spatial variation of the Goodman fatigue metric (GF) for (a) 316L and (b) L605 stent materials with optimized stent parameters.

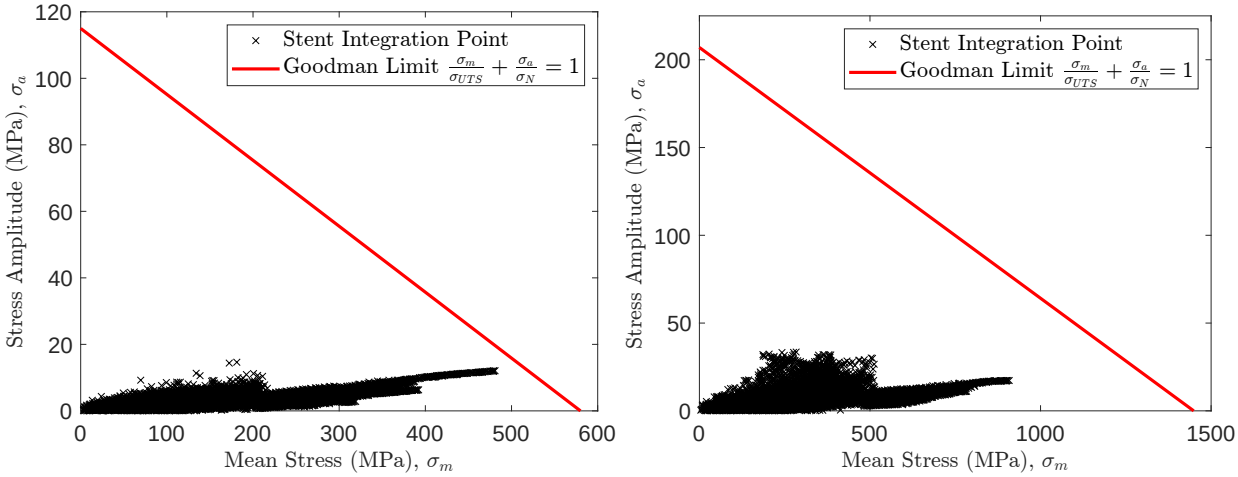

(a) (b)

Figure 6.23: Goodman fatigue diagrams for (a) 316L and (b) L605 stent materials with optimized stent parameters.

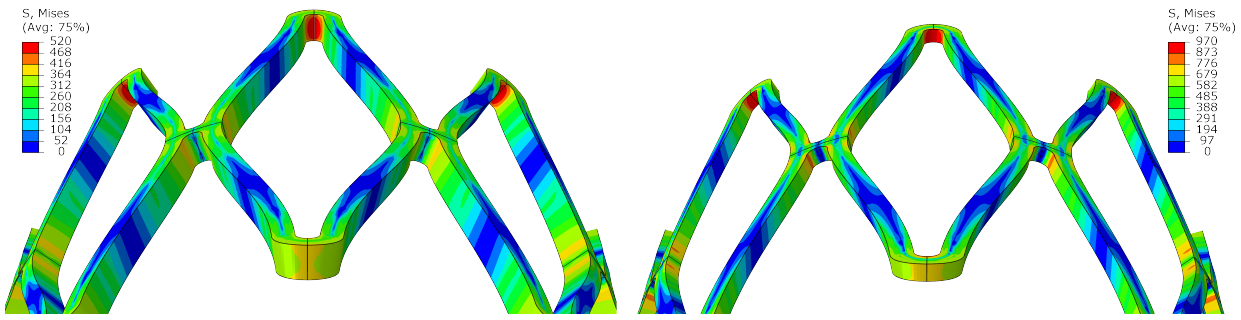

(a) (b)

Figure 6.24: Spatial variation of the von Mises stress (σ_{vm} [MPa]) for (a) 316L and (b) L605 stent materials with optimized stent parameters.

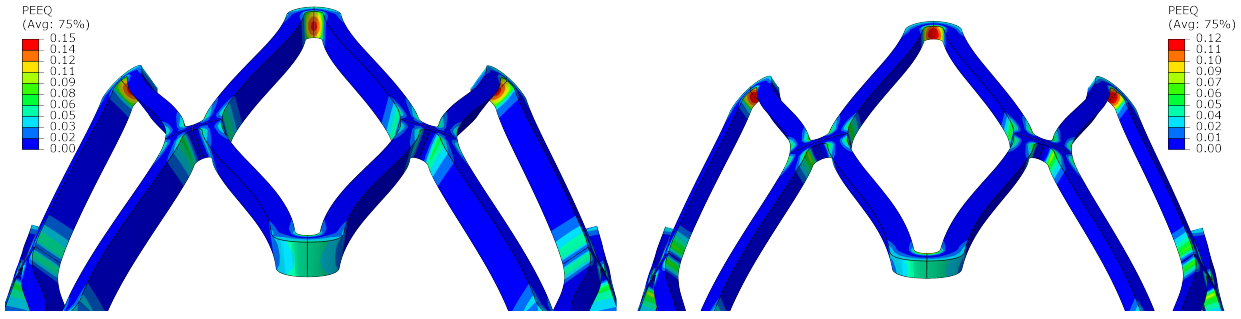

(a) (b)

Figure 6.25: Spatial variation of the equivalent plastic strain (PEEQ) for (a) 316L and (b) L605 stent materials with optimized stent parameters.

6.7 Conclusion

A multiobjective stent optimization procedure is proposed for the design of an expandable prosthetic valved conduit with particular relevance to the pediatric population born with CHD. In addition to metrics associated with fatigue failure, a measure of ductile failure during expansion is also incorporated into the optimization procedure. It is demonstrated that the proposed procedure is capable of producing a stent design with relatively low required radial force, that meets design durability criteria, and maintains sufficient radial stiffness to counteract the retractive forces of the polymeric glue layer used during construction. Pareto-optimal designs are obtained and illustrated using smooth cubic surrogate models and the relevant trade-offs between design objectives are

provided. Additionally, a single aggregate objective function is defined in which each of the original objective functions are normalized and equally weighted in order to provide a direct comparison of all designs and arrive at a single optimized result with good performance. It is shown that permanent expansion from 12mm to 16mm permanent inner diameter is achievable while maintaining the mechanical integrity of the structure. Thus, is it possible to eliminate the need for at least one open heart surgical procedure. Additionally, as we look forward to our ultimate goal of expansion to 24mm inner diameter, this study provides some confidence that this will indeed be possible since we observe desirable metrics of stent durability when the L605 stent material is employed. Expanding the design space to other stent materials and more geometric design flexibility seems quite promising in this regard.

Chapter 7

Conclusion

7.1 Scope and contribution

In this thesis multiple numerical design optimization techniques for improving structural resistance to failure are proposed. This includes two density based topology optimization formulations for achieving low weight designs with enhanced brittle fracture resistance, as presented in Chapter 2 and 3. In both formulations the brittle fracture physics are explicitly simulated during the optimization process using the phase field fracture method. In the first, we demonstrate the effect of constraining the phase field approximation of the fracture energy which ultimately results in structures with increased strength when compared to the results of typical stiffness based topology optimization formulations. Additionally, the analytical path-dependent sensitivities of the relevant functions are derived and a numerical efficiency gain is proposed for use during the sensitivity analysis, based on a Schur-complement type condensation performed at the element level. This efficiency gain is applicable to all path-dependent topology optimization problems in which local degrees of freedom at each quadrature point are spatially independent (i.e. the local degrees of freedom at one quadrature point do not explicitly depend on the local degrees of freedom at any other quadrature point). This procedure greatly improves the speed of the analytical sensitivity computation since significantly smaller linear systems must be solved.

In the second formulation for brittle fracture resistance, introduced in Chapter 3, several additional enhancements are proposed which greatly improve the topological results and numerical performance of the method. Importantly, it is shown that a judicious selection of the functions used in the topology optimization procedure is required in the case of brittle fracture physics

due primarily to the strongly nonlinear forward problem and use of gradient-based optimization methods. A new aggregate objective function is proposed in which the function sensitivities contain significantly more information, importantly including knowledge of the system state before fracture. This ultimately provides the optimizer with enough information to reduce the size of existing cracks and ultimately arrive at a design that does not fracture under the applied load. A phase field formulation with an energetic threshold is also used which helps provide increased local control of the topology. Additionally, the driving force for phase field fracture is smoothed in order to mitigate additional nonlinearity without significantly affecting the physics of the forward analysis. This procedure helped to ensure some degree of differentiability in regions near the tensile energy density threshold and significantly improved the convergence characteristics of the optimization process. It was shown that the method results in designs which remove re-entrant corners as expected and outperform those associated with a current stress-constrained topology optimization formulation. Designs were compared based on an increase in strength-to-weight ratio, ultimately showing the large improvement obtained with the proposed method with respect to the current state of the art.

In Chapter 4 design for both ductile failure and buckling resistance is addressed. The emphasis was placed on a numerically efficient formulation for increasing peak load carrying capacity and structural toughness when a ductile material is considered for the structural design. Since hundreds of forward analyses must be conducted over the course of a typical topology optimization procedure, the efficiency of the formulation is extraordinarily important in practice. Local ductile failure constraints were imposed with an aggregation-free Augmented Lagrangian method, enabling the solution of practical problems with millions of local constraints. Buckling resistance was obtained via an additional linear elastic buckling analysis that served as an efficient pseudo-problem for producing a function with sensitivities that drive support for structural members in compression. This greatly simplifies and improves the efficiency of the design optimization procedure. All of the relevant sensitivities are analytically derived for the path dependent forward problem and are numerically verified with finite differences. An additional pseudo buckling mode filter is also proposed which assisted in the removal of spurious numerical buckling modes that sometimes

occur in regions of high density. These modes are not removed from consideration using existing strain energy type filters proposed in the literature. The optimized topologies for each of three numerical examples were extracted, remeshed, and subject to a large deformation ductile phase field fracture analysis in lieu of desired experimental testing. This verification step was shown to be very important when simplified physics such as small deformation and/or linear elasticity are used during the optimization procedure as is often the case in the literature. Large gains in both peak load carrying capacity and the external work required to achieve the peak load were demonstrated for each of the numerical examples. Additionally we note that the results were obtained using calibrated constitutive properties for Aluminum 2024-T351 with experimental data provided by Bao [185] in an attempt to show realistic expected performance gains. This included calibration of the nonlinear hardening law and the triaxiality-dependent, large deformation ductile phase field fracture model used for optimized design comparison.

Chapter 5 is devoted to the numerical and experimental analysis of an additively manufactured polymeric composite in which hard inclusions are embedded in a soft matrix material. A parameterized geometry with two geometric parameters is proposed in order to methodically study the resulting failure behavior. Multiple uniaxial tension experiments with different parameter realizations were conducted to complete separation of the specimens. A large strain hyperelastic phase field fracture model is used for the numerical predictions, including an analytically derived plane stress formulation for numerically efficiency, and the analytical reduced consistent tangent tensor. It is shown that changes in the distance between 3 circular inclusions and the length of two initial notches result in different complex failure sequences, observed both experimentally and numerically. Structural resistance to failure is shown to be heavily dependent on these parameters, which is particularly useful for practicing designers. While it is expected that increasing the initial notch length decreases the structural strength, the behavior observed from changing the distance between inclusions is shown to be non-trivial. In particular, we demonstrate that decreasing this distance provides the stiffening effect of the material and an increase in strength that are typically desired, however too short of a distance results in premature failure with crack nucleation occuring in the

matrix between inclusions. Subsequent additional numerical analyses suggest that there is in fact an optimal inclusion spacing for a fixed initial notch length, which maximizes the external work required to cause catastrophic failure. Significant increases in the strength are also demonstrated with respect to the same geometry constructed without inclusions. Finally, we highlight that the numerical and experimental results are shown to be in good qualitative and quantitative agreement for the complex failure sequences observed, further demonstrating the potential of the phase field method for predicting the failure of increasingly complex materials.

In Chapter 6 a multiobjective stent optimization procedure is proposed for the design of an expandable prosthetic valved conduit with particular relevance to the pediatric population born with Congenital Heart Disease (CHD). In addition to optimizing a metric associated with high cycle fatigue failure, a measure of ductile failure during expansion is also incorporated into the optimization procedure. It is demonstrated that the proposed methodology is capable of producing a stent design with relatively low required radial force, that meets design durability criteria, and maintains sufficient radial stiffness to counteract the retractive forces of the polymeric glue layer used during construction. A set of Pareto-optimal designs is obtained using smooth cubic surrogate models and the relevant trade-offs between performance metrics are illustrated. Additionally, a single aggregate objective function is defined in which each of the original objective functions are normalized and equally weighted in order to provide a direct comparison of all designs and arrive at a single optimized result with good performance. It is shown that expansion from 12mm to 16mm permanent inner diameter is achievable while maintaining the mechanical integrity of the structure, effectively eliminating the need for at least one additional open heart surgical procedure in a child born with CHD.

7.2 Future perspectives

The contributions presented in this thesis could be further improved and expanded in a number of ways. A few of these are suggested in this section along with additional discussion and plans for future exploration.

7.2.1 Topology optimization for brittle fracture resistance

Our initial investigations using density-based topology optimization methods for brittle fracture resistance presented in Chapters 2 and 3 not only highlight the potential of including the failure physics during the optimization procedure, but also the difficulties associated with doing so. The highly nonlinear physics produce large degrees of nonlinearity in the objective and constraint functions employed, which motivated the improvements and analysis provided in Chapter 3. However, more exploration should be done in this regard, not only with respect to judicious selection or construction of functions for use during the optimization procedure, but also with respect to other numerical methods for general design optimization and/or optimizers themselves.

For example, it would be interesting to test level-set (rather than density-based) methods or novel techniques in shape optimization on this particular problem. This strategy could potentially alleviate some of the large changes in the crack path (and the resulting discontinuity in most of the typical objective/constraint functions) since only the boundary of the design is changed rather than also allowing variations of the internal structure.

As mentioned previously, most design optimization methods rely on gradient-based optimizers due to the very large number of design variables in typical problems. The highly nonlinear physics of brittle fracture, however, might be best suited for other optimization techniques with lower-dimensional design parameterizations. This might include interpolation of the density field using relatively few, intelligently constructed basis functions over the design domain. Techniques like this would also facilitate the analytical computation of function sensitivities with respect to the design variables but may also allow more robust/efficient optimization techniques to be employed. These include surrogate-based methods which might also use sensitivity data (such as Kriging) or evolving techniques in machine learning, among many other methods.

Finally we again highlight the fact that the proposed formulation ultimately removes all cracks in the final design. It would be particularly interesting if methods were developed for producing structures with a tolerance for fracture formation under extreme loading conditions. Materials such as concrete always contain some degree of cracking, but the cracks generally remain stable under

the applied loads or do not coalesce to cause catastrophic failures of the macroscopic structure. The ability to bound or optimize some measure of macroscopic structural stability under loads inducing the formation of small cracks may result in more efficient material usage. Consequently, one might expect lighter, better performing structures for situations in which large degrees of engineering conservatism may not be required.

7.2.2 Topology optimization for ductile failure and buckling resistance

The design formulation presented in Chapter 4 for resistance to ductile failure and buckling also promotes many interesting potential future studies and method enhancements. While relatively large gains in structural strength are demonstrated, the strength increase is not as pronounced as one might expect. This is partially due to the nonlinear saturation-type hardening of the material rather than the simple linear hardening models that are typically used in the literature. While including the nonlinear hardening demonstrates realistic gains in performance, it also highlights a particularly important rule of thumb for designers. If the construction material exhibits quick saturation of the hardening curve, very large gains in peak load carrying capacity should not generally be expected. However, large gains in structural toughness might still be achieved. This observation provokes one to ask whether a different material with more significant hardening characteristics would promote larger strength gains when used within the presented framework. Future analysis and numerical experimentation in this regard should clearly be examined.

While all three presented examples clearly demonstrate significant improvements in structural performance, the final example highlights a potential limitation of small strain kinematics in situations where the plastic strains are so large that localized necking of structural members may occur. Although less numerically robust in general, incorporating large strain kinematics in these situations may prove to be highly beneficial. Additionally, we have only incorporated ductile fracture constraints in the formulation. A simple extension to also account for shear failure in a manner similar to [45] should also be pursued.

The selected constraint bounds in the optimization problem statement could also be further

examined. Future studies including the effect of changing the upper bound on the volume fraction should be performed. Larger volume fractions typically lead to thicker structural members which are inherently less prone to buckling, while more stringent mass requirements may demonstrate the proposed formulation performs significantly better for particular boundary value problems. Additionally, studies changing the ductile failure constraint upper bound should also be explored in addition to those utilizing different indicators of ductile failure and whether there is a significant difference between the resulting optimized topologies and/or their performance.

It would also be interesting to systematically compare the optimized results to those obtained using linear elastic stiffness-based topology optimization with stress constraints and similar buckling analyses. This would provide a useful study for practicing designers which may illuminate whether there are significant benefits to including the nonlinear material physics.

Finally we note that while numerical models for ductile failure prediction proved to be useful for design validation, experimental verification of the optimized designs would be ideal since highly accurate numerical ductile failure prediction is still largely an open problem in the literature. Alternatively, improved calibration of an adequate numerical model for use during the verification step should be performed with additional test data in order to properly validate the model and increase confidence in the predicted performance of the optimized structures.

7.2.3 Failure behavior of hyperelastic composites

The work presented in Chapter 5 could be improved in several significant ways. Although we did not experimentally encounter large degrees of variation in macroscopic failure responses with 3D-printing direction, in general, anisotropy due to the additive manufacturing process should be anticipated and accounted for in the numerical model. This represents one area in which homogenization methods might be particularly suitable not only in determining effective macroscopic constitutive properties, but also for better understanding the mechanics between layers. Future studies should likely include some type of multiscale modeling or analysis of the material which might illuminate better phenomenological macroscopic constitutive models when used in

conjunction with relevant experimental observations and data.

Perhaps more importantly, although the load was experimentally applied at a quasistatic rate, specimen failure generally happened very rapidly. Since most polymers exhibit rate-dependent behavior it may prove extremely beneficial to include rate-dependence in the numerical constitutive model. Many nonlinear viscoelastic models could be evaluated for this purpose, while other physics, such as temperature dependence, may also prove to be important for particular engineering applications.

In order to further increase the accuracy of the numerical model, the fully three-dimensional physics should be simulated. Since we were not able to do so due to computational limitations, any one of the many mesh-adaptivity schemes in the literature would clearly be very useful in this regard. Although the computational burden may still be quite large, other techniques to accelerate the forward analyses could also be explored such as those recently proposed in [246].

Finally, the use of topology optimization methods for optimizing the shape of the inclusion phase in an effort to maximize the strength and toughness of the composite could be explored in a manner similar to [17, 18]. However, this extension would require large deformation mechanics and the associated numerically expensive explicit simulation of the failure physics during the optimization process. This is true since it was demonstrated in Chapter 5 that initial crack nucleation is not generally followed by catastrophic failure since the inclusion phase may cause crack arrest. Therefore the work required to cause complete failure of a general specimen is quite dependent on post crack nucleation behavior. However, if optimization of only the strength prior to crack nucleation is desired, then failure indicators such as the tensile energy density could be locally constrained, while omitting the explicit simulation of the failure physics for numerical efficiency in a manner similar to that outlined in Chapter 4.

7.2.4 Cardiovascular stent design for an expandable valved conduit

While a great deal of work is presented in Chapter 6, future studies of this type could be improved in multiple ways. These include calibration and use of a more accurate viscoplastic

constitutive model for the e-PTFE material, once sufficient test data for calibration of such a model is acquired. Alternative polymeric glues should also be explored in addition to Carbothane^{TM} which was selected for this study, due primarily to it's relatively low stiffness. Perhaps other candidate polymeric glues have more desirable mechanical properties. It may also be worthwhile to explore other manufacturing methods entirely in order to eliminate the polymeric glue from the design.

Furthermore, additional tests for both 316L stainless steel and L605 cobalt chromium should be conducted with specimen dimensions in the range of those considered in this dissertation. Since the strut widths and thicknesses are relatively small (on the order of 0.5mm) it is possible that larger scale continuum properties may differ significantly from those of actual stents after construction. Verification of the nonlinear hardening curves, ductile failure criteria, and metrics associated with Goodman fatigue analysis would also significantly improve confidence in the numerical results.

Additional refinements or expansions of the design space in regions where the Pareto frontier is predicted could also be further explored with high-fidelity simulations in order to improve the surrogate models and potentially increase the performance of the final design. The simulation setup itself could also be improved via inclusion of a deformable transcatheter non-compliant balloon approximation, rather than the rigid cylinder used for computational efficiency herein. Further improvements to the numerical approximation of the geometry could also be explored in order to more accurately capture that of the actual prototype.

Finally, and most importantly, a similar or improved design strategy incorporating multiple balloon dilation procedures to larger diameters should be examined with the goal of ultimately reaching the permanent inner diameter of an adult. This would alleviate the need for multiple additional open heart surgical procedures and significantly improve the quality of life of children born with CHD.

References

[1] M. P. Bendsøe and N. Kikuchi, "Generating optimal topologies in structural design using a homogenization method," *Computer Methods in Applied Mechanics and Engineering*, vol. 71, no. 2, pp. 197–224, Nov. 1988.

[2] T. Zegard and G. H. Paulino, "Bridging topology optimization and additive manufacturing," *Structural and Multidisciplinary Optimization*, vol. 53, no. 1, pp. 175–192, Jan. 2016.

[3] J. D. Deaton and R. V. Grandhi, "A survey of structural and multidisciplinary continuum topology optimization: Post 2000," *Structural and Multidisciplinary Optimization*, vol. 49, no. 1, pp. 1–38, Jan. 2014.

[4] P. Duysinx and M. P. Bendsøe, "Topology optimization of continuum structures with local stress constraints," *International Journal for Numerical Methods in Engineering*, vol. 43, no. 8, pp. 1453–1478,

[5] G. Cheng and Z. Jiang, "Study on Topology Optimization with Stress Constraints," *Engineering Optimization*, vol. 20, no. 2, pp. 129–148, Nov. 1992.

[6] C. Le, J. Norato, T. Bruns, C. Ha, and D. Tortorelli, "Stress-based topology optimization for continua," *Structural and Multidisciplinary Optimization*, vol. 41, no. 4, pp. 605–620, Apr. 2010.

[7] F. Senhora, O. Giraldo-Londono, I. Menezes, and G. H. Paulino, "Topology optimization with local stress constraints: A stress aggregation-free approach.," *Struct. Multidiscip. Optim.*, 2020.

[8] O. Giraldo-Londono and G. H. Paulino, "A unified approach for topology optimization with local stress constraints considering various failure criteria: Von Mises, Drucker–Prager, Tresca, Mohr–Coulomb, Bresler– Pister and Willam–Warnke," *Proceedings of the Royal Society A: Mathematical, Physical and Engineering Sciences*, vol. 476, no. 2238, p. 20 190 861, Jun. 2020, Publisher: Royal Society.

[9] M. P. Bendsøe and A. R. Díaz, "A method for treating damage related criteria in optimal topology design of continuum structures," *Structural optimization*, vol. 16, no. 2-3, pp. 108–115, Oct. 1998.

[10] M. Jansen, G. Lombaert, M. Schevenels, and O. Sigmund, "Topology optimization of fail-safe structures using a simplified local damage model," *Structural and Multidisciplinary Optimization*, vol. 49, no. 4, pp. 657–666, Apr. 2014.

[11] O. Amir and O. Sigmund, "Reinforcement layout design for concrete structures based on continuum damage and truss topology optimization," *Structural and Multidisciplinary Optimization*, vol. 47, no. 2, pp. 157–174, Feb. 2013.

[12] O. Amir, "A topology optimization procedure for reinforced concrete structures," *Computers & Structures*, vol. 114-115, pp. 46–58, Jan. 2013.

[13] K. A. James and H. Waisman, "Failure mitigation in optimal topology design using a coupled nonlinear continuum damage model," *Computer Methods in Applied Mechanics and Engineering*, vol. 268, no. Supplement C, pp. 614–631, Jan. 2014.

[14] Kai A. James and Haim Waisman, "Topology optimization of structures under variable loading using a damage superposition approach," *International Journal for Numerical Methods in Engineering*, vol. 101, no. 5, pp. 375–406,

[15] V. J. Challis, A. P. Roberts, and A. H. Wilkins, "Fracture resistance via topology optimization," *Structural and Multidisciplinary Optimization*, vol. 36, no. 3, pp. 263–271, Sep. 2008.

[16] Z. Kang, P. Liu, and M. Li, "Topology optimization considering fracture mechanics behaviors at specified locations," *Structural and Multidisciplinary Optimization*, vol. 55, no. 5, pp. 1847–1864, May 2017.

[17] L. Xia, D. Da, and J. Yvonnet, "Topology optimization for maximizing the fracture resistance of quasi-brittle composites," *Computer Methods in Applied Mechanics and Engineering*, vol. 332, pp. 234–254, Apr. 2018.

[18] D. Da, J. Yvonnet, L. Xia, and G. Li, "Topology optimization of particle-matrix composites for optimal fracture resistance taking into account interfacial damage," *International Journal for Numerical Methods in Engineering*, vol. 0, no. 0,

[19] B. San and H. Waisman, "Optimization of Carbon Black Polymer Composite Microstructure for Rupture Resistance," *Journal of Applied Mechanics*, vol. 84, no. 2, pp. 021005–021005–13, Nov. 2016.

[20] G. A. Francfort and J. .-J. Marigo, "Revisiting brittle fracture as an energy minimization problem," *Journal of the Mechanics and Physics of Solids*, vol. 46, no. 8, pp. 1319–1342, Aug. 1998.

[21] B. Bourdin, G. A. Francfort, and J.-J. Marigo, "The Variational Approach to Fracture," *Journal of Elasticity*, vol. 91, no. 1-3, pp. 5–148, Apr. 2008.

[22] C. Miehe, F. Welschinger, and M. Hofacker, "Thermodynamically consistent phase-field models of fracture: Variational principles and multi-field FE implementations," *International Journal for Numerical Methods in Engineering*, vol. 83, no. 10, pp. 1273–1311, Sep. 2010.

[23] C. Miehe, M. Hofacker, and F. Welschinger, "A phase field model for rate-independent crack propagation: Robust algorithmic implementation based on operator splits," *Computer Methods in Applied Mechanics and Engineering*, vol. 199, no. 45, pp. 2765–2778, Nov. 2010.

[24] C. Miehe, L.-M. Schänzel, and H. Ulmer, "Phase field modeling of fracture in multi-physics problems. Part I. Balance of crack surface and failure criteria for brittle crack propagation in thermo-elastic solids," *Computer Methods in Applied Mechanics and Engineering*, vol. 294, pp. 449–485, Sep. 2015.

[25] G. Allaire, F. Jouve, and A.-M. Toader, "A level-set method for shape optimization," *Comptes Rendus Mathematique*, vol. 334, no. 12, pp. 1125–1130, Jan. 2002.

[26] B. Bourdin and A. Chambolle, "Design-dependent loads in topology optimization," *ESAIM: Control, Optimisation and Calculus of Variations*, vol. 9, pp. 19–48, 2003.

[27] A. Takezawa, S. Nishiwaki, and M. Kitamura, "Shape and topology optimization based on the phase field method and sensitivity analysis," *Journal of Computational Physics*, vol. 229, no. 7, pp. 2697–2718, Apr. 2010.

[28] O. Sigmund and K. Maute, "Topology optimization approaches," *Structural and Multidisciplinary Optimization*, vol. 48, no. 6, pp. 1031–1055, Dec. 2013.

[29] C. C. Swan and I. Kosaka, "Voigt–Reuss topology optimization for structures with nonlinear material behaviors," *International Journal for Numerical Methods in Engineering*, vol. 40, no. 20, pp. 3785–3814, 1997.

[30] K. Maute, S. Schwarz, and E. Ramm, "Adaptive topology optimization of elastoplastic structures," *Structural optimization*, vol. 15, no. 2, pp. 81–91, Apr. 1998.

[31] S. Schwarz, K. Maute, and E. Ramm, "Topology and shape optimization for elastoplastic structural response," *Computer Methods in Applied Mechanics and Engineering*, vol. 190, no. 15, pp. 2135–2155, Jan. 2001.

[32] M. Bogomolny and O. Amir, "Conceptual design of reinforced concrete structures using topology optimization with elastoplastic material modeling," *International Journal for Numerical Methods in Engineering*, vol. 90, no. 13, pp. 1578–1597, Jun. 2012.

[33] J. Kato, H. Hoshiba, S. Takase, K. Terada, and T. Kyoya, "Analytical sensitivity in topology optimization for elastoplastic composites," *Structural and Multidisciplinary Optimization*, vol. 52, no. 3, pp. 507–526, Sep. 2015.

[34] L. Li, G. Zhang, and K. Khandelwal, "Design of energy dissipating elastoplastic structures under cyclic loads using topology optimization," *Structural and Multidisciplinary Optimization*, vol. 56, no. 2, pp. 391–412, Aug. 2017.

[35] G. Zhang, L. Li, and K. Khandelwal, "Topology optimization of structures with anisotropic plastic materials using enhanced assumed strain elements," *Structural and Multidisciplinary Optimization*, vol. 55, no. 6, pp. 1965–1988, Jun. 2017.

[36] O. Amir, "Stress-constrained continuum topology optimization: A new approach based on elasto-plasticity," *Structural and Multidisciplinary Optimization*, vol. 55, no. 5, pp. 1797–1818, May 2017.

[37] P. B. Nakshatrala and D. A. Tortorelli, "Topology optimization for effective energy propagation in rate-independent elastoplastic material systems," *Computer Methods in Applied Mechanics and Engineering*, vol. 295, pp. 305–326, Oct. 2015.

[38] N. Ivarsson, M. Wallin, and D. Tortorelli, "Topology optimization of finite strain viscoplastic systems under transient loads," *International Journal for Numerical Methods in Engineering*, vol. 114, no. 13, pp. 1351–1367, 2018.

[39] R. Alberdi and K. Khandelwal, "Bi-material topology optimization for energy dissipation with inertia and material rate effects under finite deformations," *Finite Elements in Analysis and Design*, vol. 164, pp. 18–41, Oct. 2019.

[40] M. Wallin, V. Jönsson, and E. Wingren, "Topology optimization based on finite strain plasticity," *Structural and Multidisciplinary Optimization*, vol. 54, no. 4, pp. 783–793, Oct. 2016.

[41] F. Fritzen, L. Xia, M. Leuschner, and P. Breitkopf, "Topology optimization of multiscale elastoviscoplastic structures," *International Journal for Numerical Methods in Engineering*, vol. 106, no. 6, pp. 430–453, May 2016.

[42] R. Alberdi and K. Khandelwal, "Design of periodic elastoplastic energy dissipating microstructures," *Structural and Multidisciplinary Optimization*, vol. 59, no. 2, pp. 461–483, Feb. 2019.

[43] J. Fin, L. A. Borges, and E. A. Fancello, "Structural topology optimization under limit analysis," *Structural and Multidisciplinary Optimization*, vol. 59, no. 4, pp. 1355–1370, Apr. 2019.

[44] R. Alberdi and K. Khandelwal, "Topology optimization of pressure dependent elastoplastic energy absorbing structures with material damage constraints," *Finite Elements in Analysis and Design*, vol. 133, pp. 42–61, Oct. 2017.

[45] L. Li and K. Khandelwal, "Design of fracture resistant energy absorbing structures using elastoplastic topology optimization," *Structural and Multidisciplinary Optimization*, pp. 1–29, Jun. 2017.

[46] R. A. Alberdi, "Computational Methods for Multiscale Analysis and Design of Nonlinear Multifunctional Materials and Structures for Energy Management," Ph.D. University of Notre Dame, United States – Indiana, 2019.

[47] L. Li, G. Zhang, and K. Khandelwal, "Topology optimization of energy absorbing structures with maximum damage constraint," *International Journal for Numerical Methods in Engineering*, vol. 112, no. 7, pp. 737–775, 2017.

[48] ——, "Failure resistant topology optimization of structures using nonlocal elastoplastic-damage model," *Structural and Multidisciplinary Optimization*, pp. 1–30, Apr. 2018.

[49] P. Michaleris, D. A. Tortorelli, and C. A. Vidal, "Tangent operators and design sensitivity formulations for transient non-linear coupled problems with applications to elastoplasticity," *International Journal for Numerical Methods in Engineering*, vol. 37, no. 14, pp. 2471–2499, Jul. 1994.

[50] Alberdi Ryan, Zhang Guodong, Li Lei, and Khandelwal Kapil, "A unified framework for nonlinear path-dependent sensitivity analysis in topology optimization," *International Journal for Numerical Methods in Engineering*, vol. 0, no. 0, Feb. 2018.

[51] W. Wang, P. M. Clausen, and K.-U. Bletzinger, "Efficient adjoint sensitivity analysis of isotropic hardening elastoplasticity via load steps reduction approximation," *Computer Methods in Applied Mechanics and Engineering*, vol. 325, pp. 612–644, Oct. 2017.

[52] C. B. Dilgen, S. B. Dilgen, D. R. Fuhrman, O. Sigmund, and B. S. Lazarov, "Topology optimization of turbulent flows," *Computer Methods in Applied Mechanics and Engineering*, vol. 331, pp. 363–393, Apr. 2018.

[53] M. M. Neves, H. Rodrigues, and J. M. Guedes, "Generalized topology design of structures with a buckling load criterion," *Structural optimization*, vol. 10, no. 2, pp. 71–78, Oct. 1995.

[54] K. Maute, "Topologie- und Formoptimierung von dünnwandigen Flächentragwerken," Ph.D. dissertation, Bericht Nr. 25, Institut für Baustatik, Universität Stuttgart, 1998.

[55] S. Rahmatalla and C. C. Swan, "Continuum Topology Optimization of Buckling-Sensitive Structures," *AIAA Journal*, vol. 41, no. 6, pp. 1180–1189, 2003, Publisher: American Institute of Aeronautics and Astronautics _eprint: https://doi.org/10.2514/2.2062.

[56] R. Kemmler, A. Lipka, and E. Ramm, "Large deformations and stability in topology optimization," *Structural and Multidisciplinary Optimization*, vol. 30, no. 6, pp. 459–476, Dec. 2005.

[57] E. Lindgaard and J. Dahl, "On compliance and buckling objective functions in topology optimization of snap-through problems," *Structural and Multidisciplinary Optimization*, vol. 47, no. 3, pp. 409–421, Mar. 2013.

[58] N. L. Pedersen and P. Pedersen, "Buckling load optimization for 2D continuum models, with alternative formulation for buckling load estimation," *Structural and Multidisciplinary Optimization*, vol. 58, no. 5, pp. 2163–2172, Nov. 2018.

[59] R. Reitinger and E. Ramm, "Buckling and imperfection sensitivity in the optimization of shell structures," *Thin-Walled Structures*, Buckling Strength of Imperfection-sensitive Shells, vol. 23, no. 1, pp. 159–177, Jan. 1995.

[60] M. M. Neves, O. Sigmund, and M. P. Bendsøe, "Topology optimization of periodic microstructures with a penalization of highly localized buckling modes," *International Journal for Numerical Methods in Engineering*, vol. 54, no. 6, pp. 809–834, 2002, _eprint: https://onlinelibrary.wiley.com/doi/pdf/10.1002/nme.449.

[61] C. R. Thomsen, F. Wang, and O. Sigmund, "Buckling strength topology optimization of 2D periodic materials based on linearized bifurcation analysis," *Computer Methods in Applied Mechanics and Engineering*, vol. 339, pp. 115–136, Sep. 2018.

[62] M. P. Bendsøe and O. Sigmund, *Topology Optimization: Theory, Methods, and Applications*, 2nd ed. Berlin Heidelberg: Springer-Verlag, 2004, ISBN: 978-3-540-42992-0.

[63] X. Gao and H. Ma, *Topology optimization of continuum structures under buckling constraints*, Sep. 2015.

[64] X. Gao, L. Li, and H. Ma, "An Adaptive Continuation Method for Topology Optimization of Continuum Structures Considering Buckling Constraints," *International Journal of Applied Mechanics*, vol. 09, no. 07, p. 1 750 092, Oct. 2017, Publisher: Imperial College Press.

[65] F. Ferrari and O. Sigmund, "Revisiting topology optimization with buckling constraints," *Structural and Multidisciplinary Optimization*, vol. 59, no. 5, pp. 1401–1415, May 2019.

[66] T. W. Chin and G. Kennedy, "Large-Scale Compliance-Minimization and Buckling Topology Optimization of the Undeformed Common Research Model Wing," in *57th AIAA/ASCE/AHS/ASC Structures, Structural Dynamics, and Materials Conference*, ser. AIAA SciTech Forum, American Institute of Aeronautics and Astronautics, Jan. 2016.

[67] F. Ferrari and O. Sigmund, "Towards solving large-scale topology optimization problems with buckling constraints at the cost of linear analyses," *Computer Methods in Applied Mechanics and Engineering*, vol. 363, p. 112 911, May 2020.

[68] S. Kaliszky and J. Lógó, "Discrete optimal design of elasto-plastic trusses using compliance and stability constraints," *Structural optimization*, vol. 15, no. 3, pp. 261–268, Jun. 1998.

[69] S. Schwarz and E. Ramm, "Sensitivity analysis and optimization for non-linear structural response," *Engineering Computations*, vol. 18, no. 3/4, pp. 610–641, Jan. 2001, Publisher: MCB UP Ltd.

[70] E. S. Greenhalgh, *Failure analysis and fractography of polymer composites*. CRC press, 2009.

[71] X. Wang, M. Jian, Z. Zhou, J. Gou, and D. Hui, "3d printing of polymer matrix composites: A review and prospective | Elsevier Enhanced Reader," *Composites Part B*, no. 110, pp. 442–458, 2017.

[72] R. O. Ritchie, "The conflicts between strength and toughness," *Nature Materials*, vol. 10, no. 11, pp. 817–822, Nov. 2011.

[73] V. Slesarenko, N. Kazarinov, and S. Rudykh, "Distinct failure modes in bio-inspired 3d-printed staggered composites under non-aligned loadings," *Smart Materials and Structures*, vol. 26, no. 3, p. 035 053, Mar. 2017.

[74] V. Slesarenko, K. Y. Volokh, J. Aboudi, and S. Rudykh, "Understanding the strength of bioinspired soft composites," *International Journal of Mechanical Sciences*, vol. 131-132, pp. 171–178, Oct. 2017.

[75] L. S. Dimas, G. H. Bratzel, I. Eylon, and M. J. Buehler, "Tough composites inspired by mineralized natural materials: Computation, 3d printing, and testing," *Advanced Functional Materials*, vol. 23, no. 36, pp. 4629–4638, 2013, ISBN: 1616-3028.

[76] F. Libonati, G. X. Gu, Z. Qin, L. Vergani, and M. J. Buehler, "Bone-Inspired Materials by Design: Toughness Amplification Observed Using 3d Printing and Testing," *Advanced Engineering Materials*, vol. 18, no. 8, pp. 1354–1363, 2016, ISBN: 0001410105.

[77] M. Ryvkin, V. Slesarenko, A. Cherkaev, and S. Rudykh, "Fault-tolerant elasticplastic lattice material," *Philosophical Transactions of the Royal Society A*, Jan. 2020, 00000.

[78] A. R. Studart, "Additive manufacturing of biologically-inspired materials," *Chemical Society Reviews*, vol. 45, no. 2, pp. 359–376, Jan. 2016, 00160.

[79] Z. Jia, Y. Yu, S. Hou, and L. Wang, "Biomimetic architected materials with improved dynamic performance," *Journal of the Mechanics and Physics of Solids*, vol. 125, pp. 178–197, Apr. 2019, 00008.

[80] L. Liu and Y. Li, "Predicting the mixed-mode I/II spatial damage propagation along 3d-printed soft interfacial layer via a hyperelastic softening model," *Journal of the Mechanics and Physics of Solids*, vol. 116, pp. 17–32, Jul. 2018, 00010.

[81] V. Slesarenko and S. Rudykh, "Towards mechanical characterization of soft digital materials for multimaterial 3d-printing," *International Journal of Engineering Science*, vol. 123, pp. 62–72, Feb. 2018, arXiv: 1710.05187 Publisher: Elsevier Ltd.

[82] G. X. Gu, M. Takaffoli, and M. J. Buehler, "Hierarchically Enhanced Impact Resistance of Bioinspired Composites," *Advanced Materials*, vol. 29, no. 28, p. 1 700 060, 2017, 00072.

[83] M. J. Borden, C. V. Verhoosel, M. A. Scott, T. J. R. Hughes, and C. M. Landis, "A phase-field description of dynamic brittle fracture," *Computer Methods in Applied Mechanics and Engineering*, vol. 217-220, pp. 77–95, Apr. 2012.

[84] M. Ambati, T. Gerasimov, and L. De Lorenzis, "A review on phase-field models of brittle fracture and a new fast hybrid formulation," *Computational Mechanics*, vol. 55, no. 2, pp. 383–405, Feb. 2015.

[85] F. P. Duda, A. Ciarbonetti, P. J. Sánchez, and A. E. Huespe, "A phase-field/gradient damage model for brittle fracture in elastic-plastic solids," *International Journal of Plasticity*, vol. 65, pp. 269–296, 2015.

[86] T. T. Nguyen, J. Yvonnet, Q. Z. Zhu, M. Bornert, and C. Chateau, "A phase-field method for computational modeling of interfacial damage interacting with crack propagation in realistic microstructures obtained by microtomography," *Computer Methods in Applied Mechanics and Engineering*, vol. 312, pp. 567–595, 2016.

[87] C. McAuliffe and H. Waisman, "A unified model for metal failure capturing shear banding and fracture," *International Journal of Plasticity*, vol. 65, pp. 131–151, Feb. 2015.

[88] M. Arriaga and H. Waisman, "Combined stability analysis of phase-field dynamic fracture and shear band localization," *International Journal of Plasticity*, vol. 96, pp. 81–119, 2017.

[89] M. Ambati, R. Kruse, and L. De Lorenzis, "A phase-field model for ductile fracture at finite strains and its experimental verification," *Computational Mechanics*, vol. 57, no. 1, pp. 149–167, Jan. 2016.

[90] M. J. Borden, T. J. R. Hughes, C. M. Landis, A. Anvari, and I. J. Lee, "A phase-field formulation for fracture in ductile materials: Finite deformation balance law derivation, plastic degradation, and stress triaxiality effects," *Computer Methods in Applied Mechanics and Engineering*, Phase Field Approaches to Fracture, vol. 312, pp. 130–166, Dec. 2016.

[91] Z. A. Wilson and C. M. Landis, "Phase-field modeling of hydraulic fracture," *Journal of the Mechanics and Physics of Solids*, vol. 96, pp. 264–290, 2016.

[92] C. Miehe and S. Mauthe, "Phase field modeling of fracture in multi-physics problems. part iii. crack driving forces in hydro-poro-elasticity and hydraulic fracturing of fluid-saturated porous media," *Computer Methods in Applied Mechanics and Engineering*, vol. 304, pp. 619–655, 2016.

[93] A. Mikelić, M. F. Wheeler, and T. Wick, "Phase-field modeling of a fluid-driven fracture in a poroelastic medium," *Computational Geosciences*, vol. 19, no. 6, pp. 1171–1195, Dec. 2015.

[94] J. Choo and W. Sun, "Coupled phase-field and plasticity modeling of geological materials: From brittle fracture to ductile flow," *Computer Methods in Applied Mechanics and Engineering*, vol. 330, pp. 1–32, Mar. 2018.

[95] M. Paggi and J. Reinoso, "Revisiting the problem of a crack impinging on an interface:a modeling framework for the interaction between the phase field approach for brittle fracture and the interface cohesive zone model," *Computer Methods in Applied Mechanics and Engineering*, vol. 321, pp. 145–172, 2017.

[96] C. V. Verhoosel and R. d. Borst, "A phase-field model for cohesive fracture," *International Journal for Numerical Methods in Engineering*, vol. 96, no. 1, pp. 43–62, 2013.

[97] S. Teichtmeister, D. Kienle, F. Aldakheel, and M.-A. Keip, "Phase field modeling of fracture in anisotropic brittle solids," *International Journal of Non-Linear Mechanics*, vol. 97, pp. 1–21, 2017.

[98] R. Shen, H. Waisman, Z. Yosibash, and G. Dahan, "A novel phase field method for modeling the fracture of long bones," *International Journal for Numerical Methods in Biomedical Engineering*, vol. 35, no. 8, 2019.

[99] C. Miehe and L.-M. Schänzel, "Phase field modeling of fracture in rubbery polymers. part i: Finite elasticity coupled with brittle failure," *Journal of the Mechanics and Physics of Solids*, vol. 65, pp. 93–113, 2014.

[100] J. Wu, C. McAuliffe, H. Waisman, and G. Deodatis, "Stochastic analysis of polymer composites rupture at large deformations modeled by a phase field method," *Computer Methods in Applied Mechanics and Engineering*, Phase Field Approaches to Fracture, vol. 312, pp. 596–634, Dec. 2016.

[101] B. San and H. Waisman, "Optimization of Carbon Black Polymer Composite Microstructure for Rupture Resistance," *Journal of Applied Mechanics*, vol. 84, no. 2, Feb. 2017.

[102] A. Raina and C. Miehe, "A phase-field model for fracture in biological tissues," *Biomechanics and Modeling in Mechanobiology*, vol. 15, no. 3, pp. 479–496, Jun. 2016.

[103] O. Gültekin, H. Dal, and G. A. Holzapfel, "Numerical aspects of anisotropic failure in soft biological tissues favor energy-based criteria: A rate-dependent anisotropic crack phase-field model," *Computer Methods in Applied Mechanics and Engineering*, vol. 331, pp. 23–52, 2018.

[104] B. Talamini, Y. Mao, and L. Anand, "Progressive damage and rupture in polymers," *Journal of the Mechanics and Physics of Solids*, vol. 111, pp. 434–457, Feb. 2018.

[105] Y. Mao and L. Anand, "A theory for fracture of polymeric gels," *Journal of the Mechanics and Physics of Solids*, vol. 115, pp. 30–53, Jun. 2018.

[106] C. Bilgen and K. Weinberg, "On the crack-driving force of phase-field models in linearized and finite elasticity," *Computer Methods in Applied Mechanics and Engineering*, vol. 353, pp. 348–372, Aug. 2019.

[107] A. Kumar, G. A. Francfort, and O. Lopez-Pamies, "Fracture and healing of elastomers: A phase-transition theory and numerical implementation," *Journal of the Mechanics and Physics of Solids*, vol. 112, pp. 523–551, Mar. 2018.

[108] S. Yin, W. Yang, J. Kwon, A. Wat, M. A. Meyers, and R. O. Ritchie, "Hyperelastic phase-field fracture mechanics modeling of the toughening induced by Bouligand structures in natural materials," *Journal of the Mechanics and Physics of Solids*, vol. 131, pp. 204–220, Oct. 2019.

[109] P. J. Loew, B. Peters, and L. A. A. Beex, "Rate-dependent phase-field damage modeling of rubber and its experimental parameter identification," *Journal of the Mechanics and Physics of Solids*, vol. 127, pp. 266–294, Jun. 2019.

[110] B. Yin and M. Kaliske, "Fracture simulation of viscoelastic polymers by the phase-field method," *Computational Mechanics*, Sep. 2019.

[111] J.-Y. Wu, V. P. Nguyen, C. Thanh Nguyen, D. Sutula, S. Bordas, and S. Sinaie, "Phase field modelling of fracture," *Advances in Applied Mechanics*, vol. 53, 2019.

[112] T. Heister, M. F. Wheeler, and T. Wick, "A primal-dual active set method and predictor-corrector mesh adaptivity for computing fracture propagation using a phase-field approach," *Computer Methods in Applied Mechanics and Engineering*, vol. 290, pp. 466–495, Jun. 2015.

[113] K. Y. Volokh, "Characteristic length of damage localization in rubber," *International Journal of Fracture*, vol. 168, no. 1, pp. 113–116, Mar. 2011.

[114] K. Y. Volokh, "Fracture as a material sink," *Materials Theory*, vol. 1, no. 1, p. 3, May 2017.

[115] A. Faye, Y. Lev, and K. Y. Volokh, "The effect of local inertia around the crack-tip in dynamic fracture of soft materials," *Mechanics of Soft Materials*, vol. 1, p. 4, Feb. 2019.

[116] J. I. E. Hoffman, "Congenital Heart Disease: Incidence and Inheritance," *Pediatric Clinics of North America*, Congenital Heart Disease, vol. 37, no. 1, pp. 25–43, Feb. 1990.

[117] M. D. Reller, M. J. Strickland, T. Riehle-Colarusso, W. T. Mahle, and A. Correa, "Prevalence of Congenital Heart Defects in Metropolitan Atlanta, 1998-2005," *The Journal of Pediatrics*, vol. 153, no. 6, pp. 807–813, Dec. 2008.

[118] J. I. E. Hoffman and S. Kaplan, "The incidence of congenital heart disease," *Journal of the American College of Cardiology*, vol. 39, no. 12, pp. 1890–1900, Jun. 2002.

[119] C. T. Mai, T. Riehle-Colarusso, A. O'Halloran, J. D. Cragan, R. S. Olney, A. Lin, M. Feldkamp, L. D. Botto, R. Rickard, M. Anderka, M. Ethen, C. Stanton, J. Ehrhardt, and M. Canfield, "Selected birth defects data from population-based birth defects surveillance programs in the United States, 2005–2009: Featuring critical congenital heart defects targeted for pulse oximetry screening," *Birth Defects Research Part A: Clinical and Molecular Teratology*, vol. 94, no. 12, pp. 970–983, 2012, _eprint: https://onlinelibrary.wiley.com/doi/pdf/10

[120] A. R. Castaneda, J. E. Mayer, R. A. Jonas, J. E. Lock, D. L. Wessel, and P. R. Hickey, "The neonate with critical congenital heart disease: Repair—A surgical challenge," *The Journal of Thoracic and Cardiovascular Surgery*, vol. 98, no. 5, Part 2, pp. 869–875, Nov. 1989.

[121] C. D. Morris and V. D. Menashe, "25-Year Mortality After Surgical Repair of Congenital Heart Defect in Childhood: A Population-Based Cohort Study," *JAMA*, vol. 266, no. 24, pp. 3447–3452, Dec. 1991.

[122] M. S. Cabrera, C. W. J. Oomens, C. V. C. Bouten, A. J. J. C. Bogers, S. P. Hoerstrup, and F. P. T. Baaijens, "Mechanical analysis of ovine and pediatric pulmonary artery for heart valve stent design," *Journal of Biomechanics*, vol. 46, no. 12, pp. 2075–2081, Aug. 2013.

[123] M. S. Cabrera, C. W. J. Oomens, and F. P. T. Baaijens, "Understanding the requirements of self-expandable stents for heart valve replacement: Radial force, hoop force and equilibrium," *Journal of the Mechanical Behavior of Biomedical Materials*, vol. 68, pp. 252–264, Apr. 2017.

[124] Q. Wang, E. Sirois, and W. Sun, "Patient-specific modeling of biomechanical interaction in transcatheter aortic valve deployment," *Journal of Biomechanics*, vol. 45, no. 11, pp. 1965–1971, Jul. 2012.

[125] S. Tzamtzis, J. Viquerat, J. Yap, M. J. Mullen, and G. Burriesci, "Numerical analysis of the radial force produced by the Medtronic-CoreValve and Edwards-SAPIEN after transcatheter aortic valve implantation (TAVI)," *Medical Engineering & Physics*, vol. 35, no. 1, pp. 125–130, Jan. 2013.

[126] S. Schievano, A. M. Taylor, C. Capelli, P. Lurz, J. Nordmeyer, F. Migliavacca, and P. Bonhoeffer, "Patient specific finite element analysis results in more accurate prediction of stent fractures: Application to percutaneous pulmonary valve implantation," *Journal of Biomechanics*, vol. 43, no. 4, pp. 687–693, Mar. 2010.

[127] E. Sirois, Q. Wang, and W. Sun, "Fluid Simulation of a Transcatheter Aortic Valve Deployment into a Patient-Specific Aortic Root," *Cardiovascular Engineering and Technology*, vol. 2, no. 3, pp. 186–195, Sep. 2011.

[128] F. Sulejmani, A. Pokutta-Paskaleva, O. Salazar, M. Karimi, and W. Sun, "Mechanical and structural analysis of the pulmonary valve in congenital heart defects: A presentation of two case studies," *Journal of the Mechanical Behavior of Biomedical Materials*, vol. 89, pp. 9–12, Jan. 2019.

[129] *Finally, A Heart Valve for Children*, The Charles Stark Draper Laboratory, Inc., 2018.

[130] P. M. Sullivan, P. C. Wong, R. Kim, and F. F. Ing, "Further percutaneous dilation of a Melody® valve in the mitral position to accommodate somatic growth in a small child: Lessons learned," *Cardiology in the Young*, vol. 29, no. 2, pp. 235–237, Feb. 2019, Publisher: Cambridge University Press.

[131] S. C. Hofferberth, M. Y. Saeed, L. Tomholt, M. C. Fernandes, C. J. Payne, K. Price, G. R. Marx, J. J. Esch, D. W. Brown, J. Brown, P. E. Hammer, R. W. Bianco, J. C. Weaver, E. R. Edelman, and P. J. d. Nido, "A geometrically adaptable heart valve replacement," *Science Translational Medicine*, vol. 12, no. 531, Feb. 2020, Publisher: American Association for the Advancement of Science Section: Research Article.

[132] I. Manavitehrani, P. Ebrahimi, I. Yang, S. Daly, A. Schindeler, A. Saxena, D. G. Little, D. F. Fletcher, F. Dehghani, and D. S. Winlaw, "Current Challenges and Emergent Technologies for Manufacturing Artificial Right Ventricle to Pulmonary Artery (RV-PA) Cardiac Conduits," *Cardiovascular Engineering and Technology*, vol. 10, no. 2, pp. 205–215, Jun. 2019.

[133] N. W. Bressloff, G. Ragkousis, and N. Curzen, "Design Optimisation of Coronary Artery Stent Systems," *Annals of Biomedical Engineering*, vol. 44, no. 2, pp. 357–367, Feb. 2016.

[134] G. S. Karanasiou, M. I. Papafaklis, C. Conway, L. K. Michalis, R. Tzafriri, E. R. Edelman, and D. I. Fotiadis, "Stents: Biomechanics, Biomaterials, and Insights from Computational Modeling," *Annals of Biomedical Engineering*, vol. 45, no. 4, pp. 853–872, Apr. 2017.

[135] M. Azaouzi, N. Lebaal, A. Makradi, and S. Belouettar, "Optimization based simulation of self-expanding Nitinol stent," *Materials & Design*, vol. 50, pp. 917–928, Sep. 2013.

[136] J. Bashar and K. Jayabal, "Analysis and Selection of Bio-stents Using Finite Element Method," in *Advances in Applied Mechanical Engineering*, H. K. Voruganti, K. K. Kumar, P. V. Krishna, and X. Jin, Eds., ser. Lecture Notes in Mechanical Engineering, Singapore: Springer, 2020, pp. 485–493.

[137] F. Migliavacca, L. Petrini, M. Colombo, F. Auricchio, and R. Pietrabissa, "Mechanical behavior of coronary stents investigated through the finite element method," *Journal of Biomechanics*, vol. 35, no. 6, pp. 803–811, Jun. 2002.

[138] C. Lally, F. Dolan, and P. J. Prendergast, "Cardiovascular stent design and vessel stresses: A finite element analysis," *Journal of Biomechanics*, vol. 38, no. 8, pp. 1574–1581, Aug. 2005.

[139] J. Bedoya, C. A. Meyer, L. H. Timmins, M. R. Moreno, and J. E. Moore, "Effects of Stent Design Parameters on Normal Artery Wall Mechanics," *Journal of Biomechanical Engineering*, vol. 128, no. 5, pp. 757–765, Oct. 2006, Publisher: American Society of Mechanical Engineers Digital Collection.

[140] N. Li, H. Zhang, and H. Ouyang, "Shape optimization of coronary artery stent based on a parametric model," *Finite Elements in Analysis and Design*, vol. 45, no. 6, pp. 468–475, May 2009.

[141] M. Azaouzi, A. Makradi, J. Petit, S. Belouettar, and O. Polit, "On the numerical investigation of cardiovascular balloon-expandable stent using finite element method," *Computational Materials Science*, vol. 79, pp. 326–335, Nov. 2013.

[142] S. Tammareddi, G. Sun, and Q. Li, "Multiobjective robust optimization of coronary stents," *Materials & Design*, vol. 90, pp. 682–692, Jan. 2016.

[143] L. H. Timmins, M. R. Moreno, C. A. Meyer, J. C. Criscione, A. Rachev, and J. E. Moore, "Stented artery biomechanics and device design optimization," *Medical & Biological Engineering & Computing*, vol. 45, no. 5, pp. 505–513, May 2007.

[144] A. Schiavone, L. G. Zhao, and A. A. Abdel-Wahab, "Dynamic simulation of stent deployment – effects of design, material and coating," *Journal of Physics: Conference Series*, vol. 451, p. 012 032, Jul. 2013, Publisher: IOP Publishing.

[145] H. Li, X. Wang, Y. Wei, T. Liu, J. Gu, Z. Li, M. Wang, D. Zhao, A. Qiao, and Y. Liu, "Multi-Objective Optimizations of Biodegradable Polymer Stent Structure and Stent Microinjection Molding Process," *Polymers*, vol. 9, no. 1, p. 20, Jan. 2017, Number: 1 Publisher: Multidisciplinary Digital Publishing Institute.

[146] R. W. Blair, N. J. Dunne, A. B. Lennon, and G. H. Menary, "Multi-objective optimisation of material properties and strut geometry for poly(L-lactic acid) coronary stents using response surface methodology," *PLOS ONE*, vol. 14, no. 8, e0218768, Aug. 2019, Publisher: Public Library of Science.

[147] M. M. Torki, S. Hassanajili, and M. M. Jalisi, "Design optimizations of PLA stent structure by FEM and investigating its function in a simulated plaque artery," *Mathematics and Computers in Simulation*, vol. 169, pp. 103–116, Mar. 2020.

[148] W. Wu, L. Petrini, D. Gastaldi, T. Villa, M. Vedani, E. Lesma, B. Previtali, and F. Migliavacca, "Finite Element Shape Optimization for Biodegradable Magnesium Alloy Stents," *Annals of Biomedical Engineering*, vol. 38, no. 9, pp. 2829–2840, Sep. 2010.

[149] C. Chen, J. Chen, W. Wu, Y. Shi, L. Jin, L. Petrini, L. Shen, G. Yuan, W. Ding, J. Ge, E. R. Edelman, and F. Migliavacca, "In vivo and in vitro evaluation of a biodegradable magnesium vascular stent designed by shape optimization strategy," *Biomaterials*, vol. 221, p. 119 414, Nov. 2019.

[150] R. Clune, D. Kelliher, J. C. Robinson, and J. S. Campbell, "NURBS modeling and structural shape optimization of cardiovascular stents," *Structural and Multidisciplinary Optimization*, vol. 50, no. 1, pp. 159–168, Jul. 2014.

[151] H. Li and X. Wang, "Design optimization of balloon-expandable coronary stent," *Structural and Multidisciplinary Optimization*, vol. 48, no. 4, pp. 837–847, Oct. 2013.

[152] H. Li, J. Gu, M. Wang, D. Zhao, Z. Li, A. Qiao, and B. Zhu, "Multi-objective optimization of coronary stent using Kriging surrogate model," *BioMedical Engineering OnLine*, vol. 15, no. 2, p. 148, Dec. 2016.

[153] J. A. Grogan, S. B. Leen, and P. E. McHugh, "Optimizing the design of a bioabsorbable metal stent using computer simulation methods," *Biomaterials*, vol. 34, no. 33, pp. 8049–8060, Nov. 2013.

[154] S. Pant, G. Limbert, N. P. Curzen, and N. W. Bressloff, "Multiobjective design optimisation of coronary stents," *Biomaterials*, vol. 32, no. 31, pp. 7755–7773, Nov. 2011.

[155] S. Pant, N. W. Bressloff, and G. Limbert, "Geometry parameterization and multidisciplinary constrained optimization of coronary stents," *Biomechanics and Modeling in Mechanobiology*, vol. 11, no. 1, pp. 61–82, Jan. 2012.

[156] X. Shen, H. Zhu, J. Jiang, Y. Deng, and S. Ji, "Multi-Objective Optimization Design of Balloon-Expandable Coronary Stent," *Cardiovascular Engineering and Technology*, vol. 10, no. 1, pp. 10–21, Mar. 2019.

[157] A. L. Marsden, J. A. Feinstein, and C. A. Taylor, "A computational framework for derivative-free optimization of cardiovascular geometries," *Computer Methods in Applied Mechanics and Engineering*, vol. 197, no. 21, pp. 1890–1905, Apr. 2008.

[158] T. J. Gundert, A. L. Marsden, W. Yang, and J. F. LaDisa, "Optimization of Cardiovascular Stent Design Using Computational Fluid Dynamics," *Journal of Biomechanical Engineering*, vol. 134, no. 1, Jan. 2012, Publisher: American Society of Mechanical Engineers Digital Collection.

[159] F. Bozsak, D. Gonzalez-Rodriguez, Z. Sternberger, P. Belitz, T. Bewley, J.-M. Chomaz, and A. I. Barakat, "Optimization of Drug Delivery by Drug-Eluting Stents," *PLOS ONE*, vol. 10, no. 6, e0130182, Jun. 2015, Publisher: Public Library of Science.

[160] M. J. Borden, "Isogeometric analysis of phase-field models for dynamic brittle and ductile fracture," thesis, Aug. 2012.

[161] H. Amor, J.-J. Marigo, and C. Maurini, "Regularized formulation of the variational brittle fracture with unilateral contact: Numerical experiments," *Journal of the Mechanics and Physics of Solids*, vol. 57, no. 8, pp. 1209–1229, Aug. 2009.

[162] M. P. Bendsøe, "Optimal shape design as a material distribution problem," *Structural optimization*, vol. 1, no. 4, pp. 193–202, Dec. 1989.

[163] M. Zhou and G. I. N. Rozvany, "The COC algorithm, Part II: Topological, geometrical and generalized shape optimization," *Computer Methods in Applied Mechanics and Engineering*, Second World Congress on Computational Mechanics, vol. 89, no. 1, pp. 309–336, Aug. 1991.

[164] O. Sigmund and J. Petersson, "Numerical instabilities in topology optimization: A survey on procedures dealing with checkerboards, mesh-dependencies and local minima," *Structural optimization*, vol. 16, no. 1, pp. 68–75, Aug. 1998.

[165] T. E. Bruns and D. A. Tortorelli, "Topology optimization of non-linear elastic structures and compliant mechanisms," *Computer Methods in Applied Mechanics and Engineering*, vol. 190, no. 26, pp. 3443–3459, Mar. 2001.

[166] J. K. Guest, J. H. Prévost, and T. Belytschko, "Achieving minimum length scale in topology optimization using nodal design variables and projection functions," *International Journal for Numerical Methods in Engineering*, vol. 61, no. 2, pp. 238–254, Sep. 2004.

[167] F. Wang, B. S. Lazarov, and O. Sigmund, "On projection methods, convergence and robust formulations in topology optimization," *Structural and Multidisciplinary Optimization*, vol. 43, no. 6, pp. 767–784, Jun. 2011.

[168] D. Roylance, *Introduction to Fracture Mechanics*, MIT Open Courseware.

[169] R. L. Taylor, *FEAP - Finite Element Analysis Program*. University of California, Berkeley, 2014.

[170] S. Balay, S. Abhyankar, M. F. Adams, J. Brown, P. Brune, K. Buschelman, L. Dalcin, V. Eijkhout, W. D. Gropp, D. Kaushik, M. G. Knepley, D. A. May, L. C. McInnes, R. T. Mills, T. Munson, K. Rupp, P. Sanan, B. F. Smith, S. Zampini, H. Zhang, and H. Zhang, "PETSc Users Manual," Argonne National Laboratory, Tech. Rep. ANL-95/11 - Revision 3.9, 2018.

[171] A. Wachter and L. T. Biegler, "On the implementation of an interior-point filter line-search algorithm for large-scale nonlinear programming," *Mathematical Programming*, vol. 106, no. 1, pp. 25–57, Mar. 2006.

[172] A. B. Lambe and A. Czekanski, "Topology optimization using a continuous density field and adaptive mesh refinement," *International Journal for Numerical Methods in Engineering*, vol. 113, no. 3, pp. 357–373,

[173] *CUBIT Geometry and Mesh Generation Toolkit, v15.2*. Sandia National Laboratories, Dec. 2016.

[174] U. Ayachit, *The ParaView Guide: A Parallel Visualization Application*. USA: Kitware, Inc., 2015, ISBN: 1930934300.

[175] J. D. Hunter, "Matplotlib: A 2d graphics environment," *Computing In Science & Engineering*, vol. 9, no. 3, pp. 90–95, 2007.

[176] X. Zhang, C. Vignes, S. W. Sloan, and D. Sheng, "Numerical evaluation of the phase-field model for brittle fracture with emphasis on the length scale," *Computational Mechanics*, vol. 59, no. 5, pp. 737–752, May 2017.

[177] P. Duysinx, "Topology Optimization with Different Stress Limit in Tension and Compression," May 1999.

[178] P. Liu, Y. Luo, and Z. Kang, "Multi-material topology optimization considering interface behavior via XFEM and level set method," *Computer Methods in Applied Mechanics and Engineering*, vol. 308, pp. 113–133, Aug. 2016.

[179] K. Pham, H. Amor, J.-J. Marigo, and C. Maurini, "Gradient Damage Models and Their Use to Approximate Brittle Fracture," *International Journal of Damage Mechanics*, vol. 20, no. 4, pp. 618–652, May 2011.

[180] M. Klinsmann, D. Rosato, M. Kamlah, and R. M. McMeeking, "An assessment of the phase field formulation for crack growth," *Computer Methods in Applied Mechanics and Engineering*, vol. 294, pp. 313–330, Sep. 2015.

[181] F. Wang, B. S. Lazarov, O. Sigmund, and J. S. Jensen, "Interpolation scheme for fictitious domain techniques and topology optimization of finite strain elastic problems," *Computer Methods in Applied Mechanics and Engineering*, vol. 276, pp. 453–472, Jul. 2014.

[182] J. B. Russ and H. Waisman, "Topology optimization for brittle fracture resistance," *Computer Methods in Applied Mechanics and Engineering*, vol. 347, pp. 238–263, Apr. 2019.

[183] K. Svanberg, "The method of moving asymptotes—a new method for structural optimization," *International Journal for Numerical Methods in Engineering*, vol. 24, no. 2, pp. 359–373, Feb. 1987.

[184] F. V. Senhora, "Topology Optimization with Stress Constraints: An Aggregation-Free Approach," Dissertacao de Mestrado, Pontificia Universidade Catolica do Rio de Janeiro, Rio de Janeiro, 2017.

[185] Y. Bao, "Prediction of ductile crack formation in uncracked bodies," Thesis, Massachusetts Institute of Technology, 2003.

[186] Y. Bao and T. Wierzbicki, "A Comparative Study on Various Ductile Crack Formation Criteria," *Journal of Engineering Materials and Technology*, vol. 126, no. 3, pp. 314–324, Jul. 2004.

[187] E. Voce, "A Practical Strain Hardening Function," *Metallurgica*, vol. 51, pp. 219–226, 1955.

[188] E. de Souza Neto, D. Peric, and D. Owen, *Computational Methods for Plasticity: Theory and Applications | Wiley*. Wiley, 2011, Library Catalog: www.wiley.com.

[189] J. C. Simo and T. J. R. Hughes, *Computational Inelasticity*, ser. Interdisciplinary Applied Mathematics. New York: Springer-Verlag, 1998, ISBN: 978-0-387-97520-7.

[190] J. C. Simo, "A framework for finite strain elastoplasticity based on maximum plastic dissipation and the multiplicative decomposition: Part I. Continuum formulation," *Computer Methods in Applied Mechanics and Engineering*, vol. 66, no. 2, pp. 199–219, Feb. 1988.

[191] T. Wierzbicki, Y. Bao, Y. Lee, and Y. Bai, "Calibration and evaluation of seven fracture models," *International Journal of Mechanical Sciences*, vol. 47, no. 4, pp. 719–743, Apr. 2005.

[192] E. Corona and B. Reedlun, "A review of macroscopic ductile failure criteria," Sandia National Laboratories, Tech. Rep. Sandia Report SAND2013-7989, 2013.

[193] H. Hooputra, H. Gese, H. Dell, and H. Werner, "A comprehensive failure model for crashworthiness simulation of aluminium extrusions," *International Journal of Crashworthiness*, vol. 9, no. 5, pp. 449–464, Sep. 2004, Publisher: Taylor & Francis _eprint: https://doi.org/10.1533/ijcr.2004.0

[194] G. R. Johnson and W. H. Cook, "Fracture characteristics of three metals subjected to various strains, strain rates, temperatures and pressures," *Engineering Fracture Mechanics*, vol. 21, no. 1, pp. 31–48, Jan. 1985.

[195] W. L. Kolmogorov, "Spannungen Deformationen Bruch," *Metallurgija*, p. 230, 1970.

[196] Y. Bao and T. Wierzbicki, "On fracture locus in the equivalent strain and stress triaxiality space," *International Journal of Mechanical Sciences*, vol. 46, no. 1, pp. 81–98, Jan. 2004.

[197] Y. Bai and T. Wierzbicki, "A new model of metal plasticity and fracture with pressure and Lode dependence," *International Journal of Plasticity*, vol. 24, no. 6, pp. 1071–1096, Jun. 2008.

[198] Y. Bai and T. Wierzbicki, "Application of extended mohr coulomb criterion to ductile fracture," *International Journal of Fracture*, vol. 161, no. 1, p. 1, Nov. 2009.

[199] R. de Borst, M. Crisfield, J. Remmers, and C. Verhoosel, *Nonlinear Finite Element Analysis of Solids and Structures*, 2nd Edition. Wiley, 2012, Library Catalog: www.wiley.com, ISBN: 978-0-470-66644-9.

[200] V. Hernandez, J. E. Roman, and V. Vidal, *SLEPc: A scalable and flexible toolkit for the solution of eigenvalue problems*, Sep. 2005.

[201] A. J. Torii and J. R. d. Faria, "Structural optimization considering smallest magnitude eigenvalues: A smooth approximation," *Journal of the Brazilian Society of Mechanical Sciences and Engineering*, vol. 39, no. 5, pp. 1745–1754, May 2017.

[202] B. S. Lazarov and O. Sigmund, "Filters in topology optimization based on Helmholtz-type differential equations," *International Journal for Numerical Methods in Engineering*, vol. 86, no. 6, pp. 765–781, May 2011.

[203] J. Nocedal and S. Wright, *Numerical Optimization*, 2nd ed., ser. Springer Series in Operations Research and Financial Engineering. New York: Springer-Verlag, 2006, ISBN: 978-0-387-30303-1.

[204] M. Bruggi, "On an alternative approach to stress constraints relaxation in topology optimization," *Structural and Multidisciplinary Optimization*, vol. 36, no. 2, pp. 125–141, Aug. 2008.

[205] H. C. Rodrigues, J. M. Guedes, and M. P. Bendsøe, "Necessary conditions for optimal design of structures with a nonsmooth eigenvalue based criterion," *Structural optimization*, vol. 9, no. 1, pp. 52–56, Feb. 1995.

[206] J. B. Russ and H. Waisman, "A novel topology optimization formulation for enhancing fracture resistance with a single quasi-brittle material," *International Journal for Numerical Methods in Engineering*, vol. 121, no. 13, pp. 2827–2856, 2020.

[207] D. Arndt, W. Bangerth, T. C. Clevenger, D. Davydov, M. Fehling, D. Garcia-Sanchez, G. Harper, T. Heister, L. Heltai, M. Kronbichler, R. M. Kynch, M. Maier, J.-P. Pelteret, B. Turcksin, and D. Wells, "The `deal.II` library, version 9.1," *Journal of Numerical Mathematics*, vol. 27, no. 4, pp. 203–213, 2019.

[208] M. Heroux, R. Bartlett, V. H. R. Hoekstra, J. Hu, T. Kolda, R. Lehoucq, K. Long, R. Pawlowski, E. Phipps, A. Salinger, H. Thornquist, R. Tuminaro, J. Willenbring, and A.

Williams, "An Overview of Trilinos," Sandia National Laboratories, Tech. Rep. SAND2003-2927, 2003.

[209] S. Balay, S. Abhyankar, M. F. Adams, J. Brown, P. Brune, K. Buschelman, L. Dalcin, A. Dener, V. Eijkhout, W. D. Gropp, D. Karpeyev, D. Kaushik, M. G. Knepley, D. A. May, L. C. McInnes, R. T. Mills, T. Munson, K. Rupp, P. Sanan, B. F. Smith, S. Zampini, H. Zhang, and H. Zhang, "PETSc users manual," Argonne National Laboratory, Tech. Rep. ANL-95/11 - Revision 3.13, 2020.

[210] V. Hernandez, J. E. Roman, and V. Vidal, "SLEPc: A scalable and flexible toolkit for the solution of eigenvalue problems," *ACM Trans. Math. Software*, vol. 31, no. 3, pp. 351–362, 2005.

[211] K. Svanberg, "MMA and GCMMA – two methods for nonlinear optimization," Tech. Rep., 2007, p. 15.

[212] M. Aguilo, J. Robbins, B. Clark, and R. Viertel, *PLATO Topology Optimization Software*, May 2020.

[213] J. Li and S. Rudykh, "Tunable microstructure transformations and auxetic behavior in 3D-printed multiphase composites: The role of inclusion distribution," *Composites Part B: Engineering*, vol. 172, pp. 352–362, Sep. 2019.

[214] J. Li, V. Slesarenko, P. I. Galich, and S. Rudykh, "Instabilities and pattern formations in 3D-printed deformable fiber composites," *Composites Part B: Engineering*, vol. 148, pp. 114–122, Sep. 2018.

[215] J. Li, V. Slesarenko, and S. Rudykh, "Auxetic multiphase soft composite material design through instabilities with application for acoustic metamaterials," *Soft Matter*, vol. 14, no. 30, pp. 6171–6180, 2018.

[216] S. Rudykh, C. Ortiz, and M. C. Boyce, "Flexibility and protection by design: Imbricated hybrid microstructures of bio-inspired armor," *Soft Matter*, vol. 11, no. 13, pp. 2547–2554, 2015.

[217] V. Slesarenko and S. Rudykh, "Harnessing viscoelasticity and instabilities for tuning wavy patterns in soft layered composites," *Soft Matter*, vol. 12, no. 16, pp. 3677–3682, 2016.

[218] S. Rudykh and M. C. Boyce, "Transforming Small Localized Loading into Large Rotational Motion in Soft Anisotropically Structured Materials," *Advanced Engineering Materials*, vol. 16, no. 11, pp. 1311–1317, 2014.

[219] Y. Li, N. Kaynia, S. Rudykh, and M. C. Boyce, "Wrinkling of Interfacial Layers in Stratified Composites," *Advanced Engineering Materials*, vol. 15, no. 10, pp. 921–926, 2013.

[220] N. Arora, A. Batan, J. Li, V. Slesarenko, and S. Rudykh, "On the Influence of Inhomogeneous Interphase Layers on Instabilities in Hyperelastic Composites," *Materials*, vol. 12, no. 5, p. 763, Jan. 2019.

[221] C. Hesch and K. Weinberg, "Thermodynamically consistent algorithms for a finite-deformation phase-field approach to fracture," *International Journal for Numerical Methods in Engineering*, vol. 99, no. 12, pp. 906–924, 2014.

[222] C. Hesch, A. J. Gil, R. Ortigosa, M. Dittmann, C. Bilgen, P. Betsch, M. Franke, A. Janz, and K. Weinberg, "A framework for polyconvex large strain phase-field methods to fracture," *Computer Methods in Applied Mechanics and Engineering*, vol. 317, pp. 649–683, Apr. 2017.

[223] S. Tang, G. Zhang, T. F. Guo, X. Guo, and W. K. Liu, "Phase field modeling of fracture in nonlinearly elastic solids via energy decomposition," *Computer Methods in Applied Mechanics and Engineering*, vol. 347, pp. 477–494, Apr. 2019.

[224] N. A. Hocine, M. N. Abdelaziz, and A. Imad, "Fracture problems of rubbers: J-integral estimation based upon eta factors and an investigation on the strain energy density distribution as a local criterion," *International Journal of Fracture*, vol. 117, no. 1, pp. 1–23, Sep. 2002.

[225] K. Y. Volokh, "On modeling failure of rubber-like materials," *Mechanics Research Communications*, vol. 37, no. 8, pp. 684–689, Dec. 2010.

[226] Stratasys Ltd., *Vero material data sheet*, https://www.stratasys.com/-/media/files/material-spec-sheets/vero-material-data-sheet.pdf, 2018.

[227] S. Ltd., *PolyJet 3D Printers Systems and Materials Overview*, https://www.stratasys.com/-/media/files/printer-spec-sheets/polyjet-3d-printers-systems-materials-spec-sheet.pdf, 2018.

[228] H. Rappel, L. A. A. Beex, J. S. Hale, L. Noels, and S. P. A. Bordas, "A Tutorial on Bayesian Inference to Identify Material Parameters in Solid Mechanics," *Archives of Computational Methods in Engineering*, Jan. 2019.

[229] P. Hauseux, J. S. Hale, S. Cotin, and S. P. A. Bordas, "Quantifying the uncertainty in a hyperelastic soft tissue model with stochastic parameters," *Applied Mathematical Modelling*, vol. 62, pp. 86–102, Oct. 2018.

[230] K. Y. Volokh and J. Aboudi, "Aneurysm strength can decrease under calcification," *Journal of the Mechanical Behavior of Biomedical Materials*, vol. 57, pp. 164–174, Apr. 2016.

[231] S. Raayai-Ardakani, D. Rachelle Earl, and T. Cohen, "The intimate relationship between cavitation and fracture," *Soft Matter*, vol. 15, no. 25, pp. 4999–5005, 2019.

[232] "FluoroFlex™ ePTFE," International Polymer Engineering, Tempe, AZ, Tech. Rep., 2020.

[233] "Aromatic Carbothane AC-4075A," The Lubrizol Corporation, Cleveland, OH, Tech. Rep., 2020.

[234] *FreeCAD: Your own 3D parametric modeler*, Version 0.18-16146.

[235] *ABAQUS/Standard User's Manual, Version 2019*. United States: Dassault Systèmes Simulia Corp, 2019.

[236] M. Ando and Y. Takahashi, "Ten-year experience with handmade trileaflet polytetrafluoroethylene valved conduit used for pulmonary reconstruction," *The Journal of Thoracic and Cardiovascular Surgery*, vol. 137, no. 1, pp. 124–131, Jan. 2009.

[237] J. Li, Q. Luo, Z. Xie, Y. Li, and Y. Zeng, "Fatigue life analysis and experimental verification of coronary stent," *Heart and Vessels*, vol. 25, no. 4, pp. 333–337, Jul. 2010.

[238] R. V. Marrey, R. Burgermeister, R. B. Grishaber, and R. O. Ritchie, "Fatigue and life prediction for cobalt-chromium stents: A fracture mechanics analysis," *Biomaterials*, vol. 27, no. 9, pp. 1988–2000, Mar. 2006.

[239] FDA, "Non-Clinical Engineering Tests and Recommended Labeling for Intravascular Stents and Associated Delivery Systems - Guidance for Industry and FDA Staff," Tech. Rep., Apr. 2010.

[240] J. P. McGarry, B. P. O'Donnell, P. E. McHugh, and J. G. McGarry, "Analysis of the mechanical performance of a cardiovascular stent design based on micromechanical modelling," *Computational Materials Science*, vol. 31, no. 3, pp. 421–438, Nov. 2004.

[241] K. D. Everett, C. Conway, G. J. Desany, B. L. Baker, G. Choi, C. A. Taylor, and E. R. Edelman, "Structural Mechanics Predictions Relating to Clinical Coronary Stent Fracture in a 5 Year Period in FDA MAUDE Database," *Annals of Biomedical Engineering*, vol. 44, no. 2, pp. 391–403, Feb. 2016.

[242] J. R. Rice and D. M. Tracey, "On the ductile enlargement of voids in triaxial stress fields," *Journal of the Mechanics and Physics of Solids*, vol. 17, no. 3, pp. 201–217, Jun. 1969.

[243] A. L. Gurson, "Continuum Theory of Ductile Rupture by Void Nucleation and Growth: Part I-Yield Criteria and Flow Rules for Porous Ductile Media," *Journal of Engineering Materials and Technology*, vol. 99, no. 1, pp. 2–15, Jan. 1977, Publisher: American Society of Mechanical Engineers Digital Collection.

[244] MATLAB, *version R2020a*. Natick, Massachusetts: The MathWorks, Inc., 2020.

[245] A. L. Custódio, J. F. A. Madeira, A. I. F. Vaz, and L. N. Vicente, "Direct Multisearch for Multiobjective Optimization," *SIAM Journal on Optimization*, vol. 21, no. 3, pp. 1109–1140, Jul. 2011, Publisher: Society for Industrial and Applied Mathematics.

[246] J.-Y. Wu, Y. Huang, H. Zhou, and V. P. Nguyen, "Three-dimensional phase-field modeling of mode I + II/III failure in solids," *Computer Methods in Applied Mechanics and Engineering*, vol. 373, p. 113 537, Nov. 2020.

[247] C. Miehe, "Comparison of two algorithms for the computation of fourth-order isotropic tensor functions," *Computers & Structures*, vol. 66, no. 1, pp. 37–43, Jan. 1998.

[248] J. Bonet and R. D. Wood, *Nonlinear Continuum Mechanics for Finite Element Analysis*, 2nd ed. Cambridge University Press, 2008.

[249] J. R. Rice, "A Path Independent Integral and the Approximate Analysis of Strain Concentration by Notches and Cracks," *Journal of Applied Mechanics*, vol. 35, no. 2, pp. 379–386, Jun. 1968.

[250] C. F. Shih, B. Moran, and T. Nakamura, "Energy release rate along a three-dimensional crack front in a thermally stressed body," *International Journal of Fracture*, vol. 30, no. 2, pp. 79–102, Feb. 1986.

[251] J. Peng, Y. Wang, Q. Dai, X. Liu, L. Liu, and Z. Zhang, "Effect of Stress Triaxiality on Plastic Damage Evolution and Failure Mode for 316L Notched Specimen," *Metals*, vol. 9, no. 10, p. 1067, Oct. 2019, Number: 10 Publisher: Multidisciplinary Digital Publishing Institute.

[252] Q. Wang, Y. Ren, M. Babar Shahzad, W. Zhang, X. Pan, S. Zhang, and D. Zhang, "Design and characterization of a novel nickel-free cobalt-base alloy for intravascular stents," *Materials Science and Engineering: C*, vol. 77, pp. 565–571, Aug. 2017.

[253] "ASTM E8/E8M Test Methods for Tension Testing of Metallic Materials," ASTM International, Tech. Rep.

[254] S. Ebnesajjad, "7 - Properties, Characteristics, and Applications of Expanded PTFE (ePTFE) Products," in *Expanded PTFE Applications Handbook*, ser. Plastics Design Library, S. Ebnesajjad, Ed., Oxford: William Andrew Publishing, Jan. 2017, pp. 163–170, ISBN: 978-1-4377-7855-7.

[255] J. Bergström, "8 - viscoplasticity models," in *Mechanics of Solid Polymers*, J. Bergström, Ed., William Andrew Publishing, 2015, pp. 371–436, ISBN: 978-0-323-31150-2.

[256] R. W. Ogden and D. G. Roxburgh, "A pseudo–elastic model for the Mullins effect in filled rubber," *Proceedings of the Royal Society of London. Series A: Mathematical, Physical and Engineering Sciences*, vol. 455, no. 1988, pp. 2861–2877, Aug. 1999, Publisher: Royal Society.

Appendix A

A.1 Fourth order constitutive tensor for spectral split of elastic energy density

For completeness we provide the detailed form of the constitutive tensor in the case of the spectral split of the stored elastic energy density used in Chapters 2 and 3. Generally, linearization of the constitutive law requires a fourth-order tensor, $\mathbb{C} = \frac{\partial \boldsymbol{\sigma}}{\partial \boldsymbol{\varepsilon}}$. The fourth-order constitutive tensor required in the case of the spectral split of the elastic energy density may be written using the eigenpairs of the strain tensor as

$$\begin{aligned}\mathbb{C} = &\sum_{i=1}^{3}\sum_{j=1}^{3}\frac{\partial s_i}{\partial \varepsilon_j}\boldsymbol{n}_i \otimes \boldsymbol{n}_i \otimes \boldsymbol{n}_j \otimes \boldsymbol{n}_j \\ &+ \frac{1}{2}\sum_{i=1}^{3}\sum_{\substack{j=1 \\ i\neq j}}^{3}\frac{s_i - s_j}{\varepsilon_i - \varepsilon_j}\boldsymbol{n}_i \otimes \boldsymbol{n}_j \otimes \left(\boldsymbol{n}_i \otimes \boldsymbol{n}_j + \boldsymbol{n}_j \otimes \boldsymbol{n}_i\right)\end{aligned} \tag{A.1.1}$$

where,

$$\begin{aligned}\frac{\partial s_i}{\partial \varepsilon_j} = &\left((1-d)^2 + k\right)\left(\lambda\frac{\left\langle\sum_{a=1}^{3}\varepsilon_a\right\rangle_+}{\sum_{a=1}^{3}\varepsilon_a} + 2\mu\frac{\langle\varepsilon_i\rangle_+}{\varepsilon_i}\delta_{ij}\right) \\ &+ \left(\lambda\frac{\left\langle\sum_{a=1}^{3}\varepsilon_a\right\rangle_-}{\sum_{a=1}^{3}\varepsilon_a} + 2\mu\frac{\langle\varepsilon_i\rangle_-}{\varepsilon_i}\delta_{ij}\right)\end{aligned} \tag{A.1.2}$$

$$\frac{s_i - s_j}{\varepsilon_i - \varepsilon_j} = \frac{2\mu}{\varepsilon_i - \varepsilon_j}\left(\left((1-d)^2 + k\right)\left[\langle\varepsilon_i\rangle_+ - \left\langle\varepsilon_j\right\rangle_+\right] + \left[\langle\varepsilon_i\rangle_- - \left\langle\varepsilon_j\right\rangle_-\right]\right) \tag{A.1.3}$$

Note that we replace $\frac{s_i - s_j}{\varepsilon_i - \varepsilon_j}$ by $\frac{\partial s_i}{\partial \varepsilon_i} - \frac{\partial s_j}{\partial \varepsilon_i}$ whenever ε_i is equal to ε_j, and s_i represents to the i^{th} principal stress. We refer the interested reader to Miehe [247] and Klinsmann et al. [180] for further details.

A.2 Smooth threshold physics comparison

Here we demonstrate the negligible effect of the smooth threshold function introduced in Equation (3.2.15) on the physics of the forward analyses in Chapter 3. The portal frame geometry in Figure 3.6 with numerical parameters provided in Table 3.2 are used with the exception of the smoothing parameter, η_{ks}. The geometry is discretized with 11,454 quadrilateral elements and the pseudo-densities are set to 1. The frame is loaded until fracture using the unsmooth threshold provided in Equation (3.2.14). This analysis is repeated using the smooth threshold and two different values of the smoothing parameter, η_{ks}. The plots of the corresponding force vs. displacement and fracture energy vs. displacement curves are provided in Figure A.1. It is clear from the figures that there is negligible difference in the physics for the chosen values of η_{ks}.

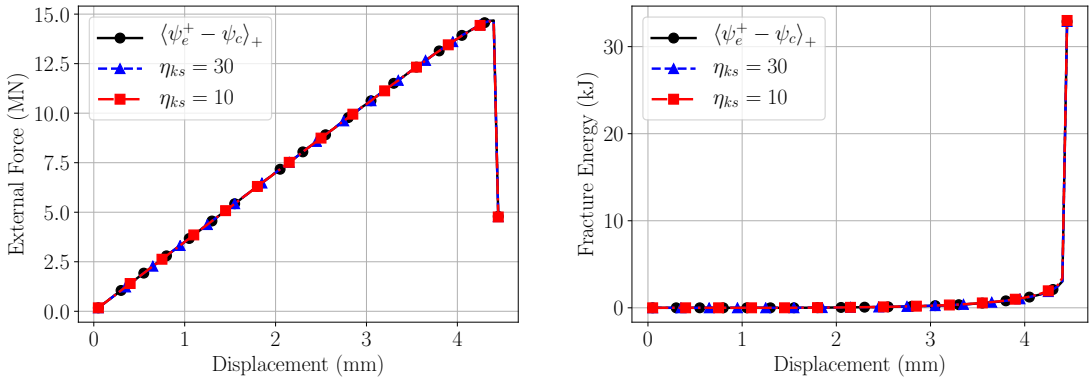

(a) (b)

Figure A.1: Smooth threshold comparison to the nonsmooth threshold function (a) force vs. displacement and (b) fracture energy vs. displacement

A.3 Stress minimization formulation used for comparison

In addition to comparing the results of our formulation in Chapter 3 against those of work-constrained volume minimization with linear elasticity, we also compare our results against a volume-constrained stress-minimization formulation. In particular we have implemented the formulation proposed by Le et al. [6],

$$\begin{aligned} \underset{\boldsymbol{\theta}}{\text{minimize}} \quad & \left[\sum_{e=1}^{N_{elem}} V_e \sigma_e^p\right]^{\frac{1}{p}} \\ \text{subject to} \quad & 0 \leq \theta_e \leq 1, \ e = 1, \ldots, N_{elem} \\ & \Lambda(\boldsymbol{\rho}) \leq \Lambda_{max} \\ & \boldsymbol{K}\boldsymbol{u} = \boldsymbol{f_{ext}} \end{aligned}$$

where σ_e is the Mises equivalent stress evaluated at the center of element, e. Note that $\boldsymbol{K}$ refers to the standard global stiffness matrix from linear elasticity. This formulation is selected to provide a straightforward basis for comparison with the designs obtained using the phase field physics. In particular we constrain the volume to be identical to our result with the highest peak load prior to failure. Additionally, we need not select an arbitrary upper bound for the stress or place an additional work constraint on the optimizer. As mentioned in Le et al. [6], taking larger values of the parameter p will likely make the formulation more susceptible to local minima. We have empirically found that a value of 10 provides the best performing design for the portal frame example, however we apply a different strategy for the L-bracket example as briefly mentioned in Section 3.4.2.

Appendix B

B.1 Return mapping algorithm

The standard radial return mapping algorithm outlined in [188] is utilized in Chapter 4. The only exception is the calculation of the pressure which has been previously provided in Equation (4.2.15). The algorithm begins with the local state variables (ε_n^p, α_n) known at pseudo-time, t_n, and the total strain tensor (ε_{n+1}). The elastic trial state is computed via

$$\varepsilon_{n+1}^{p^{trial}} = \varepsilon_n^p \tag{B.1.1}$$

$$\alpha_{n+1}^{trial} = \alpha_n \tag{B.1.2}$$

$$\boldsymbol{s}_{n+1}^{trial} = 2\mu\mathbb{P}_{dev} : \left(\varepsilon_{n+1} - \varepsilon_{n+1}^{p^{trial}}\right) \tag{B.1.3}$$

$$\boldsymbol{\sigma}_{n+1}^{trial} = p_{n+1}\boldsymbol{I} + \boldsymbol{s}_{n+1}^{trial} \tag{B.1.4}$$

We define $q_{n+1}^{trial} = \sqrt{\frac{3}{2}\boldsymbol{s}_{n+1}^{trial} : \boldsymbol{s}_{n+1}^{trial}}$ for convenience. If $\Phi(\boldsymbol{\sigma}_{n+1}^{trial}, \alpha_{n+1}^{trial}) \leq 0$ then the step is elastic and the trial state is accepted, which results in

$$\varepsilon_{n+1}^p = \varepsilon_{n+1}^{p^{trial}} \tag{B.1.5}$$

$$\alpha_{n+1} = \alpha_{n+1}^{trial} \tag{B.1.6}$$

$$\boldsymbol{\sigma}_{n+1} = p_{n+1}\boldsymbol{I} + \boldsymbol{s}_{n+1}^{trial} \tag{B.1.7}$$

$$\mathbb{C}_{n+1}^{dev} = 2\mu\mathbb{P}_{dev} \tag{B.1.8}$$

Otherwise, we solve the reduced system of local state equations for the increment in the plastic multiplier, $\Delta\gamma$, via the Newton solution of the nonlinear equation,

$$f(\Delta\gamma) = q_{n+1}^{trial} - 3\mu\Delta\gamma - \sigma_y(\alpha_n + \Delta\gamma) = 0 \tag{B.1.9}$$

and with the newly obtained value of $\Delta\gamma$ we update the local state variables via the following expressions.

$$\boldsymbol{\sigma}_{n+1} = p_{n+1}\boldsymbol{I} + \left(1 - \frac{\Delta\gamma\ 3\mu}{q_{n+1}^{trial}}\right)\boldsymbol{s}_{n+1}^{trial} \tag{B.1.10}$$

$$\boldsymbol{\varepsilon}_{n+1}^{p} = \boldsymbol{\varepsilon}_{n}^{p} + \Delta\gamma\boldsymbol{N} \tag{B.1.11}$$

$$\alpha_{n+1} = \alpha_n + \Delta\gamma \tag{B.1.12}$$

$$\mathbb{C}_{n+1}^{dev} = 2\mu\left(1 - \frac{\Delta\gamma\ 3\mu}{q_{n+1}^{trial}}\right)\mathbb{P}_{dev} + 6\mu^2\left(\frac{\Delta\gamma}{q_{n+1}^{trial}} - \frac{1}{3\mu + \frac{d\sigma_y}{d\alpha}\Big|_{\alpha_{n+1}}}\right)\boldsymbol{N}\otimes\boldsymbol{N} \tag{B.1.13}$$

B.2 Parameter selection

B.2.1 Ductile failure criterion

Here we briefly outline the calibration procedure used for the ductile failure criterion, Equation (4.2.20) substituting Equation (4.2.21) with three material parameters ($\hat{d}_1$, $\hat{d}_2$, and $\hat{d}_3$) in this study. The parameters were obtained by repeating the 3 axisymmetric uniaxial tension simulations shown in Bao and Wierzbicki [186] for Aluminum 2024-T351 plate, each with a different notch size which imparts a different stress triaxiality state at the specimen center. The commercial finite element code ABAQUS [235] was used in order to reproduce their results and obtain the required information for calibration of the integral criterion in Equation (4.2.20). This includes the stress triaxiality and equivalent plastic strain predictions at the location of failure of the round bars recorded up until the point of experimental failure. The hardening curve provided in [186] was obtained via a plot digitizer and each of the three round bar tensile experiments were re-simulated. These results are

compared to those reported in [186] in Figure B.1 and a good match is observed in all cases. The

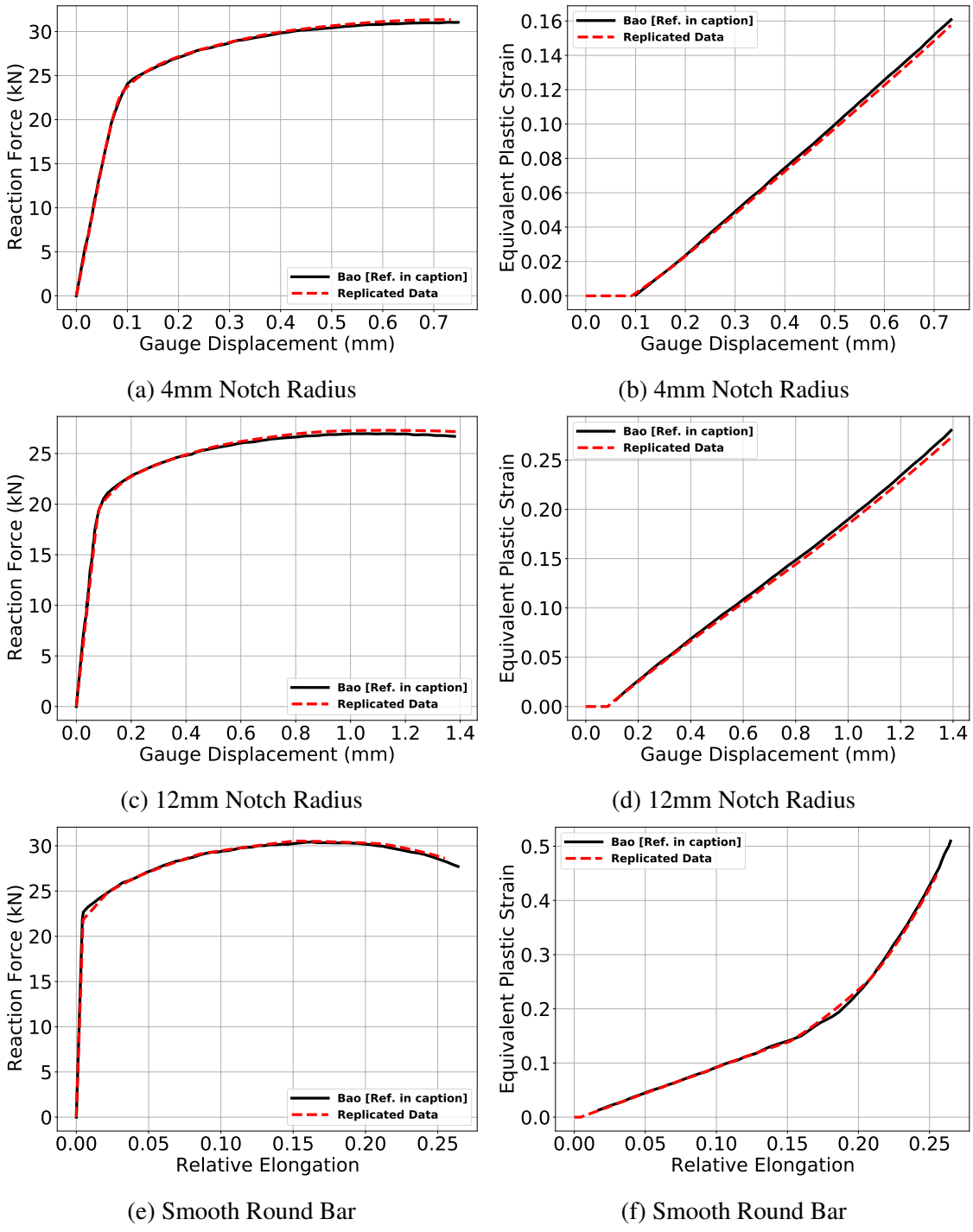

(a) 4mm Notch Radius

(b) 4mm Notch Radius

(c) 12mm Notch Radius

(d) 12mm Notch Radius

(e) Smooth Round Bar

(f) Smooth Round Bar

Figure B.1: Reproduced data from Bao and Wierzbicki [196] for 3 round bar tensile tests.

numerical data was used to calibrate the integral criterion in Equation (4.2.20) using the Johnson-Cook form of the plastic strain to failure in Equation (4.2.21) such that it equals a value of 1 for each

of the three experiments at the crack initiation point. A nonlinear least squares method was used to calibrate each of the three parameters in Equation (4.2.21) such that the value of D_f at failure was equal to 1. This resulted in the parameter values ($\hat{d}_1 = 0.0728$, $\hat{d}_2 = 1.1355$, $\hat{d}_3 = -2.8013$) that were previously provided in the text. The evolution of the ductile failure measure (D_f of Equation (4.2.20)) at the center of each specimen is shown against the equivalent plastic strain in Figure B.2.

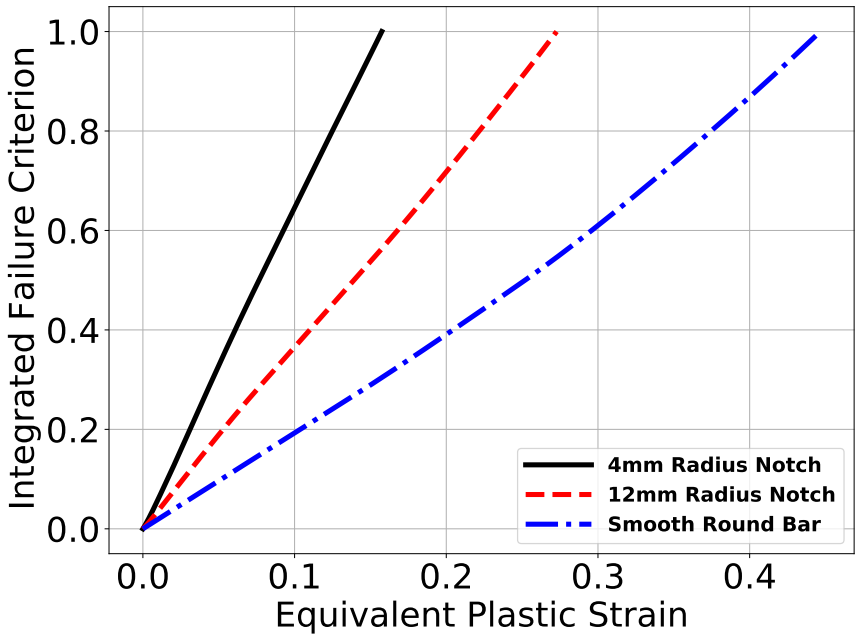

Figure B.2: Evolution of the calibrated ductile failure criterion for each of the 3 round bar specimens.

B.2.2 Elastoplastic hardening and fracture

Next, we briefly provide the calibration procedure employed for the elastoplastic material properties and the properties associated with the phase field fracture model used in Chapter 4. The calibration of the hardening curve parameters was performed via a nonlinear least squares fit of the data provided by Bao and Wierzbicki [186], while the elastic modulus and Poisson's ratio were taken as reported in Bao [185]. These parameters are provided in Table 4.1 of Section 4.5 and are used in all numerical examples in Chapter 4.

The parameters associated with the fracture model are provided in Table 4.2 of Section 4.5. The value of G_c was estimated using data from Ambati et al. [89] with a reported value of

$G_c = 360[kJ/mm^2]$ for smooth round bars of Al-5052. Using the conversion provided in Borden et al. [90] for an equivalent G_c with the cubic degradation function, we estimated G_c to be $108[kJ/mm^2]$. In the absence of an abundance of test data, l_0 was selected as small as possible given our own computational limitations. The three round tensile specimens of Bao and Wierzbicki [186] were used to calibrate the remaining parameters via 3D numerical simulations with symmetry boundary conditions for computational tractability. Finally we note the large-deformation kinematics of the phase field model were necessary in order to calibrate the parameters due to the onset of necking prior to failure observed experimentally for all 3 specimens. The calibrated force vs. displacement curves are provided in Figure B.3 with the associated phase field fracture illustrations in Figure B.4.

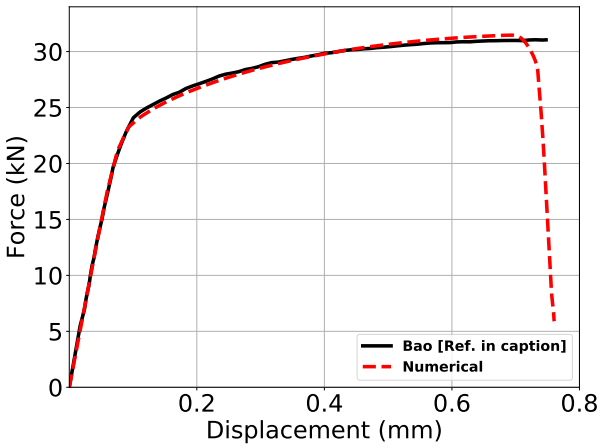

(a) 4mm Notch Radius

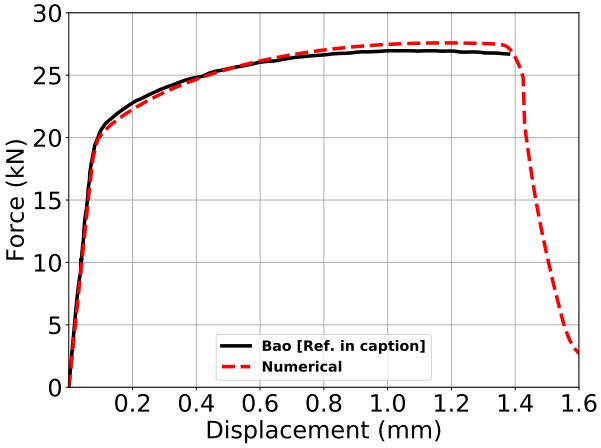

(b) 12mm Notch Radius

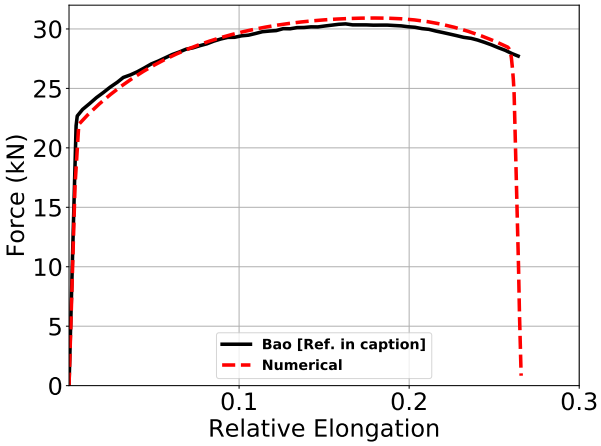

(c) Smooth Round Bar

Figure B.3: Force vs. displacement curve comparison between Bao and Wierzbicki [196] experimental data and numerical model outlined in Section 4.5

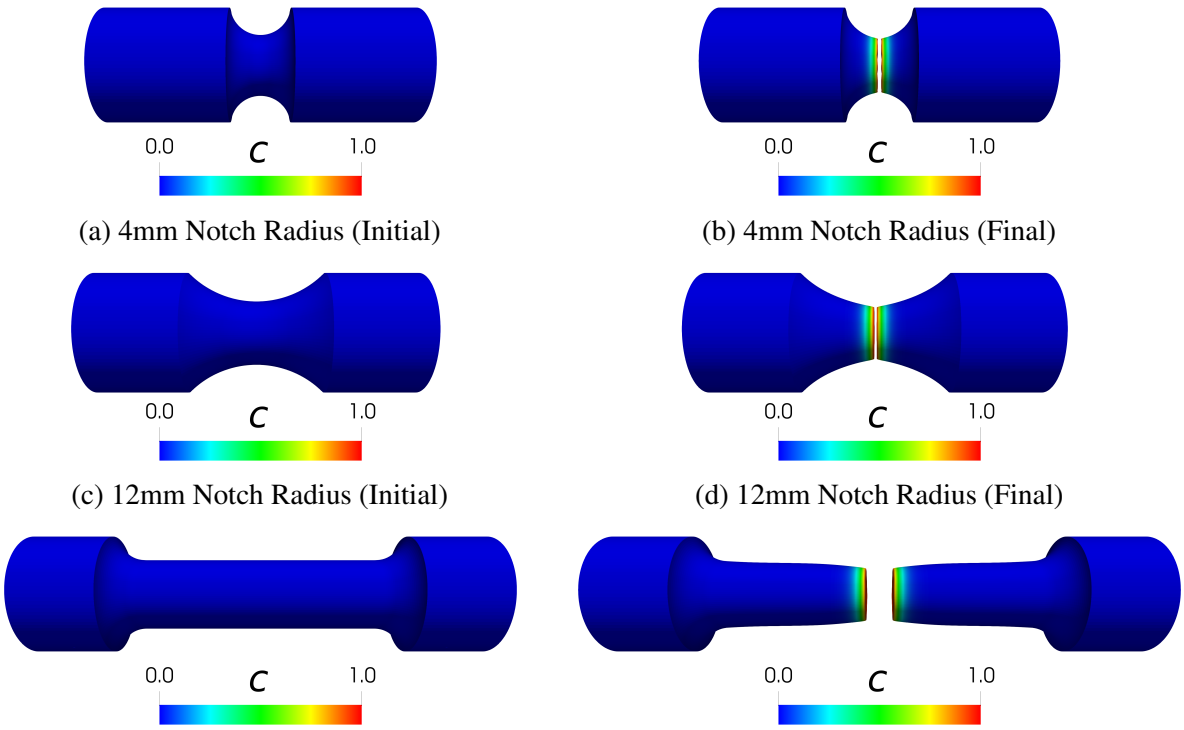

(a) 4mm Notch Radius (Initial)

(b) 4mm Notch Radius (Final)

(c) 12mm Notch Radius (Initial)

(d) 12mm Notch Radius (Final)

(e) Smooth Round Bar (Initial)

(f) Smooth Round Bar (Final)

Figure B.4: Round bar ductile failure simulation results after calibration. Both, initial and final numerical configurations are shown along with the contours of the phase field parameter.

Appendix C

C.1 Validation of plane stress approximation

In an effort to validate the choice of a plane stress assumption employed in Chapter 5 versus the alternative plane strain assumption in two space dimensions, we provide numerical evidence with a single representative geometry. Numerical simulations without the phase field fracture physics were performed utilizing the plane stress assumption, a plane strain formulation, and the full three-dimensional representation. The plane strain and three-dimensional simulations were performed using exactly the same form of strain energy density used in Chapter 5 (namely, Equation 5.2.3) and volumetric-locking is alleviated using a standard mean-dilatation formulation consistent with Bonet and Wood [248]. For the three-dimensional analyses, we use a standard 8-node hexahedral element with first order Lagrange shape functions. An identical in-plane mesh is created for all three cases and the three-dimensional mesh is created by extruding this two-dimensional mesh in the out-of-plane direction with 6 elements through the specimen thickness. We choose an initial notch length corresponding to 10% of the specimen width and a distance between inclusion centers of 24 $[mm]$. Symmetry is employed and one-quarter of the geometry is modeled with relevant symmetric boundary conditions as illustrated in Figure C.1 (note that we may employ symmetric boundary conditions in this instance since the center inclusion is not shifted).

Identical elastic material parameters are used for all three models, corresponding to those provided in Section 5.3.3. Each model is subjected to a representative prescribed displacement of 7.5 $[mm]$ which corresponds to 15 $[mm]$ of stretch when symmetry is not employed. The plane

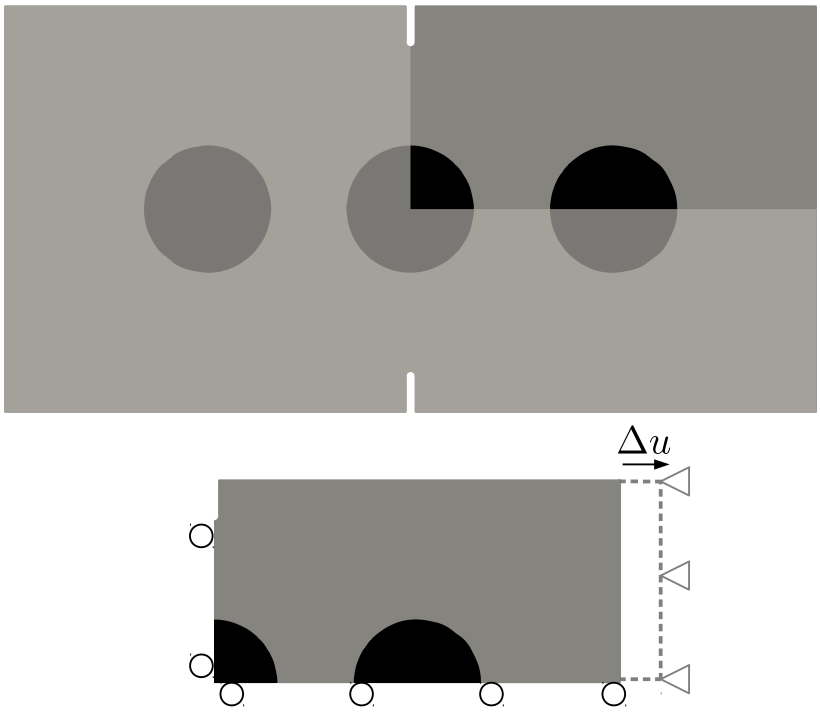

Figure C.1: Boundary conditions for plane stress validation problem

stress assumption is then justified using the plots of the strain energy density in Figure C.3, along the lines shown in Figure C.2 (note that these two regions correspond to those in which cracks typically initiate). Additionally we provide the relevant force-displacement curves for the global problem in Figure C.4.

The strain energy density near the notch tip is clearly best approximated in two-dimensions via a plane stress assumption as evidenced by the line plot in Figure C.3a. The strain energy density between inclusions illustrated in Figure C.3b follows the same general trend as shown for the three-dimensional case, however, plane stress slightly under-predicts this quantity due to the out-of-plane stiffening effect of the rigid inclusions. This stiffening effect also manifests itself in terms of the overall force versus displacement curves provided in Section 5.4.2. For a distance between inclusions of 18 $[mm]$ the under-predicted stiffness is clearly visible. However, for the geometry investigated in this section, Figure C.4 shows very minor stiffness deviation with respect to the three-dimensional formulation. It is also clear from this figure that a plane strain approximation significantly over-predicts the external load, further justifying the use of the plane

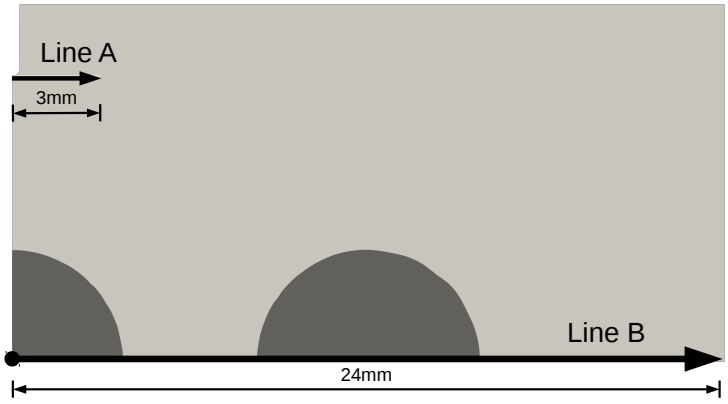

Figure C.2: Lines along which the strain energy density is compared. In three-dimensions the lines lie in the plane at the center of the out-of-plane thickness.

stress approximation used in Chapter 5.

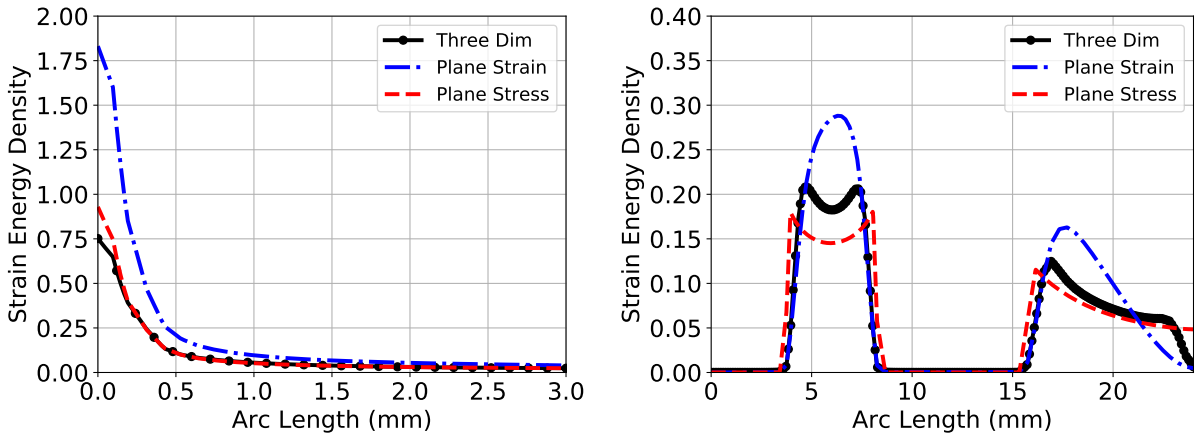

Figure C.3: Line plots of strain energy density along (a) Line A and (b) Line B as illustrated in Figure C.2

C.2 Force-displacement correlation with failure sequences

Here we briefly illustrate a few key points on the force-displacement curves previously presented in Chapter 5, correlated with the system state for two representative examples: one in which the initial crack forms between inclusions and one in which it initiates from the notch tip. These two

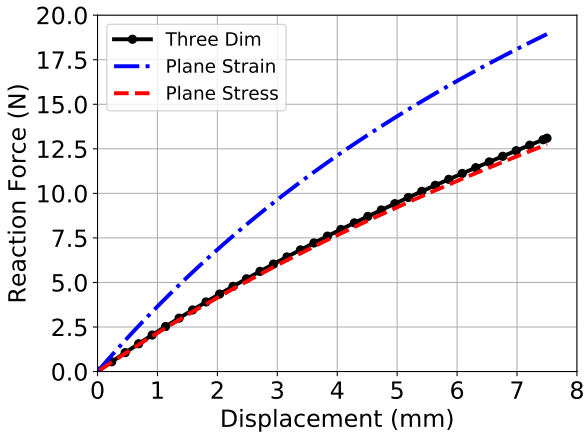

Figure C.4: Force vs. displacement curves illustrating the consistency of the plane stress approximation with that of the three-dimensional formulation.

types of behavior are exhibited in the set of force-displacement curves provided in Section 5.4.2. Generally, initiation between inclusions is accompanied by a force-displacement response with a single peak and subsequent steep decline to zero force. This is demonstrated for N10D18 in Figure C.5 with states A1-A2. In the other case, the crack initiates at the notch tip, propagates until it is arrested by the center inclusion, and stiffening occurs until either the crack continues around the inclusion or a secondary crack initiates between inclusions. This is demonstrated for the N10D30 case below with sequence snapshots labeled B1-B4.

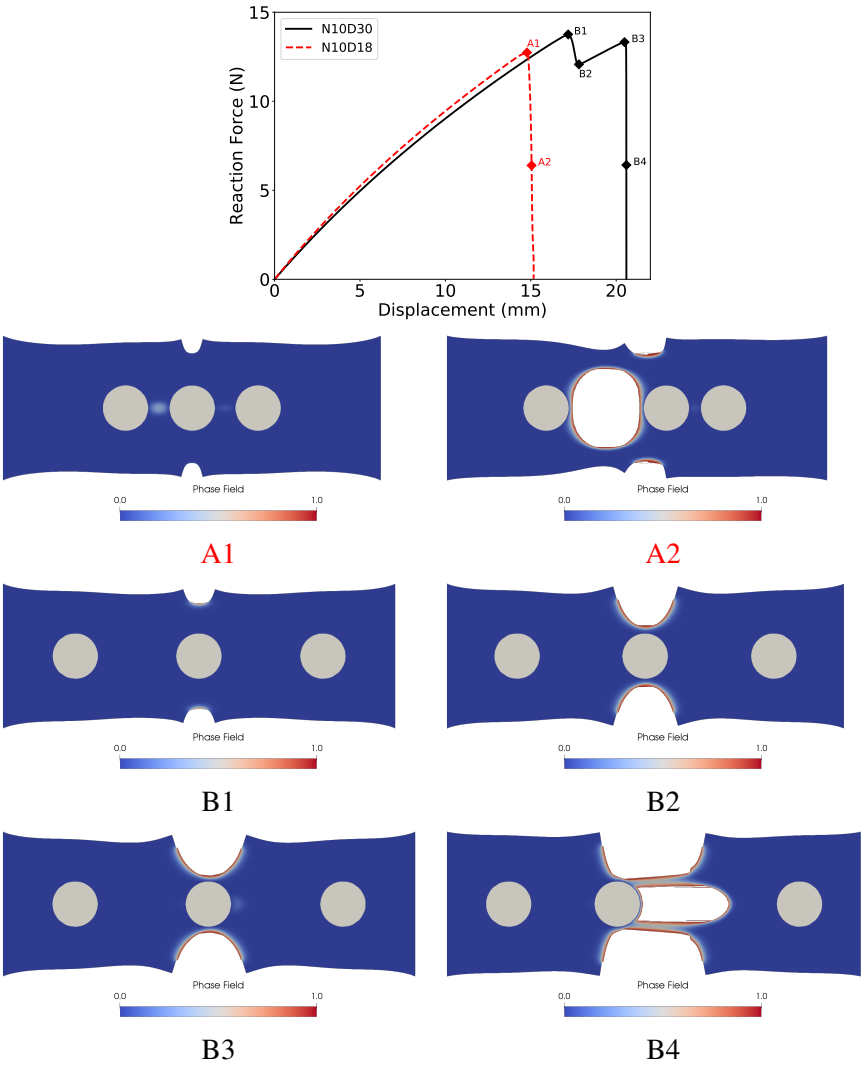

Figure C.5: (A1 - A2) N10D18 and (B1 - B4) N10D30 numerical snapshots

C.3 J-Integral calculations

In an effort to further analyze the crack initiation behavior of the phase field method employed in Chapter 5, contour integrals are computed for certain geometries at the numerically predicted crack initiation point. The commercial finite element code, ABAQUS [235], is used to perform the J-Integral (Rice [249]) computation where the implementation follows the formulation of Shih et al. [250].

Three different notch lengths (N05, N10, N20) are considered, with and without inclusions. These particular geometries were selected since cracks clearly initiate at the notch tip rather than between rigid inclusions or in the bulk material. This allows computation and comparison of the J-Integral values computed at the predicted initiation point (i.e. the notch tip). Generally, crack initiation in the phase field formulation is not clearly defined. Here we define initiation to occur when the peak value of the phase field at the notch-tip has reached 0.25, corresponding to the critical value analytically obtained by Borden et al. [83] in the context of the standard phase field formulation (although it was derived for the small deformation case).

The same material properties presented previously are used in ABAQUS and a force-versus-displacement curve comparison is shown in Figure C.6. A representative result is also provided in Figure C.7 where the notch tip mesh is illustrated. It is expected that the value of the J-Integral is independent of the geometry at the crack initiation point when the material parameters are the same. Seven values are obtained for each geometry corresponding to seven different contour paths around the crack tip. The path-independence of the J-integral is clearly demonstrated in Table C.1. Although there is some variation in the converged value with respect to geometry, the variation is not very large. In light of this we conclude that the phase field formulation employed herein predicts crack growth to occur when approximately the same strain energy release rate is achieved. Nevertheless, more investigations of this type for different geometries are likely needed in order to draw a stronger conclusion.

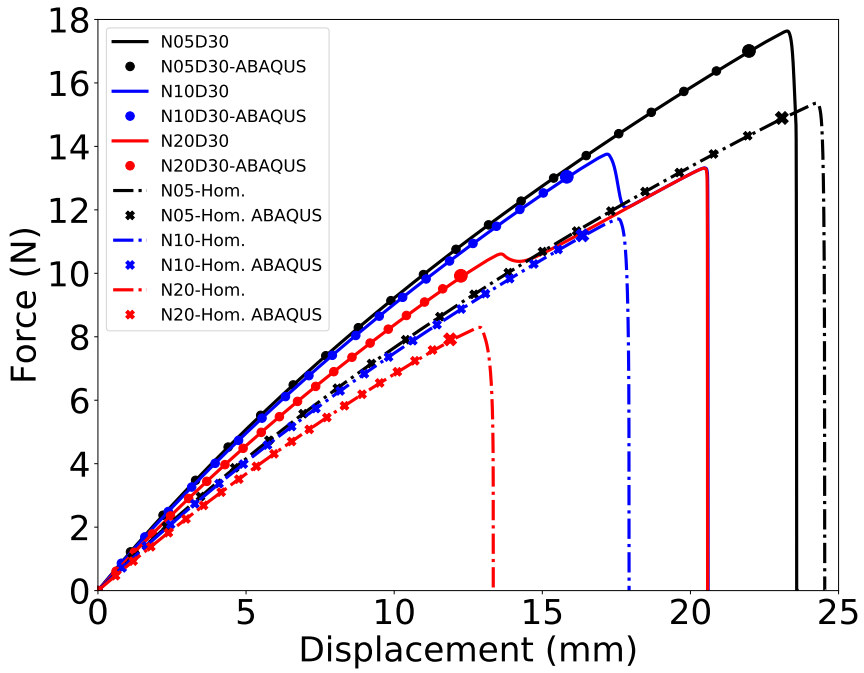

Figure C.6: Force vs. displacement comparison with ABAQUS. The final ABAQUS marker (which is enlarged) represents the load at which we define crack initiation in each case. Note that “Hom." refers to predictions with homogeneous TP material (i.e. geometry without stiff inclusions).

Table C.1: J-Integral values computed for 6 geometries.

	Contour Path						
	1	**2**	**3**	**4**	**5**	**6**	**7**
N05	0.478	0.478	0.478	0.477	0.477	0.477	0.477
N10	0.503	0.502	0.502	0.501	0.501	0.501	0.501
N20	0.518	0.517	0.517	0.517	0.516	0.516	0.516
N05D30	0.481	0.481	0.481	0.480	0.480	0.480	0.480
N10D30	0.507	0.506	0.506	0.506	0.506	0.505	0.505
N20D30	0.524	0.523	0.523	0.523	0.523	0.522	0.522
Mean	0.502	0.501	0.501	0.501	0.501	0.500	0.500
Std. Dev.	0.019	0.019	0.019	0.019	0.019	0.019	0.019

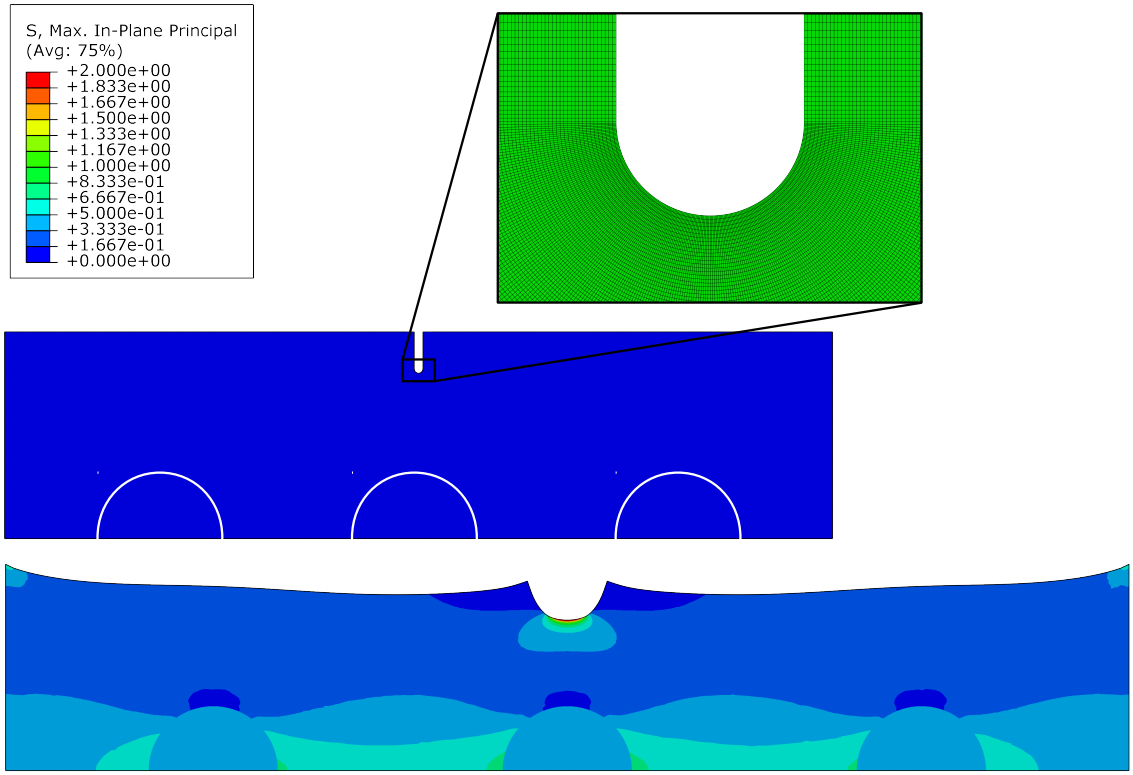

Figure C.7: ABAQUS result illustration for the N10D30 geometry and notch-tip mesh used for the J-Integral calculation. Note that symmetry along the horizontal plane is employed. Both the undeformed and deformed configurations are presented where the contours illustrate the maximum in-plane principal stress distribution.

Appendix D

D.1 Expandable valved conduit constitutive model calibration

D.1.1 Stainless Steel 316L

The uniaxial tension test data provided in [251] is used for calibration of a J_2-plasticity model for 316L stainless steel. An elastic modulus of 193 GPa and Poisson's ratio of 0.27 is assumed and the nonlinear hardening curve is extracted from the test data and used to finely tune the macroscopic response up to the point of experimentally observed failure. The numerical geometry is exactly as reported in [251] for the smooth bar without notches. Results from the calibration procedure are shown in Figure D.1 and a very good match between the nominal stress and strain data is observed.

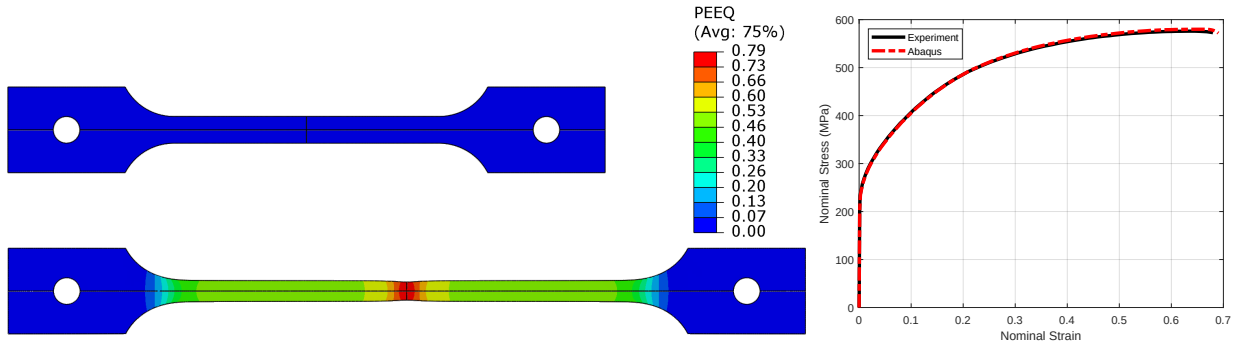

(a) (b)

Figure D.1: Numerical uniaxial test sequence used in the calibration to 316L stainless steel experimental data presented in [251]. Contours in (a) illustrate the equivalent plastic strain field (PEEQ) over the initial undeformed configuration and the deformed configuration immediately preceding the experimentally determined failure point.

The critical value of the hydrostatic ductile failure criterion stated in Equation (D.1.1), where $\bar{\varepsilon}_p^f$ represents the equivalent plastic strain at failure, is then computed at the center of the specimen in a manner consistent with [186], using numerical integration of the computed stress triaxiality over the equivalent plastic strain history. A critical value, $DF_{crit} = 0.269$, was obtained and is used herein for 316L stainless steel.

$$DF_{crit} = \int_0^{\bar{\varepsilon}_p^f} \frac{p}{\sigma_{vm}} \, d\bar{\varepsilon}_p \tag{D.1.1}$$

D.1.2 L605 Cobalt Chromium

Similar to the constitutive model for 316L, J_2-plasticity is also employed for L605. The model is calibrated using uniaxial tension test data obtained from [252]. An elastic modulus of 196 GPa and Poisson's ratio of 0.29 are used while the nonlinear hardening curve is extracted from the experimental data and calibrated up until the point of experimentally observed failure. The numerical model employs a 5mm diameter geometry with dimensions in accordance with the ASTM E8M standard [253]. The results of the model calibration up to the point immediately preceding failure of the specimen are shown in Figure D.2.

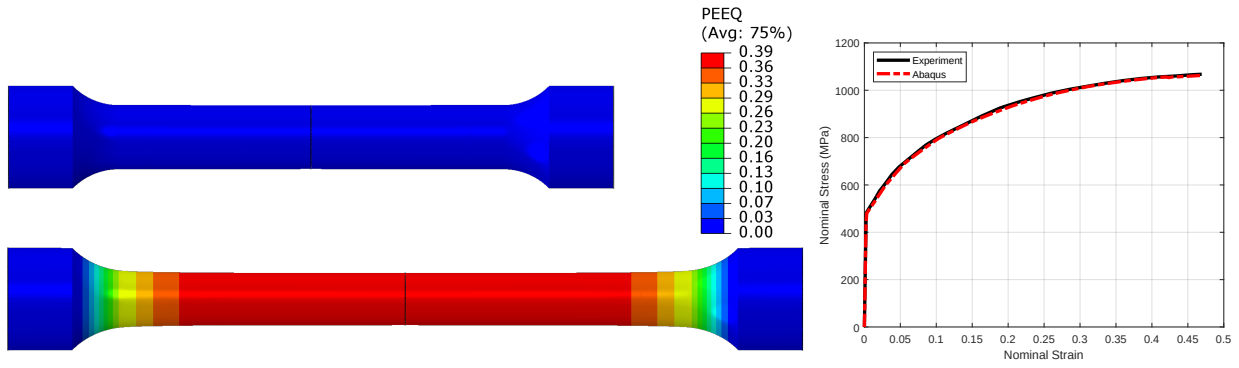

(a) (b)

Figure D.2: Numerical uniaxial test sequence used in the calibration to L605 experimental data presented in [252]. Contours in (a) illustrate the equivalent plastic strain field (PEEQ) over the initial undeformed configuration and the deformed configuration immediately preceding failure.

In a similar manner to the discussion in the previous subsection, the critical value of the

hydrostatic ductile failure criterion is computed at the center of the specimen using numerical integration of the predicted stress triaxiality over the equivalent plastic strain history. A critical value, $DF_{crit} = 0.131$, was obtained and is used in this work for the L605 material.

D.1.3 e-PTFE conduit material

While the actual mechanical constitutive behavior of e-PTFE is extraordinarily complex [254], we approximate its mechanical response using a built-in material model in Abaqus [235] intended for modeling the permanent set that is observed in some elastomers and thermoplastics. The constitutive model we select consists of an Ogden-type hyperelastic strain energy density with two series terms (shown in Equation (D.1.2)), and a multiplicative split of the deformation gradient into elastic and plastic parts (i.e. $\boldsymbol{F} = \boldsymbol{F}^e \boldsymbol{F}^p$).

$$U(\boldsymbol{F}^e) = \sum_{i=1}^{2} \frac{2\mu_i}{\alpha_i^2} \left(\bar{\lambda}_1^{\alpha_i} + \bar{\lambda}_2^{\alpha_i} + \bar{\lambda}_3^{\alpha_i} - 3 \right) + \sum_{i=1}^{2} \frac{1}{D_i} (J-1)^2 \tag{D.1.2}$$

The plastic deformation is integrated employing the pioneering work of Simo [190]. In the above expression, $\{\lambda_i\}$, represent the elastic principal stretches and $J = \det \boldsymbol{F} = \det \boldsymbol{F}^e$ represents the dilatation since the plastic deformation is assumed to be isochoric. The remainder of the variables are material parameters which are provided in Table D.1 below. Eventually, a more complex viscoplastic material model should be employed in order to better approximate the mechanical response of e-PTFE, such as one of those outlined in [255]. Samples of e-PTFE were obtained from International Polymer Engineering [232]. Subsequent mechanical tests were performed in air at ambient temperature (approximately 25°C) using an Instron MicroTester 5848 (Instron, Norwood, Massachusetts), and all measurements were taken from distinct samples. Sample nominal strain was measured using the machine crosshead displacement. Rectangular strips (1x4cm and 0.605mm thick) with a 15mm gauge length between the machine grips were uniaxially stretched to a single predetermined strain at a strain rate of $0.0067 \frac{1}{s}$. The samples were then immediately unloaded, and the grips were returned to the 15mm gauge length at the same rate. The amount of immediately

recoverable deformation was denoted by the point of return to zero stress. The sample was then removed from the machine grips and allowed to recover viscoelastically. Prior to the start of the test, the gauge length between the grip edges was also marked with a marker. After removal from the testing machine, the amount of strain in the sample was tracked by measuring the distance between these marks. The permanent set (i.e. final nominal strain) was measured 24 hours after the end of the unloading step. The calibration results for two cycles of uniaxial tension to different levels of peak strain and subsequent unloading to the permanent plastically deformed state, including an approximate Mullin's damage model, are shown in Figure D.3. Additionally, the elastoplastic hardening curve is given in Table D.2 and the parameters associated with the Ogden-Roxburgh Mullins damage model [256] are shown in Table D.3.

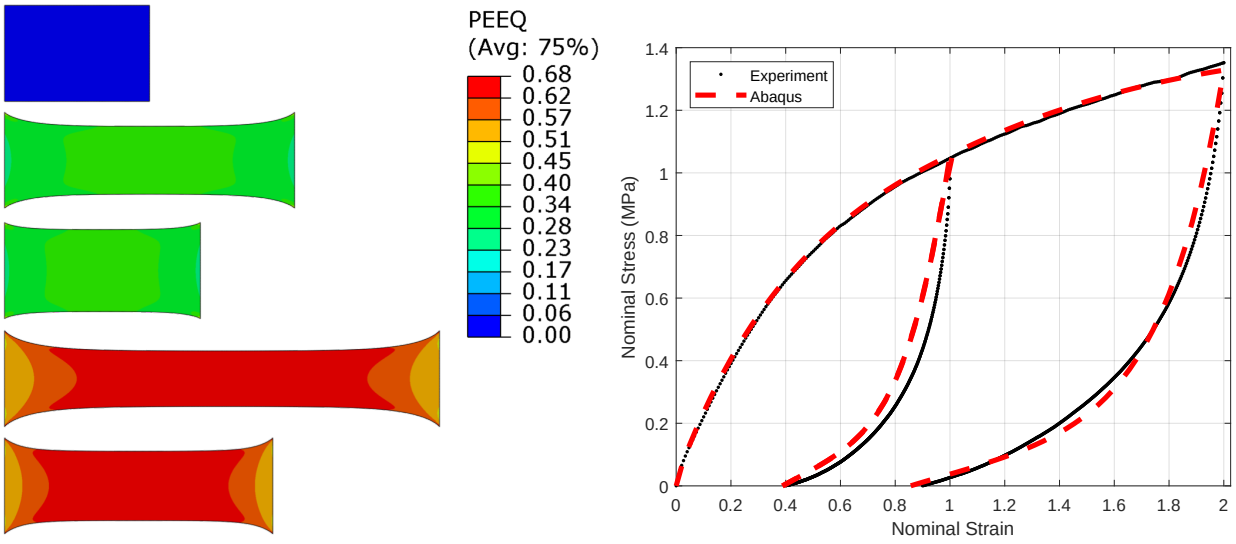

(a) (b)

Figure D.3: Numerical uniaxial test sequence used for material model calibration to e-PTFE experimental data. Contours in (a) illustrate the equivalent plastic strain field over each configuration in the deformation sequence.

Table D.1: e-PTFE hyperelasticity material parameters

$\mu_1\ [MPa]$	α_1	$\mu_2\ [MPa]$	α_2	$D_1\ [1/MPa]$	$D_2\ [1/MPa]$
$1.008(10^{-4})$	25.0	1.26312	3.18637	0.06419	0

Table D.2: e-PTFE multilinear elastoplastic hardening curve (yield stress, σ_y, vs. equivalent plastic strain)

$\bar{\varepsilon}_p$	σ_y $[MPa]$
0	0.0507
0.3365	2.1
0.6419	4.0554
6.4185	41.048

Table D.3: e-PTFE Mullin's damage model parameters (see the Abaqus User's Manual [235])

r	m $[N \cdot mm]$	β
1.223	0	0.785

D.1.4 Carbothane polymeric glue

Since the polymeric glue, Carbothane^{TM}, exhibits very little plastic deformation in the strain range of interest, we omit the elastoplastic physics and approximate the glue region mechanical response with an Ogden type hyperelastic model including two series terms (i.e. Equation D.1.2). A uniaxial tension experiment similar to that described in the previous subsection was conducted in order to calibrate this material model. To prepare the material samples, pellets of Carbothane^{TM} AC-4075A [233] were dissolved in N,N-Dimethylacetamide (DMAc, 99.5%, ACROS Organics, Fair Lawn, New Jersey) to create a viscous solution. After the dissipation of bubbles (approximately 24 hours), the polymer solution was cast onto a flat plate and then dried in an oven for 1 hour at 80°C and ambient pressure. The resulting polymer film was cut into individual specimens for testing, and the thicknesses of the specimens (0.282mm) were measured using a digital thickness gauge (Mitutoyo 547-526S, Mitutoyo Corporation, Tokyo, Japan). Material model calibration results are

illustrated in Figure D.4 with corresponding parameters provided in Table D.4 below. Note that the material is assumed to be incompressible.

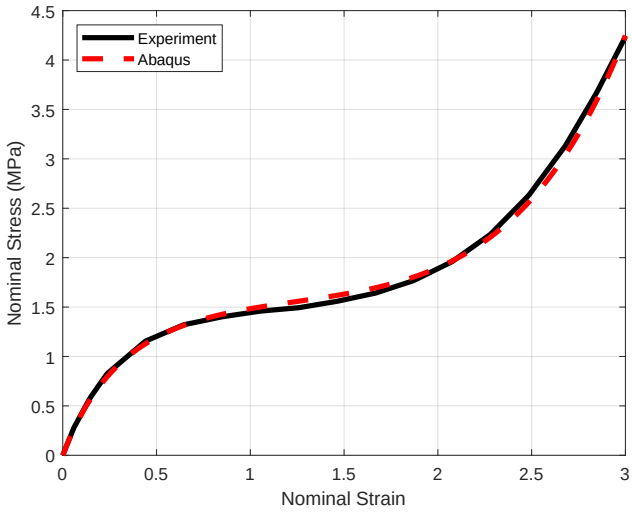

Figure D.4: Hyperelastic model calibration result for Carbothane^{TM}

Table D.4: Carbothane^{TM} hyperelastic material parameters

$\mu_1\ [MPa]$	α_1	$\mu_2\ [MPa]$	α_2	$D_1\ [1/MPa]$	$D_2\ [1/MPa]$
$6.2(10^{-4})$	8.062	1.656	-1.55	0	0